Spring 5-15-2022

Trace Metal Speciation and Impacts on Iron Oxide Transformations and Biogeochemical Cycling

Jinshu Yan
Washington University in St. Louis

WASHINGTON UNIVERSITY IN ST. LOUIS

Department of Earth and Planetary Sciences

Dissertation Examination Committee:
Jeffrey G. Catalano, Chair
Alexander S. Bradley
David A. Fike
Daniel E. Giammar
Kun Wang

Trace Metal Speciation and Impacts on Iron Oxide Transformations and Biogeochemical Cycling

by
Jinshu Yan

A dissertation presented to

the Graduate School

of Washington University in

partial fulfillment of the

requirements for the degree

of Doctor of Philosophy

May 2022
St. Louis, Missouri

TABLE OF CONTENTS

LIST OF FIGURES

CHAPTER 2

LIST OF TABLES

CHAPTER 2

CHAPTER 3

CHAPTER 4

ACKNOWLEDGEMENTS

When I look back to my life at the end of this journey, I have found these five-and-a-half years fulfilled with ups and downs, successes and failures, happiness and frustrations. But my heart is still full of gratitude. First and foremost, I would like to thank my advisor, Jeff Catalano, for his continuous guidance and assistance. He has patiently assisted me with all aspects of my research, from experiment design, results discussion, to thesis revision. It has been my honor to work with him, and I have learned substantially from him on what it takes to be a good researcher. He acted as a role model for me, not only academically but also in life. This journey cannot be made without his guidance and support. I would then like to thank the rest of my committee members for their valuable discussions and suggestions to my research. They have provided me with precious guidance and advice on different mindsets. I would also like to thank Washington University in St. Louis and U.S. Department of Energy, Office of Science, Office of Biological and Environmental Research for financial support of my research projects.

I would like to thank my smart and wonderful group members in the Aqueous Geochemistry and Mineralogy Laboratory. The company from them has made my repeated experiments and extensive writings and presentations a more pleasant experience. I want to give a special acknowledgement to Dr. Elaine Flynn. She has helped me substantially with the method development and analysis of my research, and I am thankful for her expertise and patience that helped me through lots of difficulties. I also want to thank my fellow graduate students in the Earth and Planetary Science Department that I have had the pleasure of meeting, especially my friends Zhengyang Zhou and Zhen Tian, for their generous help both in academic research and in life.

I am also deeply thankful for my family, especially my parents. The pandemic outbreak in my home city has made us suffer, but we got through this together. Our hearts tied close though we are thousands of miles apart. I also want to thank my husband Tian Li especially. I am grateful for his company and comfort anytime when I feel upset. He has taken more responsibility for housework so that I could focus more on my research. I could not have reached this milestone without the love and understanding from my family.

While the pursuit of a doctoral degree is undoubtedly challenging, it is still super exciting and rewarding. I am grateful for everyone I have met and everything I have experienced here, and I am ready for the next step on the new journey.

Jinshu Yan

Washington University in St. Louis

May 2022

ABSTRACT OF THE DISSERTATION

Trace Metal Speciation and Impacts on Iron Oxide Transformations and Biogeochemical Cycling

by

Jinshu Yan

Doctor of Philosophy in Earth and Planetary Sciences

Washington University in St. Louis, 2022

Professor Jeffrey G. Catalano, Chair

Trace metals in anoxic aquatic systems are of great importance for iron oxide transformations and biogeochemical cycling. The presence of trace metal can alter iron oxide transformations under anoxic conditions. Trace metals are also essential for microbially-mediated biogeochemical processes occurring in anoxic wetland soils and stream bed sediments, but low availability of these elements may inhibit anaerobic element cycling and transformations. Trace metal speciation is also vital for understanding the environmental control on nutrients and contaminants. Three projects were conducted to explore trace metal speciation and its associated effect on iron oxide transformations and biogeochemical cycling. First, the Fe(II)-promoted conversion of ferrihydrite to more crystalline phases was investigated in the presence of Zn to examine how trace metals impact and are affected by iron oxide mineral transformation pathways. Second, trace metal speciation was investigated in three distinct subsurface aquatic systems to evaluate the natural variability in the controls on metal behavior in uncontaminated systems. Third, the influence of trace metal availability on CH_4 production was investigated for two wetland soils.

Ferrihydrite, a ubiquitous iron oxide in soils, sediments, and aquatic systems, transforms to other more thermodynamically stable iron oxides through aging, and this process can be catalyzed by the presence of dissolved Fe(II). However, the impact of trace metals on Fe(II)-catalyzed ferrihydrite phase transformations at ambient temperatures and the associated effects on trace metal speciation has seen limited study. In this dissertation, phase transformations of ferrihydrite containing the trace metal zinc in its structure were investigated during aging at ambient temperature in the presence of two different dissolved Fe(II) concentrations at pH 7. X-ray diffraction reveals that low Fe(II) concentration (0.2 mM) generates hematite plus minor lepidocrocite, whereas high Fe(II) concentration (1.0 mM) produces a magnetite-lepidocrocite mixture. Control experiments demonstrate that Zn promotes hematite formation and inhibits goethite formation during ferrihydrite transformations. Extended X-ray absorption fine structure spectroscopy suggests that zinc partitions into the newly formed phases, with a shift from tetrahedral to a mixture of tetrahedral and octahedral coordination in the 0.2 mM Fe(II) system and taking on a spinel-like local structure in the 1.0 mM Fe(II) reaction products. This work indicates that substituting elements in ferrihydrite may play a key role in promoting the formation of hematite in low temperature systems, such as soils or sediments. In addition, the retention of zinc in the products of ferrihydrite phase transformations shows that trace metal micronutrients and contaminants may not be mobilized under circumneutral conditions despite the formation of more crystalline iron oxides.

Solid-phase speciation is likely a critical control on trace metal availability but has seen limited study in anoxic systems having concentrations similar to geological background levels, where metal limitations may be most prevalent. We have investigated trace metal concentrations and solid-phase speciation in three freshwater subsurface aquatic systems: marsh wetland soils,

riparian wetland soils, and the sediments of a streambed. These systems displayed low solid-phase trace metal concentrations, generally at or below geological background levels. All soils and sediments were dominated by quartz but varied in clay mineralogy as well as the organic matter, total sulfur, and total iron contents. Quantitative analysis of copper, nickel, and zinc X-ray absorption near-edge structure spectra revealed similar metal speciation across all sites: adsorbed species, substituents in clay mineral structures, and metal bound to inorganic and organic forms of reduced sulfur. Trace metals bound to reduced sulfur occurred at every site, but the fractional abundance of sulfur-bound species showed no relationship with soil or sediment total sulfur content, which varied by two orders of magnitude. More broadly, the observations in this study suggest that trace metal speciation in freshwater wetland soils and stream sediments is consistently dominated by a small set of recurring components which are distinct for each metal. This may represent a general geochemical phenomenon in anoxic soils and sediments containing trace metals at background concentrations (as low as 3 $\mu g\ g^{-1}$) that was not predicted from systems that are contaminated with or naturally-enriched in copper, nickel, or zinc.

Freshwater wetland soils are foci of biogeochemical cycling as they serve as key sources of methane to the atmosphere. Nickel is notably recognized as playing key roles in the enzymatic pathways of methanogenesis. Low availability of trace metals limits microbial element cycling in laboratory studies, but the occurrence of such limitations in natural subsurface aquatic systems is poorly understood. Microcosm incubation studies were carried out using two distinct wetland soils to explore the effect of dissolved nickel concentrations on methane production. Dissolved nickel concentrations were substantially lower than the optimal range for methanogenesis identified in pure culture studies but both wetland soils continuously produced methane over a 7 to 10 week incubation period. Methane production by the marsh wetland soils did not change

when dissolved Ni concentrations were increased to 0.5 to 4 µM through amendment to parallel incubations, indicating a lack of Ni limitation. In contrast, amending the riparian wetland soil to increase dissolved Ni concentrations to 0.4 to 1.3 µM simulated up to a ~75% increase in methane production from 3 to 10 weeks of incubation time. The water at the marsh wetland contained substantially greater dissolved sulfate concentration than for the riparian wetland (576 µM versus 8 µM), which may have impacted apparent methane production through substrate competition or promotion of anaerobic methane oxidation. Incubations of marsh wetland soils in sulfate-free water also displayed no evidence for nickel limitations. This study indicates that methane production by freshwater wetland soils displays variable responses to changing nickel availability.

This work improves our understanding of the role of trace metals in anoxic aquatic systems. In Fe(II)-induced ferrihydrite transformations, the trace metal Zn alters transformation pathways of ferrihydrite and partially incorporates into the resulting crystalline iron oxides. Such transformations may preserve chemical or isotopic signatures associated with Zn in modern soils or aquatic systems as well as in the sedimentary record. In freshwater wetland soils and stream sediments, trace metal speciation is consistently dominated by a small set of recurring components which are distinct for each metal. Trace metals also play key roles in carbon and nitrogen biogeochemical cycling. Low nickel availability is known to limit methane production in wetland soils, but such limitation occur to variable extents in freshwater wetlands despite the naturally low dissolved concentration of this trace metal in natural aquatic systems.

CHAPTER 1

INTRODUCTION

1.1 BACKGROUND

1.1.1 The Biological Roles of Trace Metals

Trace metals are elements that usually have very low concentrations in the environment. Despite their low abundances, trace metal play essential roles in agriculture, biology, and the cycling of nutrients and contaminants in natural environments. Trace metals can work as important micronutrients for the development of crops. The presence of Zn was a necessary requirement for plant growth (Rengel and Graham, 1995), and Co and Ni were shown to increase plant height and number of branches (Eman et al., 2007; Shen et al., 2018). Cu is vital for plant nutrient as it participates in photosynthesis (Dolmella and Bandoli, 1993).

Trace metals are also relevant to the function of microorganisms. Zn plays important roles in the synthesis of DNA, the function of protein, and the stabilization of immune system (Chasapis et al., 2012; Andreini et al., 2006; Rink and Gabriel, 2000). Zn is also a cofactor of a RNA polymerase (Li et al., 2000; Cuzic and Hartmann, 2005). Ni is a necessary component of plant and bacterial urease (Fishbein et al., 1976; Freyermuth et al., 2000). Deficiency of trace metals could inhibit the growth of microorganisms.

Trace metals also have important roles in carbon and nitrogen cycling. An array of metalloenzymes that contain Ni, Co, Cu, Zn, and other trace elements in cofactors are essential to metabolic pathways involved in methanogenesis (Thauer, 1998; Glass and Orphan, 2012), denitrification (Nojiri et al., 2007), nitrous oxide reduction (Brown et al., 2000), ammonia

oxidation (Gilch et al., 2009; Gilch et al., 2010), and aerobic methanotrophy (Semrau et al., 2010; Chistoserdova, 2011; Sirajuddin and Rosenzweig, 2015). They are also believed to be essential to anaerobic methane oxidation (Scheller et al., 2010; Thauer, 2011) and mercury methylation (Parks et al., 2013; Podar et al., 2015). Trace metals are especially vital in several aspects of methanogen biology. Their use in active sites of essential enzymes is particularly important, but metals also may play a role in inhibiting sulfide toxicity, in binding other nutrients (e.g., phosphate), and as toxins (Oleszkiewicz and Sharma, 1990). The essential role of trace metals in the metabolic pathways of methanogens (Glass and Orphan, 2012) suggests that low trace metal availability may limit methanogenesis in natural systems.

1.1.2 Trace Metal Occurrences

Trace metals can commonly be found in freshwater wetlands and have various sources. Sources of trace metals include parent material, influent water, and atmospheric deposition. Trace metals are naturally present in parent rock and soil, often contained in oxide, silicate, carbonate, and sulfide minerals, although the latter is rare in non-marine wetland settings. Trace metals in the oxidized surface layer of wetlands can be absorbed to Fe, Mn, and Al oxide minerals (Gambrell, 1994), and this may limit the ability of trace metals to migrate into the anaerobic subsurface of wetland soils (Dube et al., 2001). Trace metals can also be introduced to wetlands through surface and groundwater flow, with water depositions dependent on the local geology, climate, and the source of the water (Gambrell, 1994). Trace metals can be released through wetland soils into water column (Ma and Rao, 1997), or can be lost from the wetland through leaching to ground water and surface runoff. Hydrologic inputs from anthropogenic contamination in human-impacted systems can also make large contributions of trace metals

(Sheoran and Sheoran, 2006; Rouff et al., 2013). Metal additions, including Cd, Cr, Cu, Fe, Ni, Mn, Pb, and Zn may be brought in by both dry and wet deposition (Dollar et al., 2001), and the latter has been found to be the dominant source of metals in most wetlands (Connan et al., 2013). While trace metals are primarily hosted by Fe-Mn oxides in natural aerosols, they could also be associated with anthropogenic particulates from coal and oil burning as well as smelting activities (Rahn and Lowenthal, 1985). Mining and processing of uranium ore and nuclear materials may also release trace metals to the environment (Reilly et al., 2018; Xu et al., 2019).

1.1.3 Trace Metal Contamination, Availability, and Controls

Excessive trace metal concentrations caused by heavy metal pollution has long been a challenge for human health and the environment as metal accumulation can lead to toxicity in plants, soils, and sediments (Giller et al., 1998; He et al., 2005). Metal contamination could impair water safety, degrade air quality, and cause harm to the well-being of human and animals through anthropogenic activities and migration up the food chain (Nabulo et al., 2010; Ercilla-Montserrat et al., 2018; Zamora-Ledezma et al., 2021). For instance, microbial biomass is negatively affected by elevated levels of Cu and Zn (Wang et al., 2007), and long exposure of Ni increase bacteria antibiotic resistance in soils (Hu et al., 2017). Deficiency and toxicity can both occur in soil and aquatic systems, and these are often determined by chemical processes that control trace metal availability.

The availability of trace metals is expected to be controlled by their chemical speciation rather than bulk concentration (Worms et al., 2006; Harmsen, 2007). Contaminants may reside in a bound form, associated with soil or sediments, or in a released from in the dissolved phase (National Research Council, 2003). The processing of trace metals by soils can be done through

three major processes: precipitation and dissolution, adsorption and desorption, and complexation and dissociation (He et al., 2005). Soil components are highly relevant with the forms and bioavailability of trace metals. The soluble or exchangeable fraction of metals is typically most available for assimilation by soil microorganisms, while metals bound to carbonate minerals, Fe-Mn oxides, and organic matter have to become mobilized, which depends on the soil pH, redox conditions, and chelation by soluble organic ligands (Ma and Rao, 1997). Wetland soils, especially mineral-based systems, typically show circumneutral pH conditions upon inundation, limiting trace metal mobility (Ponnamperuma, 1972). In contrast, wetland soils rich in organic matter are often acidic when water saturated, solubilizing trace metals. Long-term experimental flooding that lowered soil pH and promoted anaerobic redox conditions has also shown increased concentrations of porewater Fe, Co, and Ni, while porewater Zn concentration increased under oxidizing conditions (Shaheen et al., 2014).

The fate and transport of metal ions is often controlled by sorption to high surface area materials, such as iron oxide minerals (Brown and Parks, 2001; Scheinost et al., 2001; Manceau et al., 2007; Gustafsson et al., 2011; Eickhoff et al., 2014; Tian et al., 2017). In freshwater soil-river systems, iron oxides can serve as nanovectors for trace metal transport, and their transport can be affected by different processes (Hassellöv and von der Kammer, 2008). Secondary iron oxide minerals are important scavengers for trace metal contaminants in acid mine drainage, where the transformation of iron oxides are common (Baleeiro et al., 2018). Aging of metals sorbed to ferrihydrite could enhance their retention, possibly through incorporation (Schultz et al., 1987; Ainsworth et al., 1994; Ford et al., 1997). In addition, metals present during iron oxide minerals formation may coprecipitate into the mineral structure (Martínez and McBride, 1998; Ford et al., 1999; Dai et al., 2017).

1.2 FE(II)-CATALYZED FERRIHYDRITE TRANSFORMATION

Ferrihydrite is ubiquitous in soils and aquatic environments (Combes et al., 1990; Jambor and Dutrizac, 1998; Cornell and Schwertmann, 2003). It has been shown that iron oxides can effectively adsorb or occlude trace metal cations (Jenne, 1968; Lee, 1975; Gambrell, 1994). Because of ferrihydrite's high surface area and nanocrystalline property, the fate and transport of metal ions is often controlled by sorption to ferrihydrite (Brown and Parks, 2001; Scheinost et al., 2001; Manceau et al., 2007; Gustafsson et al., 2011; Eickhoff et al., 2014; Tian et al., 2017). One of ferrihydrite's most distinct property is ferrihydrite's metastability. Ferrihydrite is thermodynamically unstable with respect to other more crystalline iron oxides such as lepidocrocite, goethite, and hematite (Navrotsky et al., 2008), and transforms over time to these more stable phases (Schwertmann and Taylor, 1972; Cornell and Schwertmann, 2003). Ferrihydrite phase transformations can be influenced by various factors, such as temperature, ligand type, and pH (Fischer and Schwertmann, 1975; Schwertmann et al., 1999; Cornell and Schwertmann, 2003). For instance, chloride favors the transformation of ferrihydrite to lepidocrocite, while sulfate supports the conversion to both goethite and lepidocrocite (Hansel et al., 2005; Liu et al., 2008). Variations in pH also affect the formation of magnetite, the relative amounts of goethite and lepidocrocite produced, and the rate of ferrihydrite transformation (Hansel et al., 2005; Boland et al., 2014).

Besides all the external factors, ion substitution can also impact ferrihydrite transformations. Divalent metal cations has been proved to either promote or inhibit ferrihydrite transformation in Fe(II)-free systems at elevated temperature (Cornell, 1988; Martínez and McBride, 1998). Aluminum substitution diminishes secondary mineralization and enhances

preservation of ferrihydrite, requiring greater Fe(II) concentrations to induce transformation compared to Al-free ferrihydrite (Masue-Slowey et al., 2011; Hansel et al., 2011). However, no prior studies have explored the effect of substituting Zn on ferrihydrite transformation pathway. Despite the extensive study of ferrihydrite conversion to other minerals, the role of incorporated trace metals in affecting Fe(II)-catalyzed ferrihydrite transformations and the resulting fate of such metals is poorly understood at ambient temperatures.

1.3 ENVIRONMENTAL CONTROLS OF TRACE METAL SPECIATION IN WETLAND SOILS AND SEDIMENTS

Subsurface aquatic systems in freshwater environments, such as wetland soils and stream sediments, are foci of diverse anaerobic biogeochemical processes (Bowden, 1987; McClain et al., 2003; Kocar and Fendorf, 2009; Zarnetske et al., 2011; Arora et al., 2016; Neumann et al., 2016). Denitrification and methanogenesis in freshwater aquatic systems are two important contributors to the budget of the atmospheric greenhouses gases N_2O and CH_4, respectively (Groffman et al., 1998; Glatzel et al., 2008; Bouwman et al., 2013; Kirschke et al., 2013; Tian et al., 2015; Zhang et al., 2017). There is a growing recognition of the importance of trace metal availability in affecting biogeochemical processes (Basiliko and Yavitt, 2001; Glass and Orphan, 2012; Jacquot et al., 2014). Elements that include cobalt, nickel, copper, and zinc serve as key reaction centers in metalloenzymes (Gärtner et al., 1993; Ermler et al., 1997; Thauer, 1998; Brown et al., 2000; Parks et al., 2013; Zheng et al., 2016) while their low availability has been documented in laboratory studies to inhibit methanogenesis, nitrous oxide reduction to nitrogen, and mercury methylation (Schönheit et al., 1979; Granger and Ward, 2003; Ekstrom and Morel, 2008; Glass and Orphan, 2012; Lu et al., 2018). The geochemistry of trace metals in aquatic

systems may thus have a direct impact on biogeochemical cycling of carbon, nutrients, and contaminants.

Trace metal availability in wetland soils and stream sediments is often controlled by their chemical speciation (Worms et al., 2006; Harmsen, 2007; Zhao et al., 2016). Metal speciation is well studied in contaminated soils and sediments as well as those naturally elevated in trace metals. For example, copper sulfides and metallic copper are often generated in nanoparticulate form in contaminated soils upon flooding (Weber et al., 2009a; Weber et al., 2009b; Fulda et al., 2013a; Hofacker et al., 2013; Xia et al., 2018; Cervi et al., 2021), with organic matter then potentially stabilizing these phases under oxic conditions (Fulda et al., 2013b; Mantha et al., 2019). Ni occurs coprecipitated with iron sulfides and in the octahedral sheets of clay minerals in diverse coastal sediments (Noël et al., 2015; Noël et al., 2017; Merrot et al., 2019). Zinc occurs as sulfide forms under anoxic conditions in metalliferous peatlands (Yoon et al., 2012) and contaminated lake sediments (Webb and Gaillard, 2015), and as zinc carbonate, adsorbed zinc, and possibly zinc oxide in contaminated wetland (Bostick et al., 2001). However, less is known regarding the chemical forms of trace metals in systems having concentrations similar to geological background levels (Webb and Gaillard, 2015; Mehlhorn et al., 2018).

1.4 METHANE PRODUCTION IN NATURAL WETLAND SOILS AND SEDIMENTS

Freshwater wetlands are the single largest natural source of the greenhouse gas CH_4, and also works as primary control on the variability of CH_4 emissions (Bousquet et al., 2006; Chen and Prinn, 2006; Dlugokencky et al., 2009; Bousquet et al., 2011; Kirschke et al., 2013). Wetlands are vital for carbon sequestration and are considered the largest fresh water carbon sinks (Spahni et al., 2011; Daugherty et al., 2019). Emission from wetlands are the single largest

natural contributor to atmospheric methane (Whalen, 2005). These emissions are affected by a series of biogeochemistry factors, such as organic carbon content, trace metal availability, and sulfate and iron concentrations. The large radiative forcing induced by increasing CH_4 concentrations in the atmosphere makes it critical to understand the chemical and physical parameters that affect CH_4 production in wetlands.

CH_4 is produced in the anaerobic subsurface of wetlands through microbial carbon cycling (Serrano-Silva et al., 2014). Methanogens that involve in metabolic pathway all require trace metals to function (Patel et al., 1978; Thauer, 1998; Glass and Orphan, 2012; Glass et al., 2014). There are a plenty of studies that have investigated pure cultures of methanogens and anaerobic bioreactors in laboratories, which have found that limited availability of trace metals inhibits methanogenesis. But very few studies have been done to explore such limitations on natural wetland soils. The potential importance of trace metal availability on methane production limitation in wetland soils and sediments has been overlooked.

1.5 RESEARCH OBJECTIVES

The goal of this dissertation is to investigate trace metal speciation in anoxic aquatic systems and its impact on iron oxide transformations and biogeochemical cycling of carbon. The objectives of this research resulted in three specific studies outlined in the following chapters.

CHAPTER 2: Impact of Zn Substitution on Fe(II)-induced Ferrihydrite Transformation Pathways

The transformation of ferrihydrite to other iron oxides can be affected by various factors: Fe(II) concentrations, pH, temperatures, ligand types, and substituted ions. Extensive studies have investigated the transformation of ferrihydrite to other more stable iron oxides under

different circumstances, but the role of incorporated trace metals in affecting Fe(II)-catalyzed ferrihydrite transformations and the resulting fate of such metals is poorly understood at ambient temperatures. This study thus aims to explore the behavior of Zn during Fe(II)-induced ferrihydrite transformations at 22°C. Transformation products, Zn and Fe concentrations, and Zn speciation were recorded during and after the reaction.

CHAPTER 3: Consistent Controls on Trace Metal Micronutrient Speciation in Wetland Soils and Stream Sediments

Prior studies have provided significant insights into trace metal species in anoxic subsurface systems that are contaminated with or naturally elevated in metals. But it is unclear whether systems that are not contaminated or naturally-enriched in trace metals display the same controls on metal speciation. In this work, we seek to assess the variability in trace metal speciation in the subsurface of diverse freshwater subsurface aquatic systems. We have investigated three aquatic systems: a marsh wetland, a riparian wetland, and the sediments of a stream bed. The three field sites are geologically-distinct regions, each representing a different type of subsurface aquatic system. In this study, major element and trace metal concentrations, dissolved and extractable nutrients, and soil and sediment mineralogy were evaluated at these sites. X-ray absorption spectroscopy evaluated bulk sulfur and iron speciation and quantified the solid-phase speciation of nickel, copper, and zinc. Metal speciation was also compared across sites to identify the dominant forms of trace metals occurring in subsurface aquatic systems.

CHAPTER 4: Evaluation of Potential Nickel Limitations on Methane Production from Marsh and Riparian Wetland Soils

This chapter studies the potential limitation of CH_4 production by the low availability of nickel. The requirement of Ni for methanogens optimal growth is exceptionally high, while prior

works lack adequate discussion of trace metals' impact on natural freshwater wetland systems to date. In this case, incubation studies were done on soils from the marsh wetland and riparian wetland to study the impact of Ni addition on CH_4 production. Gas samples were collected and measured chromatographically over the course of the experiments to compare methane production under different Ni amendments.

1.6 REFERENCES

Ainsworth C. C., Gassman P. L., Pilon J. L. and Van Der Sluys W. G. (1994) Cobalt, cadmium, and lead sorption to hydrous iron oxide: Residence time effect. *Soil Sci. Soc. Am. J.* **58**, 1615–1623.

Arora B., Spycher N. F., Steefel C. I., Molins S., Bill M., Conrad M. E., Dong W., Faybishenko B., Tokunaga T. K., Wan J., Williams K. H. and Yabusaki S. B. (2016) Influence of hydrological, biogeochemical and temperature transients on subsurface carbon fluxes in a flood plain environment. *Biogeochemistry* **127**, 367–396.

Baleeiro A., Fiol S., Otero-Fariña A. and Antelo J. (2018) Surface chemistry of iron oxides formed by neutralization of acidic mine waters: Removal of trace metals. *Appl. Geochemistry* **89**, 129–137.

Basiliko N. and Yavitt J. B. (2001) Influence of Ni, Co, Fe, and Na additions on methane production in Sphagnum-dominated Northern American peatlands. *Biogeochemistry* **52**, 133–153.

Boland D. D., Collins R. N., Miller C. J., Glover C. J. and Waite T. D. (2014) Effect of solution and solid-phase conditions on the Fe(II)-accelerated transformation of ferrihydrite to lepidocrocite and goethite. *Environ. Sci. Technol.* **48**, 5477–5485.

Bostick B. C., Hansel C. M., La Force M. J. and Fendorf S. (2001) Seasonal fluctuations in zinc speciation within a contaminated wetland. *Environ. Sci. Technol.* **35**, 3823–3829.

Bousquet P., Ciais P., Miller J. B., Dlugokencky E. J., Hauglustaine D. A., Prigent C., Van Der Werf G. R., Peylin P., Brunke E. G., Carouge C., Langenfelds R. L., Lathière J., Papa F., Ramonet M., Schmidt M., Steele L. P., Tyler S. C. and White J. (2006) Contribution of anthropogenic and natural sources to atmospheric methane variability. *Nature* **443**, 439–443.

Bousquet P., Ringeval B., Pison I., Dlugokencky E. J., Brunke E. G., Carouge C., Chevallier F., Fortems-Cheiney A., Frankenberg C., Hauglustaine D. A., Krummel P. B., Langenfelds R. L., Ramonet M., Schmidt M., Steele L. P., Szopa S., Yver C., Viovy N. and Ciais P. (2011) Source attribution of the changes in atmospheric methane for 2006-2008. *Atmos. Chem. Phys.* **11**, 3689–3700.

Bouwman A. F., Beusen A. H. W., Griffioen J., Van Groenigen J. W., Hefting M. M., Oenema O., Van Puijenbroek P. J. T. M., Seitzinger S., Slomp C. P. and Stehfest E. (2013) Global trends and uncertainties in terrestrial denitrification and N_2O emissions. *Philos. Trans. R. Soc. B Biol. Sci.* **368**, 20130112.

Bowden W. B. (1987) The biogeochemistry of nitrogen in freshwater wetlands. *Biogeochemistry* **4**, 313–348.

Brown G. E. and Parks G. A. (2001) Sorption of trace elements on mineral surfaces: Modern perspectives from spectroscopic studies, and comments on sorption in the marine environment. *Int. Geol. Rev.* **43**, 963–1073.

Brown K., Tegoni M., Prudêncio M., Pereira A. S., Besson S., Moura J. J., Moura I. and Cambillau C. (2000) A novel type of catalytic copper cluster in nitrous oxide reductase. *Nat. Struct. Biol.* **7**, 191–195.

Cervi E. C., Clark S., Boye K. E., Gustafsson J. P., Baken S. and Burton G. A. (2021) Copper transformation, speciation, and detoxification in anoxic and suboxic freshwater sediments. *Chemosphere* **282**, 131063.

Chasapis C. T., Spiliopoulou C. A., Loutsidou A. C. and Stefanidou M. E. (2012) Zinc and human health: An update. *Arch. Toxicol.* **86**, 521–534.

Chen Y. H. and Prinn R. G. (2006) Estimation of atmospheric methane emissions between 1996 and 2001 using a three-dimensional global chemical transport model. *J. Geophys. Res. Atmos.* **111**, D10307.

Chistoserdova L. (2011) Modularity of methylotrophy, revisited. *Environ. Microbiol.* **13**, 2603–2622.

Combes J. M., Manceau A. and Calas G. (1990) Formation of ferric oxides from aqueous solutions: A polyhedral approach by X-ray Absorption Spectroscopy: II. Hematite formation from ferric gels. *Geochim. Cosmochim. Acta* **54**, 1083–1091.

Connan O., Maro D., Hébert D., Roupsard P., Goujon R., Letellier B. and Le Cavelier S. (2013) Wet and dry deposition of particles associated metals (Cd, Pb, Zn, Ni, Hg) in a rural wetland site, Marais Vernier, France. *Atmos. Environ.* **67**, 394–403.

Cornell R. M. (1988) The influence of some divalent cations on the transformation of ferrihydrite to more crystalline products. *Clay Miner.* **23**, 329–332.

Cornell R. M. and Schwertmann U. (2003) *The Iron Oxides*., VCH Publishers, New York.

Cuzic S. and Hartmann R. K. (2005) Studies on Escherichia coli RNase P-RNA with Zn^{2+} as the catalytic cofactor. *Nucleic Acids Res.* **33**, 2464–2474.

Dai C., Lin M. and Hu Y. (2017) Heterogeneous Ni- and Cd-bearing ferrihydrite precipitation and recrystallization on quartz under acidic pH condition. *ACS Earth Sp. Chem.* **1**, 621–628.

Daugherty E. E., McKee G. A., Bergstrom R., Burton S., Pallud C., Hubbard R. M., Kelly E. F., Rhoades C. C. and Borch T. (2019) Hydrogeomorphic controls on soil carbon composition in two classes of subalpine wetlands. *Biogeochemistry* **145**, 161–175.

Dlugokencky E. J., Bruhwiler L., White J. W. C., Emmons L. K., Novelli P. C., Montzka S. A., Masarie K. A., Lang P. M., Crotwell A. M., Miller J. B. and Gatti L. V. (2009) Observational constraints on recent increases in the atmospheric CH_4 burden. *Geophys. Res. Lett.* **36**, L18803.

Dollar N. L., Souch C. J., Filippelli G. M. and Mastalerz M. (2001) Chemical fractionation of metals in wetland sediments: Indiana Dunes national lakeshore. *Environ. Sci. Technol.* **35**, 3608–3615.

Dolmella A. and Bandoli G. (1993) The biological chemistry of the elements. The inorganic chemistry of life. *Inorganica Chim. Acta* **211**, 247.

Dube A., Zbytniewski R., Kowalkowski T., Cukrowska E. and Buszewski B. (2001) Adsorption and migration of heavy metals in soil. *Polish J. Environ. Stud.* **10**, 1–10.

Eickhoff M., Obst M., Schröder C., Hitchcock A. P., Tyliszczak T., Martinez R. E., Robbins L. J., Konhauser K. O. and Kappler A. (2014) Nickel partitioning in biogenic and abiogenic ferrihydrite: The influence of silica and implications for ancient environments. *Geochim. Cosmochim. Acta* **140**, 65–79.

Ekstrom E. B. and Morel F. M. M. (2008) Cobalt limitation of growth and mercury methylation in sulfate-reducing bacteria. *Environ. Sci. Technol.* **42**, 93–99.

Eman E., Gad N. and Badran M. (2007) Effect of cobalt and nickel on plant growth, yield and flavonoids content of hibiscus sabdariffa L. *Aust. J. Basic Appl. Sci.* **1**, 73–78.

Ercilla-Montserrat M., Muñoz P., Montero J. I., Gabarrell X. and Rieradevall J. (2018) A study on air quality and heavy metals content of urban food produced in a Mediterranean city (Barcelona). *J. Clean. Prod.* **195**, 385–395.

Ermler U., Grabarse W., Shima S., Goubeaud M. and Thauer R. K. (1997) Crystal structure of methyl-coenzyme M reductase: The key enzyme of biological methane formation. *Science* **278**, 1457–1462.

Fischer W. R. and Schwertmann U. (1975) The formation of hematite from amorphous iron(III)hydroxide. *Clays Clay Miner.* **23**, 33–37.

Fishbein W. N., Smith M. J., Nagarajan K. and Scurzi W. (1976) The first natural nickel metalloenzyme: urease. In *Fed. Proc* p. 1680.

Ford R. G., Bertsch P. M. and Farley K. J. (1997) Changes in transition and heavy metal partitioning during hydrous iron oxide aging. *Environ. Sci. Technol.* **31**, 2028–2033.

Ford R. G., Kemner K. M. and Bertsch P. M. (1999) Influence of sorbate-sorbent interactions on the crystallization kinetics of nickel- and lead-ferrihydrite coprecipitates. *Geochim. Cosmochim. Acta* **63**, 39–48.

Freyermuth S. K., Bacanamwo M. and Polacco J. C. (2000) The soybean Eu3 gene encodes an Ni-binding protein necessary for urease activity. *Plant J.* **21**, 53–60.

Fulda B., Voegelin A., Ehlert K. and Kretzschmar R. (2013a) Redox transformation, solid phase speciation and solution dynamics of copper during soil reduction and reoxidation as affected by sulfate availability. *Geochim. Cosmochim. Acta* **123**, 385–402.

Fulda B., Voegelin A., Maurer F., Christl I. and Kretzschmar R. (2013b) Copper redox transformation and complexation by reduced and oxidized soil humic acid. 1. X-ray absorption spectroscopy study. *Environ. Sci. Technol.* **47**, 10903–10911.

Gambrell R. P. (1994) Trace and toxic metals in wetlands-a review. *J. Environ. Qual.* **23**, 883–

891.

Gärtner P., Ecker A., Fischer R., Linder D., Fuchs G. and Thauer R. K. (1993) Purification and properties of N^5-methyltetrahydromethanopterin: coenzyme M methyltransferase from Methanobacterium thermoautotrophicum. *Eur. J. Biochem.* **213**, 537–545.

Gilch S., Meyer O. and Schmidt I. (2009) A soluble form of ammonia monooxygenase in Nitrosomonas europaea. *Biol. Chem.* **390**, 863–873.

Gilch S., Meyer O. and Schmidt I. (2010) Electron paramagnetic studies of the copper and iron containing soluble ammonia monooxygenase from Nitrosomonas europaea. *BioMetals* **23**, 613–622.

Giller K. E., Witter E. and Mcgrath S. P. (1998) Toxicity of heavy metals to microorganisms and microbial processes in agricultural soils: A review. *Soil Biol. Biochem.* **30**, 1389–1414.

Glass J. B. and Orphan V. J. (2012) Trace metal requirements for microbial enzymes involved in the production and consumption of methane and nitrous oxide. *Front. Microbiol.* **3**, 1–20.

Glass J. B., Yu H., Steele J. A., Dawson K. S., Sun S., Chourey K., Pan C., Hettich R. L. and Orphan V. J. (2014) Geochemical, metagenomic and metaproteomic insights into trace metal utilization by methane-oxidizing microbial consortia in sulphidic marine sediments. *Environ. Microbiol.* **16**, 1592–1611.

Glatzel S., Forbrich I., Krüger C., Lemke S. and Gerold G. (2008) Small scale controls of greenhouse gas release under elevated N deposition rates in a restoring peat bog in NW Germany. *Biogeosciences* **5**, 925–935.

Granger J. and Ward B. B. (2003) Accumulation of nitrogen oxides in copper-limited cultures of denitrifying bacteria. *Limnol. Oceanogr.* **48**, 313–318.

Groffman P. M., Gold A. J. and Jacinthe P. A. (1998) Nitrous oxide production in riparian zones and groundwater. *Nutr. Cycl. Agroecosystems* **52**, 179–186.

Gustafsson J. P., Tiberg C., Edkymish A. and Kleja D. B. (2011) Modelling lead(II) sorption to ferrihydrite and soil organic matter. *Environ. Chem.* **8**, 485–492.

Hansel C. M., Benner S. G. and Fendorf S. (2005) Competing Fe(II)-induced mineralization pathways of ferrihydrite. *Environ. Sci. Technol.* **39**, 7147–7153.

Hansel C. M., Learman D. R., Lentini C. J. and Ekstrom E. B. (2011) Effect of adsorbed and substituted Al on Fe(II)-induced mineralization pathways of ferrihydrite. *Geochim. Cosmochim. Acta* **75**, 4653–4666.

Harmsen J. (2007) Measuring bioavailability: From a scientific approach to standard methods. *J. Environ. Qual.* **36**, 1420–1428.

Hassellöv M. and von der Kammer F. (2008) Iron oxides as geochemical nanovectors for metal transport in soil-river systems. *Elements* **4**, 401–406.

He Z. L., Yang X. E. and Stoffella P. J. (2005) Trace elements in agroecosystems and impacts on

the environment. *J. Trace Elem. Med. Biol.* **19**, 125–140.

Hofacker A. F., Voegelin A., Kaegi R., Weber F. A. and Kretzschmar R. (2013) Temperature-dependent formation of metallic copper and metal sulfide nanoparticles during flooding of a contaminated soil. *Geochim. Cosmochim. Acta* **103**, 316–332.

Hu H. W., Wang J. T., Li J., Shi X. Z., Ma Y. B., Chen D. and He J. Z. (2017) Long-term nickel contamination increases the occurrence of antibiotic resistance genes in agricultural soils. *Environ. Sci. Technol.* **51**, 790–800.

Jacquot J. E., Horak R. E. A., Amin S. A., Devol A. H., Ingalls A. E., Armbrust E. V., Stahl D. A. and Moffett J. W. (2014) Assessment of the potential for copper limitation of ammonia oxidation by Archaea in a dynamic estuary. *Mar. Chem.* **162**, 37–49.

Jambor J. L. and Dutrizac J. E. (1998) Occurrence and constitution of natural and synthetic ferrihydrite, a widespread iron oxyhydroxide. *Chem. Rev.* **98**, 2549–2585.

Jenne E. A. (1968) Controls on Mn, Fe, Co, Ni, Cu, and Zn concentrations in soils and water: the significant role of hydrous Mn and Fe oxides. In pp. 337–387.

Kirschke S., Bousquet P., Ciais P., Saunois M., Canadell J. G., Dlugokencky E. J., Bergamaschi P., Bergmann D., Blake D. R., Bruhwiler L., Cameron-Smith P., Castaldi S., Chevallier F., Feng L., Fraser A., Heimann M., Hodson E. L., Houweling S., Josse B., Fraser P. J., Krummel P. B., Lamarque J. F., Langenfelds R. L., Le Quéré C., Naik V., O'doherty S., Palmer P. I., Pison I., Plummer D., Poulter B., Prinn R. G., Rigby M., Ringeval B., Santini M., Schmidt M., Shindell D. T., Simpson I. J., Spahni R., Steele L. P., Strode S. A., Sudo K., Szopa S., Van Der Werf G. R., Voulgarakis A., Van Weele M., Weiss R. F., Williams J. E. and Zeng G. (2013) Three decades of global methane sources and sinks. *Nat. Geosci.* **6**, 813–823.

Kocar B. D. and Fendorf S. (2009) Thermodynamic constraints on reductive reactions influencing the biogeochemistry of arsenic in soils and sediments. *Environ. Sci. Technol.* **43**, 4871–4877.

Lee G. F. (1975) Role of hydrous metal oxides in the transport of heavy metals in the environment. In *Heavy Metals in the Aquatic Environment* pp. 149–153.

Li J., Zheng W., Kwon A. H. and Lu Y. (2000) In vitro selection and characterization of a highly efficient Zn(II)-dependent RNA-cleaving deoxyribozyme. *Nucleic Acids Res.* **28**, 481–488.

Liu H., Guo H., Li P. and Wei Y. (2008) The transformation of ferrihydrite in the presence of trace Fe(II): The effect of the anionic media. *J. Solid State Chem.* **181**, 2666–2671.

Lu X., Johs A., Zhao L., Wang L., Pierce E. M. and Gu B. (2018) Nanomolar copper enhances mercury methylation by *Desulfovibrio desulfuricans* ND132. *Environ. Sci. Technol. Lett.* **5**, 372–376.

Ma L. Q. and Rao G. N. (1997) Chemical fractionation of cadmium, copper, nickel, and zinc in contaminated soils. *J. Environ. Qual.* **26**, 259–264.

Manceau A., Lanson M. and Geoffroy N. (2007) Natural speciation of Ni, Zn, Ba, and As in ferromanganese coatings on quartz using X-ray fluorescence, absorption, and diffraction. *Geochim. Cosmochim. Acta* **71**, 95–128.

Mantha H., Schindler M. and Hochella M. F. (2019) Occurrence and formation of incidental metallic Cu and CuS nanoparticles in organic-rich contaminated surface soils in Timmins, Ontario. *Environ. Sci. Nano* **6**, 163–179.

Martínez C. E. and McBride M. B. (1998) Coprecipitates of Cd, Cu, Pb and Zn in iron oxides: Solid phase transformation and metal solubility after aging and thermal treatment. *Clays Clay Miner.* **46**, 537–545.

Masue-Slowey Y., Loeppert R. H. and Fendorf S. (2011) Alteration of ferrihydrite reductive dissolution and transformation by adsorbed As and structural Al: Implications for As retention. *Geochim. Cosmochim. Acta* **75**, 870–886.

McClain M. E., Boyer E. W., Dent C. L., Gergel S. E., Grimm N. B., Groffman P. M., Hart S. C., Harvey J. W., Johnston C. A., Mayorga E., McDowell W. H. and Pinay G. (2003) Biogeochemical hot spots and hot moments at the interface of terrestrial and aquatic ecosystems. *Ecosystems* **6**, 301–312.

Mehlhorn J., Besold J., Lezama Pacheco J. S., Gustafsson J. P., Kretzschmar R. and Planer-Friedrich B. (2018) Copper mobilization and immobilization along an organic matter and redox gradient - Insights from a Mofette Site. *Environ. Sci. Technol.* **52**, 13698–13707.

Merrot P., Juillot F., Noël V., Lefebvre P., Brest J., Menguy N., Guigner J. M., Blondeau M., Viollier E., Fernandez J. M., Moreton B., Bargar J. R. and Morin G. (2019) Nickel and iron partitioning between clay minerals, Fe-oxides and Fe-sulfides in lagoon sediments from New Caledonia. *Sci. Total Environ.* **689**, 1212–1227.

Nabulo G., Young S. D. and Black C. R. (2010) Assessing risk to human health from tropical leafy vegetables grown on contaminated urban soils. *Sci. Total Environ.* **408**, 5338–5351.

National Research Council (2003) *Bioavailability of contaminants in soils and sediments: processes, tools, and applications*., National Academies Press.

Navrotsky A., Mazeina L. and Majzlan J. (2008) Size-driven structural and thermodynamic complexity in iron oxides. *Science* **319**, 1635–1638.

Neumann R. B., Blazewicz S. J., Conaway C. H., Turetsky M. R. and Waldrop M. P. (2016) Modeling CH_4 and CO_2 cycling using porewater stable isotopes in a thermokarst bog in Interior Alaska: results from three conceptual reaction networks. *Biogeochemistry* **127**, 57–87.

Noël V., Juillot F., Morin G., Marchand C., Ona-Nguema G., Viollier E., Prévot F., Dublet G., Maillot F., Delbes L., Marakovic G., Bargar J. R. and Brown G. E. (2017) Oxidation of Ni-rich mangrove sediments after isolation from the sea (Dumbea Bay, New Caledonia): Fe and Ni behavior and environmental implications. *ACS Earth Sp. Chem.* **1**, 455–464.

Noël V., Morin G., Juillot F., Marchand C., Brest J., Bargar J. R., Muñoz M., Marakovic G.,

Ardo S. and Brown G. E. (2015) Ni cycling in mangrove sediments from New Caledonia. *Geochim. Cosmochim. Acta* **169**, 82–98.

Nojiri M., Xie Y., Inoue T., Yamamoto T., Matsumura H., Kataoka K., Deligeer, Yamaguchi K., Kai Y. and Suzuki S. (2007) Structure and function of a hexameric copper-containing nitrite reductase. *Proc. Natl. Acad. Sci. U. S. A.* **104**, 4315–4320.

Oleszkiewicz J. A. and Sharma V. K. (1990) Stimulation and inhibition of anaerobic processes by heavy metals-A review. *Biol. Wastes* **31**, 45–67.

Parks J. M., Johs A., Podar M., Bridou R., Hurt R. A., Smith S. D., Tomanicek S. J., Qian Y., Brown S. D., Brandt C. C., Palumbo A. V., Smith J. C., Wall J. D., Elias D. A. and Liang L. (2013) The genetic basis for bacterial mercury methylation. *Science* **339**, 1332–1335.

Patel G. B., Khan A. W. and Roth L. A. (1978) Optimum levels of sulphate and iron for the cultivation of pure cultures of methanogens in synthetic media. *J. Appl. Bacteriol.* **45**, 347–356.

Podar M., Gilmour C. C., Brandt C. C., Soren A., Brown S. D., Crable B. R., Palumbo A. V., Somenahally A. C. and Elias D. A. (2015) Global prevalence and distribution of genes and microorganisms involved in mercury methylation. *Sci. Adv.* **1**, e1500675.

Ponnamperuma F. N. (1972) The chemistry of submerged soils. *Adv. Agron.* **24**, 29–96.

Rahn K. A. and Lowenthal D. H. (1985) Pollution aerosol in the Northeast: Northeastern-Midwestern contributions. *Science* **228**, 275–284.

Reilly D. D., Athon M. T., Corbey J. F., Leavy I. I., McCoy K. M. and Schwantes J. M. (2018) Trace element migration during UF4 bomb reduction: Implications to metal fuel production, worker health and safety, and nuclear forensics. *J. Nucl. Mater.* **510**, 156–162.

Rengel Z. and Graham R. D. (1995) Importance of seed Zn content for wheat growth on Zn-deficient soil - II. Grain yield. *Plant Soil* **173**, 267–274.

Rink L. and Gabriel P. (2000) Zinc and the immune system. *Proc. Nutr. Soc.* **59**, 541–552.

Rouff A. A., Eaton T. T. and Lanzirotti A. (2013) Heavy metal distribution in an urban wetland impacted by combined sewer overflow. *Chemosphere* **93**, 2159–2164.

Scheinost A. C., Abend S., Pandya K. I. and Sparks D. L. (2001) Kinetic controls on Cu and Pb sorption by ferrihydrite. *Environ. Sci. Technol.* **35**, 1090–1096.

Scheller S., Goenrich M., Boecher R., Thauer R. K. and Jaun B. (2010) The key nickel enzyme of methanogenesis catalyses the anaerobic oxidation of methane. *Nature* **465**, 606–608.

Schönheit P., Moll J. and Thauer R. K. (1979) Nickel, cobalt, and molybdenum requirement for growth of *Methanobacterium thermoautotrophicum*. *Arch. Microbiol.* **123**, 105–107.

Schultz M. F., Benjamin M. M. and Ferguson J. F. (1987) Adsorption and desorption of metals on ferrihydrite: Reversibility of the reaction and sorption properties of the regenerated solid. *Environ. Sci. Technol.* **21**, 863–869.

Schwertmann U., Friedl J. and Stanjek H. (1999) From Fe(III) ions to ferrihydrite and then to hematite. *J. Colloid Interface Sci.* **223**, 215–223.

Schwertmann U. and Taylor R. M. (1972) The transformation of lepidocrocite to goethite. *Clays Clay Miner.* **20**, 151–158.

Semrau J. D., Dispirito A. A. and Yoon S. (2010) Methanotrophs and copper. *FEMS Microbiol. Rev.* **34**, 496–531.

Serrano-Silva N., Sarria-Guzmán Y., Dendooven L. and Luna-Guido M. (2014) Methanogenesis and methanotrophy in soil: A review. *Pedosphere* **24**, 291–307.

Shaheen S. M., Rinklebe J., Rupp H. and Meissner R. (2014) Temporal dynamics of pore water concentrations of Cd, Co, Cu, Ni, and Zn and their controlling factors in a contaminated floodplain soil assessed by undisturbed groundwater lysimeters. *Environ. Pollut.* **191**, 223–231.

Shen Y., Xiang Y., Xu E., Ge X. and Li Z. (2018) Major co-localized QTL for plant height, branch initiation height, stem diameter, and flowering time in an alien introgression derived Brassica napus DH population. *Front. Plant Sci.* **9**, 1–13.

Sheoran A. S. and Sheoran V. (2006) Heavy metal removal mechanism of acid mine drainage in wetlands: A critical review. *Miner. Eng.* **19**, 105–116.

Sirajuddin S. and Rosenzweig A. C. (2015) Enzymatic oxidation of methane. *Biochemistry* **54**, 2283–2294.

Spahni R., Wania R., Neef L., Van Weele M., Pison I., Bousquet P., Frankenberg C., Foster P. N., Joos F., Prentice I. C. and Van Velthoven P. (2011) Constraining global methane emissions and uptake by ecosystems. *Biogeosciences* **8**, 1643–1665.

Thauer R. K. (2011) Anaerobic oxidation of methane with sulfate: On the reversibility of the reactions that are catalyzed by enzymes also involved in methanogenesis from CO_2. *Curr. Opin. Microbiol.* **14**, 292–299.

Thauer R. K. (1998) Biochemistry of methanogenesis: a tribute to Marjory Stephenson:1998 Marjory Stephenson Prize Lecture. *Microbiology* **144**, 2377–2406.

Tian H., Chen G., Lu C., Xu X., Ren W., Zhang B., Banger K., Tao B., Pan S., Liu M., Zhang C., Bruhwiler L. and Wofsy S. (2015) Global methane and nitrous oxide emissions from terrestrial ecosystems due to multiple environmental changes. *Ecosyst. Heal. Sustain.* **1**, 1–20.

Tian L., Shi Z., Lu Y., Dohnalkova A. C., Lin Z. and Dang Z. (2017) Kinetics of cation and oxyanion adsorption and desorption on ferrihydrite: Roles of ferrihydrite binding sites and a unified model. *Environ. Sci. Technol.* **51**, 10605–10614.

Wang Y., Shi J., Lin Q., Chen X. and Chen Y. (2007) Heavy metal availability and impact on activity of soil microorganisms along a Cu/Zn contamination gradient. *J. Environ. Sci.* **19**, 848–853.

Webb S. M. and Gaillard J. F. (2015) Zinc speciation in contaminated sediments: quantitative determination of zinc coordination by X-ray absorption spectroscopy. *Aquat. Geochemistry* **21**, 295–312.

Weber F. A., Voegelin A., Kaegi R. and Kretzschmar R. (2009a) Contaminant mobilization by metallic copper and metal sulphide colloids in flooded soil. *Nat. Geosci.* **2**, 267–271.

Weber F. A., Voegelin A. and Kretzschmar R. (2009b) Multi-metal contaminant dynamics in temporarily flooded soil under sulfate limitation. *Geochim. Cosmochim. Acta* **73**, 5513–5527.

Whalen S. C. (2005) Biogeochemistry of methane exchange between natural wetlands and the atmosphere. *Environ. Eng. Sci.* **22**, 73–94.

Worms I., Simon D. F., Hassler C. S. and Wilkinson K. J. (2006) Bioavailability of trace metals to aquatic microorganisms: importance of chemical, biological and physical processes on biouptake. *Biochimie* **88**, 1721–1731.

Xia B., Qiu H., Knorr K. H., Blodau C. and Qiu R. (2018) Occurrence and fate of colloids and colloid-associated metals in a mining-impacted agricultural soil upon prolonged flooding. *J. Hazard. Mater.* **348**, 56–66.

Xu L., Yang H., Liu Y. and Zhou Y. (2019) Uranium leaching using citric acid and oxalic acid. *J. Radioanal. Nucl. Chem.* **321**, 815–822.

Yoon S. joung, Yáñez C., Bruns M. A., Martínez-Villegas N. and Martínez C. E. (2012) Natural zinc enrichment in peatlands: Biogeochemistry of ZnS formation. *Geochim. Cosmochim. Acta* **84**, 165–176.

Zamora-Ledezma C., Negrete-Bolagay D., Figueroa F., Zamora-Ledezma E., Ni M., Alexis F. and Guerrero V. H. (2021) Heavy metal water pollution: A fresh look about hazards, novel and conventional remediation methods. *Environ. Technol. Innov.* **22**, 101504.

Zarnetske J. P., Haggerty R., Wondzell S. M. and Baker M. A. (2011) Dynamics of nitrate production and removal as a function of residence time in the hyporheic zone. *J. Geophys. Res. Biogeosciences* **116**, G01025.

Zhang Z., Zimmermann N. E., Stenke A., Li X., Hodson E. L., Zhu G., Huang C. and Poulter B. (2017) Emerging role of wetland methane emissions in driving 21st century climate change. *Proc. Natl. Acad. Sci. U. S. A.* **114**, 9647–9652.

Zhao C. M., Campbell P. G. C. and Wilkinson K. J. (2016) When are metal complexes bioavailable? *Environ. Chem.* **13**, 425–433.

Zheng K., Ngo P. D., Owens V. L., Yang X. P. and Mansoorabadi S. O. (2016) The biosynthetic pathway of coenzyme F430 in methanogenic and methanotrophic archaea. *Science* **354**, 339–342.

CHAPTER 2

IMPACT OF ZN SUBSTITUTION ON FE(II)-INDUCED FERRIHYDRITE TRANSFORMATION PATHWAYS

Published as: Yan J., Frierdich A. J. and Catalano J. G. (2022) Impact of Zn substitution on Fe(II)-induced ferrihydrite transformation pathways. Geochim. Cosmochim. Acta 320, 143–160.

2.1 ABSTRACT

Iron oxide minerals are ubiquitous in soils, sediments, and aquatic systems and influence the fate and availability of trace metals. Ferrihydrite is a common iron oxide of nanoparticulate size and poor crystallinity, serving as a thermodynamically unstable precursor to more crystalline phases. While aging induces such phase transformations, these are accelerated by the presence of dissolved Fe(II). However, the impact of trace metals on Fe(II)-catalyzed ferrihydrite phase transformations at ambient temperatures and the associated effects on trace metal speciation has seen limited study. In the present work, phase transformations of ferrihydrite that contains the trace metal zinc in its structure were investigated during aging at ambient temperature in the presence of two different Fe(II) concentrations at pH 7. X-ray diffraction reveals that low Fe(II) concentration (0.2 mM) generates hematite plus minor lepidocrocite, whereas high Fe(II) concentration (1.0 mM) produces a magnetite-lepidocrocite mixture. In both cases, a substantial fraction of ferrihydrite remains after 12 days. In contrast, zinc-free ferrihydrite forms primarily lepidocrocite and goethite in the presence of 0.2 mM Fe(II), with minor hematite and a trace of ferrihydrite remaining. For 1.0 mM Fe(II), magnetite, goethite, and lepidocrocite form when zinc is absent, leaving no residual ferrihydrite. Transformations of zinc-ferrihydrite produce a transient release of zinc to solution, but this is nearly quantitatively removed into the mineral products after 1 hour. Extended X-ray absorption fine structure spectroscopy suggests that zinc partitions into the newly formed phases, with a shift from tetrahedral to a mixture of tetrahedral and octahedral coordination in the 0.2 mM Fe(II) system and taking on a spinel-like local structure in the 1.0 mM Fe(II) reaction products. This work indicates that substituting elements in ferrihydrite may play a key role in promoting the formation of hematite in low temperature systems, such as soils or sediments. In addition, the retention of zinc in the products of ferrihydrite phase transformation shows that trace metal micronutrients and contaminants may

not be mobilized under circumneutral conditions despite the formation of more crystalline iron oxides. Furthermore, mass balance requires that the abundance and isotopic composition of iron oxide-associated zinc, and possibly other trace metals, in the rock record may be retained during diagenetic phase transformations of ferrihydrite if catalyzed by dissolved Fe(II).

2.2 INTRODUCTION

Ferrihydrite is a ubiquitous, naturally occurring iron oxide that is commonly found in soils and aquatic environments (Combes et al., 1990; Jambor and Dutrizac, 1998; Cornell and Schwertmann, 2003). It has high surface area and is nanocrystalline, producing greater reactivity compared to other iron oxides (Hiemstra, 2013; Hiemstra, 2015). The fate and transport of metal ions is often controlled by sorption to ferrihydrite and other iron oxide minerals (Brown and Parks, 2001; Scheinost et al., 2001; Manceau et al., 2007; Gustafsson et al., 2011; Eickhoff et al., 2014; Tian et al., 2017). Aging of metals sorbed to ferrihydrite enhances their retention, possibly through incorporation (Schultz et al., 1987; Ainsworth et al., 1994; Ford et al., 1997). In addition, metals present during ferrihydrite formation may coprecipitate into the mineral structure (Martínez and McBride, 1998; Ford et al., 1999; Dai et al., 2017).

Ferrihydrite is thermodynamically unstable with respect to more crystalline iron oxides such as lepidocrocite, goethite, and hematite (Navrotsky et al., 2008), and transforms over time to these more stable phases (Schwertmann and Taylor, 1972; Cornell and Schwertmann, 2003). Such transformations play essential roles in determining iron oxide mineralogy in soils (Kämpf and Schwertmann, 1983; Nørnberg et al., 2009; Jiang et al., 2018) as well as modern and ancient sedimentary systems (Chan et al., 2007; Bekker et al., 2010). Ferrihydrite phase transformations involve competitive processes influenced by various factors, such as temperature, ligand type, and pH (Fischer and Schwertmann, 1975; Schwertmann et al., 1999; Cornell and Schwertmann, 2003). Despite being thermodynamically stable (Navrotsky et al., 2008), hematite is only observed to form from ferrihydrite at elevated temperature or after long aging times. Hematite formation from a ferrihydrite precursor occurs rapidly at temperatures of 50 to 100°C (Fischer and Schwertmann, 1975; Johnston and Lewis, 1983; Liu et al., 2005; Das et al., 2011; Soltis et

al., 2016; Jiang et al., 2018) but at 4 to 30°C requires years of aging (Schwertmann and Murad, 1983; Schwertmann et al., 1999; Schwertmann et al., 2000b; Schwertmann et al., 2000a; Schwertmann et al., 2004; Das et al., 2011). Goethite is promoted over hematite at cooler temperature, higher humidity, and at either acidic or alkaline pH (Torrent et al., 1982; Schwertmann and Murad, 1983; Nagano et al., 1994; Das et al., 2011; Zhang et al., 2018).

Similar to heating, dissolved Fe(II) induces rapid transformation of ferrihydrite to more crystalline phases. At ambient temperatures this process yields lepidocrocite, goethite, and, at elevated Fe(II) concentrations, magnetite (Tronc et al., 1992; Hansel et al., 2003; Hansel et al., 2005; Pedersen et al., 2005; Yee et al., 2006; Liu et al., 2007; Yang et al., 2010; Hansel et al., 2011; Boland et al., 2013; Boland et al., 2014; Liu et al., 2016; Tomaszewski et al., 2016; Jones et al., 2017). Hematite also occurs when ferrihydrite reacts with dissolved Fe(II) at elevated temperatures, typically 60 °C or greater (Hansel et al., 2005; Liu et al., 2005; Pedersen et al., 2005; Liu et al., 2008; Wang et al., 2015). Fe(II)-catalyzed transformations to goethite and lepidocrocite involve adsorption and electron transfer at the mineral surface, producing a reactive Fe(III) species that facilitates mass transfer, growth, and formation of new phases (Boland et al., 2014; Sheng et al., 2020b). Ligand type impacts ferrihydrite transformation pathways: chloride favors the transformation of ferrihydrite to lepidocrocite, while sulfate supports the conversion to both goethite and lepidocrocite (Hansel et al., 2005; Liu et al., 2008). Variations in pH affect the formation of magnetite, the relative amounts of goethite and lepidocrocite produced, and the rate of ferrihydrite transformation (Hansel et al., 2005; Boland et al., 2014). Surface adsorbates, including silicic acid and organic matter, both slow ferrihydrite transformation and alter the final minerals that form (Jones et al., 2009; Wang et al., 2015; Thomasarrigo et al., 2018; Xiao et al., 2018; Zhou et al., 2018; Thomasarrigo et al., 2019; Sheng et al., 2020a). Aluminum substitution

diminishes secondary mineralization and enhances preservation of ferrihydrite, requiring greater Fe(II) concentrations to induce transformation compared to Al-free ferrihydrite (Masue-Slowey et al., 2011; Hansel et al., 2011).

Trace metals also impact ferrihydrite transformations. At 70°C, coprecipitated divalent metal cations may either promote or inhibit ferrihydrite transformation in Fe(II)-free systems (Cornell, 1988; Martínez and McBride, 1998). Dissolved Zn alters thermal transformation products of ferrihydrite at 70°C, increasing hematite content at the expense of goethite through a Zn-maghemite precursor while also forming franklinite, although the latter requires high Zn concentrations to form (Sakakibara et al., 2019). At ambient temperature, adsorbed divalent cations (Liu et al., 2016) or rare earth elements (Fei et al., 2018) inhibit Fe(II)-catalyzed ferrihydrite transformations and alter the amounts of goethite, lepidocrocite, and magnetite that formed. No prior studies have reported that metals promote hematite formation near 25°C or cooler.

Despite the extensive study of ferrihydrite conversion to other minerals, the role of incorporated trace metals in affecting Fe(II)-catalyzed ferrihydrite transformations and the resulting fate of such metals is poorly understood at ambient temperatures. This study thus investigates the behavior of Zn during Fe(II)-induced ferrihydrite transformations at 22°C. Zinc was selected for study because it has been shown to homogeneously distribute when coprecipitated with ferrihydrite (Martin et al., 2005) and promotes hematite formation from ferrihydrite during thermal transformation at 70°C (Sakakibara et al., 2019). Dissolved Fe(II) catalyzes ferrihydrite phase transformations, similar to elevated temperatures, and Zn may thus provide a possible route to low-temperature hematite formation. Batch aging experiments were carried out in which Zn-substituted ferrihydrite was exposed to 0.2 mM or 1.0 mM dissolved

Fe(II) at pH 7 for 12 days. These Fe(II) concentrations were selected for investigation because they span the range used in prior studies and are anticipated to produce different ferrihydrite transformation products (Tronc et al., 1992; Hansel et al., 2003; Hansel et al., 2005; Pedersen et al., 2005; Yee et al., 2006; Liu et al., 2007; Yang et al., 2010; Hansel et al., 2011; Boland et al., 2013; Boland et al., 2014; Liu et al., 2016; Tomaszewski et al., 2016; Jones et al., 2017). X-ray diffraction (XRD) patterns collected over the course of the experiment tracked the mineralogical evolution, with mineral abundances quantified via Rietveld refinement. Concentrations of dissolved Zn and Fe were measured over time to study the release and uptake of Zn as well as the consumption and adsorption of Fe(II). X-ray absorption fine structure (XAFS) spectra were obtained to evaluate the coordination state of Zn associated with iron oxide minerals at different aging times.

2.3 MATERIALS AND METHODS

2.3.1 Mineral Synthesis

Zn-substituted ferrihydrite was synthesized using a modification of previously described methods for the 2-line form of this mineral (Schwertmann and Cornell, 2000). A substitution level of ~2 mol.% Zn was selected to provide a concentration that is observable using spectroscopic methods (Waychunas et al., 2002), would potentially affect ferrihydrite transformation processes (Liu et al., 2016; Sakakibara et al., 2019), and was expected to result in homogeneous substitution (Martin et al., 2005). 73.5 mL of 5 M sodium hydroxide was added dropwise over 20 minutes into a 125 mL solution containing 0.98 M ferric nitrate and 0.02 M zinc chloride that was continuously stirred. The introduction of sodium hydroxide transiently increases pH until Fe(III) hydrolysis and precipitation occurs. Solution pH was continuously measured during base addition and maintained below pH 11 to prevent the formation of goethite;

The final pH of the solution was 8.29. The resulting suspension was then centrifuged at 15000 rpm for 20 minutes. After centrifugation, the majority of the supernatant was decanted off, and the precipitate was resuspended in ultrapure water (>18.2 MΩ cm) and then centrifuged again. This process was repeated 6 times until the particles would no longer settle during centrifugation, indicating a substantial decrease in ionic strength. After the final centrifugation, ferrihydrite was resuspended in ultrapure water; the pH of this suspension was 6.9. The suspension was then freeze dried and stored in polypropylene bottles wrapped in aluminum foil at room temperature. The drying step was done to inhibit changes in ferrihydrite properties associated with aging as a suspension (Hiemstra et al., 2019) and to maintain a single batch of Zn-substituted ferrihydrite for use in multiple experiments. Zn-free ferrihydrite was prepared using the same procedure but with the initial 125 mL solution containing 1.0 M ferric nitrate and no added zinc chloride.

2.3.2 Mineral Transformation Experiments

All solutions were prepared in an anaerobic chamber (Coy Laboratory Products) in a ~3% H_2 and ~97% N_2 atmosphere that was circulated over a Pd catalyst to eliminate residual O_2. Ultrapure water was deoxygenated by bubbling for at least 5 hours with ultrahigh purity N_2 (<1 ppmv O_2) before being transferred into the glove box. The oxygen level in the deoxygenated ultrapure water was further lowered by sparging with anaerobic chamber atmosphere that was first bubbled through a 10% pyrogallol and 40% potassium hydroxide solution, which serves as a secondary oxygen trap that also scavenges CO_2. Dissolved oxygen was measured colorimetrically using CHEMets test kit K-7540 to confirm a concentration below the ~1 μg/L detection limit. Synthesized ferrihydrite with and without structural Zn was brought into the

glove box at least 48 hours prior to use. All salts used were ACS reagent grade or better and were prepared in the anaerobic chamber as stock solutions.

Experiments were conducted in solutions containing final concentrations of 10 mM sodium chloride, 1 mM 3-(N-Morpholino) propanesulfonic acid (MOPS, a pH buffer with a pKa value of 7.20), and either 1.0 mM or 0.2 mM dissolved Fe(II), prepared from iron(II) chloride tetrahydrate. The initial pH was adjusted to 7.0 using 0.1 N NaOH and 0.1 N HCl. A Zn-substituted ferrihydrite suspension was prepared at an initial concentration of 4 g/L of ground, freeze-dried ferrihydrite in deoxygenated deionized water. A desired volume of the suspension was injected into to the sample solution to reach a final concentration of 1 g/L. Addition of Zn-ferrihydrite marked the start of the reaction. Each experiment was conducted in a 500 mL polypropylene bottle with the fluid continuously stirred using a magnetic stirrer with a PTFE-coated magnet. The bottle was wrapped in aluminum foil to inhibit photoreduction and the cap was sealed using vinyl tape to decrease the possibility of residual oxygen in the anaerobic chamber from inadvertently oxidizing the solution. The pH of the solution was checked, recorded, and adjusted back to 7.00±0.05 daily during the reaction. 20 mL subsamples of the well-mixed suspension were removed after 2 minutes, 5 minutes, 15 minutes, 1 hour, 2 hours, 4 hours, 7 hours, 1 day, 3 days, 5 days, 7 days, and 12 days. Each was immediately filtered using a 0.22 μm mixed cellulose ester (MCE) membrane in a polypropylene syringe filter enclosure. Ferrihydrite aggregation was adequate to allow separation of particles from the fluid via filtration as confirmed by the lack of dissolved Fe measured in Fe(II)-free control samples. The filtered fluids were then removed from the anaerobic chamber and acidified with 2% trace metal grade nitric acid before dissolved Fe and Zn concentrations were measured by inductively-coupled plasma mass spectrometry (ICP-MS) using a Thermo iCAP Q instrument. Uncertainties in the

measured concentrations were calculated from the uncertainties in the calibration curve parameters determined by regression. Minerals collected on the filter membranes were dried in a vacuum desiccator inside the anaerobic chamber for further characterization.

A series of control experiments were carried out to evaluate possible sources of experimental error and to assess the impact of dissolved Fe(II) and substituting Zn on the reactions. Ferrihydrite-free control experiments were prepared with the same fluid composition as described above (a duplicate set for each Fe(II) concentration) in order to evaluate possible sample contamination with Zn, as has been noted in prior work (Kay, 2004; Bryan et al., 2015; Garçon et al., 2017). Two additional control experiments (one for each Fe(II) concentration) replicated the mineralogical transformation studies described above but added Zn-free ferrihydrite instead of Zn-substituted ferrihydrite. Mineral and filtered fluid samples were collected after 12 days of reaction for these control experiments. Dissolved concentrations were obtained using inductively-coupled plasma optical emission spectrometry (ICP-OES) using a Thermo iCap 7400 Duo instrument. The fluid compositional results of the ferrihydrite-free and Zn-free control experiments are described in the Supplementary Material, and the mineral transformation products in the Zn-free control studies are described in Section 3.2.3.

2.3.3 Mineral characterization

Mineral solids were analyzed by powder X-ray diffraction (XRD) using a Bruker d8 Advance diffractometer equipped with a Cu X-ray tube operating at 40 kV and 40 mA. The initial synthetic ferrihydrite samples and the solids collected after selected reaction times were studied. Minerals were ground using an agate mortar and pestle and mounted on a zero-background silicon sample holder. XRD scans were performed from 15° to 85° with a 0.02° step-

size, 0.5 s count time per step at a rotation rate of 15 rotations per minute. A LynxEye XE energy-dispersive silicon-strip detector was used for data collection in a continuous scan mode, with each of the 192 detector strips measuring the same angular position for the specified counting time. This yielded a total integration time of 96 s per 2θ value. The Diffrac.Eva application was used for initial phase identification. Rietveld refinement of the XRD patterns determined the quantitative abundances of crystalline phases and the semi-quantitative abundance of ferrihydrite using a partially empirical approach (see Supplementary Material). Fitting was conducted in the Profex (Doebelin and Kleeberg, 2015) interface to BGMN (Bergmann et al., 1998). Brunauer-Emmett-Teller (BET) specific surface area of each synthesized mineral was determined by collecting N_2 gas adsorption isotherms using a Quantachrome Autosorb-1 Instrument. The Zn concentration in Zn-substituted ferrihydrite was determined by acid digestion. 5 mg of ferrihydrite was dissolved in 10 mL of 4 M hydrochloric acid at 70°C. The solution was then diluted 1:100 using 2% trace metal grade nitric acid and measured by ICP-MS.

2.3.4 X-ray absorption fine structure spectroscopy

Zn K-edge XAFS spectra, including the X-ray absorption near-edge structures (XANES) and extended X-ray absorption fine-structure (EXAFS) regions, were measured on the initial Zn-ferrihydrite, a Zn-substituted hematite standard, and the solid-phase products formed from reaction of Zn-ferrihydrite with 0.2 mM Fe(II) for 2 h and 12 d, with 1.0 mM Fe(II) after 12 days. Preparation of the Zn-substituted hematite standard was described in a prior study (Frierdich et al., 2012). Ferrihydrite and its transformation products were collected on 0.22 μM MCE filter membranes, which were sealed between two sheets of Kapton film. Data collection

was performed on beamline 12-BM-B at the Advanced Photon Source (APS) at Argonne National Laboratory. The beamline employed a Si (111) fixed offset monochromator which was detuned 30% to reduce the harmonic content of the beam. Toroidal focusing and flat mirrors were used to increase usable X-ray flux and further reduce harmonics, with focusing effects resulting in a beam of ~700 μm diameter. Zn K-edge data were collected in fluorescence yield with a 13-element energy-dispersive Ge detector. Aluminum foil was used to selectively reduce the Fe fluorescence intensity in order to prevent detector saturation. Between three and nine scans were collected and averaged per sample, depending on the signal intensity. No variations were observed among the individual spectra in the XANES region and the only change in the EXAFS spectra among scans were random fluctuations in high-k region associated with noise. An additional standard of Zn adsorbed to hematite was prepared by reacting 0.2 mM zinc chloride with 4 g L^{-1} synthetic hematite in a 0.01 M sodium chloride solution for 5 days at pH 7.5. Details of the hematite synthesis and sample preparation follow procedures described previously (Frierdich et al., 2011). The Zn K-edge XAFS spectrum of this additional sample was measured at APS beamline 20-BM-B using similar optics and detector details as those described above.

The X-ray energy for all measurements was calibrated by setting the maximum in the first derivative of the X-ray absorption near-edge structure spectrum of a Zn metal foil to 9659 eV for the Zn K-edge. XAFS spectral scans were averaged using the Athena (Ravel and Newville, 2005) interface to IFEFFIT (Newville, 2001). The normalized and background subtracted k3-weighted EXAFS spectra of Zn were fitted to structural models in SixPACK (Webb, 2005) using phase and amplitude functions generated from the structure of franklinite (Verwey and Heilmann, 1947) using FEFF 7.02 (Ankudinov and Ravel, 1998). Spectra were fit

in k-space over a range of 3.0 to 11.3 Å and in R-space from 1.0 to 4.0 Å for all samples and standards. The coordination number (N), interatomic distances (R), σ^2 (a Debye−Waller-type factor based on a Gaussian distribution of interatomic distances), and ΔE_0 were refined using nonlinear least-squares fitting. For samples with weak or potentially overlapping second-shell features, σ^2 was fixed at 0.008 based on typical values observed in prior studies (Waychunas et al., 2002; Gräfe and Sparks, 2005; Frierdich and Catalano, 2012). The amplitude reduction factor (S02) was fixed at 0.9 for spectral fitting. Linear combination fitting in select cases was conducted in Athena.

2.4 RESULTS

2.4.1 Characterization of Zn-ferrihydrite and Zn-free Ferrihydrite

XRD revealed that Zn-ferrihydrite contained no detectable crystalline impurities, yielding a pattern consistent with that of 2-line ferrihydrite (Fig. 2.1a). While not exployed in the present work, a prior study employing a similar co-precipitation method found no accessory phases, such as $Zn(OH)_2$, using transmission electron microscopy (Martin et al., 2005). Zn-free ferrihydrite generated an XRD pattern generally indistinguishable from the Zn-substituted phase. The Zn content of the substituted ferrihydrite determined by acid digestion was 2.2 mol.%, close to the target substitution level of 2.0 mol.%. The BET specific surface areas for Zn-free ferrihydrite and Zn-ferrihydrite were 297 m^2/g and 233 m^2/g, respectively. Structural analysis of the Zn K-edge EXAFS spectrum (Fig. 2.1b) of Zn-ferrihydrite shows that Zn substituted in tetrahedral configuration, as indicated by the Zn-O interatomic distance and coordination number (Table 2.1). The Zn-Fe distance of ~3.45 Å (Table 2.1) indicates corner-sharing between a zinc tetrahedron and an iron octahedron, a geometry also consistent with zinc substituting into the

proposed tetrahedral iron site in ferrihydrite (Michel et al., 2007; Michel et al., 2010; Maillot et al., 2011).

Table 2.1. Results of structural model fitting of Zn K-edge EXAFS spectra.

Sample	**Shell**	**N**[a]	**R (Å)**[b]	**σ^2 (Å^2)**[c]	**ΔE_0 (eV)**[d]	**χ_v^{2}**[e]
Zn-ferrihydrite	O	4.2(4)[f]	1.97(1)	0.0064(9)	0(1)	18.88
	Fe	6(2)	3.45(1)	0.017(3)		
Zn-hematite	O	3	1.98(1)	0.0052(9)	1(2)	13.32
	O	3	2.20(2)	0.013(3)		
	Fe	3.5(3)	2.98(1)	0.008		
	Fe	1.4(4)	3.33(2)	0.008		
Zn adsorbed to hematite	O	6.2(5)	2.014(6)	0.012(1)	-2(1)	2.15
	Fe	0.2(2)	3.28(6)	0.008		
0.2 mM Fe(II), 2 hr	O	3.9(5)	1.966(8)	0.006(1)	1(1)	14.64
	Fe	6(3)	3.43(2)	0.018(5)		
0.2 mM Fe(II), 12 d	O	3.0(2)	1.98(1)	0.004(1)	1(2)	3.30
	O	1.6(2)	2.14(2)	0.004(1)		
	Fe	0.8(2)	2.98(2)	0.008		
	Fe	0.7(3)	3.39(3)	0.008		
1.0 mM Fe(II), 12 d	O	4(1)	1.97(1)	0.005(2)	1(2)	15.44
	Fe	18(5)	3.50(2)	0.015(3)		

[a]Coordination number. [b]Interatomic distance. [c]Debye-Waller factor. [d]Difference in the threshold Fermi level between data and theory. [e]Reduced chi squared, a goodness-of-fit parameter (Kelly et al., 2008). [f]Values in parentheses are fitting uncertainties in the last digit, reported at the 1σ level. Parameters without uncertainties were held constant during fitting.

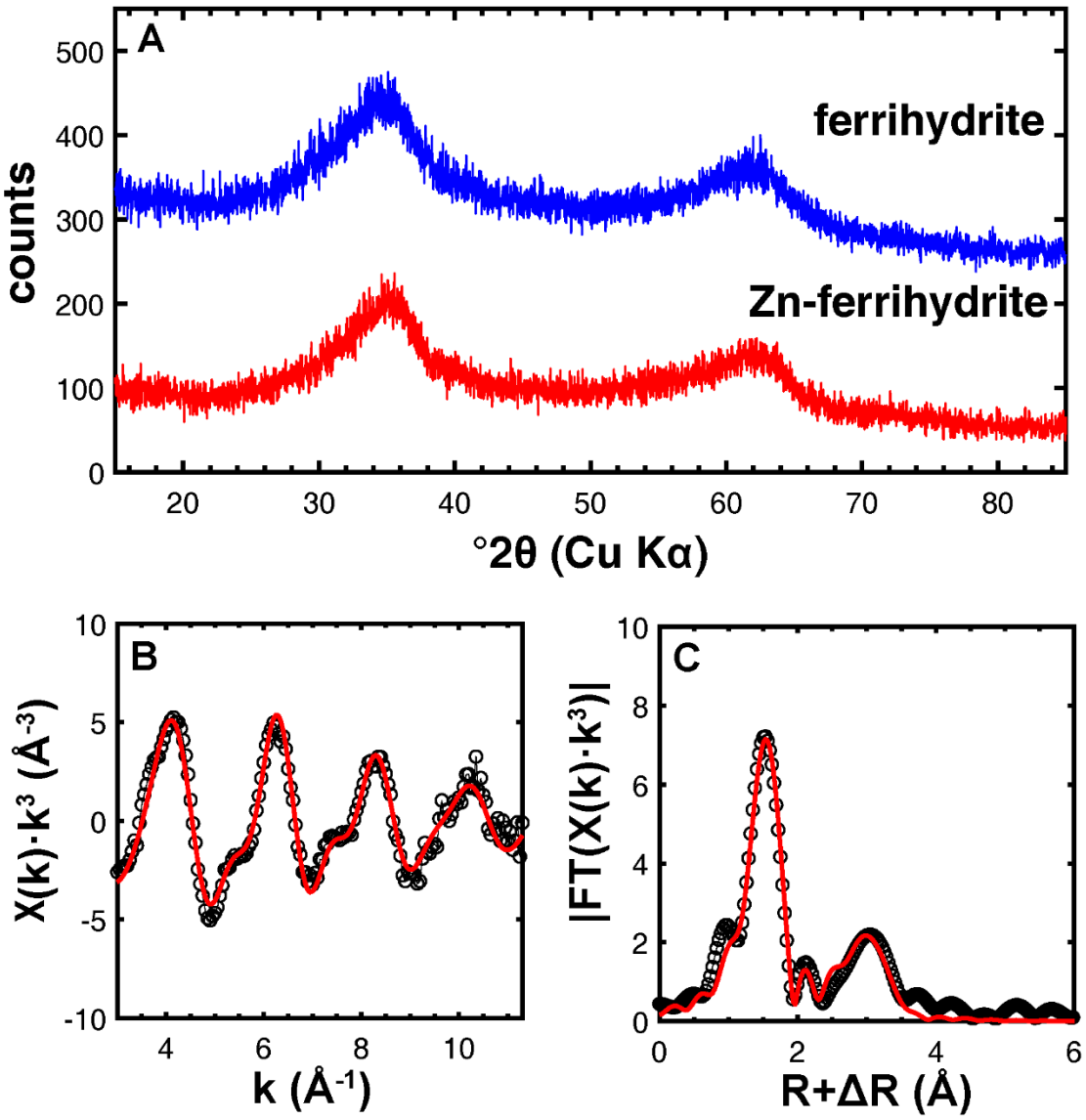

Figure 2.1. (a) XRD patterns of as-synthesized Zn-free ferrihydrite and Zn-ferrihydrite. (b) Data (dotted) and structural model fit (lines) of Zn K-edge EXAFS spectra (left) and Fourier Transform magnitude (right) of Zn-ferrihydrite.

2.4.2 Phase Transformations of Zn-ferrihydrite

2.4.2.1 Transformations in 0.2 mM Fe(II)

Upon contact with 0.2 mM dissolved Fe(II), Zn-ferrihydrite showed no evidence of converting to more crystalline phases over the first few hours of reaction (Fig. 2.2). By 1 d of

reaction, initial hematite peaks appeared in the XRD pattern, with both hematite and lepidocrocite clearly present after 3 d of reaction. These continued to grow in through the 12 d duration of the experiment (Fig. 2.2). The broad ferrihydrite peaks persisted throughout much of the reaction, with weak background features present at ~35° and ~63° 2θ. Rietveld refinement of the XRD data (Fig. A2.2) quantified the crystalline phases formed and provided a semi-quantitative estimate of ferrihydrite abundance (Fig. 2.3) using an empirical approach described in the Supplementary Material. This analysis shows that hematite was the dominant crystalline product formed from Zn-ferrihydrite over the course of reaction, with lepidocrocite present as 10-20 wt.% of the crystalline phases. Ferrihydrite transformed slowly and only partially converted to crystalline phases after 12 d of reaction, with more than 50 wt.% of the initial ferrihydrite remaining (Fig. 2.3).

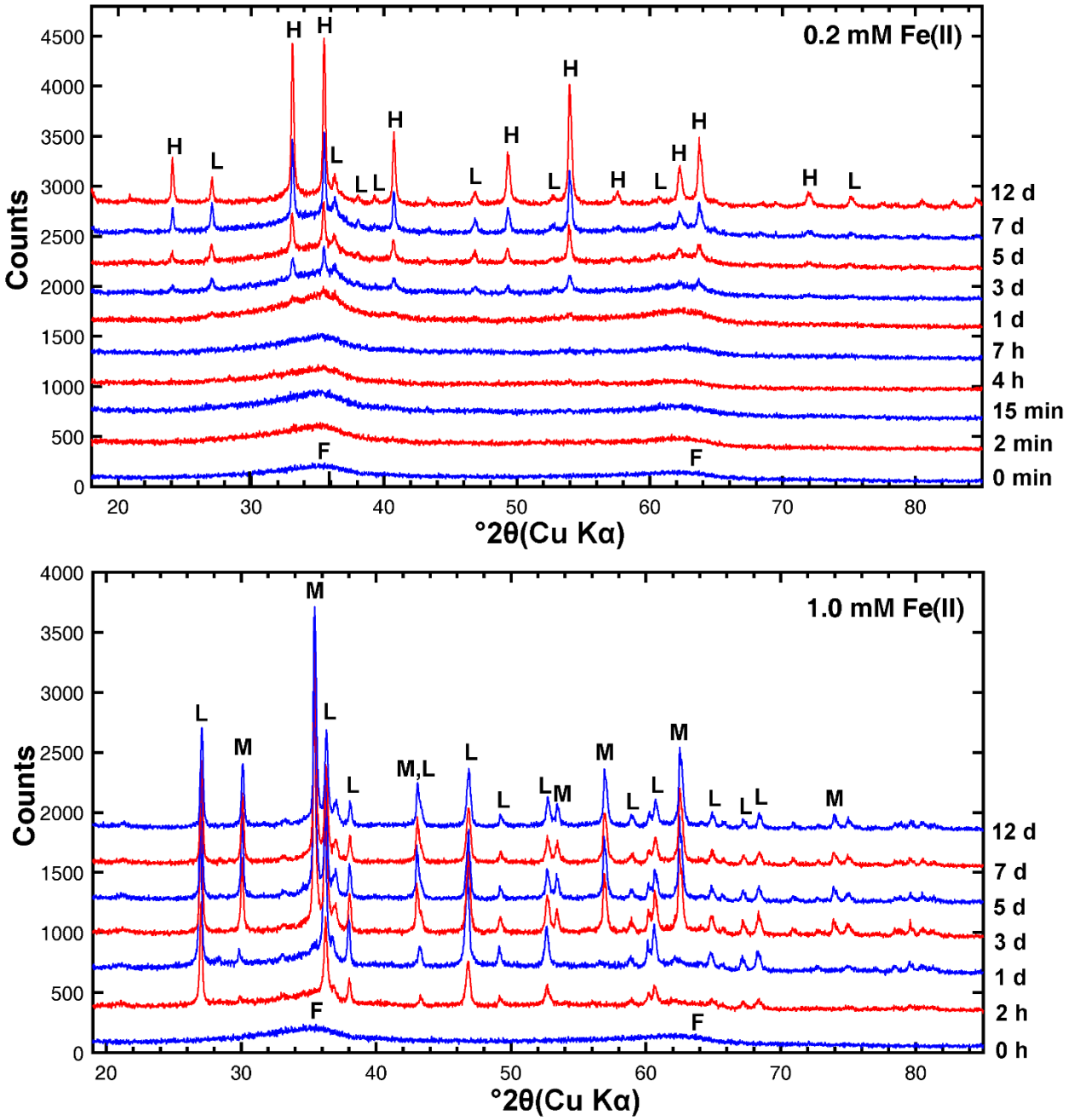

Figure 2.2. XRD patterns of the solid phase products of Zn-ferrihydrite reaction with (top) 0.2 mM Fe(II) and (bottom) 1.0 mM Fe(II). Diagnostic peaks are labeled to indicate mineral phases: F=ferrihydrite, L=lepidocrocite, H=hematite, M=magnetite.

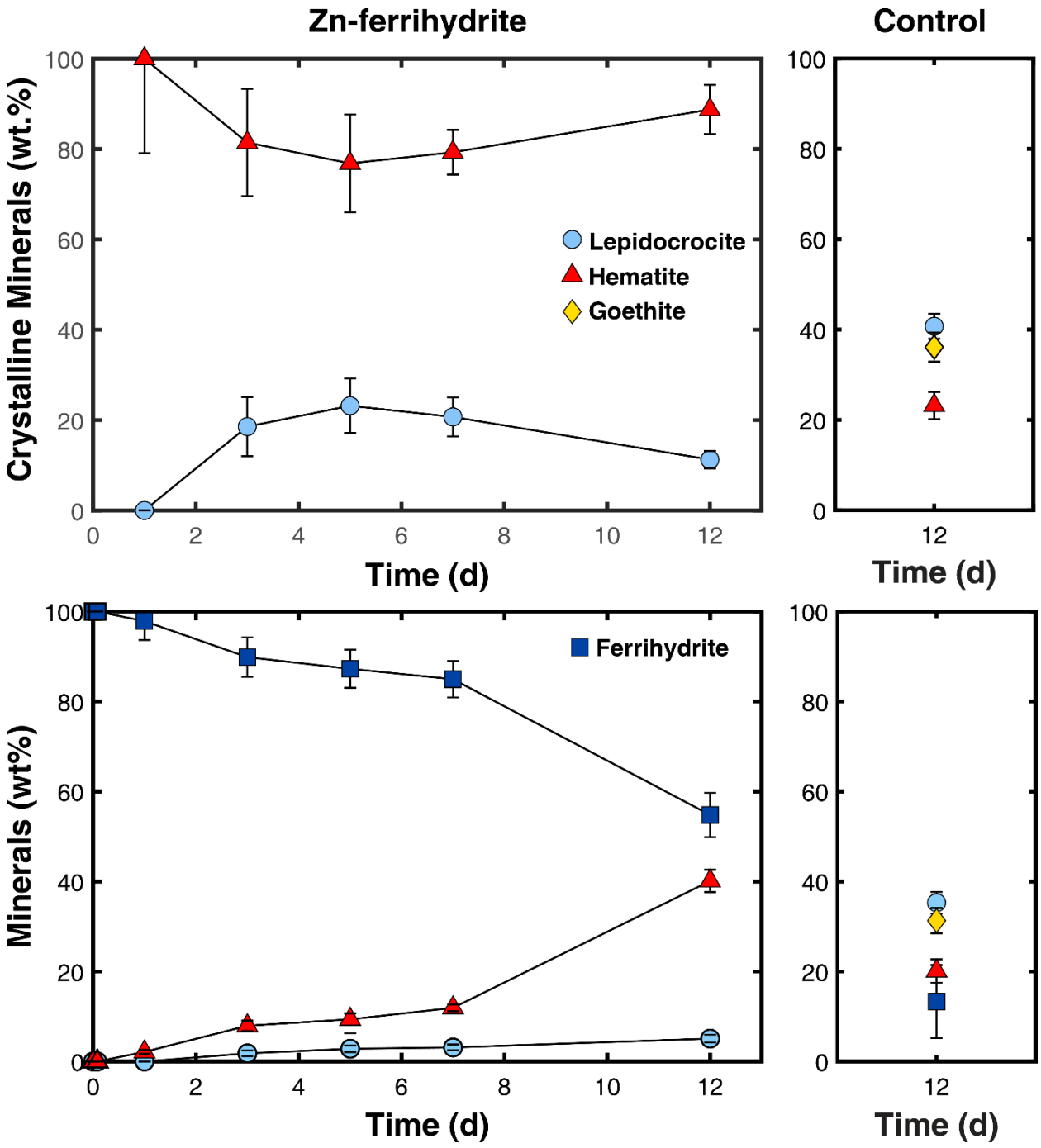

Figure 2.3. Fractional abundances of crystalline minerals (top) and of all minerals present (bottom) determined by Rietveld refinement for reaction of 0.2 mM dissolved Fe(II) with Zn-ferrihydrite (left) or a Zn-free ferrihydrite control (right).

2.4.2.2 Transformations in 1.0 mM Fe(II)

In a 1.0 mM Fe(II) solution, Zn-ferrihydrite transformed more rapidly (Fig. 2.2). After 2 h of reaction, the first time point sampled, substantial lepidocrocite peaks were present. Magnetite peaks appeared in the XRD pattern after 1 d and became substantial components after 3 d of reaction. The relative peak intensities of lepidocrocite and magnetite were stable between 5 and 12 d of reaction. Similar to the 0.2 mM Fe(II) experiment, the data continued to have a background feature near ~35° 2θ, suggesting that some ferrihydrite remained unreacted. Rietveld refinement of the XRD data (Fig. A2.3) confirms that lepidocrocite dominated the crystalline products over the first day of reaction but this evolved to a subequal mixture with magnetite that appeared to stabilize in relative proportions by 5 d of reaction (Fig. 2.4). While Zn-ferrihydrite transformation was more rapid compared to the 0.2 mM Fe(II) experiment, a substantial residual component (~35 wt.%) remained after 12 d (Fig. 2.4).

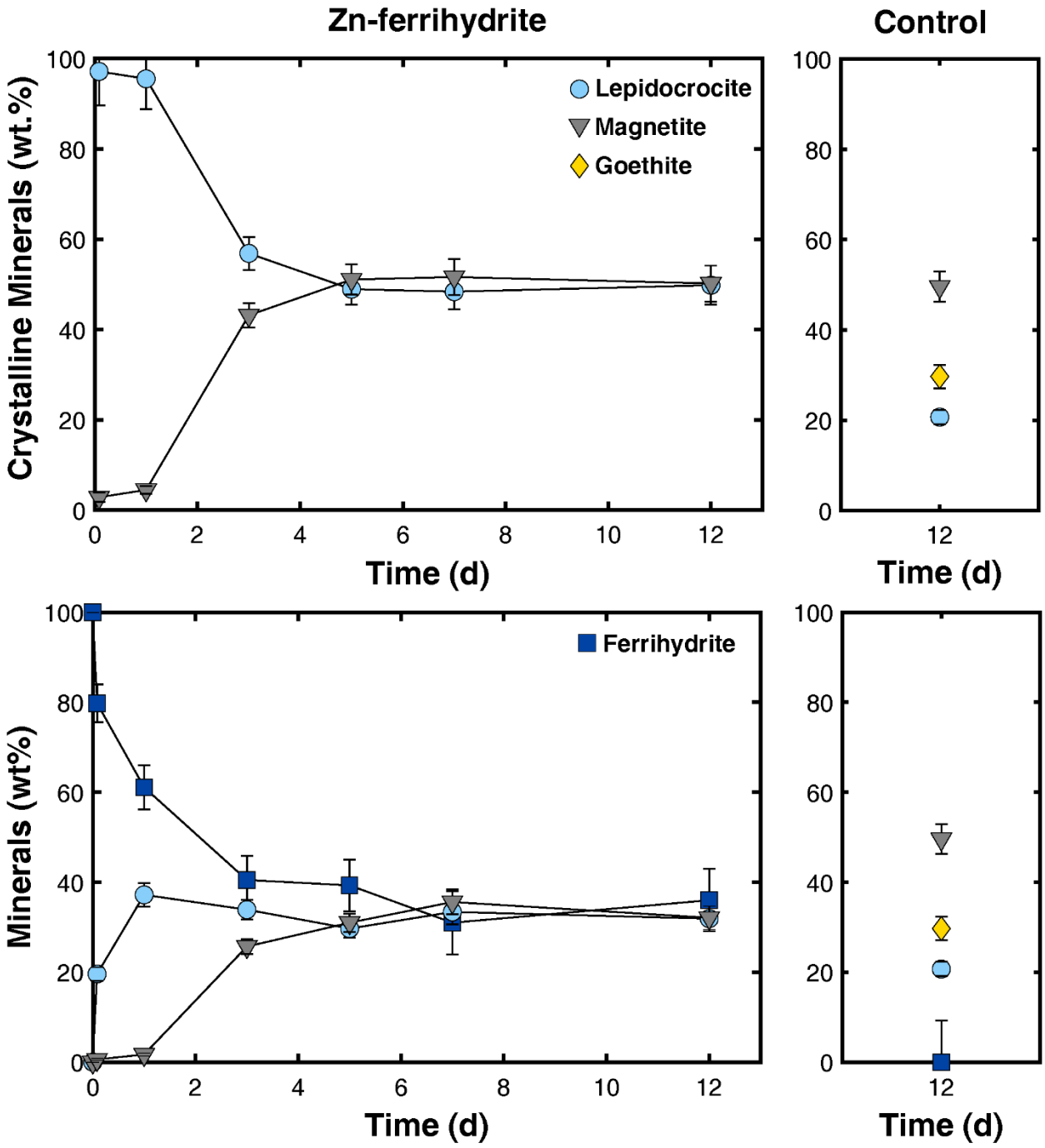

Figure 2.4. Fractional abundances of crystalline minerals (top) and of all minerals present (bottom) determined by Rietveld refinement for reaction of 1.0 mM dissolved Fe(II) with Zn-ferrihydrite (left) or a Zn-free ferrihydrite control (right).

2.4.2.3 Transformations in Control Experiments with Zn-free Ferrihydrite

Control experiments were conducted to evaluate the role of Zn and Fe(II) in generating the observed mineral products (Fig. 2.5). Aging Zn-ferrihydrite for 12 d in the absence of dissolved Fe(II) yielded no detectable phase transformation, with the XRD pattern preserving the features of 2-line ferrihydrite (Fig. 2.5). Zn-free ferrihydrite reacted with 0.2 mM dissolved Fe(II) for 12 d produced substantial lepidocrocite and goethite peaks and minor hematite peaks in the XRD pattern (Fig. 2.5). Notably, goethite was absent in the Zn-ferrihydrite experiment under the same conditions and aging time (Fig. 2.2). Full-pattern fitting via Rietveld refinement (Fig. A2.4) required a mixture of lepidocrocite, goethite, and hematite to reproduce the data. This showed that the crystalline products contained ~35 wt.% goethite, which did not form when the starting solid was Zn-ferrihydrite. The lepidocrocite content of the crystalline phases was also substantially increased for Zn-free ferrihydrite. In addition, hematite was only ~25 wt.% of the crystalline fraction of the solids compared to >80 wt.% of the crystalline phases in the Zn-ferrihydrite experiment. Only ~10 wt.% ferrihydrite remained after reaction, compared to >50 wt.% for Zn-ferrihydrite.

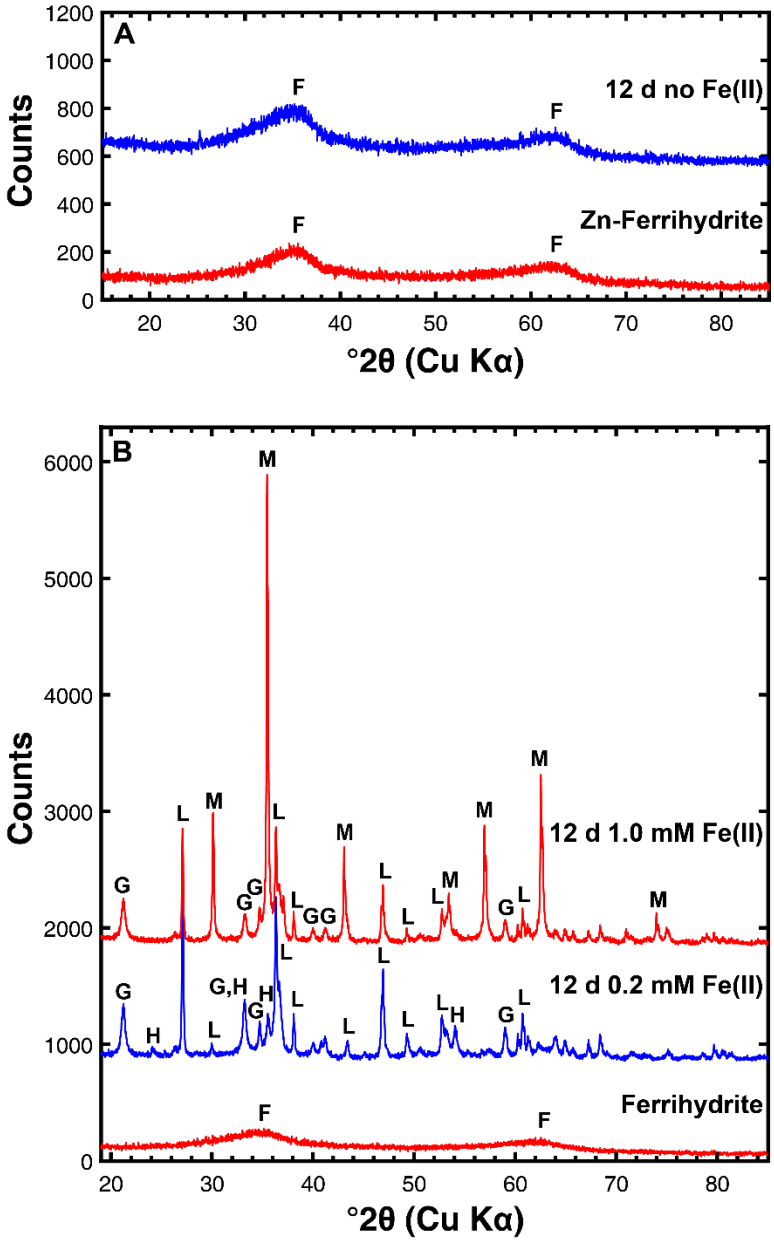

Figure 2.5. XRD patterns of (A) initial Zn-ferrihydrite (Zn-fh) and Zn-ferrihydrite aged for 12 days in the absence of Fe(II); (B) initial Zn-free ferrihydrite (fh) and Zn-free ferrihydrite reacted with 0.2 mM Fe(II) or 1.0 mM Fe(II) for 12 days. Diagnostic peaks are labeled to indicate mineral phases: F=ferrihydrite, L=lepidocrocite, H=hematite, G=goethite, M=magnetite.

Reaction of Zn-free ferrihydrite with 1.0 mM dissolved Fe(II) for 12 d also produced distinct mineralogy compared to Zn-ferrihydrite. While a mixture of magnetite and lepidocrocite

still formed, goethite was also present, similar to the 0.2 mM Fe(II) control experiment. Magnetite abundance was ~50 wt.% of the crystalline products, approximately the same percentage as in the Zn-ferrihydrite experiment, but less lepidocrocite formed at the expense of goethite (Fig. 2.3). Ferrihydrite was below detection limit, producing greater conversion of Zn-free ferrihydrite compared to Zn-ferrihydrite.

2.4.3 Zinc Release and Uptake during Phase Transformations

2.4.3.1 Dissolved Concentrations during Transformation in 0.2 mM Fe(II)

Zinc release and uptake and the removal of dissolved iron were monitored during the transformation of Zn-ferrihydrite in the presence of 0.2 mM Fe(II). At the beginning of the reaction, Zn was rapidly released to solution, with a dissolved concentration of ~30 μM Zn at the first time point (Fig. 2.6A), corresponding to 14% of the initial solid-phase Zn. Zn was then progressively taken up into the solid phase, with near-complete removal of Zn initially released to the fluid. On the third day, Zn concentration reached the lowest value of 0.5 μM and then gradually increased to 1.6 μM by the end of the 12 d experiment. The residual dissolved Zn consisted of less than 1% of the total Zn in the system, indicating that more than 99% Zn was retained in the solid phase during phase transformation after the brief transient release during the first few minutes of reaction. The dissolved Fe concentration (Fig. 2.6B) similarly decreased rapidly at the beginning of the reaction and then gradually increased from day 3 to 12. The final dissolved Fe concentration was 20 μM, indicating that 90% of the initial dissolved Fe(II) was bound to the solid phase.

2.4.3.2 Dissolved Concentrations during Transformation in 1.0 mM Fe(II)

The concentrations of dissolved Zn and Fe for Zn-ferrihydrite in contact with an initial 1.0 mM Fe(II) solution (Fig. 2.6C,D) followed patterns similar to the experiment with lower Fe(II) concentration (Fig. 2.6A,B). At the beginning of the reaction, ~31 μM Zn was rapidly released from Zn-ferrihydrite. Within one day, the dissolved Zn concentration displayed a drastic drop. After the third day of reaction, Zn concentration in the solution was ~0.3 μM, which is < 1% of the initial Zn concentration. More than 99% of Zn was retained in the solid phase.

The dissolved Fe concentration experienced a sharp drop during the first hour of reaction followed by a slower decline to less than 10 μM by day 5, with >99% of the initial dissolved Fe(II) partitioning into the solid phase. During the period of large declines in dissolved Fe(II) concentration, the pH drifted down from pH 7.0 to as low as 6.6, despite the presence of a buffer in the experiment. At each sampling point the pH was thus manually adjusted to back to 7.0±0.1 by dropwise addition of 0.1 M NaOH (Fig. A2.5). This adjustment was performed after removal of an aliquot of the suspension for fluid and solid-phase analyses.

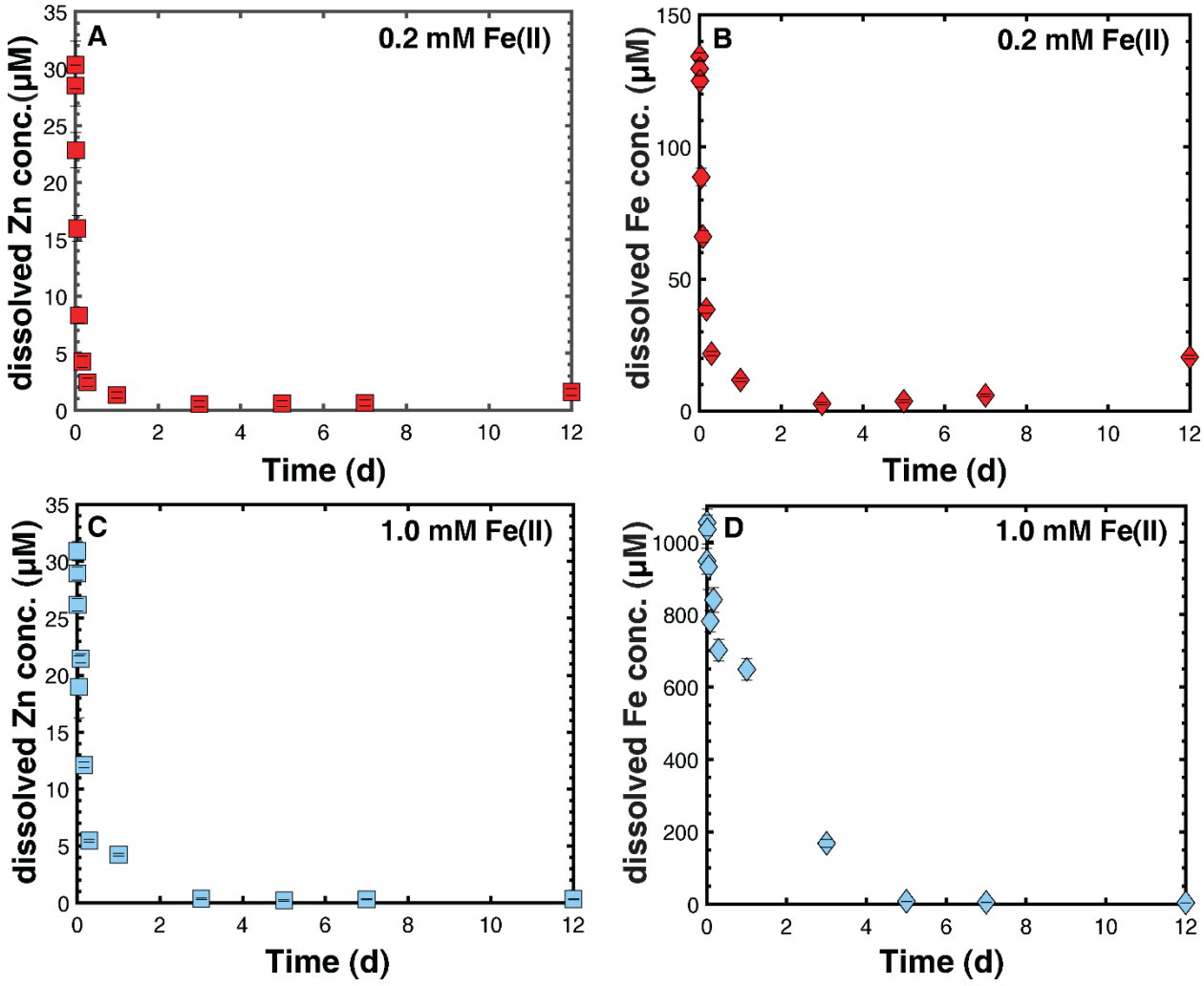

Figure 2.6. Dissolved Zn and Fe concentrations change with time during Zn-ferrihydrite transformation induced by 0.2 mM Fe(II) and 1.0 mM Fe(II).

2.4.4 Spectroscopic Characterization of Zn

The interaction of Zn with ferrihydrite during phase transformation can be inferred from the structural information provided by EXAFS spectroscopy. Zn has various coordination states, with tetrahedral and octahedral Zn most common (Waychunas et al., 2002). Previous studies have reported that Zn(II) adsorbs on ferrihydrite as a tetrahedral complex, maintaining this geometry but with a greater number of Fe neighbors when coprecipitated (Waychunas et al.,

2002; Juillot et al., 2008). In contrast, dissolved Zn(II) is octahedrally coordinated and surface complexes on hematite and goethite occur as both tetrahedral and octahedral species (Juillot et al., 2008; Ha et al., 2009). Zn substitutes into hematite and goethite as octahedral species, although these may be substantially distorted (Frierdich and Catalano, 2012; Bylaska et al., 2019). These observations are noted as they guide the structural model fitting approach used in this study.

The EXAFS spectra show that Zn coordination changed substantially during Fe(II)-catalyzed phase transformations of ferrihydrite (Fig. 2.7). During transformations induced by 0.2 mM Fe(II), the EXAFS spectrum of a sample collected after 2 h show little variation from the initial unreacted Zn-ferrihydrite (Fig. 2.7). Structural analysis confirms that Zn coordination did not detectably change over this time period (Table 2.1). In contrast, after 12 d of reaction with 0.2 mM Fe(II) the EXAFS spectrum is clearly different from the initial Zn-ferrihydrite. Spectral fitting (Table 2.1) show that a mixture of octahedral and tetrahedral Zn was present and a second Zn-Fe distance occurred at 2.97 Å. In addition, the longer Zn-Fe distance shortens slightly to 3.39 Å (Fig. 2.7). These distances are similar to those observed for Zn substituting into hematite (Table 2.1), the dominant ferrihydrite transformation product in the sample. Visually, the EXAFS spectrum of the 12 d sample displays features that similar to those displayed by Zn in hematite, although weaker in amplitude. These include a shift to lower k of the maxima near 4 $Å^{-1}$ and two apparent oscillations between 7 and 9 $Å^{-1}$ (Fig. 2.7).

Reaction of Zn-ferrihydrite with 1.0 mM Fe(II) for 12 d produces more substantial changes in the EXAFS spectrum of Zn (Fig. 2.7). Notably, the spectrum has similar fine-structure as the spectrum of franklinite, but with weaker oscillations. Structural model fitting (Table 2.1) is consistent with Zn occupying a tetrahedral site in a ferrite spinel structure. For

example, Zn in franklinite has 4 oxygen neighbors at 1.98 Å and 12 iron neighbors at 3.50 Å (Pavese et al., 2000) and the tetrahedral site in magnetite has 12 iron neighbors at 3.48 Å (Fleet, 1981).

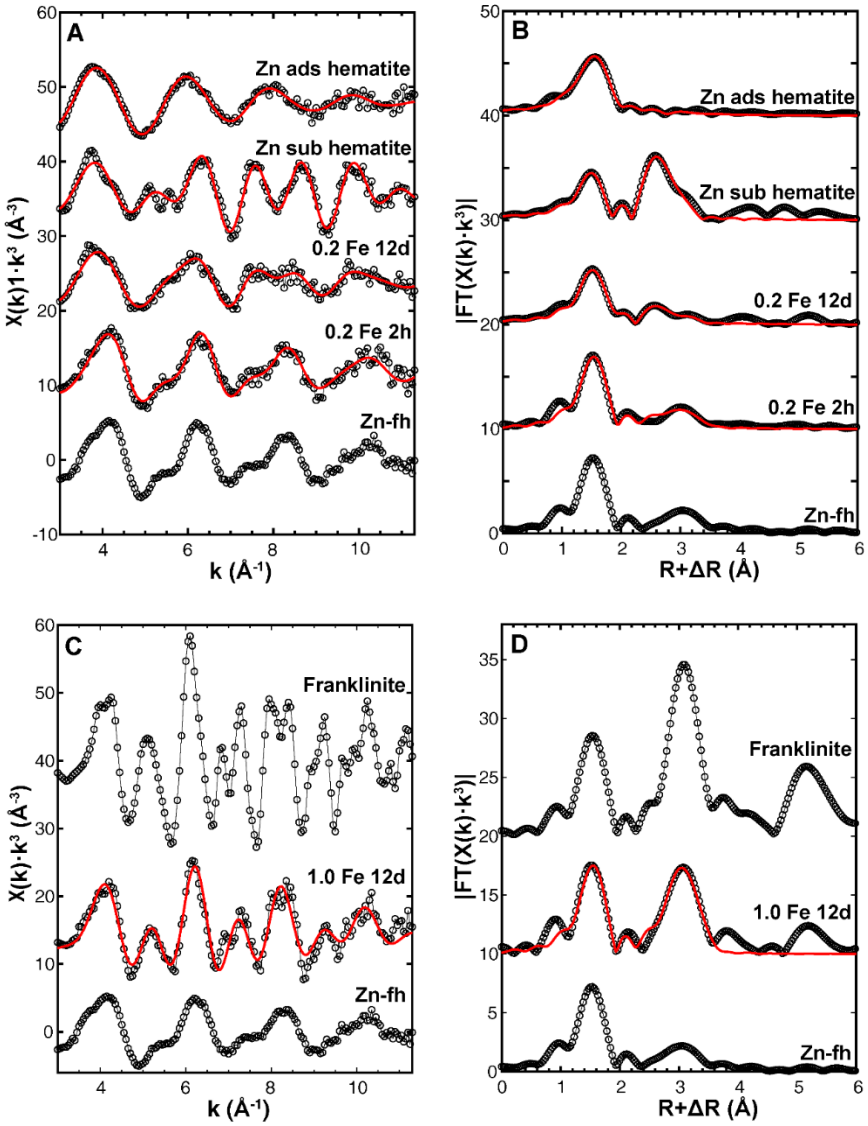

Figure 2.7. Data (dotted) and structural model fit (lines) of Zn K-edge EXAFS spectra and Fourier Transform magnitude of samples and standards associated with aging of Zn-ferrihydrite with (top) 0.2 mM Fe(II) and (bottom) 1.0 mM Fe(II). Individual spectra are: Zn-fh: unreacted Zn-ferrihydrite; 0.2 Fe 2h: Zn-ferrihydrite reacted with 0.2 mM Fe(II) for 2 h; 0.2 Fe 12d: Zn-ferrihydrite reacted with 0.2 mM Fe(II) for 12 d ; Zn sub hematite: Zn substituted in hematite; Zn

ads hematite: Zn adsorbed to hematite; 1.0 Fe 12d: Zn-ferrihydrite reacted with 1.0 mM Fe(II) for 12 days; franklinite: $ZnFe_2O_4$.

2.5 DISCUSSION

2.5.1 Impact of Fe(II) Concentration on Ferrihydrite Transformation Pathways

Multiple prior studies demonstrate that Fe(II) concentration determines whether Fe(II) acts as a catalyst or reactant during ferrihydrite phase transformations (Tronc et al., 1992; Hansel et al., 2003; Hansel et al., 2005; Pedersen et al., 2005; Yang et al., 2010; Boland et al., 2014). In general, Fe(II) concentrations below approximately 0.4 mM favor the catalysis of ferrihydrite conversion to more crystalline Fe(III) (oxyhyd)roxides, including goethite and lepidocrocite (Yee et al., 2006; Liu et al., 2007), while at higher concentrations Fe(II) is consumed to also generate magnetite (Hansel et al., 2003; Hansel et al., 2005; Pedersen et al., 2005; Yang et al., 2010). The Fe(II) concentration needed to generate magnetite varies among different studies and is likely impacted by pH, ferrihydrite concentration, the anions present, and other factors. Our studies are consistent with past experiments, finding that 0.2 mM dissolved Fe(II) initiates only catalytic transformations, with all products consisting of ferric iron minerals. The higher concentration explored, 1.0 mM, generated substantial magnetite via reaction between Fe(II) and ferrihydrite. Note that while the fractional abundance of crystalline products of Zn-ferrihydrite transformation was dominated by lepidocrocite at early times, the absolute abundance (Table A2.1) increases to 37±3 wt.% after 1 d before stabilizing at 32±3 wt.% by 12 d. It thus appears to be little to no lepidocrocite conversion to magnetite; lepidocrocite simply forms first with ample Zn-ferrihydrite remaining. The absolute abundance of lepidocrocite at 1 d is affected by the amount of ferrihydrite identified using our semi-quantitative method via Rietveld refinement,

and the potential small decline in absolute lepidocrocite abundance over time may reflect systematic errors in the analysis rather than real changes in mineralogy.

2.5.2 Impact of Zinc on Ferrihydrite Transformation Pathways

2.5.2.1 Promotion of Low-Temperature Hematite Formation

While hematite is the most thermodynamically stable phase among the common iron oxides in aqueous environments, its formation from ferrihydrite at ambient temperatures is slow (Cornell and Schwertmann, 2003) and the addition of Fe(II) under such conditions is not reported to produce this phase on timescales up to 9 days. Ferrihydrite stored in water over a large range of pH values (2 to 12) at temperatures of 4 to 30 °C converted to hematite after 9.3 to 12.6 years (Schwertmann et al., 1999), with hematite first apparent at 25 °C after 100s of days at pH 7 (Das et al., 2011). Hematite can also be produced at short timescales by heating ferrihydrite in water at elevated temperatures (Johnston and Lewis, 1983; Das et al., 2011). In addition, hematite was generated after heating ferrihydrite for 180 days at 45 °C and 55 °C at a relative humidity of nearly 100% (Torrent et al., 1982). This demonstrates that ferrihydrite to hematite conversion is kinetically slow without a catalyst present or thermal input. While catalytic ferrihydrite transformations induced by Fe(II) have not been reported to produce hematite at ambient temperatures (Hansel et al., 2003; Hansel et al., 2005; Pedersen et al., 2005; Lee et al., 2006; Boland et al., 2014), this product is observed for Fe(II)-ferrihydrite systems when heated at 60°C to 100°C (Liu et al., 2005; Liu et al., 2007; Liu et al., 2008).

In contrast to prior work, the present study observed rapid hematite formation from Zn-substituted 2-line ferrihydrite at room temperature (22 °C) at pH 7. Hematite clearly nucleated within three days of reaction, with the first signs of hematite in XRD patterns possibly present

after one day. In addition, hematite was the dominant (>80%) crystalline product throughout the reaction. The rapid and pervasive formation of hematite is clearly related to the presence of substituting Zn as only minor hematite formed in the Zn-free control study. The promotion of hematite by Zn has been previously demonstrated in a recent thermal transformation study conducted at 70°C (Sakakibara et al., 2019). However, the present study is the first to document that Zn promotes rapid hematite formation from ferrihydrite at ambient temperatures.

2.5.2.2 Inhibition of Goethite Formation

Zinc also appears to inhibit goethite formation during Fe(II)-promoted ferrihydrite transformation. This phase was absent in studies of Zn-ferrihydrite but was a substantial crystalline product in the Zn-free control experiments. The formation of substantial goethite from Zn-free ferrihydrite in 0.2 mM Fe(II) was accompanied by greater lepidocrocite formation than in the Zn-ferrihydrite studies. In contrast, more goethite formed from Zn-free ferrihydrite at the apparent expense of lepidocrocite in 1.0 mM Fe(II). Zinc does not clearly affect the formation of magnetite, with similar amounts forming from Zn-ferrihydrite and Zn-free ferrihydrite. This demonstrates that Zn affects crystallization pathways beyond promoting hematite formation. Comparison with prior work suggests that the starting form of Zn also affects the mineral products. Goethite formed during Fe(II)-catalyzed ferrihydrite when Zn was added in the dissolved phase rather than associated with the solids (Liu et al., 2016). This suggests that Zn may need to be incorporated into ferrihydrite for it to inhibit the formation of goethite during phase transformations.

2.5.2.3 Inhibition of Ferrihydrite Transformation

Zinc also slows ferrihydrite transformation, leaving a substantial residual ferrihydrite pool after 12 d. Prior work suggests that a surface competition mechanism may play a role in inhibiting transformation. Adsorption of metals of higher binding affinities than Fe(II), such as Zn(II), slow the transformation rate of ferrihydrite by obstructing the Fe(II) binding to the surface (Liu et al., 2016). Surface site competition between Fe(II) and trace metals was also suggested to affect the rate of recrystallization of metal-substituted goethite and hematite (Frierdich and Catalano, 2012). The transient release of Zn in our study and its re-adsorption on mineral surfaces may thus hinder further transformation of ferrihydrite.

2.5.3 Processes Controlling Dissolved Zn and Fe Concentrations

At the beginning of the low Fe(II) (0.2 mM) transformation experiment, Zn was transiently released into the solution. This may have been caused by rapid displacement of near-surface Zn by the adsorption of Fe(II), which also showed a rapid initial decline in concentration at the first time point (2 min). Fe(II) uptake continued over the next three days, when hematite first showed substantial nucleation; Zn concentrations also decreased during this time. We hypothesize that between the first time point and day three, Fe(II) diffused into the interior of ferrihydrite aggregates where it then adsorbed, producing the continued decline in dissolved concentration. The decrease in dissolved Fe(II) and its migration to interior surface sites would have then lessened site competition on the aggregate exterior, allowing re-adsorption of dissolved Zn. In addition, electron migration into the bulk mineral structure following Fe(II) adsorption (Williams and Scherer, 2004; Handler et al., 2009; Boland et al., 2013) may produce an Fe(III)-dominated surface, making Zn re-adsorption to ferrihydrite more favorable. The slight

rebound in dissolved Zn and Fe(II) concentrations after the third day may then relate to the increasing presence of coarser, crystalline iron oxides, which provide less specific surface area and thus a lower capacity to adsorb these species.

EXAFS spectroscopy showed that a substantial portion of the Zn initially in ferrihydrite partitions into new mineral phases. The EXAFS spectrum after reaction with 0.2 mM (Fe(II) for 12 d shows some similarities to Zn substituting in hematite. However, Zn incorporated into hematite mixed with Zn remaining in the residual ferrihydrite does not fully explain its speciation in the 12 d sample. Linear-combination fitting (Fig. 2.8) well reproduces the spectrum of Zn-ferrihydrite reacted with 0.2 mM Fe(II) for 12 d using the spectra of Zn-ferrihydrite, Zn-hematite, and Zn adsorbed to hematite (see the Supporting Materials for structural analysis of the hematite standards). This analysis indicates that a portion of the Zn (~25%) is incorporated into hematite, with ~50% in an adsorbed form and ~25% retained in ferrihydrite. This mixture of species likely explains the lower coordination number for second-shell Fe neighbors than occurs in either Zn-ferrihydrite or Zn-hematite (Table 2.1). However, the resulting low component sum (0.94) suggests that the spectral standards are not fully adequate. We attribute this to possible mixtures of tetrahedral and octahedral surface complexes (Ha et al., 2009) not well represented by the Zn adsorption to hematite standard. In addition, this analysis does not account for the minor lepidocrocite component present in the mineral assemblage because standards for Zn adsorbed on or incorporated into this phase were not available.

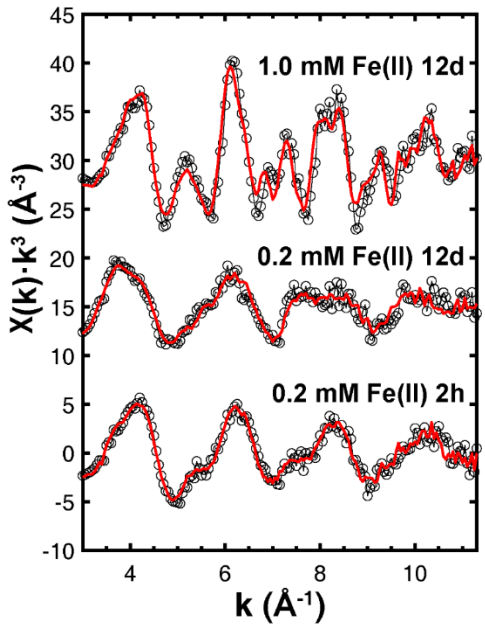

Figure 2.8. Data (black circles) and linear combination fit (red line) of Zn K-edge EXAFS spectra of Zn-ferrihydrite reacted with 0.2 mM Fe(II) for 2 hours and 12 days and with 1.0 mM Fe(II) for 12 days.

Despite these minor discrepancies, the structural analysis and linear combination fitting both indicate that a substantial fraction of Zn has redistributed from ferrihydrite to hematite and likely occurs in both incorporated and adsorbed forms. This incorporation may thus mute the impact of grain size coarsening on Zn adsorption. A portion of the increase in Zn concentration at longer aging times may also be attributable to Fe(II)-promoted recrystallization of hematite and lepidocrocite (Frierdich et al., 2011; Frierdich and Catalano, 2012; Latta et al., 2012). This has been demonstrated to release structural Zn to solution for hematite (Frierdich and Catalano, 2012). While it has not been clearly demonstrated yet for lepidocrocite, it has been shown for goethite and may be a general phenomenon for crystalline iron oxides (Frierdich and Catalano, 2012; Frierdich et al., 2012).

In the high Fe(II) (1.0 mM) ferrihydrite transformation experiment, dissolved Zn and Fe concentrations behave similarly to what is observed in low Fe(II) experiment. The rapid initial release of Zn plus the rapid decline of both concentrations can again be attributed for the adsorption-desorption processes discussed above. Notably, Zn and Fe concentrations do not rebound at the later stages of reaction, unlike the experiment at lower Fe(II) concentration. A substantial decline in dissolved Fe concentration between day 1 and 3 corresponds to a large increase in magnetite content. Adsorption may thus have been responsible for the initial decline in dissolved Fe concentration to ~0.6 mM, with the larger drop to ~5 μM caused by net Fe(II) consumption during magnetite formation. The near-complete sequestration of Zn in the solid-phase is also likely associated with Zn uptake into the magnetite structure. The EXAFS spectrum of Zn-ferrihydrite reacted with 1.0 mM Fe(II) for 12 d was similar to the spectrum of Zn in franklinite (Fig. 2.7). However, this phase was not detected via XRD (Fig. 2.2), suggesting instead that Zn likely occurred as a substituting element in the abundant magnetite that formed. Linear-combination fitting (Table 2.2) well reproduces the spectrum of Zn-ferrihydrite reacted with 1.0 mM Fe(II) for 12 d using a mixture of franklinite and Zn-ferrihydrite (Fig. 2.8). However, some features are offset in k, consistent with the effects on EXAFS spectra of slight differences in interatomic distances between franklinite and magnetite. This analysis does not account for an Zn adsorbed to magnetite or associated with lepidocrocite. For both systems studied, Zn fate is controlled by both adsorption and incorporation into the secondary iron oxide products. A recent study observed similar behavior for Ni that was initially coprecipitated with ferrihydrite, with dissolved Fe(II) inducing its transient release followed by incorporation into secondary goethite and magnetite (Zhou et al., 2021).

Table 2.2. Results of linear-combination fitting of the EXAFS spectra of ferrihydrite transformation products.

Sample	Zn-ferrihydrite	Zn-hematite	Zn adsorbed to hematite	Franklinite	χ_v^2 [a]	R-factor [a]	Component Sum
0.2 mM Fe(II), 2 hr	100±3%	0±2%	0±4%	-[b]	0.442	0.067	0.962
0.2 mM Fe(II), 12 d	26±4%	25±3%	50±5%	-	0.632	0.139	0.940
1.0 mM Fe(II), 12 d	67±5%	-	-	33±2%	1.783	0.119	1.069

[a]Goodness-of-fit parameters (Kelly et al., 2008). [b]Not included in fit.

2.5.4 Potential Mechanisms of Zinc Modification of Ferrihydrite Transformations

The near-complete retention of Zn in our experiments demonstrates that it is associated with the surfaces and structures of the reactant, ferrihydrite, and its transformation products. Solid-associated Zn potentially has multiple mechanistic roles in the modified phase transformations observed in this study. Prior work has shown that freeze-dried ferrihydrite coprecipitated with silica undergoes rapid atom exchange with dissolved Fe(II) yet is stabilized against transformation to more crystalline products (Jones et al., 2009). Silica inhibits the polymerization of Fe(III) that is needed to nucleate more crystalline iron oxide minerals (Doelsch et al., 2000; Doelsch et al., 2001; Pokrovski et al., 2003; Cismasu et al., 2014). Zinc potentially acts through a similar mechanism, stabilizing ferrihydrite by inhibiting polymerization of Fe(III) into other structural moieties. This trace metal may also inhibit nucleation of crystalline Fe(III) oxides, especially for goethite, by either interfering with the formation of labile Fe(III) (Sheng et al., 2020b) or suppressing the dissolution of ferrihydrite that precedes reprecipitation of iron as crystalline phases (Qafoku et al., 2020). Concomitant with suppression of ferrihydrite transformation to goethite and other phases, zinc likely also enhances the nucleation of hematite, as has been previously demonstrated at elevated temperature

(Sakakibara et al., 2019). The inhibition of goethite nucleation by Zn appears to be unaffected by greater Fe(II) concentrations but its incorporation into magnetite may prevent Zn from nucleating hematite.

2.5.5 Geological and Environmental Implications

2.5.5.1 Promotion of Low-Temperature Hematite Formation

This study reports rapid formation of hematite from ferrihydrite at 22°C. The presence of Zn clearly accelerates hematite formation, a product not previously observed during Fe(II)-catalyzed ferrihydrite transformation at ambient temperatures (Hansel et al., 2003; Hansel et al., 2005; Pedersen et al., 2005; Yee et al., 2006). The role of Zn itself in forming hematite in natural systems may be limited because it is unlikely that ferrihydrite in the environment will contain Zn at the level (~2 mol.%) explored in the present study, except perhaps near weathering zinc sulfide ore deposits. However, a wide array of substituting elements are commonly associated with iron oxides in nature (Schwertmann and Cornell, 2000; Cornell and Schwertmann, 2003). The present results suggest a general mechanism where substituting elements in ferrihydrite enhance the conversion to hematite, helping to nucleate this phase at temperatures lower than is typically observed in laboratory studies. While further study is warranted, impurities may play key roles in promoting low-temperature hematite formation in the environment.

2.5.5.2 Potential Impact on Metal Stable Isotope Records

The near-quantitative retention of Zn during Fe(II)-promoted phase transformations, both to ferric oxyhydroxides and to magnetite, suggests that such transformations do not perturb solid-phase trace metal stable isotope compositions. Solid-aqueous fractionation factors between Zn

adsorbed to iron oxide minerals and dissolved Zn are generally <0.5‰ in magnitude (Pokrovsky et al., 2005; Balistrieri et al., 2008; Juillot et al., 2008). We are unaware of studies of isotopic fractionation involving Zn incorporated into iron oxides, but adsorption-desorption would be a critical intermediate step that may dictate fractionation. With >99% retention in the solid phase (Section 3.3), such partitioning could alter the Zn stable isotope composition of the solid phases by <0.015‰, much less than the typical analytical precision Zn stable isotope measurements (0.04 to 0.1‰) (Balistrieri et al., 2008; Chen et al., 2009; Moynier et al., 2017). This demonstrates that the transformation processes observed in the present study will not measurably alter solid-phase Zn stable isotope compositions from that of primary ferrihydrite precipitates, such as during diagenesis. Conditions that lead to lower Zn retention, such as transformations under more acidic pH, may potentially perturb such values.

2.5.5.3 Implications for Bioessential Trace Metal Availability

Elements such as cobalt, nickel, copper, and zinc serve as key reaction centers in metalloenzymes (Gärtner et al., 1993; Ermler et al., 1997; Thauer, 1998; Brown et al., 2000; Parks et al., 2013; Zheng et al., 2016) and low availability of these metals may inhibit microbial processes in environment (Schönheit et al., 1979; Granger and Ward, 2003; Ekstrom and Morel, 2008; Glass and Orphan, 2012; Lu et al., 2018). Previous study has suggested that metal solubility can be reduced through coprecipitation with or removal by iron oxides formed during ferrihydrite transformation (Martínez and McBride, 1998). In the current work, the retention of a high portion of Zn in phase transformation products suggests that trace metal micronutrients are not mobilized by formation of more crystalline iron oxides. The observed Zn retention indicates that the availability of this metal is not enhanced during Fe(II)-promoted ferrihydrite

transformations except during the first hour of reaction. However, subsequent Zn release during Fe(II)-promoted recrystallization of the more crystalline transformation products (Frierdich et al., 2011; Frierdich and Catalano, 2012) may later enhance metal availability. Fe(II)-catalyzed transformation of ferrihydrite appears to liberate greater concentrations of Ni compared to Zn, with conversion to primarily goethite generating ~70 μM dissolved Ni concentrations (Frierdich and Catalano, 2012) whereas conversion to a goethite-magnetite mixture yielded concentrations of ~10 μM (Zhou et al., 2021). This suggests that trace metal availability during such transformations likely varies with system-specific parameters It is unclear whether similar behavior will be displayed by other bioessential metals , such as Co and Cu, as their solid-water partitioning may be distinct from Zn because of differences in ionic radii and chemical properties.

2.6 CONCLUSIONS

The trace metal Zn alters the Fe(II)-induced transformation pathways of ferrihydrite and partially incorporates into the resulting crystalline iron oxides. This study is the first to report that Zn promotes the formation of hematite at 22°C, which occurs as the dominant reaction product for systems containing 0.2 mM dissolved Fe(II). This suggests that impurity ions may be critical to the formation of hematite in low-temperature environments. In addition, Zn inhibits both goethite formation and the overall transformation of ferrihydrite to more crystalline phases. A small fraction of the ferrihydrite-bound Zn is released to solution during reaction but is rapidly taken back up into the solid phase, partially incorporating into hematite and magnetite. Near-quantitative retention of Zn demonstrates that ferrihydrite phase transformations at pH 7 from interactions with dissolved Fe(II) will preserve the Zn isotopic composition. The Zn to Fe ratio

will also be unperturbed except when magnetite or other mixed-valent phases form through net Fe(II) uptake; the additional Fe would dilute the Zn content. Such transformations may thus preserve chemical or isotopic signatures associated with Zn in modern soils or aquatic systems as well as in the sedimentary record. Finally, ferrihydrite phase transformations will not substantially limit trace metal contaminant sequestration or micronutrient availability despite the formation of more crystalline mineral products if fluid conditions favor solid-phase retention.

2.7 ACKNOWLEDGEMENTS

The project was supported by the International Center for Energy, Environment and Sustainability at Washington University in Saint Louis. Addition support for J.G.C. and J.Y. was provided by the U.S. National Science Foundation (NSF), Environmental Chemical Sciences program through award no. CHE-1709484 and the U.S. Department of Energy (DOE), Office of Science, Office of Biological and Environmental Research, Subsurface Biogeochemical Research program through award no. DE-SC0019422. Preparation of the standards for zinc associated with hematite was supported by the U.S. NSF Faculty Early Career Development Program through award no. EAR-1056480. ICP-MS analyses were performed in the Isotope Cosmochemistry laboratory at the Department of Earth and Planetary Sciences at Washington University. We thank Prof. Kun Wang and Dr. Heng Chen for their help with ICP-MS measurements. BET measurements were conducted at the Nano Research and Environmental Laboratory at Washington University. XAFS data were collected at beamline 12-BM-B at the Advanced Photon Source, a U.S. DOE Office of Science User Facility operated for the DOE Office of Science by Argonne National Laboratory under Contract No. DE-AC02-06CH11357. We thank Dr. Benjamin Reinhart for assistance with XAFS data collection. In addition, we thank

Associate Editor Caroline Peacock and three anonymous reviewers for their detailed comments that substantially improved this paper during the peer-review process.

2.8 APPENDIX

Fluid Composition in Mineral-free Control Experiments

Mineral-free control experiments were carried out in parallel to both 0.2 mM and 1.0 mM Fe(II) experiments to further ensure the accuracy of the studies involving dissolved Fe(II) and to help interpret the results. These control experiments were performed in duplicate with the In ferrihydrite-free control samples containing 10 mM M NaCl, 1 mM M MOPS, and 0.2 mM Fe(II), the Zn concentration measured after 12 d of aging was 0.11±0.03 μM, indicating that Zn contamination was not a substantial contributor to the observed results. The total dissolved Fe concentration was 210±10 μM after 12 d, the same as the initial concentration of 210±20 μM, indicating no inadvertent oxidation during the experiments. For control samples with 10 mM NaCl, 1 mM M MOPS, 1.0 mM Fe(II), and no mineral addition, the dissolved Zn concentration was 0.16±0.03 μM after 12 d, lower than the Zn concentration at all times during the experiments. The dissolved Fe concentration decreased slightly after 12 d, from an initial value of 960±20 μM to 936±6 μM. This loss of ~2.5% of the dissolved Fe(II) may have resulted from adsorption to the reactor walls, slight oxidation, or from precipitation of a small amount of $Fe(OH)_2$ or green rust. The observed Zn concentrations in both ferrihydrite-free control experiments suggest a minor amount of contamination, possibly from trace amounts of Zn in the salts used. A portion of this may be from the iron(II) chloride because the 1.0 mM Fe(II) control experiments had a greater Zn concentration than the 0.2 mM Fe(II) experiments (0.16±0.03 μM versus 0.11±0.03 μM).

Semi-Quantitative Ferrihydrite Abundance Determined via Rietveld Refinement

The nanocrystalline nature of ferrihydrite precludes accurate simulation of its powder diffraction pattern, including the intensity of features. This prevents the use of Rietveld refinements for quantitative ferrihydrite determination using XRD data. However, full pattern simulation based on a fixed structural model and sample-specific parameters (e.g., peak broadening) that reproduces a measured pattern may provide a means for semi-quantitative analysis in a Rietveld framework under controlled experimental conditions. Full pattern calculations derived from a crystal structure provide scattering intensities determined from atomic scattering factors and thus should respond to abundance changes. However, the broad nature of ferrihydrite scattering features also pose challenges in distinguishing these from background, especially at low abundances.

The semi-quantitative analysis of ferrihydrite via Rietveld refinement was thus first evaluated using mixtures with a zinc oxide standard (U.S. National Bureau of Standards SRM 674). All analysis was conducted in the Profex interface to BGMN. First, the XRD pattern of synthetic Zn-ferrihydrite was simulated (Fig. 2.1) with the crystal structure of 2 nm ferrihydrite from (Michel et al., 2007). Only the lattice parameters and a peak broadening term were allowed to vary, and the values from this initial analysis were then fixed for all subsequent analyses. Next, a series of mixtures of ferrihydrite and zinc oxide, including both pure endmembers, were analyzed via Rietveld refinement as a two-component mixture. The recovered ferrihydrite abundances (Fig. A2.1a) varied linearly with true abundance but overestimated the ferrihydrite content as its concentration decreased. A calibration curve between fitted and actual ferrihydrite abundance was generated using linear regression, with the uncertainties on the slope and intercept propagated through calculation of actual ferrihydrite abundance for unknown samples.

The accuracy of this calibration curve was next tested using data collected for synthetic mixtures of ferrihydrite and hematite. The values derived from fitting the XRD patterns of these mixtures via Rietveld refinement and then applying the calibration curve described above generally well-reproduced the true ferrihydrite abundance within ±5 wt.%, and within the one-sigma fitting uncertainty for all but one sample (Fig. A2.1b,c). Fitting uncertainties are likely underestimated at low ferrihydrite abundances because the calibration curve was generated using unweighted linear regression. While a weighted linear regression to account for the different uncertainties derived from Rietveld refinement of the initial ferrihydrite-zinc oxide data would provide a more accurate estimate of the confidence interval, it is not trivial to then propagate this through the calculation to derive actual ferrihydrite abundances. The ferrihydrite determination should thus be viewed as semi-quantitative, primarily because of underestimated uncertainties as the ferrihydrite-hematite mixtures suggest minimal systematic bias in the analysis. The absolute abundances of crystalline phases when ferrihydrite is present should thus also be considered semi-quantitative. The relative abundances of crystalline phases, however, remain quantitative.

Analysis of EXAFS Spectra of Zn Incorporated in and Adsorbed to Hematite

The synthesis and characterization of Zn-substituted hematite was previously described (Frierdich and Catalano, 2012). In that prior study, fitting a single oxygen shell to the EXAFS spectrum yielded 4±1 neighbors with an interatomic distance of 1.99±0.02 Å. This appeared to suggested that zinc was tetrahedrally coordinated, but the multiple iron neighbors were consistent with zinc occupying the iron site in the structure, which is a distorted octahedron. Recent computational work (Bylaska et al., 2019) has demonstrated that zinc occupying this distorted octahedron well reproduces the observed EXAFS spectrum. In the present work, the spectrum of zinc substituted into hematite was thus fit with two oxygen shells comprised of three

atoms each (Figure 2.7A), to reflect the distorted octahedral site in hematite. This, along with the observed iron neighbors (Table 2.1) is consistent with octahedral zinc occupying the distorted iron site in hematite.

The EXAFS spectrum of zinc adsorbed to hematite (Figure 2.7A) has more muted fine structure, consistent with a surface complex. While the coordination number for oxygen (6.2±0.5) suggests that zinc is octahedrally coordinated in this sample, the Zn-O distances is intermediate between that of tetrahedral and octahedral zinc, indicating that a mixture of species are present. The relative large σ^2 value for the shell indicates high disorder, as would be expected for a mix of four- and six-coordinated zinc. An attempt to include a second shell contribution from iron yielded a coordination number within error of zero. We attribute this to destructive interference between iron shells for inner-sphere tetrahedral and octahedral zinc species rather than indicating that zinc binds in an outer-sphere configuration.

Table A2.1. Parameters from Rietveld refinement of the XRD data and the mineral abundances after recalibration using the empirical ferrihydrite parameterization.

Time	Rietveld Refinement Results								Recalibrated Abundances				
	Fh (wt.%)	Hem (wt.%)	Lep (wt.%)	Mag (wt.%)	Goe (wt.%)	R_{wp} (%)	R_{exp} (%)	χ^2	Fh (wt.%)	Hem (wt.%)	Lep (wt.%)	Mag (wt.%)	Goe (wt.%)
0.2 mM Fe(II)													
1 d	97.9±0.2	2.1±0.2	-	-	-	8.86	7.32	1.47	98±4	2.1±0.4	-	-	-
3 d	90.0±0.5	7.8±0.4	1.8±0.2	0.4±0.1	-	8.86	7.84	1.28	90±4	8±1	1.8±0.6	0.4±0.2	-
5 d	87.6±0.4	9.2±0.4	2.8±0.2	0.5±0.1		9.26	7.80	1.41	87±4	9±1	2.8±0.7	0.5±0.3	-
7 d	85.4±0.4	11.6±0.2	3.0±0.2	-	-	9.13	7.51	1.48	85±4	11.9±0.7	3.1±0.7	-	-
12 d	59.5±0.9	36.0±0.7	4.6±0.3	-	-	9.65	7.50	1.66	55±5	40±3	5±1	-	-
Control	29.6±1.6	16.3±0.7	28.7±0.7	-	25.4±0.8	9.41	7.91	1.42	13±8	20±3	35±2	-	31±3
1.0 mM Fe(II)													
2 h	80.7±0.5	-	18.7±0.5	0.6±0.1	-	11.12	9.35	1.41	80±4	-	20±2	0.6±0.2	-
1 d	64.6±0.8	-	33.8±0.8	1.6±0.1	-	10.64	8.09	1.73	61±5	-	37±3	1.7±0.3	-
3 d	48.5±1.0	-	29.3±0.6	22.2±0.5	-	10.45	8.05	1.69	41±5	-	34±2	26±2	-
5 d	47.6±1.1	-	25.6±0.6	26.8±0.6	-	11.66	8.86	1.73	39±6	-	30±2	31±2	-
7 d	41.7±1.4	-	28.2±0.8	30.1±0.8	-	11.74	8.90	1.74	31±7	-	33±3	36±3	-
12 d	45.2±1.4	-	27.3±0.8	27.5±0.7	-	12.85	8.78	2.14	36±7	-	32±3	32±3	-
Control	16.9±1.9	-	17.2±0.5	41.2±0.9	24.7±0.7	10.20	7.89	1.67	0±9	-	21±2	50±3	30±3

*Mineral labels: ferrihydrite = Fh, hematite = Hem, lepidocrocite = Lep, magnetite = Mag, goethite = Goe.

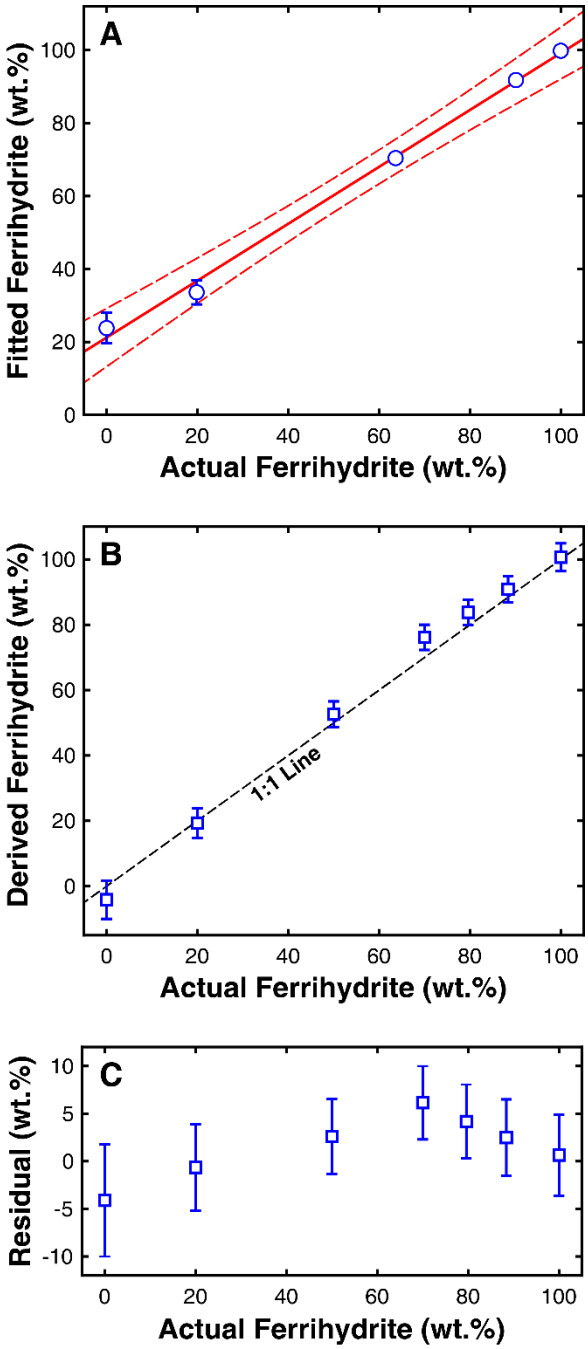

Figure A2.1. (A) Ferrihydrite abundances in 1:1 mixtures with zinc oxide versus actual ferrihydrite abundances. Error bars represent the fitting uncertainty derived from Rietveld refinement; data without errors have uncertainties smaller than the symbol. Also shown is the linear regression line and 95% confidence intervals. (B) Abundances of ferrihydrite in 1:1 mixtures with hematite derived from Rietveld refinement using the empirical calibration curve obtained from zinc oxide mixtures compared to actual abundances. Error bars account for both uncertainties obtained from Rietveld refinement and in the calibration curve. (C) Residual values representing the difference between derived and actual ferrihydrite abundances in mixtures with hematite.

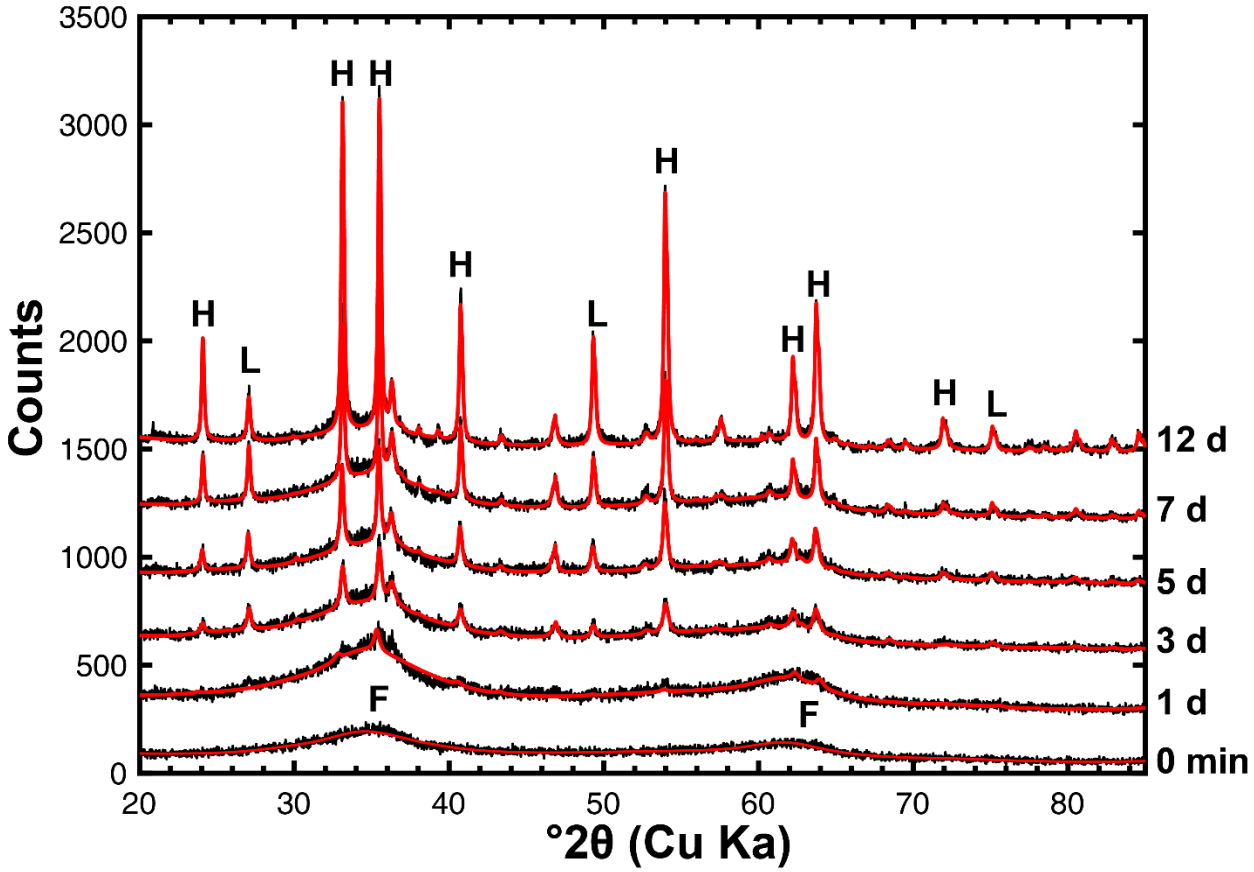

Figure A2.2. Rietveld refinement fit of XRD data (red) and XRD data (black) of mineral composition changed over time during 12-day Zn-ferrihydrite transformation experiment in 0.2 mM Fe(II)

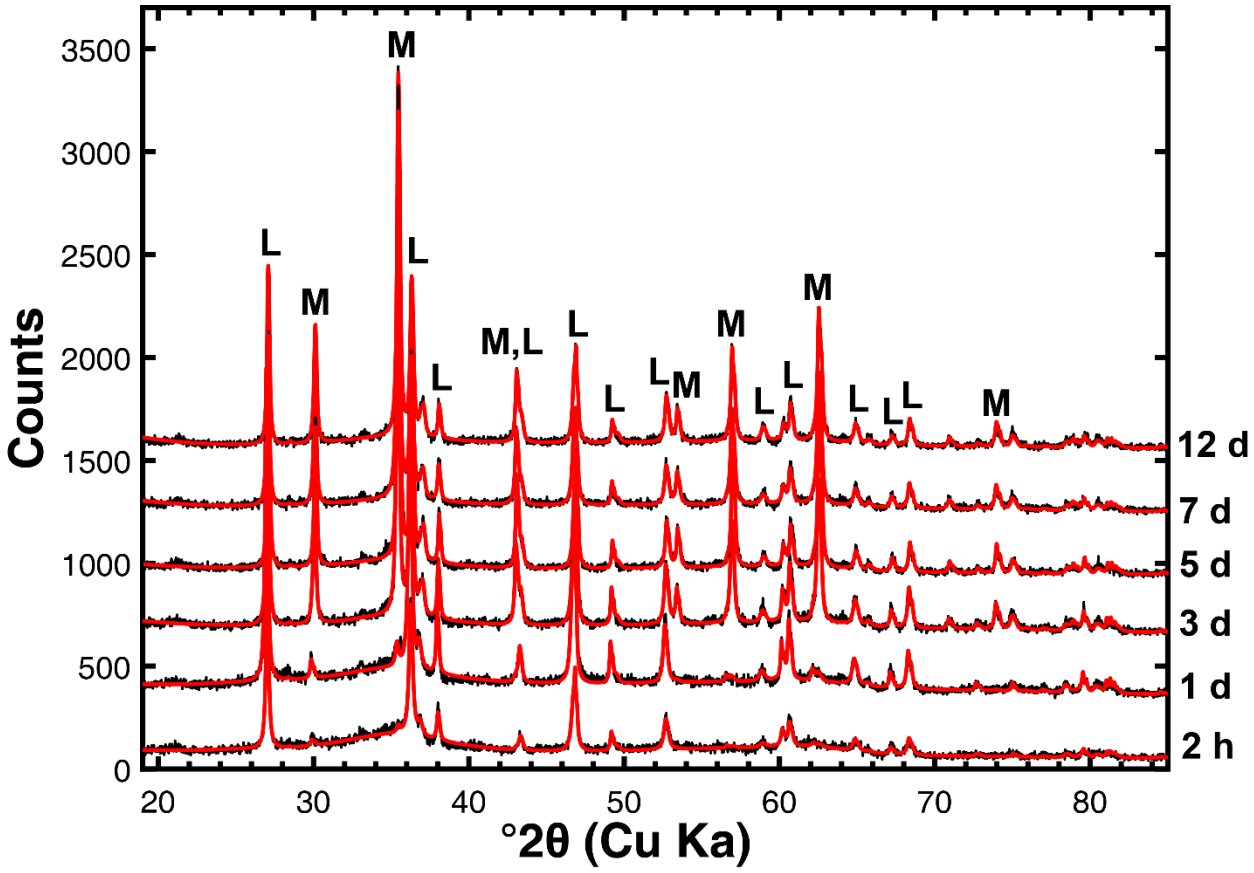

Figure A2.3. Rietveld refinement fit of XRD data (red) and XRD data (black) of mineral composition changed over time during 12-day Zn-ferrihydrite transformation experiment in 1.0 mM Fe(II)

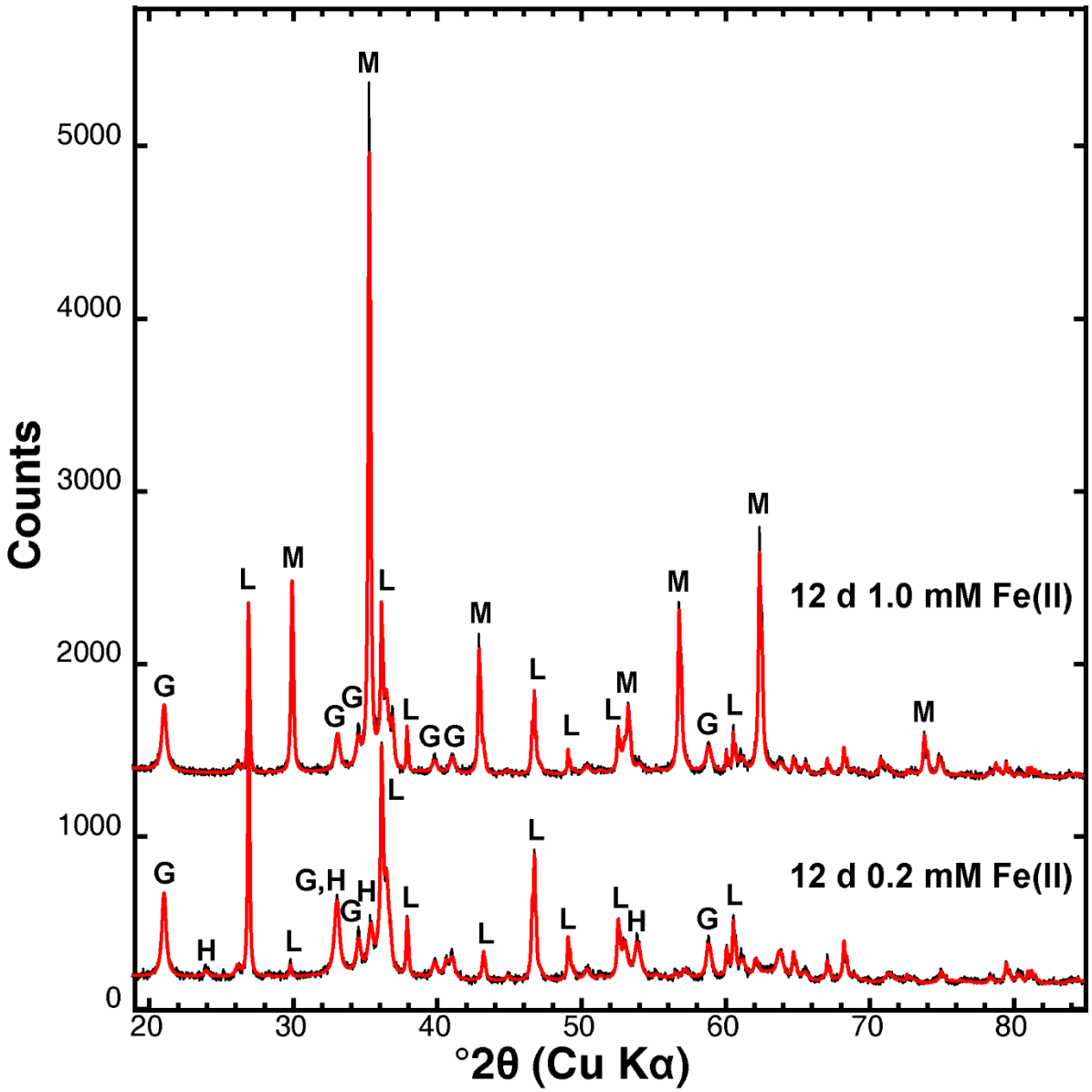

Figure A2.4. Rietveld refinement fit of XRD data (red) and XRD data (black) of mineral composition of the control experiments using Zn-free ferrihydrite.

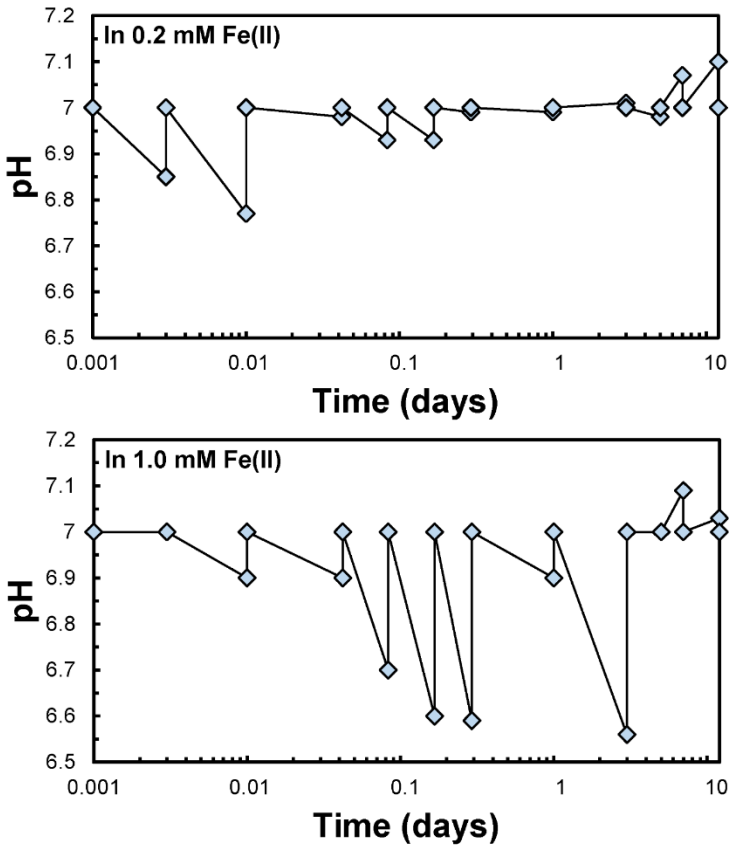

Figure A2.5. Drift in the pH during Zn-ferrihydrite transformation induced by 0.2 mM or 1.0 mM Fe(II). At each sampling point the pH was adjusted back to 7.0±0.1 by dropwise addition of 0.1 M NaOH

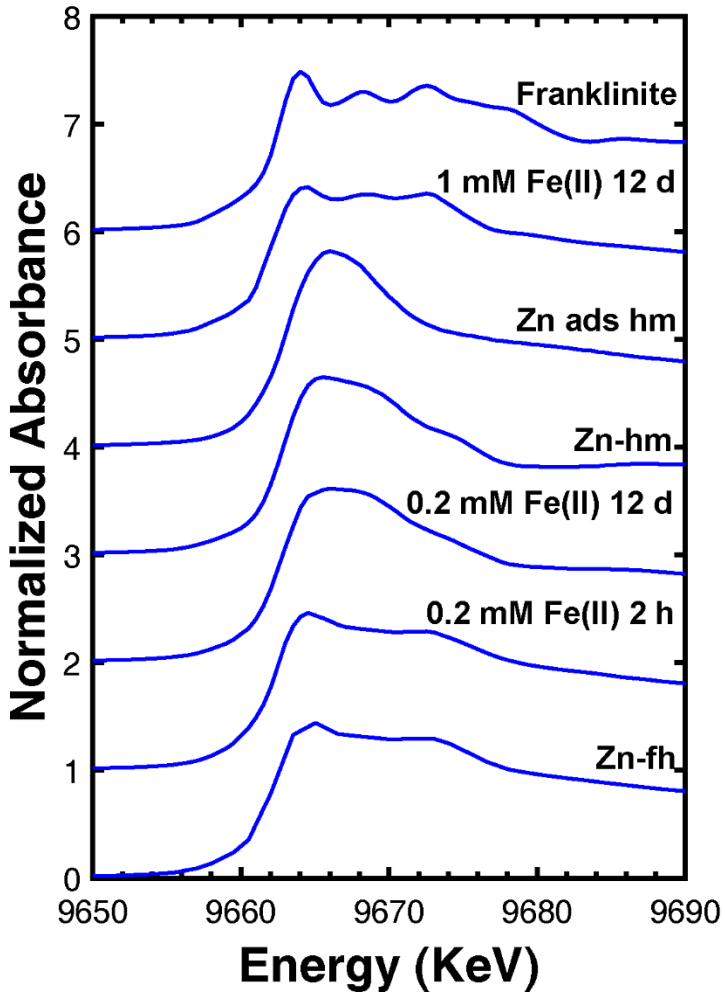

Figure A2.6. Zn K-edge XANES spectra of Zn-ferrihydrite (Zn-fh), Zn-ferrihydrite reacted with 0.2 mM Fe(II) for 2 hours and 12 days, standards of Zn incorporated in (Zn-hm) and adsorbed on (Zn ads hm) hematite, Zn-ferrihydrite reacted with 1.0 mM Fe(II) for 12 days, and franklinite.

2.9 REFERENCES

Ainsworth C. C., Gassman P. L., Pilon J. L. and Van Der Sluys W. G. (1994) Cobalt, cadmium, and lead sorption to hydrous iron oxide: Residence time effect. *Soil Sci. Soc. Am. J.* **58**, 1615–1623.

Ankudinov A. and Ravel B. (1998) Real-space multiple-scattering calculation and interpretation of x-ray-absorption near-edge structure. *Phys. Rev. B - Condens. Matter Mater. Phys.* **58**, 7565–7576.

Balistrieri L. S., Borrok D. M., Wanty R. B. and Ridley W. I. (2008) Fractionation of Cu and Zn isotopes during adsorption onto amorphous Fe(III) oxyhydroxide: Experimental mixing of acid rock drainage and ambient river water. *Geochim. Cosmochim. Acta* **72**, 311–328.

Bekker A., Slack J. F., Planavsky N., Krapež B., Hofmann A., Konhauser K. O. and Rouxel O. J. (2010) Iron formation: The sedimentary product of a complex interplay among mantle, tectonic, oceanic, and biospheric processes. *Econ. Geol.* **105**, 467–508.

Bergmann J., Friedel P. and Kleeberg R. (1998) BGMN—a new fundamental parameters based Rietveld program for laboratory X-ray sources, its use in quantitative analysis and structure investigations. *CPD Newsl.* **20**, 5–8.

Boland D. D., Collins R. N., Glover C. J. and David Waite T. (2013) An in situ quick-EXAFS and redox potential study of the Fe(II)-catalysed transformation of ferrihydrite. *Colloids Surfaces A Physicochem. Eng. Asp.* **435**, 2–8.

Boland D. D., Collins R. N., Miller C. J., Glover C. J. and Waite T. D. (2014) Effect of solution and solid-phase conditions on the Fe(II)-accelerated transformation of ferrihydrite to lepidocrocite and goethite. *Environ. Sci. Technol.* **48**, 5477–5485.

Brown G. E. Jr. and Parks G. A. (2001) Sorption of trace elements on mineral surfaces: Modern perspectives from spectroscopic studies, and comments on sorption in the marine environment. *Int. Geol. Rev.* **43**, 963–1073.

Brown K., Tegoni M., Prudêncio M., Pereira A. S., Besson S., Moura J. J., Moura I. and Cambillau C. (2000) A novel type of catalytic copper cluster in nitrous oxide reductase. *Nat. Struct. Biol.* **7**, 191–195.

Bryan A. L., Dong S., Wilkes E. B. and Wasylenki L. E. (2015) Zinc isotope fractionation during adsorption onto Mn oxyhydroxide at low and high ionic strength. *Geochim. Cosmochim. Acta* **157**, 182–197.

Bylaska E. J., Catalano J. G., Mergelsberg S. T., Saslow S. A., Qafoku O., Prange M. P. and Ilton E. S. (2019) Association of defects and zinc in hematite. *Environ. Sci. Technol.* **53**, 13687–13694.

Chan M. A., Ormö J., Park A. J., Stich M., Souza-Egipsy V. and Komatsu G. (2007) Models of iron oxide concretion formation: Field, numerical, and laboratory comparisons. *Geofluids* **7**, 356–368.

Chen J.-B., Louvat P., Gaillardet J. and Birck J.-L. (2009) Direct separation of Zn from dilute aqueous solutions for isotope composition determination using multi-collector ICP-MS. *Chem. Geol.* **259**, 120–130.

Cismasu A. C., Michel F. M., Tcaciuc A. P. and Brown G. E. Jr. (2014) Properties of impurity-bearing ferrihydrite III. Effects of Si on the structure of 2-line ferrihydrite. *Geochim. Cosmochim. Acta* **133**, 168–185.

Combes J. M., Manceau A. and Calas G. (1990) Formation of ferric oxides from aqueous solutions: A polyhedral approach by X-ray Absorption Spectroscopy: II. Hematite

formation from ferric gels. *Geochim. Cosmochim. Acta* **54**, 1083–1091.
Cornell R. M. (1988) The influence of some divalent cations on the transformation of ferrihydrite to more crystalline products. *Clay Miner.* **23**, 329–332.
Cornell R. M. and Schwertmann U. (2003) *The Iron Oxides*., VCH Publishers, New York.
Dai C., Lin M. and Hu Y. (2017) Heterogeneous Ni- and Cd-bearing ferrihydrite precipitation and recrystallization on quartz under acidic pH condition. *ACS Earth Sp. Chem.* **1**, 621–628.
Das S., Hendry M. J. and Essilfie-Dughan J. (2011) Transformation of two-line ferrihydrite to goethite and hematite as a function of pH and temperature. *Environ. Sci. Technol.* **45**, 268–275.
Doebelin N. and Kleeberg R. (2015) Profex: a graphical user interface for the Rietveld refinement program BGMN. *J. Appl. Crystallogr.* **48**, 1573–1580.
Doelsch E., Rose J., Masion A., Bottero J. Y., Nahon D. and Bertsch P. M. (2000) Speciation and crystal chemistry of iron(III) chloride hydrolyzed in the presence of SiO_4 ligands. 1. An Fe K-edge EXAFS study. *Langmuir* **16**, 4726–4731.
Doelsch E., Stone W. E. E., Petit S., Masion A., Rose J., Bottero J. Y. and Nahon D. (2001) Speciation and crystal chemistry of Fe(III) chloride hydrolyzed in the presence of SiO4 ligands. 2. Characterization of Si-Fe aggregates by FTIR and 29Si solid-state NMR. *Langmuir* **17**, 1399–1405.
Eickhoff M., Obst M., Schröder C., Hitchcock A. P., Tyliszczak T., Martinez R. E., Robbins L. J., Konhauser K. O. and Kappler A. (2014) Nickel partitioning in biogenic and abiogenic ferrihydrite: The influence of silica and implications for ancient environments. *Geochim. Cosmochim. Acta* **140**, 65–79.
Ekstrom E. B. and Morel F. M. M. (2008) Cobalt limitation of growth and mercury methylation in sulfate-reducing bacteria. *Environ. Sci. Technol.* **42**, 93–99.
Ermler U., Grabarse W., Shima S., Goubeaud M. and Thauer R. K. (1997) Crystal structure of methyl-coenzyme M reductase: The key enzyme of biological methane formation. *Science* **278**, 1457–1462.
Fei Y., Hua J., Liu C., Li F., Zhu Z., Xiao T., Chen M., Gao T., Wei Z. and Hao L. (2018) Aqueous Fe(II)-induced phase transformation of ferrihydrite coupled adsorption/immobilization of rare earth elements. *Minerals* **8**, 357.
Fischer W. R. and Schwertmann U. (1975) The formation of hematite from amorphous iron(III)hydroxide. *Clays Clay Miner.* **23**, 33–37.
Fleet M. E. (1981) The structure of magnetite. *Acta Crystallogr. Sect. B Struct. Crystallogr. Cryst. Chem.* **37**, 917–920.
Ford R. G., Bertsch P. M. and Farley K. J. (1997) Changes in transition and heavy metal partitioning during hydrous iron oxide aging. *Environ. Sci. Technol.* **31**, 2028–2033.
Ford R. G., Kemner K. M. and Bertsch P. M. (1999) Influence of sorbate-sorbent interactions on the crystallization kinetics of nickel- and lead-ferrihydrite coprecipitates. *Geochim. Cosmochim. Acta* **63**, 39–48.
Frierdich A. J. and Catalano J. G. (2012) Controls on Fe(II)-activated trace element release from goethite and hematite. *Environ. Sci. Technol.* **46**, 1519–1526.
Frierdich A. J., Luo Y. and Catalano J. G. (2011) Trace element cycling through iron oxide minerals during redox-driven dynamic recrystallization. *Geology* **39**, 1083–1086.
Frierdich A. J., Scherer M. M., Bachman J. E., Engelhard M. H., Rapponotti B. W. and Catalano J. G. (2012) Inhibition of trace element release during Fe(II)-activated recrystallization of Al-, Cr-, and Sn-substituted goethite and hematite. *Environ. Sci. Technol.* **46**, 10031–10039.

Garçon M., Sauzéat L., Carlson R. W., Shirey S. B., Simon M., Balter V. and Boyet M. (2017) Nitrile, latex, neoprene and vinyl gloves: A primary source of contamination for trace element and Zn isotopic analyses in geological and biological samples. *Geostand. Geoanalytical Res.* **41**, 367–380.

Gärtner P., Ecker A., Fischer R., Linder D., Fuchs G. and Thauer R. K. (1993) Purification and properties of N^5-methyltetrahydromethanopterin: coenzyme M methyltransferase from Methanobacterium thermoautotrophicum. *Eur. J. Biochem.* **213**, 537–545.

Glass J. B. and Orphan V. J. (2012) Trace metal requirements for microbial enzymes involved in the production and consumption of methane and nitrous oxide. *Front. Microbiol.* **3**, 1–20.

Gräfe M. and Sparks D. L. (2005) Kinetics of zinc and arsenate co-sorption at the goethite-water interface. *Geochim. Cosmochim. Acta* **69**, 4573–4595.

Granger J. and Ward B. B. (2003) Accumulation of nitrogen oxides in copper-limited cultures of denitrifying bacteria. *Limnol. Oceanogr.* **48**, 313–318.

Gustafsson J. P., Tiberg C., Edkymish A. and Kleja D. B. (2011) Modelling lead(II) sorption to ferrihydrite and soil organic matter. *Environ. Chem.* **8**, 485–492.

Ha J., Trainor T. P., Farges F. and Brown G. E. Jr. (2009) Interaction of aqueous Zn(II) with hematite nanoparticles and microparticles. Part 1. EXAFS study of Zn(II) adsorption and precipitation. *Langmuir* **25**, 5574–5585.

Handler R. M., Beard B. L., Johnson C. M. and Scherer M. M. (2009) Atom exchange between aqueous Fe (II) and goethite : An Fe isotope tracer study. **43**, 1102–1107.

Hansel C. M., Benner S. G. and Fendorf S. (2005) Competing Fe(II)-induced mineralization pathways of ferrihydrite. *Environ. Sci. Technol.* **39**, 7147–7153.

Hansel C. M., Benner S. G., Neiss J., Dohnalkova A., Kukkadapu R. K. and Fendorf S. (2003) Secondary mineralization pathways induced by dissimilatory iron reduction of ferrihydrite under advective flow. *Geochim. Cosmochim. Acta* **67**, 2977–2992.

Hansel C. M., Learman D. R., Lentini C. J. and Ekstrom E. B. (2011) Effect of adsorbed and substituted Al on Fe(II)-induced mineralization pathways of ferrihydrite. *Geochim. Cosmochim. Acta* **75**, 4653–4666.

Hiemstra T. (2015) Formation, stability, and solubility of metal oxide nanoparticles: Surface entropy, enthalpy, and free energy of ferrihydrite. *Geochim. Cosmochim. Acta* **158**, 179–198.

Hiemstra T. (2013) Surface and mineral structure of ferrihydrite. *Geochim. Cosmochim. Acta* **105**, 316–325.

Hiemstra T., Mendez J. C. and Li J. (2019) Evolution of the reactive surface area of ferrihydrite: Time, pH, and temperature dependency of growth by Ostwald ripening. *Environ. Sci. Nano* **6**, 820–833.

Jambor J. L. and Dutrizac J. E. (1998) Occurrence and constitution of natural and synthetic ferrihydrite, a widespread iron oxyhydroxide. *Chem. Rev.* **98**, 2549–2585.

Jiang Z., Liu Q., Roberts A. P., Barrón V., Torrent J. and Zhang Q. (2018) A new model for transformation of ferrihydrite to hematite in soils and sediments. *Geology* **46**, 987–990.

Johnston J. H. and Lewis D. G. (1983) A detailed study of the transformation of ferrihydrite to hematite in an aqueous medium at 92°C. *Geochim. Cosmochim. Acta* **47**, 1823–1831.

Jones A. M., Collins R. N., Rose J. and Waite T. D. (2009) The effect of silica and natural organic matter on the Fe(II)-catalysed transformation and reactivity of Fe(III) minerals. *Geochim. Cosmochim. Acta* **73**, 4409–4422.

Jones A. M., Collins R. N. and Waite T. D. (2017) Redox characterization of the Fe(II)-catalyzed

transformation of ferrihydrite to goethite. *Geochim. Cosmochim. Acta* **218**, 257–272.
Juillot F., Maréchal C., Ponthieu M., Cacaly S., Morin G., Benedetti M., Hazemann J. L., Proux O. and Guyot F. (2008) Zn isotopic fractionation caused by sorption on goethite and 2-Lines ferrihydrite. *Geochim. Cosmochim. Acta* **72**, 4886–4900.
Kämpf N. and Schwertmann U. (1983) Goethite and hematite in a climosequence in southern Brazil and their application in classification of kaolinitic soils. *Geoderma* **29**, 27–39.
Kay A. R. (2004) Detecting and minimizing zinc contamination in physiological solutions. *BMC Physiol.* **4**, 1–9.
Kelly S. D., Hesterberg D. and Ravel B. (2008) Analysis of soils and minerals using X-ray absorption spectroscopy. In *Methods of Soil Analysis* Soil Science Society of America, Madison. pp. 387–463.
Latta D. E., Gorski C. A. and Scherer M. M. (2012) Influence of Fe^{2+}-catalysed iron oxide recrystallization on metal cycling. *Biochem. Soc. Trans.* **40**, 1191–1197.
Lee K., Kostka J. E. and Stucki J. W. (2006) Comparisons of structural Fe reduction in smectites by bacteria and dithionite: An infrared spectroscopic study. *Clays Clay Miner.* **54**, 195–208.
Liu C., Zhu Z., Li F., Liu T., Liao C., Lee J. J., Shih K., Tao L. and Wu Y. (2016) Fe(II)-induced phase transformation of ferrihydrite: The inhibition effects and stabilization of divalent metal cations. *Chem. Geol.* **444**, 110–119.
Liu H., Guo H., Li P. and Wei Y. (2008) The transformation of ferrihydrite in the presence of trace Fe(II): The effect of the anionic media. *J. Solid State Chem.* **181**, 2666–2671.
Liu H., Li P., Zhu M., Wei Y. and Sun Y. (2007) Fe(II)-induced transformation from ferrihydrite to lepidocrocite and goethite. *J. Solid State Chem.* **180**, 2121–2128.
Liu H., Wei Y. and Sun Y. (2005) The Formation of hematite from ferrihydrite using Fe(II) as a catalyst. *J. Mol. Catal. A Chem.* **226**, 135–140.
Lu X., Johs A., Zhao L., Wang L., Pierce E. M. and Gu B. (2018) Nanomolar copper enhances mercury methylation by *Desulfovibrio desulfuricans* ND132. *Environ. Sci. Technol. Lett.* **5**, 372–376.
Maillot F., Morin G., Wang Y., Bonnin D., Ildefonse P., Chaneac C. and Calas G. (2011) New insight into the structure of nanocrystalline ferrihydrite: EXAFS evidence for tetrahedrally coordinated iron(III). *Geochim. Cosmochim. Acta* **75**, 2708–2720.
Manceau A., Lanson M. and Geoffroy N. (2007) Natural speciation of Ni, Zn, Ba, and As in ferromanganese coatings on quartz using X-ray fluorescence, absorption, and diffraction. *Geochim. Cosmochim. Acta* **71**, 95–128.
Martin S., Zhu C., Rule J., Nuhfer N. T., Ford R., Hedges S. and Soong Y. (2005) A high-resolution TEM-AEM, pH titration, and modeling study of Zn^{2+} coprecipitation with ferrihydrite. *Geochim. Cosmochim. Acta* **69**, 1543–1553.
Martínez C. E. and McBride M. B. (1998) Coprecipitates of Cd, Cu, Pb and Zn in iron oxides: Solid phase transformation and metal solubility after aging and thermal treatment. *Clays Clay Miner.* **46**, 537–545.
Masue-Slowey Y., Loeppert R. H. and Fendorf S. (2011) Alteration of ferrihydrite reductive dissolution and transformation by adsorbed As and structural Al: Implications for As retention. *Geochim. Cosmochim. Acta* **75**, 870–886.
Michel F. M., Barrón V., Torrent J., Morales M. P., Serna C. J., Boily J. F., Liu Q., Ambrosini A., Cismasu A. C. and Brown G. E. Jr. (2010) Ordered ferrimagnetic form of ferrihydrite reveals links among structure, composition, and magnetism. *Proc. Natl. Acad. Sci. U. S. A.* **107**, 2787–2792.

Michel F. M., Ehm L., Antao S. M., Lee P. L., Chupas P. J., Liu G., Strongin D. R., Schoonen M. A. A., Phillips B. L. and Parise J. B. (2007) The structure of ferrihydrite, a nanocrystalline material. *Science* **316**, 1726–1729.

Moynier F., Vance D., Fujii T. and Savage P. (2017) The isotope geochemistry of zinc and copper. *Rev. Mineral. Geochemistry* **82**, 543–600.

Nagano T., Nakashima S., Nakayama S. and Senoo M. (1994) The use of color to quantify the effects of pH and temperature on the crystallization kinetics of goethite under highly alkaline conditions. *Clays Clay Miner.* **42**, 226–234.

Navrotsky A., Mazeina L. and Majzlan J. (2008) Size-driven structural and thermodynamic complexity in iron oxides. *Science* **319**, 1635–1638.

Newville M. (2001) IFEFFIT: Interactive XAFS analysis and FEFF fitting. *J. Synchrotron Radiat.* **8**, 322–324.

Nørnberg P., Vendelboe A. L., Gunnlaugsson H. P., Merrison J. P., Finster K. and Jensen S. K. (2009) Comparison of the mineralogical effects of an experimental forest fire on a goethite/ferrihydrite soil with a topsoil that contains hematite, maghemite and goethite. *Clay Miner.* **44**, 239–247.

Parks J. M., Johs A., Podar M., Bridou R., Hurt R. A., Smith S. D., Tomanicek S. J., Qian Y., Brown S. D., Brandt C. C., Palumbo A. V., Smith J. C., Wall J. D., Elias D. A. and Liang L. (2013) The genetic basis for bacterial mercury methylation. *Science* **339**, 1332–1335.

Pavese A., Levy D. and Hoser A. (2000) Cation distribution in synthetic zinc ferrite ($Zn_{0.97}Fe_{2.02}O_4$) from in situ high-temperature neutron powder diffraction. *Am. Mineral.* **85**, 1497–1502.

Pedersen H. D., Postma D., Jakobsen R. and Larsen O. (2005) Fast transformation of iron oxyhydroxides by the catalytic action of aqueous Fe(II). *Geochim. Cosmochim. Acta* **69**, 3967–3977.

Pokrovski G. S., Schott J., Farges F. and Hazemann J. L. (2003) Iron (III)-silica interactions in aqueous solution: Insights from X-ray absorption fine structure spectroscopy. *Geochim. Cosmochim. Acta* **67**, 3559–3573.

Pokrovsky O. S., Viers J. and Freydier R. (2005) Zinc stable isotope fractionation during its adsorption on oxides and hydroxides. *J. Colloid Interface Sci.* **291**, 192–200.

Qafoku O., Kovarik L., Bowden M. E., Nakouzi E., Sheng A., Liu J., Pearce C. I. and Rosso K. M. (2020) Nanoscale observations of Fe(ii)-induced ferrihydrite transformation. *Environ. Sci. Nano* **7**, 2953–2967.

Ravel B. and Newville M. (2005) ATHENA, ARTEMIS, HEPHAESTUS: Data analysis for X-ray absorption spectroscopy using IFEFFIT. *J. Synchrotron Radiat.* **12**, 537–541.

Sakakibara M., Tanaka M., Takahashi Y. and Murakami T. (2019) Redistribution of Zn during transformation of ferrihydrite: Effects of initial Zn concentration. *Chem. Geol.* **522**, 121–134.

Scheinost A. C., Abend S., Pandya K. I. and Sparks D. L. (2001) Kinetic controls on Cu and Pb sorption by ferrihydrite. *Environ. Sci. Technol.* **35**, 1090–1096.

Schönheit P., Moll J. and Thauer R. K. (1979) Nickel, cobalt, and molybdenum requirement for growth of Methanobacterium thermoautotrophicum. *Arch. Microbiol.* **123**, 105–107.

Schultz M. F., Benjamin M. M. and Ferguson J. F. (1987) Adsorption and desorption of metals on ferrihydrite: Reversibility of the reaction and sorption properties of the regenerated solid. *Environ. Sci. Technol.* **21**, 863–869.

Schwertmann U. and Cornell R. M. (2000) *Iron Oxides in the Laboratory: Preparation and*

Synthesis., VCH Publishers, New York.
Schwertmann U., Friedl J. and Stanjek H. (1999) From Fe(III) ions to ferrihydrite and then to hematite. *J. Colloid Interface Sci.* **223**, 215–223.
Schwertmann U., Friedl J., Stanjek H. and Schulze D. G. (2000a) The effect of Al on Fe oxides. XIX. Formation of Al-substituted hematite from ferrihydrite at 25°C and pH 4 to 7. *Clays Clay Miner.* **48**, 159–172.
Schwertmann U., Friedl J., Stanjek H. and Schulze D. G. (2000b) The effect of clay minerals on the formation of goethite and hematite from ferrihydrite after 16 years' ageing at 25°C and pH 4-7. *Clay Miner.* **35**, 613–623.
Schwertmann U. and Murad E. (1983) Effect of pH on the formation of goethite and hematite from ferrihydrite. *Clays Clay Miner.* **31**, 277–284.
Schwertmann U., Stanjek H. and Becher H.-H. (2004) Long-term in vitro transformation of 2-line ferrihydrite to goethite/hematite at 4, 10, 15 and 25°C . *Clay Miner.* **39**, 433–438.
Schwertmann U. and Taylor R. M. (1972) The transformation of lepidocrocite to goethite. *Clays Clay Miner.* **20**, 151–158.
Sheng A., Li X., Arai Y., Ding Y., Rosso K. M. and Liu J. (2020a) Citrate controls Fe(II)-catalyzed transformation of ferrihydrite by complexation of the labile Fe(III) intermediate. *Environ. Sci. Technol.* **54**, 7309–7319.
Sheng A., Liu J., Li X., Qafoku O., Collins R. N., Jones A. M., Pearce C. I., Wang C., Ni J., Lu A. and Rosso K. M. (2020b) Labile Fe(III) from sorbed Fe(II) oxidation is the key intermediate in Fe(II)-catalyzed ferrihydrite transformation. *Geochim. Cosmochim. Acta* **272**, 105–120.
Soltis J. A., Feinberg J. M., Gilbert B. and Penn R. L. (2016) Phase transformation and particle-mediated growth in the formation of hematite from 2-Line ferrihydrite. *Cryst. Growth Des.* **16**, 922–932.
Thauer R. K. (1998) Biochemistry of methanogenesis: a tribute to Marjory Stephenson:1998 Marjory Stephenson Prize Lecture. *Microbiology* **144**, 2377–2406.
Thomasarrigo L. K., Byrne J. M., Kappler A. and Kretzschmar R. (2018) Impact of organic matter on iron(II)-catalyzed mineral transformations in ferrihydrite-organic matter coprecipitates. *Environ. Sci. Technol.* **52**, 12316–12326.
Thomasarrigo L. K., Kaegi R. and Kretzschmar R. (2019) Ferrihydrite growth and transformation in the presence of ferrous iron and model organic ligands. *Environ. Sci. Technol.* **53**, 13636–13647.
Tian L., Shi Z., Lu Y., Dohnalkova A. C., Lin Z. and Dang Z. (2017) Kinetics of cation and oxyanion adsorption and desorption on ferrihydrite: Roles of ferrihydrite binding sites and a unified model. *Environ. Sci. Technol.* **51**, 10605–10614.
Tomaszewski E. J., Cronk S. S., Gorski C. A. and Ginder-Vogel M. (2016) The role of dissolved Fe(II) concentration in the mineralogical evolution of Fe (hydr)oxides during redox cycling. *Chem. Geol.* **438**, 163–170.
Torrent J., Guzman R. and Parra M. A. (1982) Influence of relative humidity on the crystallization of Fe(III) oxides from ferrihydrite. *Clays Clay Miner.* **30**, 337–340.
Tronc E., Belleville P., Jolivet J. P. and Livage J. (1992) Transformation of ferric hydroxide into spinel by Fe(II) adsorption. *Langmuir* **8**, 313–319.
Verwey E. J. W. and Heilmann E. L. (1947) Physical properties and cation arrangement of oxides with spinel structures I. Cation arrangement in spinels. *J. Chem. Phys.* **15**, 174–180.
Wang X., Zhu M., Lan S., Ginder-Vogel M., Liu F. and Feng X. (2015) Formation and

secondary mineralization of ferrihydrite in the presence of silicate and Mn(II). *Chem. Geol.* **415**, 37–46.

Waychunas G. A., Fuller C. C. and Davis J. A. (2002) Surface complexation and precipitate geometery for aqueous Zn(II) sorption on ferrihydrite I: X-ray absorption extended fine structure spectroscopy analysis. *Geochim. Cosmochim. Acta* **66**, 1119–1137.

Webb S. M. (2005) SIXpack: A graphical user interface for XAS analysis using IFEFFIT. *Phys. Scr. T* **T115**, 1011–1014.

Williams A. G. B. and Scherer M. M. (2004) Spectroscopic evidence for Fe(II)-Fe(III) electron transfer at the iron oxide-water interface. *Environ. Sci. Technol.* **38**, 4782–4790.

Xiao W., Jones A. M., Collins R. N. and Waite T. D. (2018) Investigating the effect of ascorbate on the Fe(II)-catalyzed transformation of the poorly crystalline iron mineral ferrihydrite. *Biochim. Biophys. Acta - Gen. Subj.* **1862**, 1760–1769.

Yang L., Steefel C. I., Marcus M. A. and Bargar J. R. (2010) Kinetics of Fe(II)-catalyzed transformation of 6-line ferrihydrite under anaerobic flow conditions. *Environ. Sci. Technol.* **44**, 5469–5475.

Yee N., Shaw S., Benning L. G. and Nguyen T. H. (2006) The rate of ferrihydrite transformation to goethite via the Fe(II) pathway. *Am. Mineral.* **91**, 92–96.

Zhang D., Wang S., Wang Y., Gomez M. A., Duan Y. and Jia Y. (2018) The transformation of two-line ferrihydrite into crystalline products: effect of pH and media (sulfate versus nitrate). *ACS Earth Sp. Chem.* **2**, 577–587.

Zheng K., Ngo P. D., Owens V. L., Yang X. P. and Mansoorabadi S. O. (2016) The biosynthetic pathway of coenzyme F430 in methanogenic and methanotrophic archaea. *Science* **354**, 339–342.

Zhou Z., Latta D. E., Noor N., Thompson A., Borch T. and Scherer M. M. (2018) Fe(II)-catalyzed transformation of organic matter-ferrihydrite coprecipitates: A closer look using Fe isotopes. *Environ. Sci. Technol.* **52**, 11142–11150.

Zhou Z., Latta D. E. and Scherer M. M. (2021) Natural organic matter inhibits Ni stabilization during Fe(II)-catalyzed ferrihydrite transformation. *Sci. Total Environ.* **755**, 142612.

CHAPTER 3

CONSISTENT CONTROLS ON TRACE METAL MICRONUTRIENT SPECIATION IN WETLAND SOILS AND STREAM SEDIMENTS

Published as:
Yan J., Sharma N., Flynn E. D., Giammar D. E., Schwartz G. E., Brooks S. C., Weisenhorn P., Kemner K. M., O'Loughlin E. J., Kaplan D. I. and Catalano J. G. (2022b) Consistent controls on trace metal micronutrient speciation in wetland soils and stream sediments. Geochim. Cosmochim. Acta 317, 234–25

3.1 ABSTRACT

Trace metals are essential for microbially-mediated biogeochemical processes occurring in anoxic wetland soils and stream bed sediments, but low availability of these elements may inhibit anaerobic element cycling and transformations. Solid-phase speciation is likely a critical control on trace metal availability but has seen limited study in anoxic systems having concentrations similar to geological background levels, where metal limitations may be most prevalent. We have investigated trace metal concentrations and solid-phase speciation in three freshwater subsurface aquatic systems: marsh wetland soils, riparian wetland soils, and the sediments of a streambed. These systems displayed low solid-phase trace metal concentrations, generally at or below geological background levels, which generally followed the trend Zn > Cu ≈ Ni > Co and showed no correlation with major element compositions. All soils and sediments were dominated by quartz but varied in clay mineralogy as well as the organic matter, total sulfur, and total iron contents. X-ray absorption near-edge structure (XANES) spectroscopy shows that sulfur speciation in both wetlands is dominated by organic sulfur. Elemental sulfur and iron sulfides together made up <25% of the sulfur in the wetland soils, but the distribution between inorganic and organic forms was reversed in the stream sediments. Ferrous and ferric iron in clay minerals were common species identified by both XANES and extended X-ray absorption fine structure (EXAFS) spectroscopies at all sites. Iron(III) oxides were substantial components in all but the marsh wetland soils. Quantitative analysis of copper, nickel, and zinc XANES spectra revealed similar metal speciation across all sites. Copper speciation was dominated by sulfides, adsorbed species, and minor amounts of copper bound to organic matter; no metallic copper was detected. Nickel speciation also varied little and was dominated by nickel in clay mineral octahedral sheets and nickel sulfide, with adsorbed species also present. Zinc speciation was slightly more varied, with

the marsh wetland soils and stream bed sediments containing adsorbed species, zinc associated with clay mineral structures, and zinc bound to reduced sulfur groups on organic matter, whereas the riparian wetland soils lacked clay-associated zinc but contained zinc sulfide. Trace metals bound to reduced sulfur occurred at every site, with a greater sulfur-bound fraction for copper. The fractional abundance of sulfur-bound species showed no relationship with soil or sediment total sulfur content, which varied by two orders of magnitude. More broadly, the observations in this study suggest that trace metal speciation in freshwater wetland soils and stream sediments is consistently dominated by a small set of recurring components which are distinct for each metal. This may represent a general geochemical phenomenon in anoxic soils and sediments containing trace metals at background concentrations (as low as 3 $\mu g\ g^{-1}$) that was not predicted from systems that are contaminated with or naturally-enriched in copper, nickel, or zinc.

3.2 INTRODUCTION

Subsurface aquatic systems in freshwater environments, such as wetland soils and stream sediments, are foci of diverse anaerobic biogeochemical processes (Bowden, 1987; McClain et al., 2003; Kocar and Fendorf, 2009; Zarnetske et al., 2011; Arora et al., 2016; Neumann et al., 2016). Denitrification and methanogenesis in freshwater aquatic systems serve as important sources to the atmosphere of the greenhouses gases N_2O and CH_4, respectively (Groffman et al., 1998; Glatzel et al., 2008; Bouwman et al., 2013; Kirschke et al., 2013; Tian et al., 2015; Zhang et al., 2017). Substantial mercury methylation and subsequent emission also occur in these settings (St Louis et al., 1994; Skyllberg, 2008; Schaefer et al., 2014; Riscassi et al., 2016; Singer et al., 2016; Yang et al., 2016). Many of these processes in subsurface aquatic systems also couple to the biogeochemical cycling of other elements, such as iron and sulfur (Koretsky et al., 2003; Hlaváčová et al., 2005; Hansel et al., 2015; Segarra et al., 2015; Glodowska et al., 2020).

While the biogeochemistry of aquatic systems has been widely studied from the perspective of redox conditions, substrate availability, and thermodynamic controls on metabolic processes (Falkowski et al., 1998; LaRowe and Van Cappellen, 2011; Flynn et al., 2014; Arora et al., 2016; Danczak et al., 2016; Janot et al., 2016), there is a growing recognition of the importance of trace metal availability in affecting biogeochemical processes (Basiliko and Yavitt, 2001; Glass and Orphan, 2012; Jacquot et al., 2014). Elements that include cobalt, nickel, copper, and zinc serve as key reaction centers in metalloenzymes (Gärtner et al., 1993; Ermler et al., 1997; Thauer, 1998; Brown et al., 2000; Parks et al., 2013; Zheng et al., 2016) and their low availability has been documented in laboratory studies to inhibit methanogenesis, nitrous oxide reduction to nitrogen, and mercury methylation (Schönheit et al., 1979; Granger and Ward, 2003; Ekstrom and Morel, 2008; Glass and Orphan, 2012; Lu et al., 2018). The geochemistry of trace

metals in aquatic systems may thus have a direct impact on biogeochemical cycling of carbon, nutrients, and contaminants.

The availability of trace metals in wetland soils and stream sediments is expected to be controlled by their chemical speciation rather than bulk concentration (Worms et al., 2006; Harmsen, 2007; Zhao et al., 2016). Past studies have identified an array of chemical forms of trace metals in similar types of anoxic settings, although these have often focused on locations containing elevated metal concentrations because of environmental contamination or geogenic enrichments. Of the trace metals, copper is the most widely studied in anoxic subsurface aquatic systems. Copper sulfides and metallic copper are generated in contaminated soils, often in nanoparticulate form, upon flooding (Weber et al., 2009a; Weber et al., 2009b; Fulda et al., 2013a; Hofacker et al., 2013b; Xia et al., 2018; Cervi et al., 2021), with organic matter then potentially stabilizing these phases under oxic conditions (Fulda et al., 2013b; Mantha et al., 2019). Copper sulfides were also observed in contaminated paddy soils (Yang et al., 2015; Sun et al., 2016) and a copper-rich bog (Lett and Fletcher, 1980). Binding to organic matter, including as Cu(I) species, may be important in contaminated, flooded soils with limited sulfate (Fulda et al., 2013a; Fulda et al., 2013b). A recent study examined uncontaminated transitional and anoxic soils and found copper binds extensively to organic matter but also forms copper sulfide and minor metallic copper in the anoxic zone (Mehlhorn et al., 2018).

Fewer studies have examined the speciation of other essential trace metals in subsurface aquatic systems. In diverse coastal sediments that drain ultramafic laterite deposits highly elevated in nickel, this metal occurs coprecipitated with iron sulfides and in the octahedral sheets of clay minerals (Noël et al., 2015; Noël et al., 2017; Merrot et al., 2019). While nickel speciation in other anoxic systems has seen limited study, contaminated or enriched oxic soils

contain nickel in phyllosilicate and iron oxide structures, associated with gibbsite phases in clay interlayers, and bound to organic matter (Manceau et al., 2005; McNear et al., 2007; Dublet et al., 2012; Siebecker et al., 2017; Siebecker et al., 2018). Zinc sulfide forms under anoxic conditions in metalliferous peatlands (Yoon et al., 2012), contaminated lake sediments (Webb and Gaillard, 2015), and in a contaminated wetland, along with zinc carbonate, adsorbed zinc, and possibly zinc oxide (Bostick et al., 2001). Similar to nickel, exploration of zinc in other anoxic soil systems is generally lacking, but in contaminated oxic soils zinc sulfide, zinc in phyllosilicate octahedral sheets, and adsorbed species are common (Manceau et al., 2004; Voegelin et al., 2005; Jacquat et al., 2009; Voegelin et al., 2011; Williams et al., 2011). Less is known regarding cobalt speciation because of the difficulty probing this element using available methods in the presence of iron. Binding studies suggest that adsorbed species and complexes with organic matter are important in aerobic soils (Woodward et al., 2018) and that cobalt readily incorporates into pyrite under anoxic conditions (Swanner et al., 2019).

Prior studies provide important insight into trace metal species in anoxic subsurface systems that are contaminated with or naturally elevated in metals. All metals show occurrence as sulfide phases, although some results, such as nickel associating with pyrite in coastal sediments, may not be transferable to freshwater systems that are generally low in sulfur (Brown, 1985; Wieder et al., 1985; Spratt and Morgan, 1990; Prietzel et al., 2009). Similarly, nickel and zinc often occur in clay structures, likely produced through a neoformation process (Manceau et al., 1999; Ford and Sparks, 2000; Schlegel et al., 2001; Dähn et al., 2002), but it is unclear whether such species form when metals are not elevated in concentration from contamination or natural enrichment. The solid-phase trace metal concentrations in most prior studies of metal speciation in subsurface aquatic systems (Lett and Fletcher, 1980; Bostick et al., 2001; Weber et

al., 2006; Weber et al., 2009b; Weber et al., 2009a; Yoon et al., 2012; Fulda et al., 2013b; Fulda et al., 2013a; Hofacker et al., 2015; Noël et al., 2015; Yang et al., 2015; Sun et al., 2016; Noël et al., 2017; Xia et al., 2018; Mantha et al., 2019; Merrot et al., 2019; Cervi et al., 2021) far exceed geological background levels (Rudnick and Gao, 2003): 280 to 23000 ug g^{-1} Cu versus 28±4 ug g^{-1} background, 255 to 6044 ug g^{-1} Ni versus 47±11 ug g^{-1} background, 1900 to 71000 ug g^{-1} Zn versus 67±6 ug g^{-1} background. Investigations of speciation in wetland soils and stream sediments with metal concentrations similar to geological background levels are rare (Webb and Gaillard, 2015; Mehlhorn et al., 2018). However, such metal concentrations are widespread in nature (Caritat et al., 2018) and likely representative of the large majority of freshwater wetlands and streambeds where biogeochemical carbon, nitrogen, and mercury cycling occur in terrestrial ecosystems. Anoxic subsurface systems displaying background metal levels should more frequently exhibit metal limitations on biogeochemical processes than contaminated or naturally-enriched systems However, the dominant controls on metal speciation in environments with low metal contents are unclear. A central challenge to investigating metal speciation in relevant anoxic subsurface systems is the difficulty in applying X-ray spectroscopic techniques to soils and sediments having low (<100 ug g^{-1}) element concentrations.

In this work, we assess the variability in trace metal speciation in the subsurface of diverse freshwater aquatic systems. Three field sites are investigated that are distributed over a ~1000 km transect, each occurring in geologically-distinct regions representing different types of subsurface aquatic system: marsh wetland soils, riparian wetland soils, and stream bed sediments. Duplicate soil or sediment cores and overlying surface waters were collected in two locations at each of the three study areas. Major element and trace metal concentrations, dissolved and extractable nutrients, and soil and sediment mineralogy were evaluated at these

sites. X-ray absorption spectroscopy evaluated bulk sulfur and iron speciation and quantified the solid-phase speciation of nickel, copper, and zinc. The latter measurements overcame the low concentrations of trace metals by utilizing a synchrotron beamline configuration optimized for high-sensitivity measurements. Metal speciation was compared across sites to identify the dominant forms of trace metals occurring in subsurface aquatic systems.

3.3 MATERIALS AND METHODS

3.3.1 Study Sites Descriptions

Three field sites (Fig. A3.1) were investigated to explore diverse wetland and stream settings, each of which has been previously studied in other contexts (Van Lonkhuyzen and LaGory, 1994; Van Lonkhuyzen et al., 2004; Southworth et al., 2013; Donovan et al., 2014; Riscassi et al., 2016; Flynn et al., 2017; Schwartz et al., 2019; Kaplan et al., 2020). At each site, two locations were studied to examine the variability in metal speciation in similar settings. Marsh wetlands at Argonne National Laboratory (ANL) in Lemont, Illinois, U.S.A. were sampled in October 2018. Sampling location "Marsh 1" (41°42'19.69"N 87°59'55.04"W WGS 84) is an ~1800 m^2 marsh surrounded by deciduous forest. It contained shallow surface water at the time of sampling but becomes unsaturated during prolonged dry periods. Location "Marsh 2" (41°42'6.78"N 87°59'39.66"W WGS 84) consists of a ~3700 m^2 marsh containing open water in the center surrounded by an ~15 m vegetated border; this site maintains water saturation throughout most years. Sampling locations Marsh 1 and 2 have internal designations as wetlands 401 and 405 at ANL (Van Lonkhuyzen and LaGory, 1994).

Sediments and surface waters were sampled at East Fork Poplar Creek (EFPC) in Oak Ridge, Tennessee, U.S.A. in October 2018. Sampling locations "Stream 1" (35°57'57.89"N

84°21’32.81”W WGS 84) and “Stream 2” (36°00’06.13”N 84°14’55.10”W WGS 84) are located approximately 15 km apart. Location Stream 1 is 5.4 km upstream of the mouth of the creek, and Stream 2 is in a broader stretch 22 to 23 km upstream from the mouth. Sediments were collected from the northwest or north stream bank for locations Stream 1 and Stream 2, respectively. Sampling occurred 25 days after the last significant rain event (rain >12 mm). EFPC is impacted by point source contamination with mercury, but not other metals, originating at its headwaters (Brooks and Southworth, 2011) and receives discharge from a wastewater treatment plant about midway between the two sampling locations.

The third study site is a riparian wetland in the Tims Branch (TB) watershed at the Savannah River Site in Aiken County, South Carolina, U.S.A. Samples were collected in February 2019 at two locations, “Riparian 1” (33°20'15.36"N 81°43'5.88"W WGS 84) and “Riparian 2” (33°20'9.24"N 81°43'8.04"W WGS 84). These differed in their apparent local hydrology, with Riparian 2 showing evidence of shallow groundwater inputs at the time of sampling, which was not observed at the other location. This forested site varies in its water inundation throughout the year and in summer may lack surface water for short periods of time. Note that a section of the Tims Branch watershed 1 to 2 km downstream of the sampling locations received historical discharge of drainage waters containing metals, including uranium (Kaplan et al., 2020). This discharge was introduced through a tributary and did not impact the study areas.

3.3.2 Soil and Water Sampling

At each sampling site, surface water samples were collected prior to soil or sediment coring. Subsamples of the surface waters were filtered using 0.22 µm mixed cellulose ester (MCE)

syringe filters. A portion of the filtered water was acidified to 2% nitric acid (HNO_3) in the field using concentrated trace metal grade HNO_3 for dissolved major elements and trace metal analysis. The rest of the filtered water was stored on ice and immediately divided and frozen or stored at 4° C upon return to the laboratory for nutrient and anion analysis, respectively. Field process blanks were prepared using ultrapure water (>18.2 MΩ cm) following the same procedures as the surface water samples to monitor possible metal contamination during the sampling. The pH, temperature, and conductivity of the surface waters were also measured during sampling at the marsh wetlands and stream sites using a Hanna Instruments HI98194 multiparameter meter. A meter malfunction prevented data collection at the riparian wetlands; temperature and pH data for these sampling locations are taken from measurements made in January 2019, a few weeks prior to soil and water sample collection. Measurements of pH made in August 2020 at the same sampling locations in the riparian wetlands were within 0.03 pH units of those measured in January 2019, suggesting that the pH values are temporally stable at these sites.

Duplicate soil and sediment samples from each of the two studied locations at the marsh wetland and stream sites were collected by hand-coring using 7.6 cm diameter acid-cleaned polycarbonate tubes, which were then capped and sealed in the field. Cores from the marsh site were placed in a cooler on ice and transported to Washington University, where they were extruded within six hours of sampling and then transferred to an anaerobic chamber (Coy Laboratory Products, 3% H_2/97% N_2 with Pd catalyst). Cores from the stream site were extruded within one hour of sampling in a laboratory at Oak Ridge National Laboratory, transferred to an anaerobic chamber, and then impulse sealed in polyethylene pouches. An inner pouch contained each extruded sample, and this was then sealed in an outer pouch. The gas headspace in both pouches were that of the anaerobic chamber and an oxygen scavenging sachet (BD GasPak^{TM} EZ Anaerobic

Container System Sachets with Indicator) was placed in the outer pouch to minimize the risk of leakage causing oxidation. These doubly-contained samples were removed from the anaerobic chamber after sealing, stored at 4°C, and then transported on ice to Washington University, where they were immediately transferred to an anaerobic chamber. Duplicate soil samples from each of the two study locations at the riparian wetland site were collected using 2.5 cm diameter polycarbonate tubes. These were sealed in the field, stored overnight at 4°C, and then shipped overnight to Washington University packaged with reusable ice packs, where they were then extruded and transferred to an anaerobic chamber. All cores were divided during extrusion based on visual changes in properties (e.g., soil horizons) when apparent or to divide the core length into two equal sections, with the resulting surface layer comprising the upper 4.5 to 9 cm (Table 3.1). All cores were segmented into two sections except for the second core from location Stream 2, which was longer and thus divided into three segments. For naming purposes, the core segments of each type were labeled using the convention CX-Y, with X being 1 or 2 to distinguish the duplicate cores and Y being 1, 2, or 3 (only for core 2 from location Stream 2) to indicate the segment starting with a value of 1 for the surface layer.

Table 3.1. Sample depth (cm) for soil and sediment core segments.

Sample Location	C1-1	C1-2	C2-1	C2-2
Marsh 1	0-7.5	7.5-15.3	0-9	9-18.4
Marsh 2	0-6.5	6.5-11	0-9	9-12
Riparian 1	0-4.5	4.5-9.5	0-4.5	4.5-10.5
Riparian 2	0-4.5	4.5-9.5	0-4	4-10
Stream 1	0-8	8-21.5	0-3	3-19.5
Stream 2*	0-8	8-12	0-8	8-18

*A third segment was obtained for C2 from this location over the depth range of 18 to 28.5 cm.

3.3.3 Surface Water Characterization

The field acidified surface water samples were used to determine dissolved major elements (sodium, magnesium, aluminum, silicon, potassium, calcium) using a Thermo Scientific iCap 7400 Duo inductively-coupled plasma optical emission spectrometer (ICP-OES). Dissolved trace metal (cobalt, nickel, copper, and zinc), iron, and manganese concentrations were determined by inductively-coupled plasma mass spectrometry (ICP-MS) using a PerkinElmer Elan DRC II instrument. Dissolved anions (Br^-, Cl^-, F^-, and SO_4^{2-}) in the unacidified, filtered water samples were measured using a Thermo Scientific Dionex Integrion High Pressure Ion Chromatograph (IC) using a conductivity detector. The anion concentrations were determined using a Dionex IonPac™ AS19 analytical column (4×250 mm) and Dionex IonPac™ AG19 guard column (4×50 mm) set to 30°C with the eluent generated from a Dionex eluent generator cartridge (EGC 500 KOH). The eluent concentration was set to 10 mM KOH for 10 minutes then gradually increased to 45 mM KOH over 15 minutes before holding steady at 45 mM KOH for 5 minutes. The flow rate remained constant at 1 mL min^{-1}. Dissolved nitrate, ammonium, and orthophosphate were measured

spectrophotometrically on a Seal Analytical AQ300 Discrete Multi-Chemistry Analyzer using frozen, field-filtered surface water samples that were thawed overnight at 4°C before analysis. Reagents and calibration standards were prepared using reagent grade chemicals. Ammonia was measured by reaction of a sample with hypochlorite in an alkaline solution, which is subsequently reacted with phenol in the presence of nitroferricyanide, with absorbance of the resulting blue indophenol dye measured at 660 nm. Nitrate was analyzed by reduction to nitrite by cadmium which then reacts with sulfanilamide in dilute phosphoric acid and binds to N-(1-napthyl)-ethylenediamine dihydrochloride, with the resulting azo dye detected at 520 nm. Phosphate analysis involves the reaction of samples with ammonium molybdate and potassium antimonyl tartrate in in dilute sulfuric acid, forming a complex that is then reduced by ascorbic acid, with the resulting colored complex quantified at 660 nm. Charge balance calculations and estimation of dissolved CO_2 concentrations were performed in the React module of The Geochemist's Workbench® (Bethke, 2007) version 12.0.6 using the Lawrence Livermore National Laboratory thermochemical database V8 R6 (Delaney and Lundeen, 1990). Although not measured during initial analyses because of an oversight, dissolved inorganic carbon (DIC) and dissolved organic carbon (DOC) were measured in May 2021 using a Shimadzu TOC-L total organic carbon analyzer for archived filtered (0.45 µm MCE) water samples that had been stored at 4°C.

3.3.4 Solid Phase Characterization

Soil and sediment core segments were mechanically mixed in the anaerobic chamber to homogenize the materials prior to analysis. Approximately 20 g of wet sediment from each core segment were dried in a convection oven at 40 °C for determining the moisture content of the soils and sediments and for further bulk analyses. Sediments were then ground with a pestle and mortar

and stored in glass vials. 1 g of each sediment sample was micronized in isopropanol using a McCrone Micronizing Mill to obtain a fine powder. The fine powders were then analyzed by powder X-ray diffraction (XRD) on a Bruker d8 Advance diffractometer using Cu Kα radiation (40 kV, 40 mA) and a LynxEye XE energy-dispersive silicon-strip detector. XRD patterns of all sediment segments were performed from 3° to 80° 2θ with a 0.02° 2θ step-size, a collection time of 1.0 s per step, and no sample rotation to enable measurement to low angle. The detector consists of 192 independent strips, each of which measured each 2θ position for the 1.0 s collection time, yielding a net integration time of 192 s per data point. The Bruker Diffrac.Eva application was used for phase identification using patterns generated from crystal structures contained in the Crystallography Open Database (Graulis et al., 2009).

Total nitrogen, carbon, and sulfur contents were determined using these dried soil and sediment samples by combustion elemental analysis using an Elementar vario MACRO cube CHNS analyzer. Approximately 0.1 to 0.2 g of the dried, ground soils or sediments from all core segments were measured in triplicate. The total metal concentrations in the soils and sediments were estimated using a microwave digestion analysis method (Hassan et al., 2007). Specifically, 3 mL of concentrated trace metal grade HNO_3 and 0.3 mL of 30% hydrogen peroxide (H_2O_2) were added to 0.030 g of dried soil or sediment in a PTFE microwave digester vessel. Samples were left to react at room temperature in the fume hood for 30 minutes and then digested in a CEM MARS6 microwave digestion system. The temperature was ramped from ambient to 175 °C over 10 min and then maintained at 175°C for 15 min to promote complete digestion. After the vessels cooled, samples were filtered using 0.22 µm MCE filters followed by dilution to 2% HNO_3. Triplicate digestions were prepared for each soil or sediments. Major elements (Al, Ca, Fe, K, Mg,

Na, P, and S) in the resulting fluid were analyzed using ICP-OES and trace metals (Cu, Ni, Co, and Zn) plus Mn using ICP-MS.

Extractable nitrate, ammonium, and phosphate in the sediments were measured by an equilibrium extraction method adapted from previous studies (Sparks et al., 1996; Pansu and Gautheyrou, 2006). The extractions were performed in the anaerobic chamber with 1 g of moist soil or sediments suspended in 10 mL of 2 M potassium chloride (KCl). Samples were rotated end-over-end for 1 h, allowed to settle for 30 min, and then filtered using 0.22 μm MCE syringe filters. The filtrate was stored at 4 °C prior to analysis. Nitrate, ammonium, and phosphate in the extraction fluid were analyzed using a Seal Analytical AQ300. Samples from both cores at each site were treated as duplicate measurements to assess variability. The measured moisture content was used to calculate the concentration of the nutrients per gram of soil or sediment.

3.3.5 X-ray Absorption Spectroscopy Data Collection and Analysis

To determine the speciation of sulfur, iron, and trace metals present in the soils and sediments, X-ray absorption spectra were measured for nickel, copper, and zinc in the C1-1 segments of the cores collected at each sampling location. C2-1 from location Stream 1 was also studied because XRD identified pyrite in C1-1 but not C2-1 (see Section 3.2). Cobalt was not investigated because its signal is masked by fluorescence from iron. Samples were prepared in an anaerobic chamber as wet pastes sealed in polycarbonate sample holders using two layers of Kapton tape backed with acrylic glue. The beam-facing side of samples prepared for sulfur analysis was sealed with Saint-Gobain CHR sulfur-free polyester tape with an acrylic backing. To preserve hydration and anoxic conditions, the sealed samples were then impulse sealed in polyethylene pouches, which also contained a cellulose fiber wiper moistened with deoxygenated ultrapure

water to inhibit desiccation. Reference standards (Fig. A3.3-8) that required stable hydration, such as adsorbed trace metal standards, were prepared similarly. Standards that are stable as dry solids were prepared by grinding using a mortar and pestle and spreading the resulting fine powder on cellulose acetate tape. Lists of reference standards are available in Tables S7-11, including their source, synthesis procedure, or, if data were taken from the literature, the relevant citation.

Primary data collection occurred at the Stanford Synchrotron Radiation Lightsource. Nickel, copper, and zinc K-edge spectra were collected at beamline 11-2, which employs a Si (220) double crystal, variable-exit monochromator (phi = 90° orientation) to scan the incident beam energy. A Rh-coated Si collimating mirror and detuning the monochromator to ~80% of peak intensity were used to minimize the harmonic content of the X-ray beam. Nickel, copper, and zinc metal foils were used for energy calibration, with their K-edges set to 8333, 8979, and 9659 eV, respectively. Data were collected in fluorescence-yield using a 100-pixel energy-dispersive monolithic Ge detector. This large array detector captured a substantial solid-angle of the associated X-ray fluorescence emitted by each sample, maximizing the count rate originating from trace metals in the sample. Data collection focused on the X-ray absorption near-edge structure (XANES) region because of the low signal level associated with the concentrations of the trace metals. The detector was operated in a high-resolution mode to separate the fluorescence line of interest from background, which dominated the total count rate and was thus the dominant contributor to noise in the data. Detector saturation was avoided because of the relatively low Fe content in the samples and the relative attenuation of Fe fluorescence by Al foil placed between the sample and detector. The high flux of the beamline enabled this substantial attenuation while still utilizing the full linear-range of the detector. Multiple scans were collected for each sample

and then averaged. No detectable changes in the spectra were observed, such as those caused by beam-induced damage, and no drift in energy calibration was detected.

Iron and sulfur K-edge spectra were collected at beamlines 4-3 configured with a Si (111) double-crystal monochromator (phi = 90° orientation) and a Si mirror for harmonic rejection. Sulfur XANES spectra were collected in fluorescence-yield using a Vortex ME7 silicon drift detector. All samples for sulfur measurements were removed from their polyethylene pouches and immediately chilled to ~20 K using a liquid He cryostream to prevent beam-induced redox changes while minimizing beam attenuation. Iron spectra were collected through the extended X-ray absorption fine structure (EXAFS) region in transmission at ambient temperatures. Repeated scans of sulfur and iron in a single position on each sample showed negligible changes over time. However, attempts to evaluate other positions on the samples were not successful because of diffraction into the fluorescence detector and spatially heterogeneous absorption, both of which are attributed to the substantial quartz contents of the samples. Data for some standards were collected at beamlines 5-BM-D and 12-BM-B at the Advanced Photon Source at Argonne National Laboratory. These beamlines employ Si (111) fixed-offset monochromators with a flat Rh-coated Si mirror for harmonic rejection; a toroidal Rh-coated Si mirror at 12-BM-B also provides beam focusing. Data for pure compounds were collected in transmission while those with lower target element concentrations, such as elements substituting in a mineral structure, were collected in fluorescence yield using a 12-element energy-dispersive solid-state Ge detector.

XANES spectra were averaged in the Sixpack interface (Webb, 2005) to IFEFFIT (Newville, 2001) and then background subtracted and normalized in Athena (Ravel and Newville, 2005). For the trace metal spectra, E_0 was set to 8342 eV for nickel, 8988 eV for copper, and 9659 eV for zinc. These values reflect the typical edge position of the collection of samples and are thus

shifted relative to the energies expected for these elements in their metallic forms. A linear pre-edge background was fitted to the pre-edge region (150 to 30 eV below E_0 for copper and nickel, and 60 to 30 eV below E_0 for zinc) and removed. The data were then normalized by fitting a linear function to the post-edge region (75 to 225 eV above E_0). For iron, E_0 was set to 7125 eV and a linear background was fitted 27 to 20 eV below E_0. This background range was narrow because some spectra had a glitch at lower energy and a consistent background removal was used for a all samples. Separate post-edge normalizations were used for the iron XANES and EXAFS spectra. For the XANES, normalization was again performed using a linear function fitted to 75 to 225 eV above E_0. To account for slight curvature in the data over the larger energy range covering the EXAFS region, the data were normalized using a quadratic function fitted between 150 and 540 eV above E_0. The EXAFS were extracted after fitting a spline using the Autobk algorithm in Athena (Rbkg = 0.7; k-weight = 3; k-range 3 – 11 $Å^{-1}$). The E_0 for the sulfur XANES data was set to 2472 eV, with a linear background fitted between 20 and 7 eV below E_0 and a linear post-edge normalization performed between 35 to 56 eV above E_0.

For the spectra of the trace metals, Athena was used for principal component analysis (PCA), target transformation (TT) of the spectra of standards, and linear combination fitting (LCF) of the spectra (Manceau et al., 2002). Statistical constraints on the amount of variability in a set of spectra are provided by PCA but this cannot uniquely identify the exact number of fitting components required because of limited data set size and possible co-occurrence of real species in multiple spectra (Manceau et al., 2002). Similarly, TT provides statistical support for identifying the standards most likely to occur in a set of samples, but this is also ambiguous and needs to be guided by chemical and mineralogical constraints. Further, similar species (e.g., trace metals in clay mineral structures) may display subtle variations in their spectra that would require an

impractical number of standards to fully capture. The spectrum of the actual species present in a sample may thus not be perfectly matched by that of an individual standard, but a linear mixture of two or more chemically similar standards may reproduce this well. Given these limitations and the inability to independently identify the individual trace metal species present, a combinatorial approach was used where all combinations of the spectra of relevant standards, identified by TT, were fit to the sample spectra, with the combination that minimized the reduced chi-squared value, $\chi\nu^2$ (Kelly et al., 2015) used as the final result. Fitted components were then grouped in species categories (see Section 3.4). Linear-combination fitting of sulfur XANES spectra also employed a combinatorial approach using Athena, but standards used as fitting components were selected to reproduce the features present. The spectra clearly indicated the co-occurrence of more sulfur species than there were samples, precluding use of PCA. Similarly, fitting of iron XANES and EXAFS spectra in Athena used standards based on common iron phases and mineralogy determined by XRD. We note that the insight gained from all linear combination fitting is limited by the standard spectra available. Inclusion of additional standard spectra, such as through future reuse of the data presented, may enable greater insight into the species present.

3.4 RESULTS

3.4.1 Soil and Sediment Mineralogy and Composition

The mineralogy at all sites is dominated by quartz with only minor phases showing substantial variations in occurrence (Fig. 3.1). The investigated duplicate core samples at each location yielded similar mineralogy (data from only one core are plotted) except at location Stream 1, with the surface layer of one of the two cores containing pyrite, the only detection of this phase (Fig. 3.1). Minor phases in the marsh wetland soils included smectite, illite, and kaolinite as well

as plagioclase feldspar. The riparian wetland soils differ from the marsh wetland soils, with location Riparian 2 having minor K-feldspar, kaolinite, chlorite, and gibbsite, and trace illite. In contrast, the location Riparian 1 soil contains only trace amounts of kaolinite, chlorite, and gibbsite, with no other phases detected besides the ubiquitous quartz. Note that prior studies at the Savannah River Site, which hosts the riparian wetlands, suggest that clays identified by XRD as chlorite may instead be hydroxy-interlayered vermiculite (Kaplan et al., 1997; Zaunbrecher et al., 2015). The stream sediments at both sampling locations contain minor K-feldspar, chlorite, smectite, kaolinite, and illite. No carbonate minerals were detected in any sample.

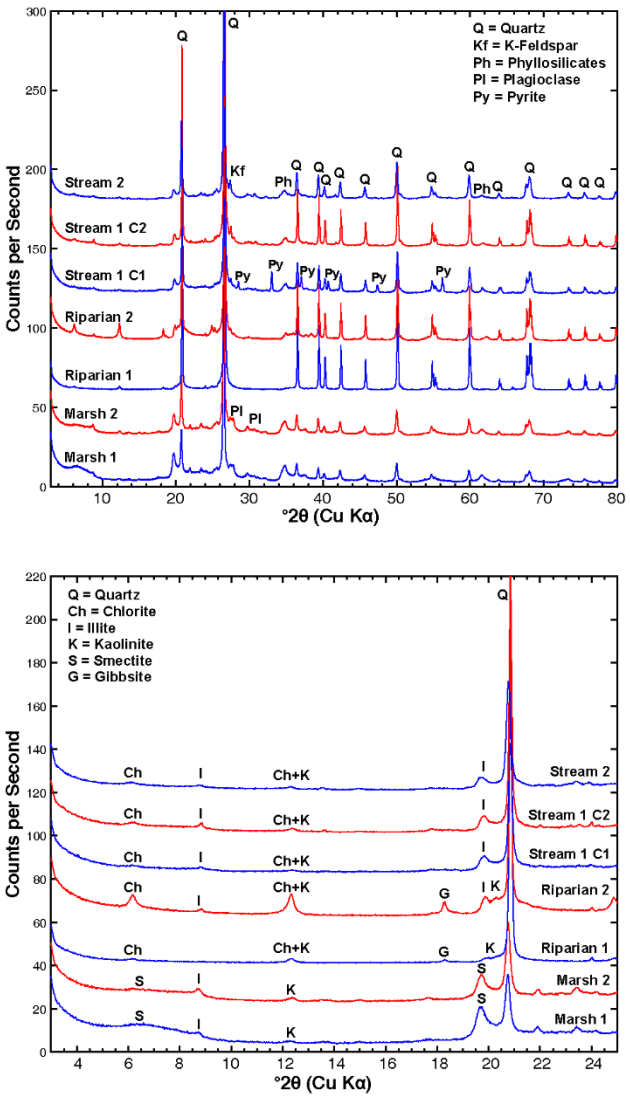

Figure 3.1. Powder X-ray diffraction (XRD) patterns of the surface soil or sediment layer over the full range (top) or the low angle region more sensitive to clay minerals. Data for duplicate cores are shown for location Stream 1 because of their distinct mineralogy.

The total carbon contents varied among the sites (Fig. 3.2), with highest concentration in the marsh soils and lesser amounts at the other two sites. Notably, the core sample containing pyrite at location Stream 1 also contained elevated organic carbon, and this was substantially lower in the pyrite-free duplicate core. It is unclear whether there is a genetic relationship between

organic carbon and pyrite as the latter had sharp X-ray diffraction lines (Fig. 3.1), suggestive of a detrital phase. Sulfur showed a similar pattern of variation as carbon despite the substantially lower concentration. The cores at location Stream 1 showed a large difference in sulfur content, again because of the presence of pyrite in one of the two duplicates. Iron contents were similar among all samples except for location Riparian 1, which contained an order of magnitude less iron, consistent with the mineralogy being dominated nearly exclusively by quartz. Manganese contents were two to three orders of magnitude lower than iron contents, with the lowest values observed in the riparian soils.

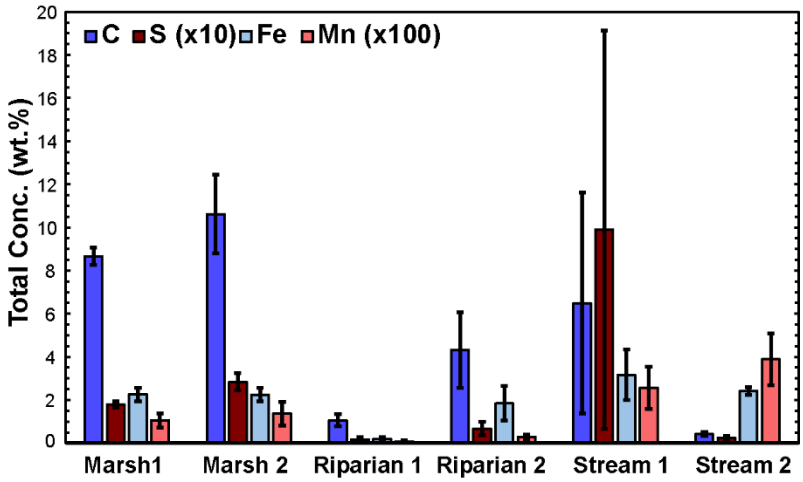

Figure 3.2. Total carbon, sulfur, iron, and manganese contents in the surface layer of the soils and sediments at the study sites. The error bars reflect the standard deviations of triplicate analyses of samples of individual cores added in quadrature to the standard deviation of the mean values for the two duplicate cores collected at each site (Data tabulated in Table A3.6).

3.4.2 Trace Metal Concentrations

3.4.2.1 Dissolved trace metals

Dissolved trace metal concentrations (Fig. 3.3) generally followed the trend of Zn > Cu ≈ Ni > Co at all the investigated sites. Dissolved Zn concentrations showed the largest absolute variation, ranging from 46 to 230 nM with no clear trend among the sites, and the values were in all cases above the 10 to 20 nM concentrations in the process blanks (Table A3.2). Similarly, dissolved Cu concentrations showed no trend among the three field sites and ranged from 20 to 80 nM. Measured Cu concentrations were substantially greater than in the process blanks except for marsh wetland location Marsh 2. Ni concentrations were similar at the marsh wetlands and stream sites, occurring in the range of 30-60 nM, but location Riparian 2 contained substantially less dissolved Ni (12 nM). One process blank from the marsh wetland contained ~130 nM dissolved Ni while all others were <10 nM. We attribute this to contamination, possibly from dust associated with >40 km hr^{-1} wind gusts during sampling at this location. Dissolved Co concentrations were low, often <10 nM, but in most cases were above the approximately 2 to 4 nM concentrations in the process blanks.

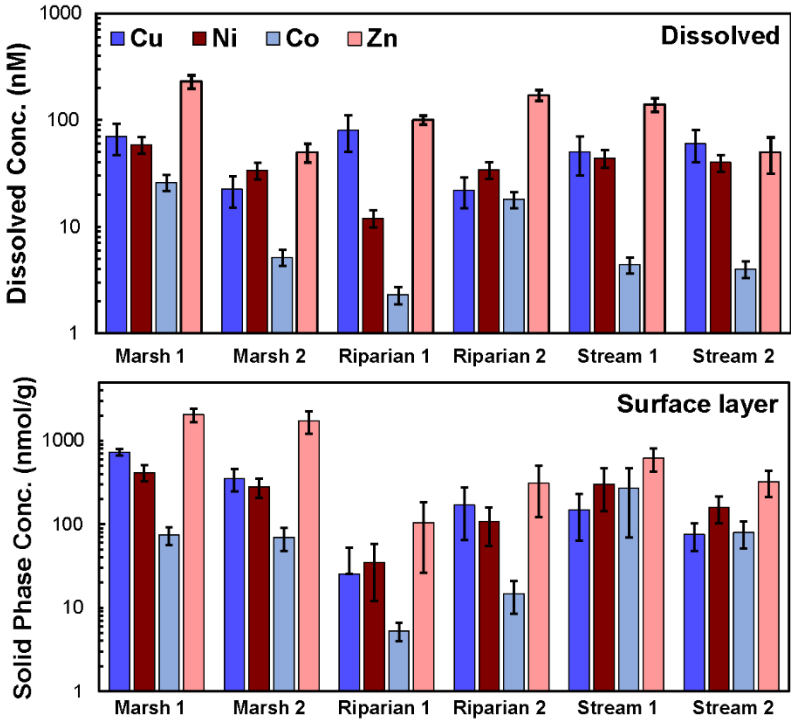

Figure 3.3. Dissolved (top) and total solid phase (bottom) trace metal concentrations for the study sites. The error bars for the dissolved concentrations are the uncertainties of individual analyses obtained from linear regression of the calibration curves. Error bars from the solid phase concentration reflect the calibration-derived uncertainties for samples from individual cores added in quadrature to the standard deviation of the mean values for the two duplicate cores collected at each site (Data tabulated in Tables A3.3 and A3.4).

3.4.2.2 Solid phase trace metals

Overall patterns of solid-phase trace metal concentrations (Fig. 3.3), as determined by microwave-assisted acid digestion, followed the same general trend as for the surface waters: Zn > Cu ≈ Ni > Co. Variations in the abundance of each trace metal among the field sites generally tracked one another. The marsh wetlands contained the highest solid-phase Cu, Ni, and Zn contents, with Co concentrations the largest in the stream site sediments, although this was likely affected by the presence of pyrite in one core. The riparian wetlands, especially location Riparian 2, had the lowest solid-phase trace metal contents, consistent with the low abundance of non-quartz

minerals and low major element (C, S, Fe, Mn) concentrations. The concentrations of the trace metals (0.3 to 18 ug g^{-1} Co, 3 to 27 µg g^{-1} Ni, 3 to 45 µg g^{-1} Cu, and 11 to 144 µg g^{-1} Zn) were similar to or well below geological background levels of 17.3±0.6 µg g^{-1} Co, 47±11 µg g^{-1} Ni, 28±4 µg g^{-1} Cu, and 67±6 µg g^{-1} Zn (Rudnick and Gao, 2003).

3.4.3 Spectroscopic Analysis of Sulfur and Iron Speciation

Seven samples in total were examined from the three field sites using sulfur K-edge XANES and iron K-edge XANES and EXAFS spectroscopy. The surface layer sample from the first core at each sampling location was examined except for location Stream 1. The duplicate cores from this location differed in their mineralogy (core 1 contained pyrite) as well as their bulk carbon, iron, sulfur, and trace metal contents. Samples from both cores from location Stream 1 were thus investigated.

3.4.3.1 Sulfur Speciation

The sulfur XANES spectra of wetland soils and stream sediments display two primary whiteline regions at 2472.6 to 2474.1 eV and 2481.1 to 2482.5 eV, with some displaying a shoulder near ~2470.5 eV (Fig. 3.4). This array of features indicate the presence of multiple sulfur oxidation states occurring in both inorganic and organic forms (Prietzel et al., 2009; Manceau and Nagy, 2012), potentially consistent with inorganic mono- and disulfide minerals, elemental sulfur, exocyclic reduced sulfur, sulfones, sulfonates, and organic or inorganic sulfates. Preliminary principal component analysis (PCA) of these spectra revealed that fine-structure features were present in all components. This indicates that the number of species in the samples was similar to

or exceeded the number of samples analyzed (seven). Further evaluation using statistical techniques, including evaluation of possible standard spectra via target transform (TT), was thus not possible as the sample set is inadequate to describe the variability in the data.

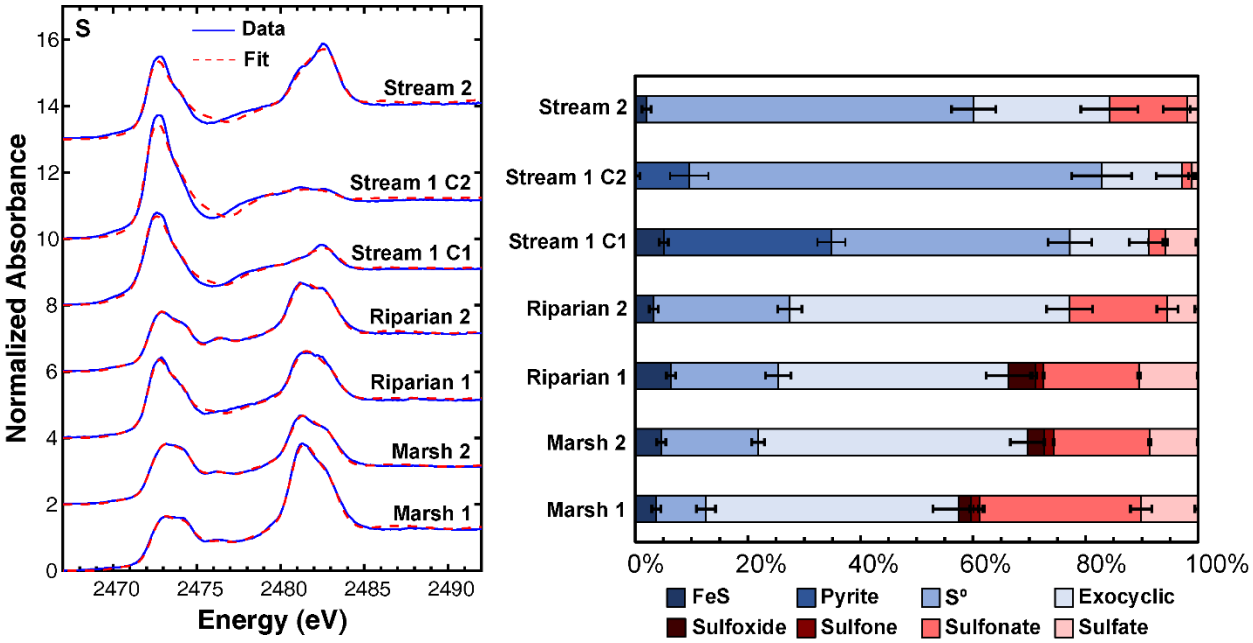

Figure 3.4. Sulfur K edge XANES spectra (solid) and fits (dashed) and the associated distribution of species for the surface layer soils and sediments at the study locations (Results tabulated in Table A3.12).

A combinatorial fitting approach was used (Manceau and Nagy, 2012) to identify the species present because of the large number of species likely present. We modified the previously-published procedure by using the reduced chi-squared ($\chi\nu^2$) as the goodness-of-fit parameter to minimize because it accounts for the removal of degrees of freedom when adding additional fitting components. The fitting results are considered semi-quantitative because the spectra of standards were taken from prior studies (Table S7) that may have differed in their energy resolutions. This

is most apparent for pyrite and elemental sulfur fitting components. Attempts to collect data on both phases after micronizing and dispersing on sulfur-free polyester tape resulted in whitelines that were lower intensity and broader than the diagnostic features in the sample spectra. This indicates that the standards suffered from over-absorption, an effect that has been widely reported in previous studies (George et al., 2008; Almkvist et al., 2010; Manceau and Nagy, 2012; Lau et al., 2017). While the systematic errors associated with the standards used could not be rectified, the fitting results still constrain which sulfur species are present and their relative abundance.

Fitting demonstrates that the wetland soils and stream sediments all contain elemental sulfur, exocyclic reduced sulfur, sulfonate, and sulfate. The latter species was best modeled using inorganic sulfate, with the combinatorial fitting not identifying an organosulfate in any sample. All samples except core 2 of location Stream 1 contained a small FeS component. However, the abundance of this phase may be underrepresented in some samples as fitting did not always fully reproduce the intensity of the shoulder at ~2470.5 eV associated with the phase. Pyrite was only observed in both samples from location Stream 1. It is likely that the C1 sample measured by XANES did not contain the substantial amount of pyrite identified by XRD. Sample alignment prior to XANES data collection involves identifying an area with spatially-uniform fluorescence, and this process likely selected for areas free of coarser pyrite grains. The sharp XRD peaks indicate pyrite in the C1 samples from location Stream 1 is well crystalline, and such grains would produce locations of spatially-varying fluorescence that would be avoided during alignment. The two marsh wetland soils and the Riparian 2 sample also contained minor amounts of sulfoxides and sulfones.

3.4.3.2 Iron Speciation

The speciation of iron was probed using both XANES and EXAFS spectra for all sampling locations except Riparian 1 (Fig. 3.5). The high quartz content in this sample prevented identification of a spatially homogeneous location and all EXAFS spectra that were attempted contained substantial artifacts; only the XANES spectrum was analyzed for this sample. Preliminary PCA of the XANES and EXAFS spectra revealed fine-structure features present in all components obtained for each spectra region. This indicates that the number of species present in the samples was equal to or greater the number of spectra measured (seven for XANES, six for EXAFS). This precluded further statistical analyses, including evaluation of potential standard spectra using TT.

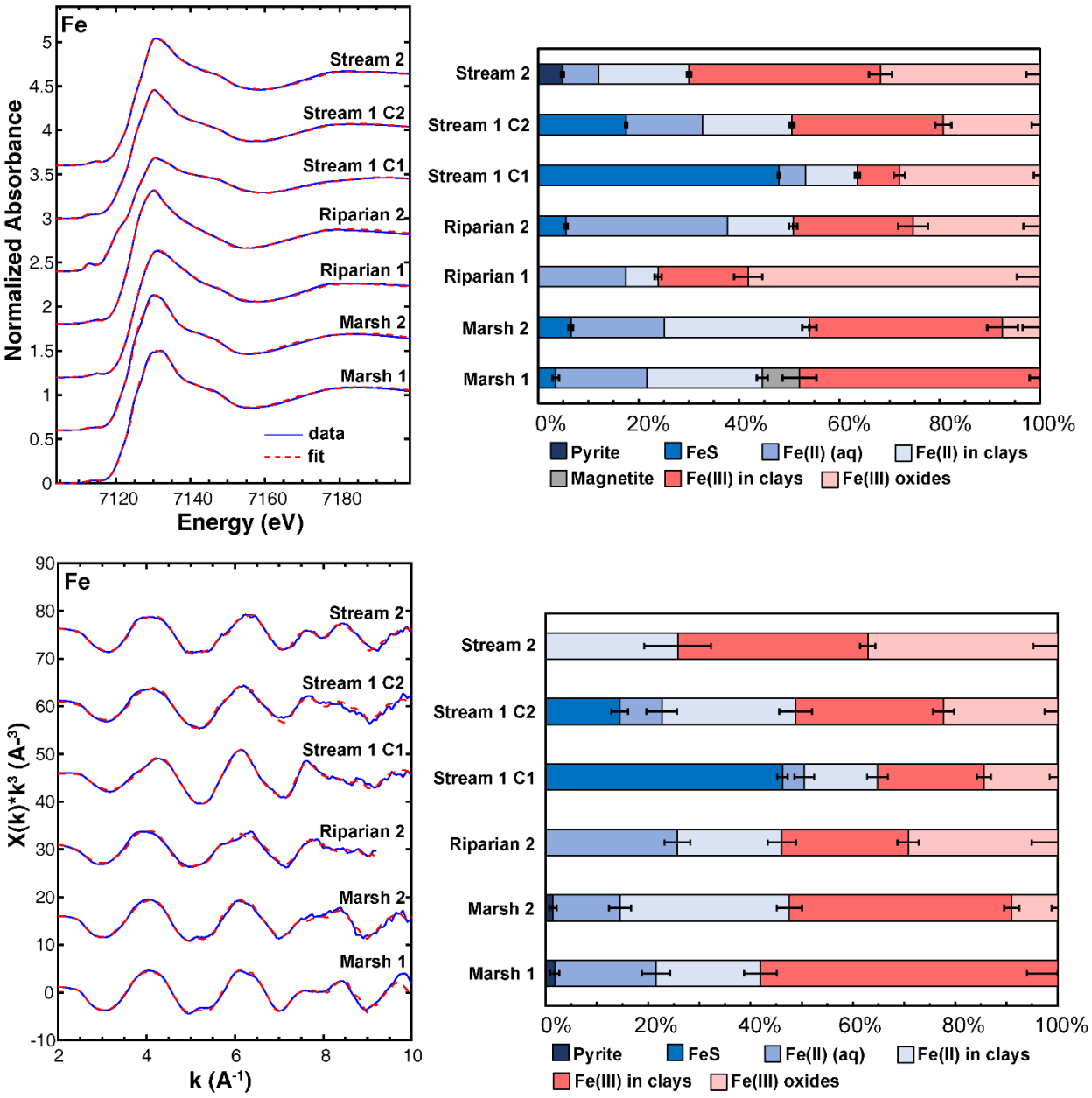

Figure 3.5. Iron K-edge XANES (top) and EXAFS (bottom) spectra (solid) and fits (dashed) and the associated distribution of species for the surface layer soils and sediments at the study locations. (Results tabulated in Tables A3.13 and A3.14).

Similar trends in overall speciation were observed among the samples through analysis of the XANES and EXAFS regions. However, quantitative agreement between the XANES and

EXAFS fitting results did not occur for all samples. Such differences can result if the standards are more crystalline than the species present, as such cases would produce similar XANES spectra but distinct EXAFS spectra associated with weaker oscillations from more disordered second shell features in less crystalline materials. These discrepancies do not affect the overall results of this study as iron speciation was investigated primarily to constrain the potential host phases for trace metals. Any solid iron species detected would occur at two to four orders of magnitude greater abundance than the trace metals.

Iron at all sites partially occurs as Fe(II) and Fe(III) in clay mineral structures, with all but location Marsh 1 showing evidence for Fe(III) oxide minerals as well. Both core samples from location Stream 1 contained FeS, with both XANES and EXAFS showing that this phase occurs in greater abundance in core 1. No pyrite was apparent in either core from location Stream 1. Similar to the sulfur case, the need to obtain data on a portion of the sample having spatially uniform absorbance may have biased the measurement by avoiding pyrite grains. Note that the iron, sulfur, and trace metal spectra (Section 3.4.), as well as XRD patterns, were each collected on different subsamples of physically homogenized core segments because of the distinct measurement requirements. The detection of pyrite in the Stream 1 samples by sulfur XANES (Fig. 3.4) is thus not necessarily contradictory to the iron speciation results. We interpret these results to indicate that iron sulfide phases are present in the samples. The XANES and EXAFS spectra are not consistent regarding FeS or pyrite occurrences in other samples. These phases have low abundances (<10 mol% of Fe) in the fitting results and may thus either be artifacts or reflect different sensitivities to minor phases. The weak shoulder at ~2470.5 in many sulfur XANES spectra is more diagnostic for a minor FeS component in many samples, suggesting this is present in small quantitates. Note that iron concentrations are an order of magnitude greater than sulfur in

most samples so an ~10% FeS component in the sulfur XANES spectra would correspond to ~1% FeS in the iron spectra. Finally, most samples required a contribution from dissolved Fe(II) to reproduce the iron XANES and EXAFS spectra. This may reflect Fe(II) adsorbed to or cation exchanged onto minerals or complexed by organic matter. While no iron-bearing primary silicates were detected in XRD, we lack available XANES and EXAFS spectra for such phases, and the dissolved Fe(II) component may at least partially account for minor occurrences of such minerals. Finally, fitting of the XANES spectra identified magnetite as a minor component of only the Marsh 1 sample, and this was not observed for any EXAFS spectrum. We thus conclude that magnetite is not an observable component of the iron speciation in the sites examined.

3.4.4 Spectroscopic Analysis of Trace Metal Speciation

XANES spectroscopy (Fig. 3.6-8) was employed to investigate solid-phase trace metal speciation using the same sample selection rationale as for the sulfur and iron measurements described above. EXAFS measurements were not possible because of the low total metal contents of the samples. Cobalt was not investigated because its fluorescence signal is masked by the iron Kβ fluorescence line. The resulting seven spectra per element were initially examined by PCA to evaluate variability in the XANES spectra for each element and to provide statistical guidance for the minimum number of components contained in each dataset. Target transform (TT) was then used to assess whether the spectra of various standards for each metal (Fig. A3.6-8) were possibly present in each dataset. Those standard spectra which could be reconstructed by TT, minus species inconsistent with the observed mineralogy or the sulfur and iron speciation, were then used in linear-combination fitting (LCF) to quantitatively assess trace metal speciation. A combinatorial

LCF approach was used, with all possible combinations of two or more standards evaluated. The fit that yielded the lowest reduced chi-squared value was then selected.

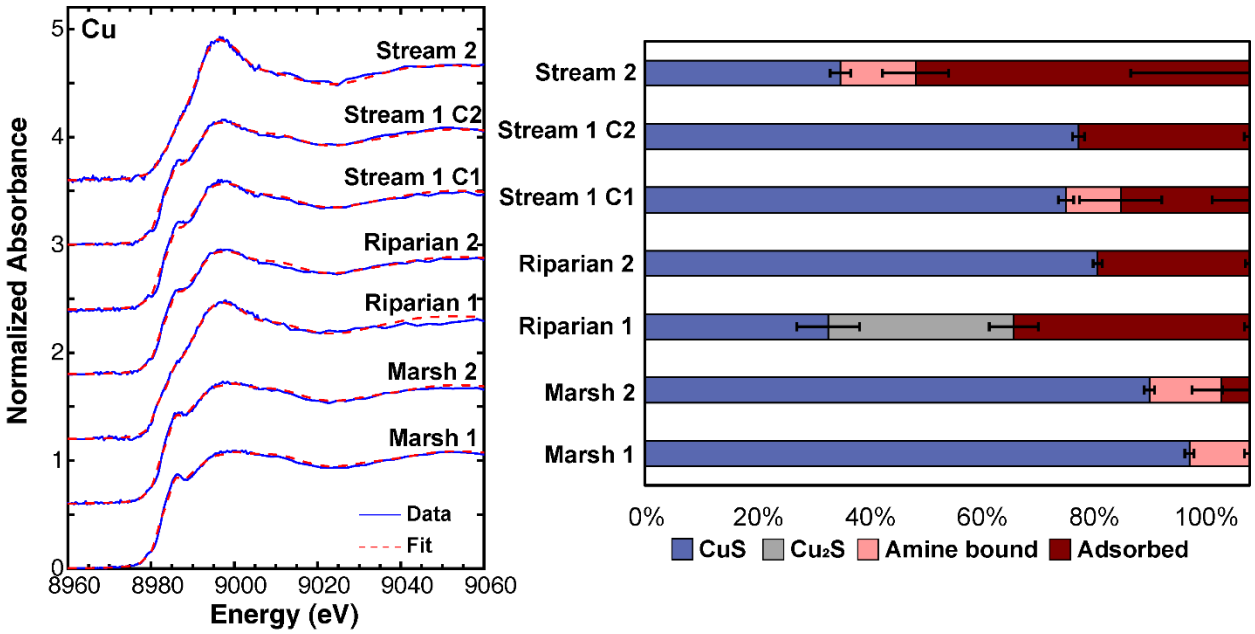

Figure 3.6. Cu-K edge XANES spectra (solid) and fits (dashed) and the associated distribution of species for the surface layer soils and sediments at the study locations (Results tabulated in Table S15).

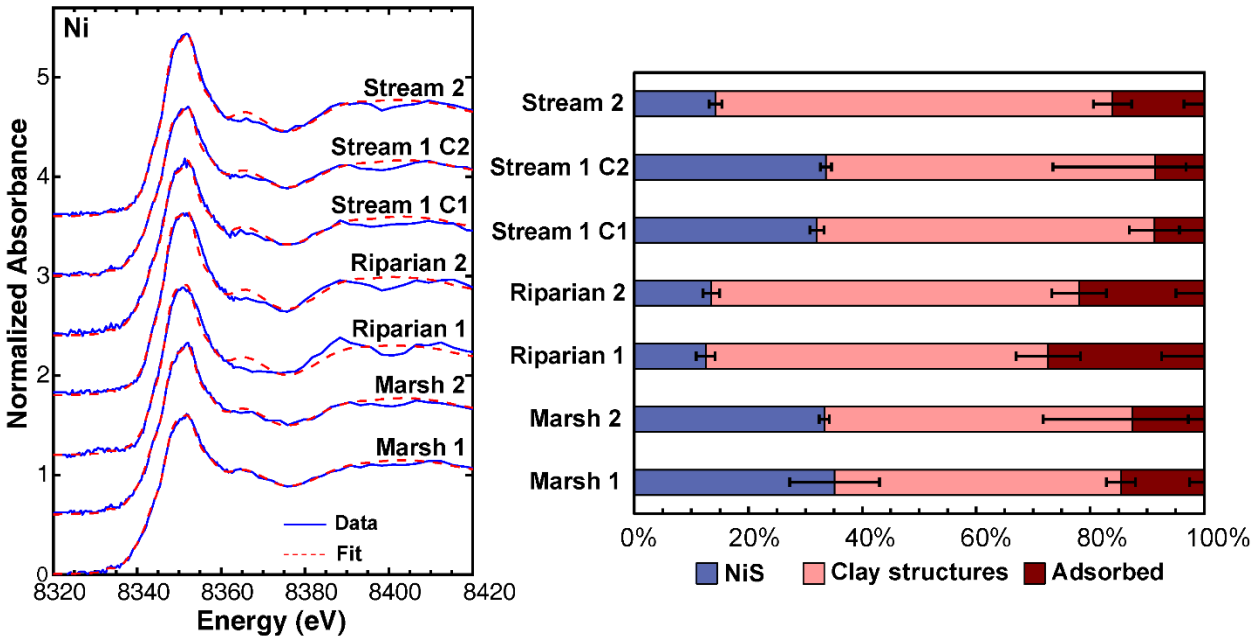

Figure 3.7. Ni-K edge XANES spectra (solid) and fits (dashed) and the associated distribution of species for the surface layer soils and sediments at the study locations (Results tabulated in Table A3.16).

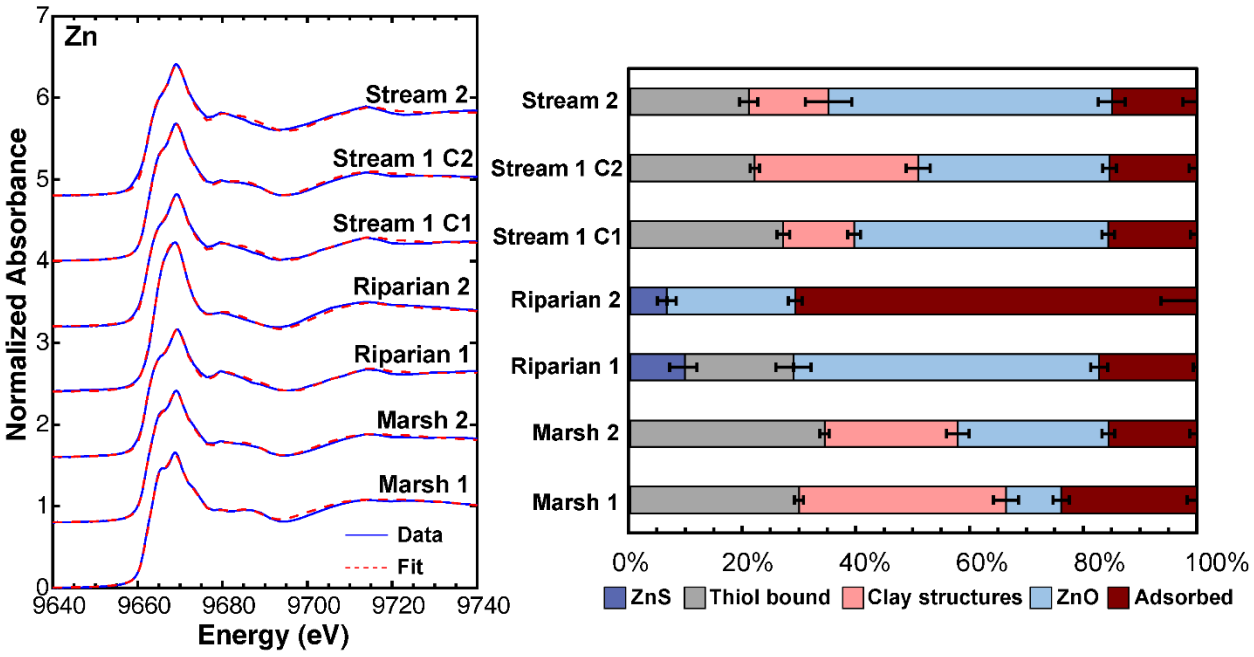

Figure 3.8. Zn-K edge XANES spectra (solid) and fits (dashed) and the associated distribution of species for the surface layer soils and sediments at the study locations (Results tabulated in Table A3.17)

This approach was motivated by the lower sensitivity of XANES spectra to specific structural environments compared to EXAFS spectra, which are unmeasurable because of the low trace metal concentrations. In recognition of this limitation, the LCF results were binned by broad species type to more accurately reflect the information obtained. While XANES spectra reflect the general coordination environment of the target element, they lack the specific structural sensitivity of EXAFS spectra. The adsorbed metal groupings included XANES fitting contributions from the spectra of aqueous ions because these are spectrally similar to some adsorbed species (Fig. A3.6-8). In addition, their spectra are expected to be indistinguishable from the spectra of cation exchanged species. Dissolved species themselves are likely a negligible contribution to the spectra

for all samples. Assuming maximum porewater trace metal concentrations of 1 μM, well above the dissolved concentrations in overlying surface waters (Fig. 3.3), aqueous species would constitute <1% of the metals per unit volume in the soil and sediment samples. The spectra of metals coordinated to carboxylic acids were also similar to the spectra of aqueous and adsorbed species and were thus binned into the adsorbed metal groupings. An analogous approach was used to establish the "clay structures" grouping, consisting of metals substituted into octahedral sheets in phyllosilicates and related phases. Clay minerals vary widely in their compositions, and the range of possible second-shell cation neighbors produces subtle variations in the fine structure features of trace metal XANES spectra. There is no method available to independently determine the composition of clay(s) hosting a trace metal in a sample. Sample spectra were thus fitted using the spectra of a series of clay standards to account for these subtle spectral variations. All such fitting components were binned into the "clay structures" grouping. The standards utilized in all analyses are thus interpreted as proxies for general classes of metal species distinguishable by their local coordination environments.

3.4.4.1 Copper Speciation

Five of the seven copper XANES spectra (Fig. 3.6), spanning samples from all three sites, displayed a clear shoulder at ~8986 eV indicative of copper bound to reduced sulfur. These include the spectra of the duplicate core samples from location Stream 1, one of which contained pyrite. Spectra from location Riparian 1 and Stream 2 displayed a weaker low-energy shoulder and stronger white line. PCA required three components to adequately reconstruct the fine structure of all of the sample spectra. TT identified covellite (CuS), chalcocite (Cu_2S), aqueous Cu(II), Cu(II) adsorbed to goethite, copper(II) citrate, copper(II) hydroxide, and Cu(II) complexed to cysteine and histidine as potential standards. While observed in prior studies (Weber et al., 2009b; Weber

et al., 2009a; Hofacker et al., 2013b; Hofacker et al., 2013a; Hofacker et al., 2015), metallic copper was poorly reconstructed and thus unlikely to be present in the samples. Combinatorial LCF results utilized all of the well-reconstructed standards in modelling the XANES spectra except for copper(II) citrate, copper(II) hydroxide, and Cu(II) complexed to cysteine, which were not present in any optimized fit. In the fitting results, the histidine complex is classified as representing amine-bound copper, and both aqueous Cu(II) and Cu(II) adsorbed to goethite representing adsorbed copper.

CuS was present in all sites studied and accounted for >70% of the copper in five of the seven samples (Fig. 3.6). Adsorbed forms of copper were the next most abundant species overall, present in all but location Marsh 1. This species type occurred in equal abundance as CuS at location Riparian 1 and was the dominant copper species in the sediments at location Stream 2. Amine-bound copper was a minor component in four samples and fitting only identified Cu_2S (30±4%) at location Riparian 1. No significant difference in CuS abundance was observed for the duplicate core samples from location Stream 1 despite one of these (C1) containing pyrite. While fitting identified a minor amine-bound copper component in one of the two duplicate cores, its occurrence is of marginal statistical significance (9±7 wt.%) and adsorbed plus amine-bound copper are effectively identical for the two samples.

3.4.4.2 Nickel Speciation

The nickel XANES spectra (Fig. 3.7) show, at most, subtle variation among all samples examined. These are limited to slight variations in the slope of the absorption edge, the height and shape of the white line at ~8352 eV, and the intensity of the weak post-edge feature at ~8367 eV.

Reconstruction of the spectra during PCA required three components to reproduce major fine-structure features. A fourth component contained features consistent with XANES fine-structure and further improved reconstructions of some spectra. TT identified nickel sulfide, Ni(II) substituting in magnetite and the octahedral sheets of serpentine and a trioctahedral Fe(II)-Mg smectite, dissolved Ni(II), Ni(II) adsorbed to goethite, and Ni(II) complexed to histidine, cysteine, glutathione, and cellulose as potential standards. Of these standards, none of the organic complexes occurred in the optimized fits to the data, and Ni(II) substituting in magnetite was not used because magnetite was not clearly identified by XRD or the iron speciation results. For the remaining standards, spectra of the Ni(II) in the octahedral sheets of serpentine and smectite were grouped as "clay structures", and Ni(II) adsorbed to goethite and in aqueous solution were grouped as adsorbed Ni.

Fitting identified Ni in clay structures, nickel sulfide, and adsorbed Ni in all samples (Fig. 3.7). Nickel in clay mineral structures was the dominant species in all samples, ranging from 50% to 70% of the total Ni. Nickel sulfide was the next most abundant species in the marsh wetlands and location Stream 1, with adsorbed nickel occurring in higher abundance in the other stream site and the riparian wetlands. Despite the presence of pyrite in one of the duplicate cores, the sulfide component of the nickel species at stream location Stream 1 were statistically identical.

The quantitative nickel speciation results likely contain systematic errors associated with the presence of a species not represented in the set of standards available. The spectra of a number of samples, most notably the riparian wetland samples, contain a weaker feature at ~8367 eV and a splitting in the broad features from 8380 to 8420 eV that are not reproduced in the fits (Fig. 3.7). Examination of published spectra of diverse organic and mineral-associated forms of nickel indicates that such features are rare in Ni K-edge XANES spectra (Kopittke et al., 2011; Van Der

Ent et al., 2018; Ratié et al., 2018; Siebecker et al., 2018). The 8380 to 8420 eV feature corresponds to the 3 to 4 $Å^{-1}$ region of the EXAFS spectrum, and this has been shown to produce a splitting when nickel occurs in Mg-rich serpentine, gibbsite (Siebecker et al., 2018), and aluminum hydroxide clusters in smectite interlayers or associated with smectite as small gibbsite particles (Nachtegaal et al., 2005), with the Al-modified smectites producing the deepest node in this split feature. The misfit of the XANES data in the 8380 to 8420 eV region is most substantial in samples containing detectable gibbsite in the XRD data, supporting the assessment that this originates from nickel species associated with aluminum hydroxides. In the grouping approach used in this study, these would be categorized as clay-associated species and thus the misfits do not fundamentally alter the observation of this group as the predominant nickel species in the samples examined. Further, the nickel sulfide content determined by the fitting is likely unaffected by the lack of an appropriate standard for this type of clay-bound nickel. Nickel sulfide has an absorption edge shifted to lower energy from all clay species and its contribution reproduces broadening of the data in the low-energy portion of the absorption edge.

3.4.4.3 Zinc Speciation

Similar to copper and nickel, the XANES spectra of zinc show only subtle variations except for sample Riparian 2, which lacks fine structure features in the white line (Fig. 3.8). At least three components are required to reconstruct the spectra during PCA, with four clearly improving reconstruction of features in some spectra. In addition, an examination of the individual components showed that up to five contained non-noise features. TT identified a large number of possible candidate species: zinc(II) oxide, sphalerite (ZnS), zinc(II) in the octahedral sheet of a trioctahedral Fe(II)-Mg smectite, a zinc-aluminum layered double hydroxide, zinc(II) adsorbed on

and incorporated into goethite, dissolved zinc(II), zinc(II) acetate, zinc(II) oxalate, zinc(II) sulfate, and zinc(II) complexed to cysteine and glutathione. Combinatorial LCF fitting did not utilize the spectra of the layered double hydroxide, zinc oxalate, and zinc incorporated into goethite in the final results. Species were grouped by category in reporting the fitting results as described for the other metals.

Zinc speciation (Fig. 3.8) was similar in the marsh wetland soils and stream site sediments, consisting of adsorbed species, zinc associated with clay mineral structures, and complexed to thiol groups. The riparian wetland soils lacked Zn in clay structures and contained sphalerite, with location Riparian 2 lacking thiol-bound zinc and location Riparian 1 containing a large adsorbed pool. In addition, a substantial zinc oxide component ranging from 10% to 54% of the zinc species occurred in all samples. Prior studies of zinc-contaminated soils have indicated that zinc oxide introduced into such settings does not persist, dissolving and transforming to new phases (Voegelin et al., 2005; Voegelin et al., 2011). An inverse correlation was observed between XANES-derived zinc oxide content and solid-phase zinc concentrations ($R = -0.81$, $p = 0.03$). These considerations suggest that the zinc oxide component may be a contaminant or data collection artifact. Notably, the cellulose acetate tape widely used for sample mounting and other purposes at synchrotron beamlines contains zinc oxide (Supplementary material text and Fig. A3.9). Zinc oxide introduced during field sampling is unlikely to have persisted and process blanks during microwave digestion did not identify zinc concentrations above the detection limit. The zinc oxide components in the XANES spectra are thus likely attributable to a background signal associated with sample cells and beamline components.

3.5 DISCUSSION

3.5.1 Lack of Elemental Correlations in Bulk Compositions

A linear regression employing maximum likelihood estimation and weighted by the bivariate uncertainties (Thirumalai et al., 2011) determined correlation coefficients (R) and p-values among pairs of the various major element and trace metal concentrations for each site. The datasets used in the analysis consisted of compositional data and associated measurement uncertainties for all sections of the duplicate cores from both sampling locations at each field site, e.g., cores 1 and 2 from the Marsh 1 and Marsh 2 locations at the marsh wetlands site. For the stream sediment site, the surface layer from core 1 at location Stream 1 contained pyrite and was removed from the dataset because it serves as an outlier that then yields spuriously large R values. In many regression analyses the pyrite-bearing sample occupied one end of a linear trend far removed from all other samples, which form a separate cluster that anchors to the opposite end of the linear trend. Removal of this one outlier datum in each analysis substantially changed the regression line and decreased the R value.

Regression of trace metal and major element abundances in the marsh wetland soils and stream sediments generally yield low R values (Fig. 3.9), indicating weak correlation among these elements. No clear relationships can be identified between the trace metal and major element contents of these soils and sediments. In contrast, large R values between the trace metals and all major elements were obtained for the riparian wetland soils (Fig. 3.9), with all having high statistical significance ($p \leq 0.003$). Further examination, however, shows that the major elements are also highly correlated with each other, and all element pairs yield large R values with small p-values. We hypothesize that the correlations among all elements (C, S, Fe, Mn, and trace metals) in the riparian wetland soils reflect variations in the minor non-quartz content in which all of these

elements reside. Variations in major element abundance thus do not provide insight into processes controlling solid-phase trace metal speciation in the soils and sediments.

Marsh Wetlands

	C	Fe	S	Mn	Co	Ni	Cu
Fe	-0.91 *0.001*						
S	0.92 *<0.001*	-0.78 *<0.001*					
Mn	0.45 *0.2*	0.68 *0.05*	-0.23 *0.2*				
Co	-0.47 *0.6*	0.59 *0.1*	-0.46 *0.2*	0.80 *0.1*			
Ni	-0.14 *0.03*	0.13 *0.9*	-0.42 *0.001*	-0.24 *0.8*	0.42 *0.04*		
Cu	0.40 *0.01*	-0.39 *0.003*	-0.14 *<0.001*	-0.66 *0.3*	-0.12 *0.05*	0.79 *0.001*	
Zn	0.69 *0.06*	-0.68 *0.01*	0.49 *0.6*	-0.38 *0.1*	0.02 *0.05*	0.64 *0.004*	0.74 *0.002*

Riparian Wetlands

	C	Fe	S	Mn	Co	Ni	Cu
Fe	0.95 *<0.001*						
S	0.98 *<0.001*	0.94 *0.004*					
Mn	0.98 *<0.001*	0.97 *<0.001*	0.98 *0.001*				
Co	0.95 *<0.001*	0.96 *<0.001*	0.96 *0.003*	0.98 *<0.001*			
Ni	0.97 *<0.001*	0.92 *<0.001*	0.98 *0.003*	0.97 *<0.001*	0.96 *<0.001*		
Cu	0.99 *<0.001*	0.93 *<0.001*	0.98 *0.003*	0.98 *<0.001*	0.97 *<0.001*	1.00 *<0.001*	
Zn	0.93 *<0.001*	0.88 *<0.001*	0.93 *<0.001*	0.95 *<0.001*	0.95 *<0.001*	0.98 *<0.001*	0.98 *<0.001*

Stream Bed

	C	Fe	S	Mn	Co	Ni	Cu
Fe	-0.78 *<0.001*						
S	0.91 *<0.001*	-0.57 *0.001*					
Mn	-0.58 *0.001*	0.85 *0.001*	-0.09 *0.002*				
Co	0.32 *1.0*	0.74 *<0.001*	-0.20 *0.001*	0.64 *0.001*			
Ni	0.52 *0.9*	0.60 *<0.001*	0.07 *0.002*	0.40 *0.001*	0.97 *<0.001*		
Cu	0.48 *0.2*	-0.16 *0.03*	0.55 *0.3*	-0.32 *0.09*	0.14 *0.02*	0.48 *0.004*	
Zn	0.61 *0.2*	0.22 *0.001*	0.66 *0.002*	0.41 *0.002*	0.73 *0.001*	0.90 *0.001*	0.90 *0.003*

Figure 3.9. Correlation coefficients (R) and associated p-values derived from weighted linear regression of the solid-phase concentrations of each element pair. Data for the stream bed site excluded the single sample containing pyrite.

3.5.2 Importance of Reduced Sulfur and Clay Minerals to Background Metal Speciation

3.5.2.1 Reduced Sulfur

In the present study, substantial fractions of copper, nickel, and zinc in all samples were bound to reduced sulfur (Fig. 3.10A), primarily as sulfide minerals for copper and nickel and as thiol groups on organic matter for zinc. Trace metals are widely reported to associate with reduced sulfur in anoxic soils and sediments in freshwater systems (Huerta-Diaz et al., 1998; Koretsky et al., 2007), but the relationship between metal speciation and sulfur content has not been previously explored. Larger fractions of copper are associated with sulfur compared to nickel and zinc, consistent with past studies of both natural and contaminated sites (Bostick et al., 2001; Weber et al., 2009b; Fulda et al., 2013a; Noël et al., 2015; Webb and Gaillard, 2015; Siebecker et al., 2018; Mantha et al., 2019). However, no clear relationship exists between the fractions of each metal bound to reduced sulfur and the total sulfur content of the soil and sediment samples (Fig. 3.10B), despite nearly two orders of magnitude variation in the concentration of sulfur (Fig. 3.2). Prior studies suggest that metal binding to reduced sulfur in flooded soils (Weber et al., 2009b; Fulda et al., 2013a) is limited by sulfide availability. Such limitations are not apparent in the present work despite the bulk sulfur content spanning the range of concentrations in these prior investigations. This different observation may originate from the focus of prior studies on either contaminated soils with substantially higher metal concentrations or soils to which sulfate was added during anoxic incubations. At the low metal concentrations observed in the marsh and riparian wetland

soils and stream sediments under examination, which are similar to crustal averages (Rudnick and Gao, 2003), sulfur contents and fractional abundances of reduced sulfur were adequate to allow similar formation of reduced sulfur-bound metals in all systems. The total solid-phase sulfur concentrations observed in the present work span the range reported in prior studies of freshwater subsurface aquatic systems (Casagrande et al., 1977; Altschuler et al., 1983; Brown, 1985; Wieder et al., 1985; Spratt and Morgan, 1990; Dail and Fitzgerald, 1999; Rozan et al., 2002; Prietzel et al., 2009; Mehlhorn et al., 2018), indicating that sulfur-bound trace metals have broad occurrences as key species in such systems regardless of the soil or sediment sulfur content.

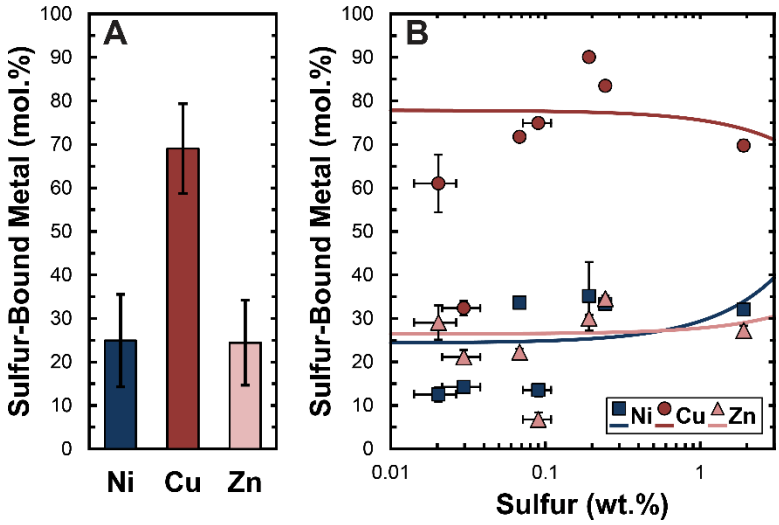

Figure 3.10. (A) Average and standard deviation of the fraction of trace metals bound to reduced sulfur as determined by XANES spectroscopy. (B) Variation in the fraction of each trace metal bound to reduced sulfur compared to the total sulfur content of the samples compared to trend lines for each metal (Cu: R = -0.06, p = 0.03; Ni: R = 0.37, p = 0.001; Zn: R = 0.18, p = 0.1) determined through linear regression weighted by the bivariate uncertainties.

3.5.2.2 Clay Minerals

Substantial prior work has demonstrated that nickel and zinc enter into clay mineral and layered double hydroxide structures in contaminated soils (Manceau et al., 2004; Voegelin et al., 2005; McNear et al., 2007; Jacquat et al., 2009; Voegelin et al., 2011), and this has also been observed for regions hosting Ni-rich ultramafic rocks (Dublet et al., 2012; Noël et al., 2015; Noël et al., 2017; Siebecker et al., 2017; Siebecker et al., 2018). However, the role of clay mineral structures in hosting trace metals in anoxic freshwater aquatic systems containing trace metals at low, background concentrations has not been previously demonstrated. The neoformation of such solids may depend on saturation state or dissolved metal concentrations (Manceau et al., 1999; Schlegel et al., 2001) and may be inhibited by organic matter (Nachtegaal and Sparks, 2003). This study demonstrates that the low trace metal contents of wetland soils and stream sediments still enable the incorporation of both nickel and zinc in clay structures, with this being the dominant nickel species in all systems. In addition, the occurrence of nickel and zinc in clay structures is independent of sulfur content and speciation, suggesting that they may be inherited from the weathering process and are resistant to disruption in the presence of sulfide.

3.5.3 Consistent Trace Metal Speciation in Wetland Soils and Stream Sediments

The study sites are distributed over a ~1000 km transect and represent different aquatic system types in geologically-distinct regions, with the marsh wetlands occurring in glacial sediments, the stream sediments draining carbonate and shale lithologies, and the riparian wetlands underlain by clastic coastal plain sediments. The riparian wetland soils are also heavily weathered compared to the other two sites, lacking smectite clay minerals at both study areas with no detectable feldspar at location Riparian 1, yielding more acidic and cation-poor local waters (Table

S1). Despite these substantial differences, the three sites investigated have overall similar trace metal speciation, with variations between the sampling locations at each site often larger than among the different field areas. These observations suggest that a small set of components consistently dominates trace metal speciation in uncontaminated freshwater subsurface aquatic systems: sulfide and adsorbed forms predominate in diverse systems for copper, with nickel and zinc also occurring in clay mineral structures. Further, similar distributions of trace metal species occur at multiple, unrelated and spatially separate field sites, which may indicate that these specific phase associations are a common feature of freshwater aquatic systems.

Limited prior studies of uncontaminated, anoxic soils and sediments generally support our hypothesis that trace metal speciation has consistent controls across many freshwater aquatic systems. A study of an anoxic soil and a peat lens formed at a natural CO_2 seep found copper bound primarily to reduced sulfur with a lesser component complexed to organic matter (Mehlhorn et al., 2018). As organic-complexed copper is classified into the adsorbed pool in the grouping scheme used in the present study, these results are consistent with our observations. Metallic copper was not observed by XANES in either our work or this prior study, suggesting it may be a substantial species only in contaminated flooded soils, where it has been frequently observed (Weber et al., 2009a; Fulda et al., 2013a; Hofacker et al., 2013b). Nickel forms sulfide and clay-associated species in anoxic coastal sediments (Noël et al., 2015; Noël et al., 2017; Merrot et al., 2019), which were also found in the present study. The greater importance of the sulfide species in these prior studies results from substantial pyrite formation caused by the reduction of the ample sulfate in seawater. These coastal systems are thus not directly comparable to freshwater aquatic systems, which typically have lower sulfate inputs (Wieder and Lang, 1988; Castro et al., 2002; Vile et al., 2003; Knorr and Blodau, 2009). However, locations within terrestrial-aquatic interfaces

where sulfur-rich groundwater mixes with fresh surface waters represent potential hot spots of reactivity which may require additional study. Further, these prior studies investigated systems with naturally elevated nickel concentrations (up to 0.5 wt.%) associated with an ultramafic laterite, potentially leading to distinct speciation. Despite these differences, the nickel sulfide pool was ubiquitous in the aquatic systems investigated here. This is likely supported by high rates of sulfate reduction in freshwater aquatic systems (Segarra et al., 2015) despite the lower total sulfate levels observed in the absence of seawater inputs. We are unaware of studies of zinc speciation in anoxic sites that are uncontaminated or lack geogenic zinc accumulations.

This study also highlights that the observations of trace metal behavior in contaminated systems often are not predictive of the behavior of these elements when they occur at natural, background levels. As noted above, metallic copper was not observed at any site in this study despite frequently being reported for contaminated soils (Weber et al., 2009a; Weber et al., 2009b; Fulda et al., 2013a; Hofacker et al., 2015). Similarly, our studies find that zinc sulfide is limited in occurrence, with zinc more commonly binding to reduced organic sulfur species. The greater abundance of zinc sulfide in contaminated settings (Bostick et al., 2001; Webb and Gaillard, 2015) may thus be more prevalent in systems receiving substantial zinc inputs.

Finally, this study suggests that greater insight into the speciation of trace metals occurring at geological background levels may be gained using modern analytical tools. The data obtained in this study for trace metals occurring at or below geological background levels was enabled by recent developments in detectors and enhancements in beam flux at synchrotron lightsources. This demonstrates that spectroscopic investigation of trace metal in other uncontaminated terrestrial aquatic systems is viable, allowing further evaluation of whether the consistent speciation observed in the present work is a general geochemical phenomenon.

3.6 CONCLUSIONS

Trace metals in marsh wetland soils, riparian wetland soils, and stream bed sediments at three field sites display a series of similar features. Relative solid-phase concentrations of trace metals followed the trend Zn > Cu ≈ Ni > Co, but their absolute abundance showed no predictive correlations with major element contents. Nickel, copper, and zinc all partially occurred as sulfur-bound species, yet the fractional abundance of these phases were insensitive to the bulk sulfur content, which varied by two orders of magnitude. Freshwater subsurface aquatic systems appear to contain adequate sulfur to stabilize sulfide minerals and metals complexed to reduced organic sulfur species despite their generally low total sulfur contents. Zinc and nickel also widely occurred in clay mineral structures, and all trace metals also occurred complexed to mineral surfaces and organic matter.

The lack of a relationship between sulfur-bound metal contents and total sulfur concentration may reflect the stability of other metal species or heterogeneous microenvironments in wetlands and stream beds. While reaction with iron might limit the availability of reduce sulfur to bind trace metals, it is difficult to envision how this would consistently generate similar fractions of metal-sulfur species across an array of soils and sediments. More broadly, similar species of each trace metal occurred in the soils and sediments at all field sites, often in similar proportions. The consistent trace metal speciation among distant and unrelated sites suggests that a small number of species may dominate freshwater wetland soils and stream sediments. Future investigation of the temporal dynamics of trace metal species in such settings may provide additional insight into the processes that yield consistent trace metal speciation across diverse freshwater aquatic systems.

3.7 ACKNOWLEDGEMENTS

This project was supported by U.S. Department of Energy, Office of Science, Office of Biological and Environmental Research, Subsurface Biogeochemical Research program through award no. DE-SC0019422 to Washington University and contract number DE-AC02-06CH11357 to Argonne National Laboratory for the Argonne Wetland Hydrobiogeochemistry Science Focus Area. Argonne National Laboratory is a U.S. Department of Energy laboratory managed by UChicago Argonne, LLC. This work was also supported by the Critical Interfaces Science Focus Area at Oak Ridge National Laboratory. Oak Ridge National Laboratory is managed by UT-Battelle, LLC, for the U.S. Department of Energy under contract DE-AC05-00OR22725. Work was conducted at the Savannah River National Laboratory under the U.S. Department of Energy Contract DE-AC09-96SR18500. N.S. was also supported by the McDonnell International Scholars Academy at Washington University. Portions of this research utilized the Stanford Synchrotron Radiation Lightsource (SSRL), SLAC National Accelerator Laboratory, which is supported by the U.S. Department of Energy (DOE), Office of Science, Office of Basic Energy Sciences under Contract No. DE-AC02-76SF00515, and the Advanced Photon Source, a U.S. DOE Office of Science User Facility, operated for the DOE Office of Science by Argonne National Laboratory under Contract No. DE-AC02-06CH11357. Ryan Davis is thanked for his assistance with beamline operations at SSRL. Preparation of select standards was performed by Ryan D. Nickerson, Kaushik Mitra, and Walter Schenkeveld. Associate Editor Owen Duckworth and four anonymous reviewers are thanked for detailed comments that improved this manuscript.

3.8 APPENDIX

Synthesis of Reference Standards

Copper citrate was made using equal volumes (100 mL) of 0.15 M copper sulfate ($CuSO_4$) and 0.1 M sodium citrate. The solutions were heated to 100°C on a heated magnetic stir plate. The $CuSO_4$ solution was added to the citrate solution while continuously stirring in the fume hood. The mixture was stirred for 2 hours at 100°C then centrifuged at 4500 rpm for 5 minutes (Beckman Coulter SX4250 rotor) and the supernatant discarded. Copper citrate was washed three times with 50 mL of ultrapure water, centrifuged, and the supernatant discarded. It was then dried in a vacuum desiccator and ground with a mortar and pestle.

Zinc oxalate was prepared by mixing an equimolar ratio of zinc nitrate ($Zn(NO_3)_2$) and oxalic acid solutions as described by (Raj et al., 2011). While stirring, 10 mL of 1 M $Zn(NO_3)_2$ was added to 20 mL of 0.5 M oxalic acid. A milky white precipitate formed immediately. The solution was centrifuged at 4500 rpm for 10 minutes and the supernatant discarded. The precipitant was then rinsed three times with 50 mL of ultrapure water, centrifuged, and the supernatant discarded. Zinc oxalate was dried in a vacuum desiccator and then ground with a mortar and pestle.

To synthesize metal-cysteine, metal-histidine, and metal-glutathione complexes, solutions with a 1:10 ratio of metal to ligand were reacted based on published methods (Kelly et al., 2002; Beauchemin et al., 2004; Montargès-Pelletier et al., 2008; Dokken et al., 2009; Manceau et al., 2013; Van Der Ent et al., 2017). All solutions were prepared in the anaerobic chamber and using deoxygenated ultrapure water. Solutions containing 7 mM of copper chloride ($CuCl_2$), nickel chloride ($NiCl_2$), or zinc nitrate ($Zn(NO_3)_2$) and 70 mM of L-cysteine hydrochloride, L-histidine hydrochloride, or glutathione (reduced) were adjusted to pH 7 ± 0.2 using NaOH. The solutions

containing the metal-ligand complexes were then removed from the anaerobic chamber and frozen. The samples were freeze-dried before being ground using a mortar and pestle.

Standards of Ni, Cu, and Zn adsorbed to goethite were also prepared. Goethite was synthesized using established methods (Schwertmann and Cornell, 2000). Briefly, 50 mL of 1 M iron nitrate ($Fe(NO_3)_3 \cdot 9H_2O$) was added to 90 mL of 5 M potassium hydroxide (KOH) over 1.5 min while continuously stirring. The solution was immediately diluted to 1 L using ultrapure water and heated at 70°C for 60 h. After cooling, the supernatant was discarded, and the goethite was rinsed three times with approximately 150 mL of ultrapure water through a vacuum filter. The goethite was stored as a suspension in ultrapure water and powder X-ray diffraction (XRD) was used to confirm that no other crystalline minerals precipitated. A solution of 0.01 M sodium chloride (NaCl), 0.001 M MOPS buffer, and 0.004 M $CuCl_2$, $NiCl_2$, or $Zn(NO_3)_2$ was reacted with 8 g/L goethite at pH 7.5. Samples were wrapped in Al foil to prevent photochemical reactions and rotated end-over-end for 24 h. They were then centrifuged at 4500 rpm and the supernatant decanted, filtered, acidified to 2% nitric acid, and analyzed via ICP-MS to confirm substantial adsorption had occurred.

Ni- and Zn-substituted trioctahedral Fe(II)-Mg smectite standards were synthesized by modifying the recipe for "Clay D" in Chemtob et al., (2015) to include 0.5 wt.% Ni or Zn, respectively, replacing an equivalent amount of Mg in the structure. Ni- and Fe(II)-substituted serpentines were prepared using a similar sol-gel procedure as used for the smectite standards. 18 mL of 0.5 M sodium metasilicate was added to 13 mL of a solution containing 1 M magnesium chloride and 0.003 M nickel chloride or iron(II) chloride. The resulting gels were aged overnight and then washed via centrifugation and decanting of the fluid, which was replaced with ultrapure water and centrifuged and decanted again. This process was repeated two additional times. The

gels were then resuspended in ultrapure water and heated in a PTFE-lined hydrothermal vessel at 200°C for 14 days. After cooling the resulting solids were separated by vacuum filtration and dried in a vacuum desiccator. XRD confirmed that poorly crystalline turbostratic lizardite was produced. Ni-substituted brucite was also prepared by mixing 20 mL of 1 M sodium hydroxide with 15 mL of 1 M magnesium chloride and 0.003 M nickel chloride. A white precipitate formed quickly and was aged overnight before washing via centrifugation and then drying in a vacuum desiccator. The formation of brucite was confirmed by XRD.

Ni- and Zn-substituted magnetite, as well as metal-free magnetite, were prepared by mixing stoichiometric amounts of iron(II) chloride and iron(III) chloride solutions. Nickel chloride and zinc chloride were added into the iron(III) chloride solution before mixing to yield an ~0.3 mol% substitution level for each metal; this step was not used in the metal-free magnetite synthesis. Sodium hydroxide was used to adjust the pH to 7.0±0.1 after fluid mixing, yielding a black precipitate. This suspension was continuously mixed overnight before being separated by vacuum filtration and then dried in a vacuum desiccator. All steps were performed in an anaerobic chamber. Magnetite was the sole product identified by XRD.

Goethite, hematite, lepidocrocite, and 2-line ferrihydrite were prepared following established procedures (Schwertmann and Cornell, 2000). The lepidocrocite was provided by Walter Schenkeveld. Mackinawite was prepared through direct precipitation in an anaerobic chamber following previously-described procedures (Swanner et al., 2019). Smectites from the Source Clay Repository were size fractionated and Na-saturated as previously described (Catalano and Brown, 2005). Preparation of all standards for data collection are described in the full manuscript.

Surface Water Composition

Major element concentrations and pH were similar among the two sampling locations at each of the field sites investigated (Table S1). While differences were observed between the three field sites, the overall water compositions were more distinct at the riparian wetlands compared to the marsh wetlands and the stream sediment sites. Surface waters in the riparian wetlands are dilute with sodium as the dominant cation (~280 µM) and pH values of 5.5 to 5.6. The marsh wetlands and stream system were more alkaline, having pH values of 7.5 to 8.1, with substantially higher calcium, magnesium, and sulfate concentrations. Sodium and chloride concentrations are higher in the stream system compared to the marsh wetlands, and the stream sites have the highest ionic strengths of the sites examined. Dissolved silica concentrations indicate that all fluids were supersaturated with respect to quartz but undersaturated with respect to amorphous silica.

Dissolved nutrient concentrations (Fig. A3.2; Table A3.5) varied substantially among the sites. Nitrate was greater than ammonium at all sampling locations except for location Riparian 2, where both were below detection limit. Notably, the stream sites had substantially elevated nitrate concentrations (160 to 210 µM) compared to the marsh and riparian wetland sites (<15 µM), because of contamination at the headwaters and wastewater treatment plant discharge. Dissolved phosphate concentrations were similar at the marsh and riparian wetlands, but the stream sites displayed slightly higher concentrations.

Alkalinity and dissolved organic carbon (DOC) were not measured at the time of sampling because of an oversight. Measurements of DOC on archived samples provide an upper bound on values in the original waters. Bicarbonate concentrations and pCO_2 were estimated using two

approaches: (1) from dissolved inorganic carbon (DIC) measurements on archived samples and (2) via charge balance constraints. For the DIC-based estimation approach, the measured water composition as well as the DIC and pH from the time of DIC measurement were input into a fully-speciated geochemical model. The pH of most samples were greater than the field-measured values because of CO_2 degassing. However, alkalinity is conserved during degassing. Field values of bicarbonate and pCO_2 were thus determined by increasing the pCO_2 in the geochemical model until the original, field-measured pH was obtained. For the charge-balance approach, measured anion concentrations were inadequate to balance the cation charge, indicating a missing bicarbonate component. This bicarbonate was added to the system in a geochemical model to reach charge balance while maintaining the field-measured pH and other aspects of the fluid composition. Both estimation approaches indicate that bicarbonate is the dominant anion in all systems and yield similar pCO_2 values (Table S1).

The marsh wetlands host Ca-Mg-HCO_3 fluids, the stream sites Ca-HCO_3 fluids, and the riparian wetlands Na-HCO_3 fluids. pCO_2 values were lowest in the marsh wetlands and highest in the riparian wetlands, with all but one location sampled being elevated above equilibrium with the atmospheric concentration. Filtered but non-acidified water samples returned to the laboratory from the riparian wetland field sites had pH values of 7.2 to 7.3 immediately upon arrival and 7.7 after prolonger storage. This is consistent with a large pH increase associated with degassing of fluids containing highly elevated pCO_2 values and suggesting that the estimated bicarbonate concentrations are relatively accurate.

Extractable Nutrients in the Soils and Sediments

Extractable ammonium (Fig. A3.2) was substantially greater than extractable nitrate at all sites, often by an order of magnitude, showing an opposite pattern of the surface waters. This is

consistent with ammonium retention via cation exchange but may also reflect denitrification. The marsh soils contained the highest extractable ammonium concentrations and were the only soils to show clear evidence for smectites in XRD (Fig. 3.1), suggesting that cation exchange was at least partially responsible for the higher ammonium concentrations. Extractable phosphate was highest in the marsh soils (Fig. A3.2), with concentrations obtained from location Stream 2 and both riparian wetland sites an order of magnitude lower.

Zinc Speciation in Cellulose Acetate Tape

Cellulose acetate tape (e.g., ScotchTM tape in the United States) is widely used for sample mounting at synchrotron lightsources. It was noted during measurements at Advanced Photon Source beamline 12-BM-B that the tape contained zinc based on its X-ray fluorescence spectrum. A Zn K-edge XANES spectrum was collected in fluorescence yield from a stack of 10 layers of tape. This is spectrally similar to the spectrum of zinc oxide (Fig. A3.9), indicating that this is the dominant form of zinc in the tape.

Table A3.1. Major elements and nutrients concentrations in surface waters.

Parameter	Marsh 1	Marsh 2	Riparian 1	Riparian 2	Stream 1	Stream 2
pH	8.10	7.62	5.58	5.49	7.51	7.60
T (°C)	4.2	4.7	13.8	14.2	12.3	14.2
Conductivity (µS)	220	371	n.a.[a]	n.a.	293	348
Ca (µM)	430±10	590±10	18±1	47±1	1280±30	1360±30
Mg (µM)	369±5	557±4	6.3±0.3	9.1±0.3	456±5	633±5
Na (µM)	70±10	220±10	296±2	258±3	670±20	800±10
K (µM)	13±2	22±2	0.8±0.1	0.8±0.2	12±1	9±3
Si (µM)	206±4	187±3	146.5±0.5	140.2±0.6	225±8	250±10
Al (µM)	-[b]	-	6.5±0.9	5.6±0.5	-	-
Fe (µM)	2.6±0.7	5±1	2.3±0.6	70±6	0.6±0.2	1.0±0.3
Mn (µM)	0.07±0.01	0.8±0.3	0.17±0.03	0.43±0.09	1.9±0.6	0.01±0.06
PO_4^{3-} (µM)	7.18±0.02	6.44±0.02	5.7±0.2	5.5±0.2	22.17±0.07	8.65±0.06
NO_3^- (µM)	5.2±0.6	14.4±0.4	3.8±0.1	-	160±30	210±30
NH_4^+ (µM)	3±1	7±5	-	-	11±7	8±1
SO_4^{2-} (µM)	410±30	332.5±0.8	10±1	13.6±0.04	217±3	396±4
F^- (µM)	2.26±0.06	3.7±0.4	1.9±0.1	1.28±0.07	14.6±0.3	22.4±0.6
Cl^- (µM)	68±4	221.8±0.4	61±2	77±1	465±5	578±7
Br^- (µM)	0.66±0.06	0.6±0.2	5±2	5±1	0.9±0.1	6.2±0.5
HCO_3^- (µM)[c]	776	1620	256	265	3100	3190
DIC_{calc} (µM[c]	801	1740	2050	2530	3350	3390
log pCO_2[c]	-3.56	-2.76	-1.44	-1.34	-2.33	-2.40
I (mM)[c]	2.8	3.9	0.38	0.44	6.0	6.9
DOC (mg C L^{-1})[d]	39.4	47.1	8.5	12.5	27.9	27.6
DIC (µM)[d]	790	2270	300	330	3920	4090
HCO_3^- (µM)[e]	764	2206	295	326	3877	4057
DIC_{calc} (µM)[e]	783	2369	2354	3110	4180	4304
log pCO_2[e]	-3.56	-2.62	-1.38	-1.25	-2.23	-2.29
I (mM)[e]	2.8	3.7	0.39	0.45	6.8	7.4
SI_{Quartz}	0.81	0.75	0.43	0.40	0.65	0.65
$SI_{Am.\ Silica}$	-0.66	-0.71	-0.95	-0.98	-0.75	-0.73

[a] Not measured. [b] Value below detection limit, 1.1 µM for Al, 2.1 µM for NO_3^-, 1.1 µM for NH_4^+. [c] Estimated values from charge balance; HCO_3^- concentration is sum of free and complexed species, with 0.1% to 1.6% occurring in complexes at all sites. [d] Measured on archived samples in May 2021. [e] Estimated values from DIC measurement after pCO_2

adjustment to match field pH; HCO_3^- concentration is sum of free and complexed species, with 0.1% to 1.6% occurring in complexes at all sites.

Table A3.2. Field blank major element and trace metal concentrations.

Conc.	Marsh 1	Marsh 2	Stream 1	Stream 2
Na (µM)	11.5±0.8	13±0.7	39±1	45±1
Al (µM)	-[a]	-	-	-
Si (µM)	-	-	-	-
Mg (µM)	-	-	-	-
K (µM)	-	-	-	-
Ca (µM)	-	-	-	-
Fe (µM)	0.3±0.1	0.3±0.1	n.a.[b]	n.a.
Mn (nM)	8±1	41±7	1.5±0.2	1.9±0.3
Co (nM)	1.7±0.3	3.7±0.7	1.5±0.3	1.6±0.3
Ni (nM)	7±1	134±24	2.4±0.5	2.7±0.5
Cu (nM)	15±5	22±7	7±2	8±3
Zn (nM)	19±3	16±2	7±1	11±1

[a] Below the limit of detection: Al =1.6 µM, Si=1.0 µM, Mg=0.51 µM, K=0.83 µM, Ca=4.7 µM.
[b] Not measured

Table A3.3. Trace metal concentrations in surface water samples.

Sample	Cu (nM)	Ni (nM)	Co (nM)	Zn (nM)
Marsh 1	70±20	60±10	26±5	230±30
Marsh 2	20±7	34±6	5±1	50±10
Riparian 1	80±30	12±2	2.3±0.4	100±10
Riparian 2	22±7	34±6	18±3	170±20
Stream 1	50±20	44±8	4.4±0.8	140±20
Stream 2	60±20	40±7	4.0±0.7	50±20

Table A3.4. Trace metal concentrations in soils and sediments.

Sample	Cu (nmol/g)	Ni (nmol/g)	Co (nmol/g)	Zn (nmol/g)
Surface layer				
Marsh 1	730±70	420±90	70±20	2100±400
Marsh 2	400±100	280±70	70±20	1700±500
Riparian 1	30±30	40±20	5±1	100±80
Riparian 2	200±100	110±50	20±6	300±200
Stream 1	150±80	300±200	300±200	600±200
Stream 2	80±30	160±60	80±30	300±100
Second layer				
Marsh 1	764±200	462±70	78±10	1833±300
Marsh 2	366±100	377±100	102±40	1547±400
Riparian 1	10±10	33±10	6±3	84±60
Riparian 2	96±80	73±40	13±5	180±100
Stream 1	84±60	184±90	95±40	483±300
Stream 2	41±20	180±90	115±60	324±200

Table A3.5. KCl-extractable nutrients concentrations in the soils and sediments.

Sample	NO_3^- (µmol/g soil)	NH_4^+ (µmol/g soil)	PO_4^{3-} (µmol/g soil)
Surface layer			
Marsh 1	0.24±0.03	13.0±0.2	0.64±0.04
Marsh 2	0.6±0.3	26±8	1.0±0.5
Riparian 1	0.15±0.02	1.03±0.02	0.057±0.001
Riparian 2	0.01±0.01	2.5±0.2	0.06±0.04
Stream 1	0.14±0.07	1.6±0.2	0.9±0.2
Stream 2	0.5±0.2	2±2	0.036±0.006
Second layer			
Marsh 1	0.245±0.009	4.9±0.3	0.35±0.02
Marsh 2	0.3±0.1	5±2	0.45±0.05
Riparian 1	0.10±0.03	0.21±0.02	0.01±0.03
Riparian 2	0.02±0.03	1±1	0.022±0.008
Stream 1	0.17±0.09	0.9±0.2	0.16±0.08
Stream 2	0.6±0.5	2±1	0.030±0.007

Table A3.6. Major element content of the soils and sediment samples.

Sample	C (wt.%)	N (wt.%)	S (wt.%)	Fe (wt.%)	Mn (wt.%)
Surface layer					
Marsh 1	8.7±0.4	0.79±0.02	0.18±0.01	2.3±0.3	0.011±0.003
Marsh 2	11±2	1.0±0.2	0.28±0.04	2.2±0.3	0.014±0.005
Riparian 1	1.1±0.3	0.3±0.1	0.018±0.009	0.20±0.08	0.0008±0.0005
Riparian 2	4±2	0.05±0.02	0.07±0.03	1.8±0.8	0.003±0.001
Stream 1	6±5	0.2±0.4	1.0±0.9	3±1	0.026±0.009
Stream 2	0.42±0.09	0.05±0.07	0.02±0.01	2.4±0.2	0.04±0.01
Second layer					
Marsh 1	6.45±0.02	0.65±0.02	0.100±0.002	2.5±0.3	0.009±0.001
Marsh 2	3.24±0.05	0.337±0.009	0.068±0.003	3.0±0.1	0.020±0.006
Riparian 1	0.19±0.03	0.017±0.002	0.014±0.008	0.19±0.08	- [a]
Riparian 2	2.8±0.2	0.168±0.010	0.045±0.006	2.0±0.5	0.0023±0.0004
Stream 1	2.14±0.03	0.160±0.004	0.065±0.005	1.4±0.2	0.016±0.006
Stream 2	0.482±0.006	0.06±0.01	0.019±0.003	2.60±0.04	0.09±0.01

[a] Below detection limit.

Table A3.7. Sulfur K-edge XANES standards and sources.

Standard	Source/Reference
Mackinawite	Swanner et al. (2019)
Pyrite	Manceau and Nagy (2012)
Elemental S	Manceau and Nagy (2012)
L-cysteine	Manceau and Nagy (2012)
4-Nitrobenzenethiol	Manceau and Nagy (2012)
Dibenzyl sulfide	Manceau and Nagy (2012)
Benzyl phenyl sulfide	Manceau and Nagy (2012)
DL-cystine	Manceau and Nagy (2012)
Dibenzyl disulfide	Manceau and Nagy (2012)
DL-methionine sulfoxide	Manceau and Nagy (2012)
Dibenzyl sulfone	Manceau and Nagy (2012)
Sodium cyclohexanesulfonate	Manceau and Nagy (2012)
Anthraquinone sulfonic acid	Bohic et al. (2012)
Chondroitine sulfate	Cuif et al. (2003)
Gypsum	Manceau and Nagy (2012)

*Data were taken from the literature when a reference is given.

Table A3.8. Iron K-edge XANES standards and sources.

Standard	Source
Mackinawite	Synthesized
Pyrite	Ward's Science
0.1 M $FeCl_2$	Salt from Sigma-Aldrich
Fe(II)-Mg Saponite	Chemtob et al. (2015)
Chlorite CCa-2	Source Clay Repository, as received
Lizardite	Synthesized
Lepidocrocite	Synthesized
Goethite	Synthesized
Hematite	Synthesized
Magnetite	Synthesized
2-line Ferrihydrite	Synthesized
Montmorillonite SAz-1	Source Clay Repository, <2 µm
Montmorillonite SWy-2	Source Clay Repository, <2 µm
Kaolinite KGa-2	Source Clay Repository, as received
Ferruginous Smectite SWa-1	Source Clay Repository, <2 µm
Nontronite NAu-1	Source Clay Repository, <0.5 µm
Nontronite NAu-2	Source Clay Repository, <0.5 µm

*Synthesis methods of the reference standards are described in the section "Synthesis of Reference Standards". Data were taken from the literature when a reference is given.

Table A3.9. Cu reference standards for EXAFS measurement and their sources.

Standard	Source/Reference
Copper(II) Acetate	Acros Organics
Copper(II) Oxalate	Alfa Aesar
Copper(II) Citrate	Synthesized
Copper(II) Sulfate	Fisher Scientific
Chalcocite (Cu_2S)	Alfa Aesar
Cu(II)-Cysteine Complex	Synthesized
Cu(II)-Histidine Complex	Synthesized
Cu(II)-Glutathione Complex	Synthesized
Covellite (CuS)	Butte, Montana, USA
Cu(II) adsorbed to goethite	Synthesized
Cu metal	EXAFS Materials
0.1 M $CuCl_2$	Salt from Sigma-Aldrich
Cu-substituted Goethite	Frierdich and Catalano (2012)
Copper(II) oxide	Frierdich and Catalano (2012)
Copper(I) oxide	Frierdich and Catalano (2012)
Copper(II) hydroxide	Alfa Aesar; See Frierdich and Catalano (2012) for data collection information.

*Synthesis methods of the reference standards are described in the section "Synthesis of Reference Standards". Data were taken from the literature when a reference is given.

Table A3.10. Ni reference standards for EXAFS measurement and their sources.

Standard	Source/Reference
Nickel(II) Acetate	Acros Organics
Nickel(II) Oxalate	Alfa Aesar
Nickel(II) Citrate	Alfa Aesar
Nickel(II) Sulfide	Alfa Aesar
Ni(II)-Cysteine Complex	Synthesized
Ni(II)-Histidine Complex	Synthesized
Ni(II)-Glutathione Complex	Synthesized
Ni(II)-Cellulose Complex	Synthesized
Ni-substituted Hematite	Frierdich et al. (2011)
Ni-substituted Goethite	Frierdich et al. (2011)
Ni-substituted Magnetite	Synthesized
Pyroxene (Augite)	Ontario, Canada
Olivine	San Carlos, Arizona, USA
Ni-substituted Brucite	Synthetized
Ni-substituted Serpentine	Synthetized
Ni-substituted Fe(II)-Mg Trioctahedral Smectite	Synthetized
Ni(II) adsorbed to goethite	Synthetized
0.1 M $NiCl_2$	Salt from Sigma-Aldrich

*Synthesis methods of the reference standards are described in the section "Synthesis of Reference Standards". Data were taken from the literature when a reference is given.

Table A3.11. Zn reference standards for EXAFS measurement and their sources.

Standard	Source/Reference
Zinc(II) Acetate	Fisher Scientific
Zinc(II) Oxalate	Synthesized
0.1 M $Zn(NO_3)_2$	Salt from J.T. Baker
Zinc(II) Sulfate	Fisher Scientific
Zn(II)-Cysteine Complex	Synthesized
Zn(II)-Histidine Complex	Synthesized
Zn(II)-Glutathione Complex	Synthesized
Franklinite	Luo et al. (2011)
Gahnite	Luo et al. (2011)
Willemite	Luo et al. (2011)
Hemimorphite	Luo et al. (2011)
Zinc(II) Hydroxide	Luo et al. (2011)
Zn-Al layered double hydroxide	Luo et al. (2011)
Zn smectite	Synthesized
Zinc(II) Oxide	Luo et al. (2011)
Hydrozincite	Luo et al. (2011)
Sphalerite	Pettus County, Missouri, USA
Zn-substituted Hematite	Frierdich and Catalano (2012a)
Zn-substituted Goethite	Frierdich and Catalano (2012a)
Zn adsorbed to goethite	Synthesized

*Synthesis methods of the reference standards are described in the section "Synthesis of Reference Standards". Data were taken from the literature when a reference is given.

Table A3.12. Sulfur XANES linear combination fitting results.

Standard	Marsh 1	Marsh 2	Riparian 1	Riparian 2	Stream 1 C1	Stream 1 C2	Stream 2
Fitting Components							
Gypsum	10.1±0.6 %	8.6±0.2	5.5±0.6 %	10.5±0.2 %	5.8±0.4 %	1.1±0.7 %	16±1%
Anthraquinone sulfonic acid	6±2%	- [a]	9±2%	-	3.0±0.4 %	1.7±0.6 %	7±3%
Sodium cyclohexanesulfonate	23±1%	17.1±0.2	9±1%	17.0±0.2	-	-	5±2%
Dibenzyl sulfone	1.6±0.4%	1.6±0.2%	-	1.5±0.2	-	-	-
DL-methionine sulfoxide	2.2±0.4%	3.0±0.2%	-	4.8±0.4%	-	-	-
Dibenzyl disulfide	-	-	35±4%	5±4%	14±3%	14±5%	21±4%
Cystine	17±2%	16±1%	6±2%	18±1%	-	-	-
Benzyl phenyl sulfide	10±3%	13±2%	-	-	-	-	-
4-Nitrobenzenethiol	10±2%	7±1%	-	-	-	-	-
Cysteine	8±3%	13±2%	8±1%	18±1%	-	-	-
Elemental S	9±2%	17±1%	24±2%	19±2%	42±4%	73±5%	50±3%
Pyrite	-	-	-	-	30±3%	10±3%	-
Mackinawite	3.7±0.8%	4.6±0.5%	3.3±0.7 %	6.4±0.6%	5±1%	-	2±1%
Component sum	1.075	0.977	1.063	1.006	1.009	1.093	1.006
R factor	0.003	0.002	0.005	0.003	0.01	0.02	0.02
χ_v^2	0.002	0.0009	0.003	0.001	0.004	0.01	0.008
Groupings							
FeS	3.7±0.8%	4.6±0.5%	3.3±0.7 %	6.4±0.6%	5±1%	-	2±1%
Pyrite	-	-	-	-	30±3%	10±3%	-
S^0	9±2%	17±1%	24±2%	19±2%	42±4%	73±5%	50±3%
Exocyclic	45±5%	48±3%	50±4%	41±4%	14±3%	14±5%	21±4%
Sulfoxide	2.2±0.4%	3.0±0.2%	-	4.8±0.4%	-	-	-
Sulfone	1.6±0.4%	1.6±0.2%	-	1.5±0.2%	-	-	-
Sulfonate	29±2%	17.1±0.2 %	17±2%	17.0±0.2 %	3.0±0.4 %	2±1%	12±4%
Sulfate (inorganic)	10.1±0.6	8.6±0.2%	5.5±0.6 %	10.5±0.2 %	5.8±0.4 %	1±1%	16±1%

[a] Not present in final fit.

Table A3.13. Iron XANES linear combination fitting results.

Standard	Marsh 1	Marsh 2	Riparian 1	Riparian 2	Stream 1 C1	Stream 1 C2	Stream 2
Fitting Components							
Pyrite	-	-	-	-	-	-	4.8±0.3%
FeS	3.5±0.7%	6.5±0.5 %	-	5.6±0.3%	48.0±0.2%	17.5±0.2 %	-
Fe(II) (aq)	18.2±0.7 %	19±1%	17.5±0.4 %	32.1±0.4 %	5.3±0.3%	15.2±0.3 %	7.2±0.3%
Fe(II)-Mg Smectite	23±1%	29±1%	-	-	10.3%±0.5 %	-	-
Chlorite	-	-	6.4±0.7%	13.1±0.8 %	-	17.7±0.5 %	18.0±0.4 %
Magnetite	7%±3%	-	-	-	-	-	-
Montmorillonite	48±2%	39±3%	-	-	8±1%	-	-
Ferruginous smectite	-	-	-	-	-	30±2%	38±2%
Kaolinite	-	-	18±3%	24±3%	-	-	-
Lepidocrocite	-	7±4%	-	-	-	-	-
Goethite	-	-	11±3%	25±3%	28±1%	19±2%	-
2-line ferrihydrite	-	-	48±2%	-	-	-	32±3%
Component sum	1.01	1.015	0.996	1.006	0.999	1.004	0.996
R factor	0.0004	0.0006	0.0001	0.0002	0.0001	0.00008	0.0001
χ_v^2	0.0001	0.0002	0.00004	0.00005	0.00002	0.00002	0.00004
Groupings							
Pyrite	-	-	-	-	-	-	4.8±0.3%
FeS	3.5±0.7%	6.5±0.5 %	-	5.6±0.3%	48.0±0.2%	17.5±0.2 %	-
Fe(II) (aq)	18.2±0.7 %	19±1%	17.5±0.4 %	32.1±0.4 %	5.3±0.3%	15.2±0.3 %	7.2±0.3%
Fe(II) in clays	23±1%	29±1%	6.4±0.7%	13.1±0.8 %	10.3±0.5%	17.7±0.5 %	18.0±0.4 %
Magnetite	7±3%	-	-	-	-	-	-
Fe(III) in clays	48±2%	39±3%	18±3%	24±3%	8±1%	30±2%	38±2%
Fe(III) oxides	-	7±4%	58±5%	25±3%	28±1%	19±2%	32±3%

[a] Not present in final fit.

Table A3.14. Iron EXAFS linear combination fitting results.

Standard	Marsh 1	Marsh 2	Riparian 2	Stream 1 C1	Stream 1 C2	Stream 2
Fitting Components						
Pyrite	1.8±0.9%	1.4±0.8%	-	-	-	-
FeS	-	-	-	46±1%	14±2%	-
Fe(II) (aq)	20±3%	13±2%	26±3%	4±2%	8±3%	-
Fe(II)-Mg Smectite	20±3%	33±2%	-	-	-	6±3%
Chlorite	-	-	20±3%	14±2%	26±3%	19±3%
Montmorillonite	24±3%	43±2%	25±2%	21±1%	29±2%	37±2%
Ferruginous smectite	34±3%	-	-	-	-	-
Lepidocrocite	-	9±1%	-	-	-	-
Goethite	-	-	-	14±2%	22±3%	27±2%
2-line ferrihydrite	-	-	13±4%	-	-	10±3%
Hematite	-	-	16±1%	-	-	-
Component sum	1.008	0.932	0.904	0.889	0.886	0.861
R factor	0.04	0.03	0.04	0.02	0.05	0.02
χ_v^2	0.3	0.2	0.2	0.1	0.3	0.1
Groupings						
Pyrite	1.8±0.9%	1.4±0.8%	-	-	-	-
FeS	-	-	-	46±1%	14±2%	-
Fe(II) (aq)	20±3%	13±2%	26±3%	4±2%	8±3%	-
Fe(II) in clays	20±3%	33±2%	20±3%	14±2%	26±3%	26±7%
Fe(III) in clays	58±6%	43±2%	25±2%	21±1%	29±2%	37±2%
Fe(III) oxides	-	9±1%	29±5%	14±2%	22±3%	37±5%

[a] Not present in final fit.

Table A3.15. Copper XANES linear combination fitting results.

Standard	**Marsh 1**	**Marsh 2**	**Riparian 1**	**Riparian 2**	**Stream 1 C1**	**Stream 1 C2**	**Stream 2**
Fitting Components							
Covellite	90±1%	83±1%	40±4%	75±1%	70±1%	72±1%	32±2%
Chalcocite	-[a]	-	30±4%	-	-	-	-
Cu(II)-Histidine	10±1%	12±5%	-	-	9±7%	-	13±5%
0.1 M $CuCl_2$	-	-	-	-	-	-	21±8%
Ads. Cu	-	5±4%	40±1%	25±1%	21±6%	28±1%	34±8%
Component sum	1.028	1.04	1.081	1.028	1.041	1.012	1.004
R factor	0.002	0.002	0.003	0.002	0.003	0.002	0.001
χ_v^2	0.0003	0.0004	0.0007	0.0004	0.0007	0.0005	0.0003
Groupings							
CuS	90±1%	83±1%	40±4%	75±1%	70±1%	72±1%	32±2%
Cu_2S	-	-	30±4%	-	-	-	-
Amine bound	10±1%	12±5%	-	-	9±7%	-	13±5%
Adsorbed	-	5±4%	40±1%	25±1%	21±6%	28±1%	55±20%

[a] Not present in final fit.

Table A3.16. Nickel XANES linear combination fitting results.

Standard	**Marsh 1**	**Marsh 2**	**Riparian 1**	**Riparian 2**	**Stream 1 C1**	**Stream 1 C2**	**Stream 2**
Fitting Components							
NiS	35±8%	33±1%	13±2%	14±1%	32±1%	34±1%	14±1%
Ni-Smectite	50±3%	45±8%	60±6%	65±5%	59±4%	45±9%	70±3%
Serpentine	-[a]	9±8%	-	-	-	13±9%	-
0.1 M $NiCl_2$	15±3%	13±3%	27±7%	22±5%	-	-	16±4%
Ads. Ni	-	-	-	-	9±4%	9±3%	-
Component sum	1.014	1.03	0.974	1.028	1.074	1.024	1.011
R factor	0.002	0.002	0.007	0.005	0.005	0.003	0.003
χ_v^2	0.0005	0.0007	0.002	0.002	0.001	0.0009	0.001
Groupings							
NiS	35±8%	33±8%	13±2%	13±1%	32±1%	34±1%	14±1%
Clay structures	50±3%	54±3%	60±6%	65±5%	59±4%	58±18%	70±3%
Adsorbed	15±3%	12±3%	27±7%	22±5%	9±4%	9±3%	16±4%

[a] Not present in final fit.

Table A3.17. Zinc XANES linear combination fitting results.

Standard	**Marsh 1**	**Marsh 2**	**Riparian 1**	**Riparian 2**	**Stream 1 C1**	**Stream 1 C2**	**Stream 2**
Fitting Components							
Zn-Smectite	36±2%	23±2%	-[a]	-	12±1%	29±2%	14±4%
ZnO	10±1%	27±1%	54±2%	23±1%	45±1%	34±1%	50±2%
Zn cysteine	30±1%	-	-	-	27±1%	22±1%	-
Zn glutathione	-	34±1%	19±3%	-	-	-	21±2%
Sphalerite	-	-	10±2%	7±2%	-	-	-
Zn Acetate	24±2%	-	-	-	-	-	-
$ZnSO_4$	-	16±1%	17±1%	-	16±1%	15±1%	15±2%
Zn Nitrate	-	-	-	41±2%	-	-	-
Ads. Zn	-	-	-	29±4%	-	-	-
Component sum	1.006	0.996	0.995	0.977	0.996	0.999	0.984
R factor	0.0004	0.0003	0.0004	0.0005	0.0007	0.0004	0.001
χ_v^2	0.02	0.0001	0.0002	0.0002	0.01	0.0001	0.05
Groupings							
ZnS	-	-	10±2%	7±2%	-	-	-
Thiol bound	30±1%	34±1%	19±3%	-	27±1%	22±1%	21±2%
Clay structures	36±2%	23±2%	-[a]	-	12±1%	29±2%	14±4%
ZnO	10±1%	27±1%	54±2%	23±1%	45±1%	34±1%	50±2%
Adsorbed	24±2%	16±1%	17±1%	70±6%	16±1%	15±1%	15±2%

[a] Not present in final fit.

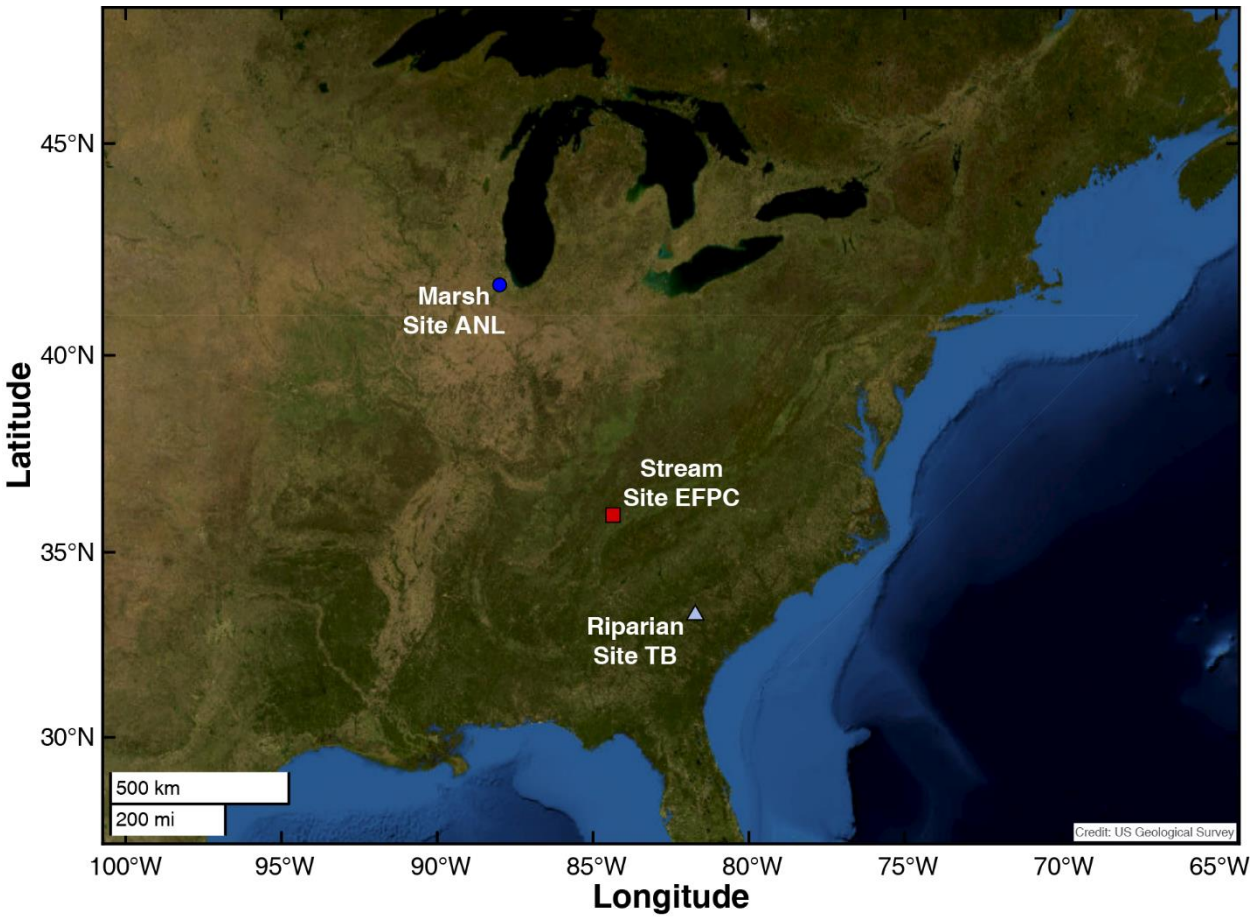

Figure A3.1. Location of the three field sites: Marsh wetlands at Argonne National Laboratory (Site ANL), stream bed sediments in the East Fork Poplar Creek (Site EFPC), and riparian wetlands in the Tims Branch watershed (Site TB). Details site descriptions and coordinates for these locations are provided in the Materials and Methods.

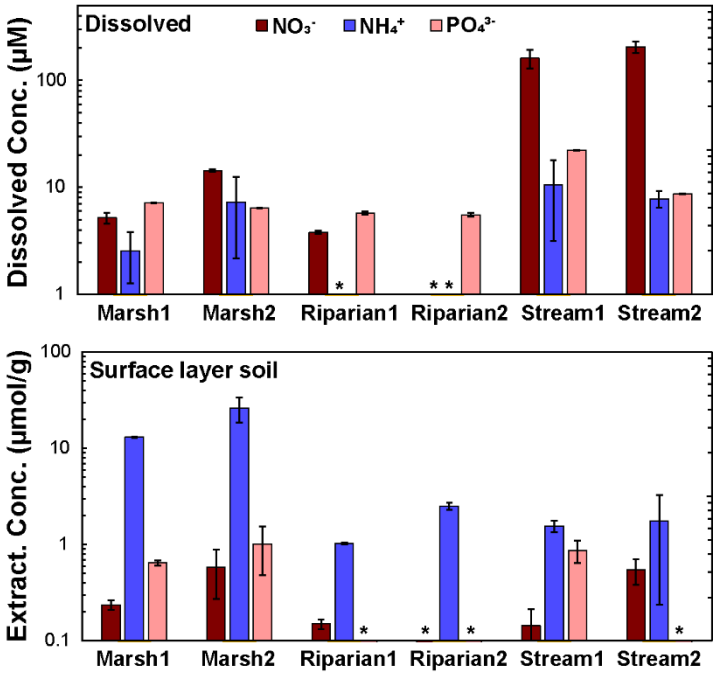

Figure A3.2. Dissolved (top) and solid-phase extractable (bottom) nitrate, ammonium, and phosphate concentrations for the study sites. Sample with an asterisk were below the ~2 µM or ~0.04 µmol/g detection limit.

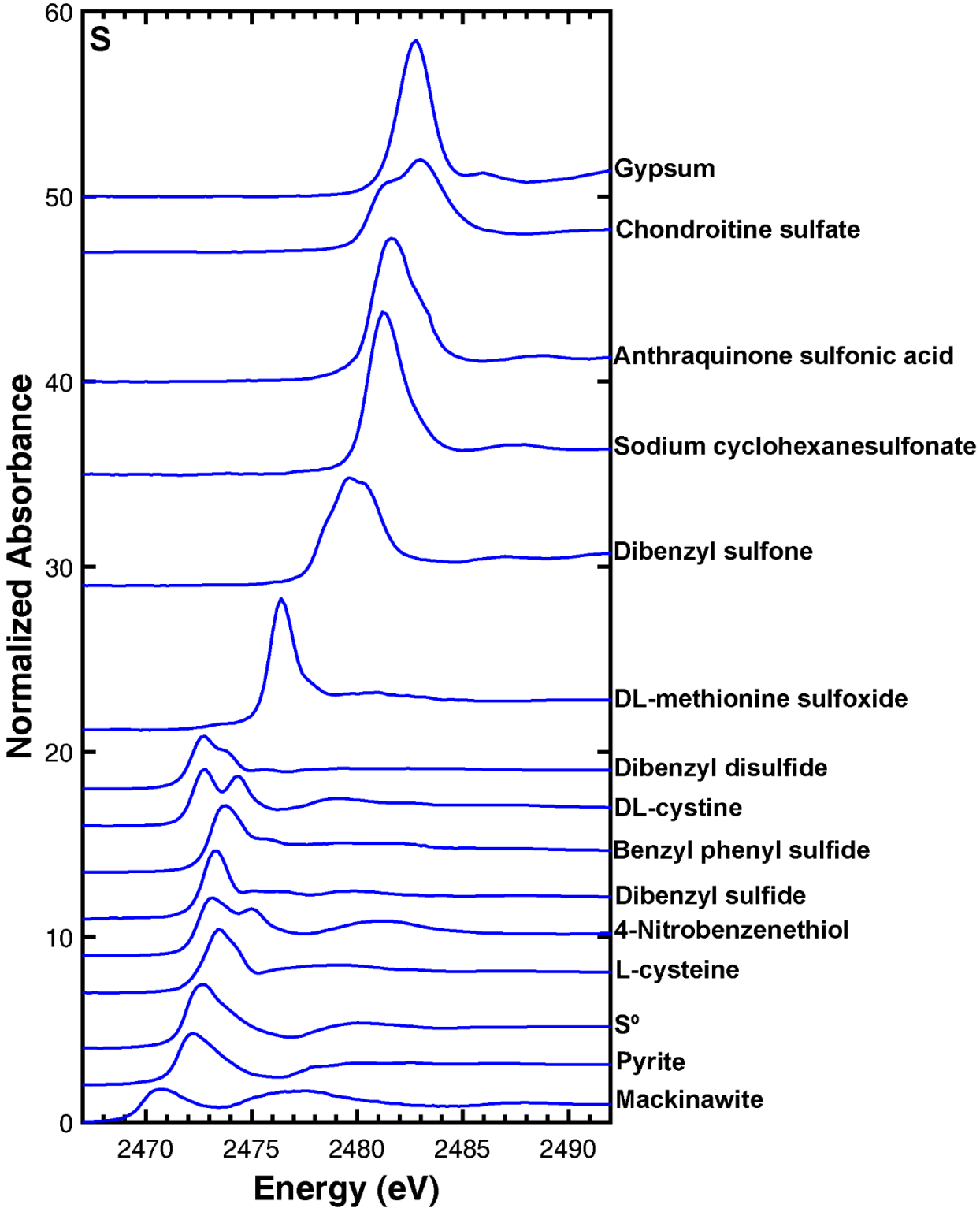

Figure A3.3. XANES spectra of sulfur reference standards. See Table A3.7 for more information. XANES spectra of sulfur reference standards. See Table A3.7 for more information.

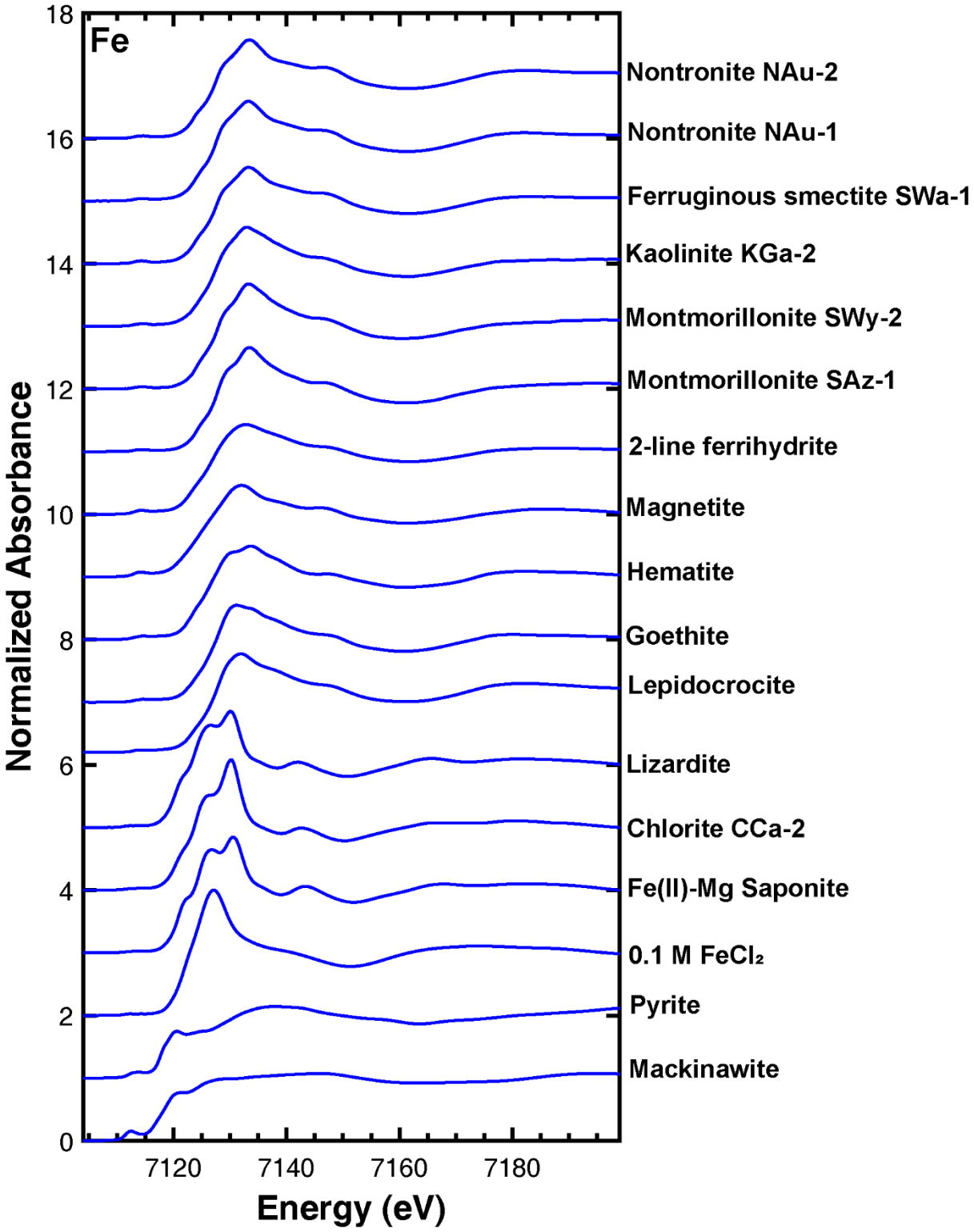

Figure A3.4. XANES spectra of iron reference standards. See Table A3.8 for more information.

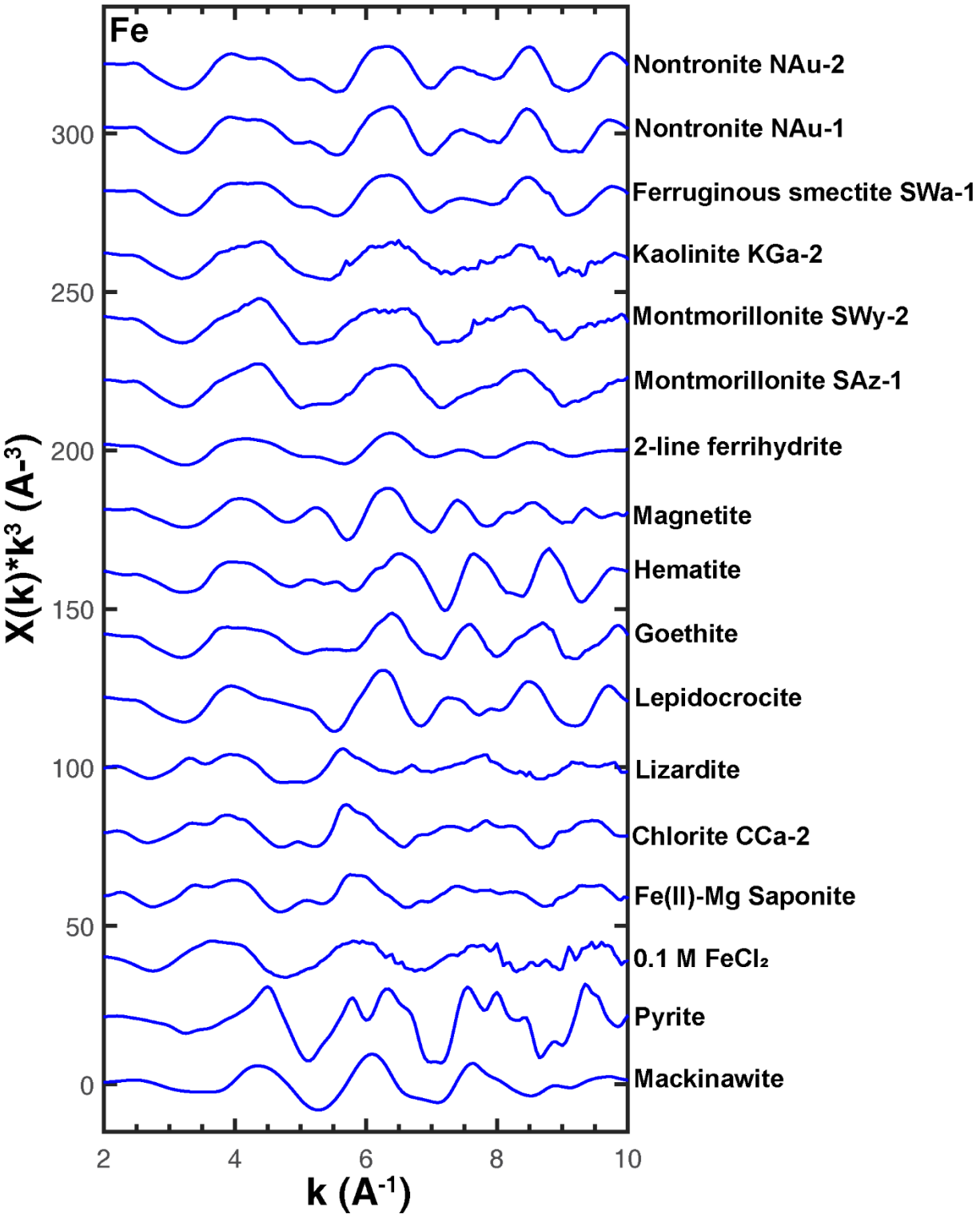

Figure A3.5. EXAFS spectra of iron reference standards. See Table A3.8 for more information.

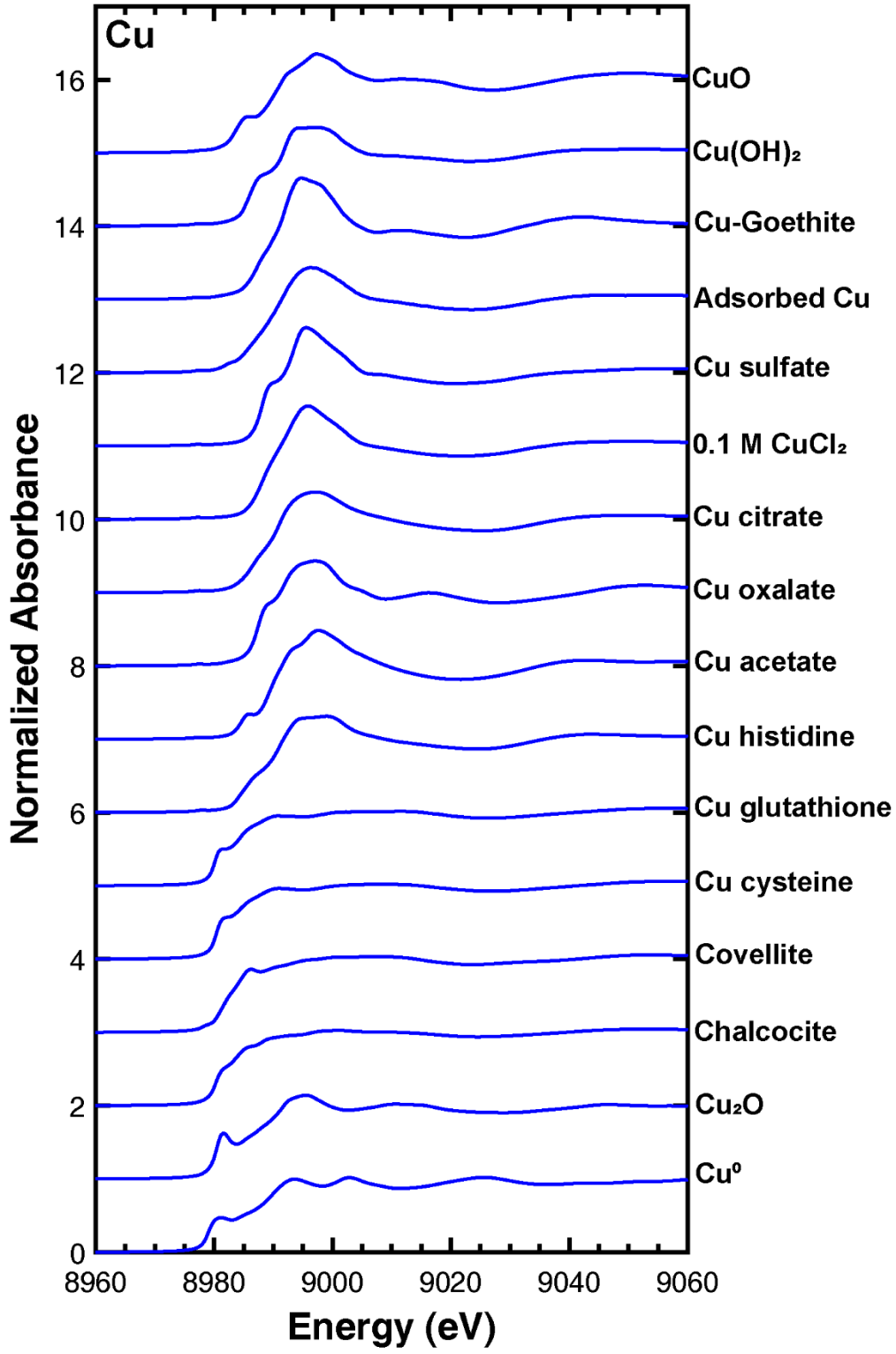

Figure A3.6. XANES spectra of copper reference standards. See Table A3.9 for more information.

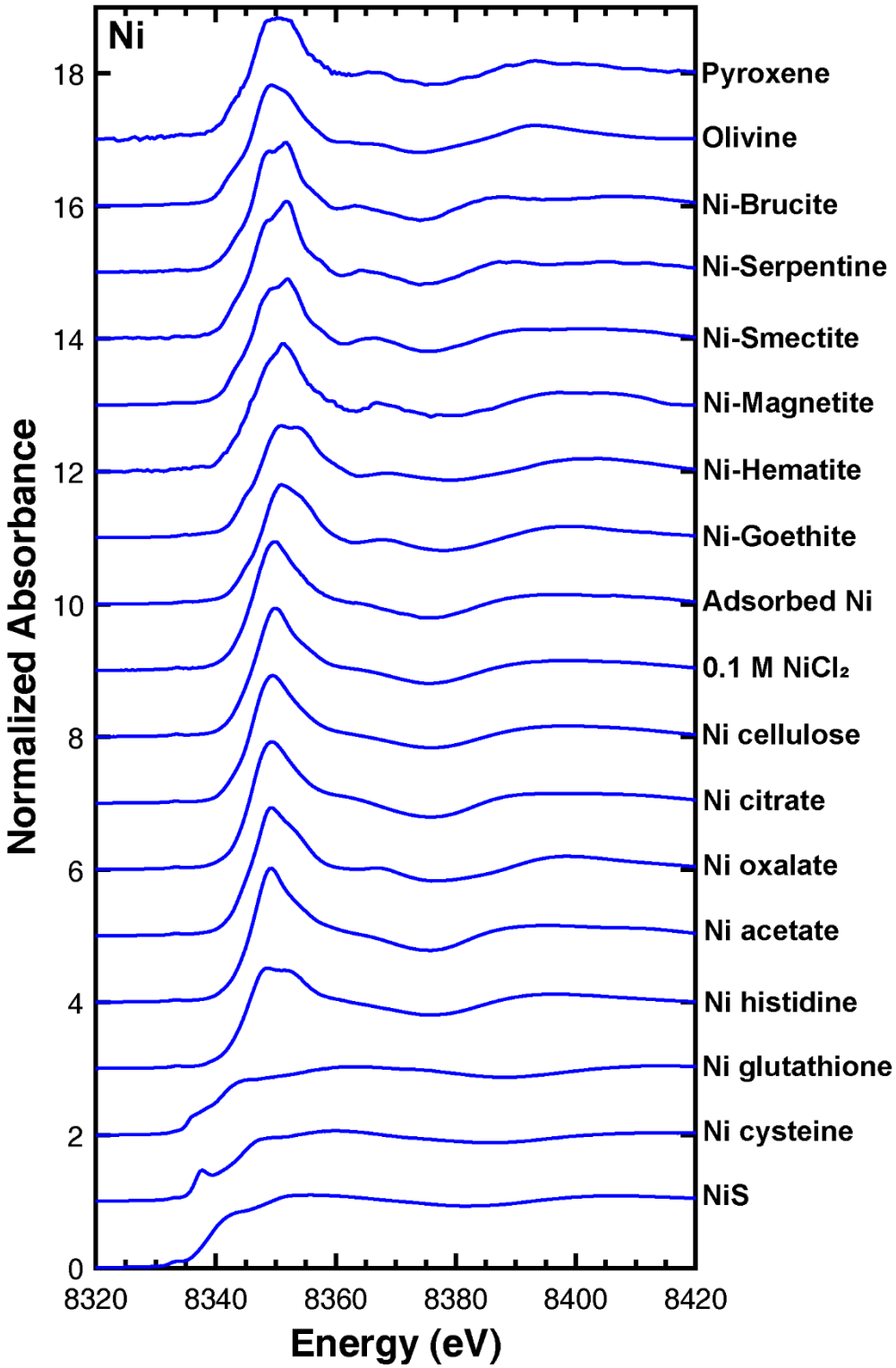

Figure A3.7. XANES spectra of nickel reference standards. See Table A3.10 for more information.

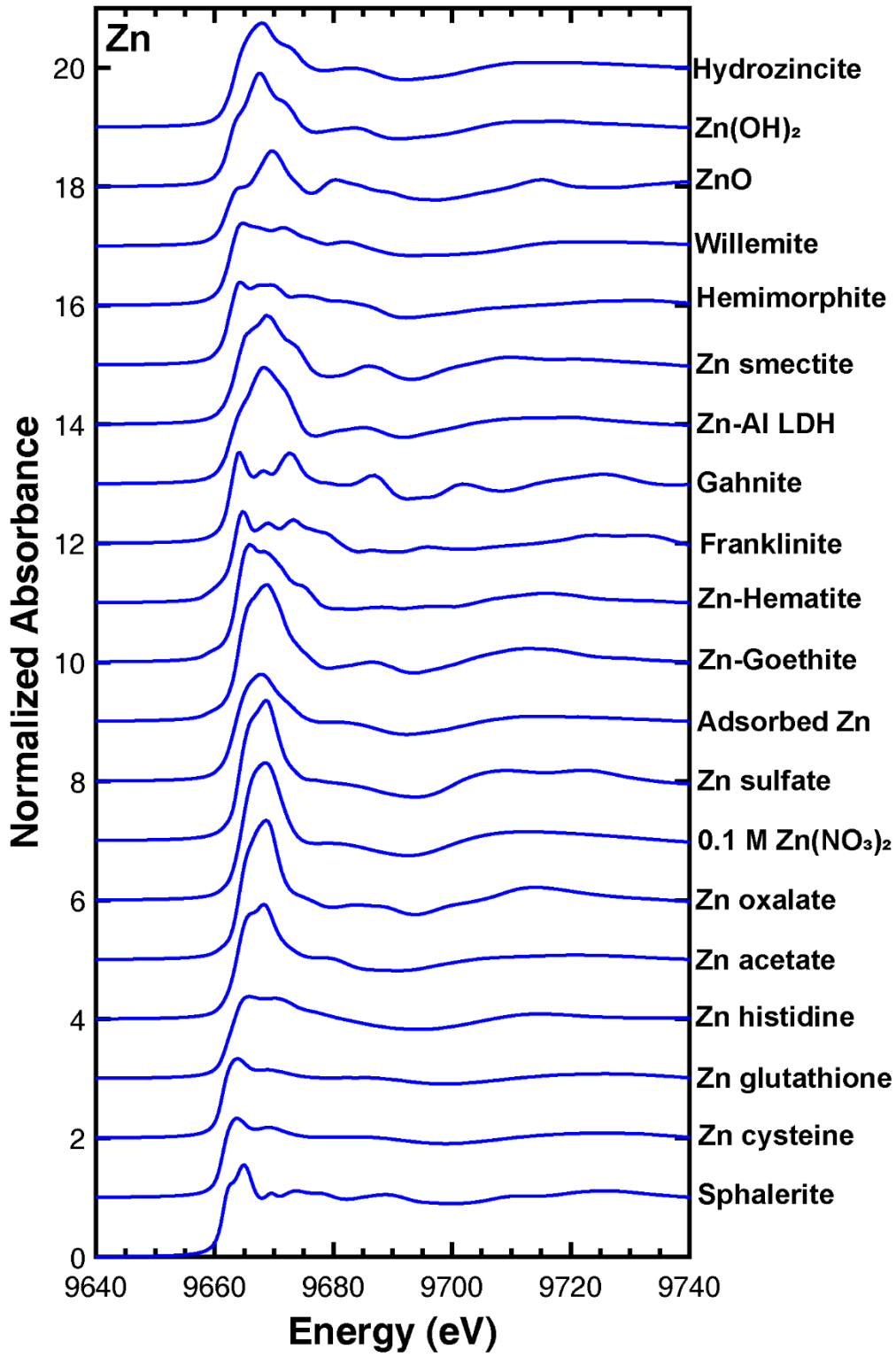

Figure A3.8. XANES spectra of zinc reference standards. See Table A3.11 for more information.

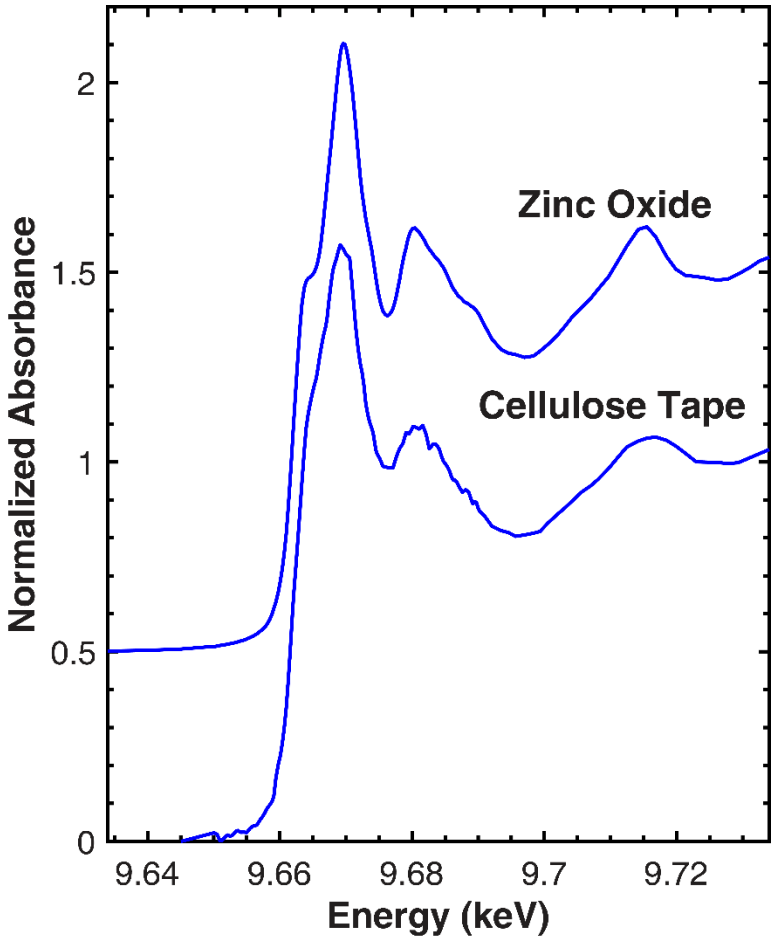

Figure A3.9. XANES spectrum of zinc in cellulose acetate tape compared to zinc oxide.

3.9 REFERENCES

Almkvist G., Boye K. and Persson I. (2010) K-edge XANES analysis of sulfur compounds: An investigation of the relative intensities using internal calibration. *J. Synchrotron Radiat.* **17**, 683–688.

Altschuler Z. S., Schnepfe M. M., Silber C. C. and Simon F. O. (1983) Sulfur diagenesis in everglades peat and origin of pyrite in coal. *Science* **221**, 221–227.

Arora B., Spycher N. F., Steefel C. I., Molins S., Bill M., Conrad M. E., Dong W., Faybishenko B., Tokunaga T. K., Wan J., Williams K. H. and Yabusaki S. B. (2016) Influence of hydrological, biogeochemical and temperature transients on subsurface carbon fluxes in a flood plain environment. *Biogeochemistry* **127**, 367–396.

Basiliko N. and Yavitt J. B. (2001) Influence of Ni, Co, Fe, and Na additions on methane production in Sphagnum-dominated Northern American peatlands. *Biogeochemistry* **52**, 133–153.

Beauchemin S., Hesterberg D., Nadeau J. and McGeer J. C. (2004) Speciation of hepatic Zn in trout exposed to elevated waterborne Zn using X-ray absorption spectroscopy. Environ. Sci. Technol. 38, 1288–1295.

Bethke C. M. (2007) *Geochemical and biogeochemical reaction modeling: Second edition*., Cambridge University Press.

Bohic S., Cotte M., Salomé M., Fayard B., Kuehbacher M., Cloetens P., Martinez-Criado G., Tucoulou R. and Susini J. (2012) Biomedical applications of the ESRF synchrotron-based microspectroscopy platform. J. Struct. Biol. 177, 248–258.

Bostick B. C., Hansel C. M., La Force M. J. and Fendorf S. (2001) Seasonal fluctuations in zinc speciation within a contaminated wetland. *Environ. Sci. Technol.* **35**, 3823–3829.

Bouwman A. F., Beusen A. H. W., Griffioen J., Van Groenigen J. W., Hefting M. M., Oenema O., Van Puijenbroek P. J. T. M., Seitzinger S., Slomp C. P. and Stehfest E. (2013) Global trends and uncertainties in terrestrial denitrification and N_2O emissions. *Philos. Trans. R. Soc. B Biol. Sci.* **368**, 20130112.

Bowden W. B. (1987) The biogeochemistry of nitrogen in freshwater wetlands. *Biogeochemistry* **4**, 313–348.

Brooks S. C. and Southworth G. R. (2011) History of mercury use and environmental contamination at the Oak Ridge Y-12 Plant. *Environ. Pollut.* **159**, 219–228.

Brown K. A. (1985) Sulphur distribution and metabolism in waterlogged peat. *Soil Biol. Biochem.* **17**, 39–45.

Brown K., Tegoni M., Prudêncio M., Pereira A. S., Besson S., Moura J. J., Moura I. and Cambillau C. (2000) A novel type of catalytic copper cluster in nitrous oxide reductase. *Nat. Struct. Biol.* **7**, 191–195.

Caritat P. de, Reimann C., Smith D. B. and Wang X. (2018) Chemical elements in the environment: Multi-element geochemical datasets from continental- to national-scale surveys on four continents. *Appl. Geochemistry* **89**, 150–159.

Casagrande D. J., Siefert K., Berschinski C. and Sutton N. (1977) Sulfur in peat-forming systems of the Okefenokee Swamp and Florida Everglades: origins of sulfur in coal. *Geochim. Cosmochim. Acta* **41**, 161–167.

Catalano J. G. and Brown G. E., Jr. (2005) Uranyl adsorption onto montmorillonite: Evaluation of binding sites and carbonate complexation. Geochim. Cosmochim. Acta 69, 2995–3005.

Castro H., Reddy K. R. and Ogram A. (2002) Composition and function of sulfate-reducing prokaryotes in eutrophic and pristine areas of the Florida Everglades. Appl. Environ. Microbiol. 68, 6129–6137.

Cervi E. C., Clark S., Boye K. E., Gustafsson J. P., Baken S. and Burton G. A. (2021) Copper transformation, speciation, and detoxification in anoxic and suboxic freshwater sediments. *Chemosphere* **282**, 131063. Available at: https://doi.org/10.1016/j.chemosphere.2021.131063.

Chemtob S. M., Nickerson R. D., Morris R. V., Agresti D. G. and Catalano J. G. (2015) Synthesis and structural characterization of ferrous trioctahedral smectites: Implications for clay mineral genesis and detectability on Mars. J. Geophys. Res. E Planets 120, 1119–1140.

Cuif J. P., Dauphin Y. Y., Doucet J., Salome M. and Susini J. (2003) XANES mapping of organic sulfate in three scleractinian coral skeletons. Geochim. Cosmochim. Acta 67, 75–83.

Dähn R., Scheidegger A. M., Manceau A., Schlegel M. L., Baeyens B., Bradbury M. H. and Morales M. (2002) Neoformation of Ni phyllosilicate upon Ni uptake on montmorillonite: A kinetics study by powder and polarized extended X-ray absorption fine structure spectroscopy. *Geochim. Cosmochim. Acta* **66**, 2335–2347.

Dail D. B. and Fitzgerald J. W. (1999) S Cycling in soil and stream sediment: Influence of season and in situ concentrations of carbon, nitrogen and sulfur. *Soil Biol. Biochem.* **31**, 1395–1404.

Danczak R. E., Sawyer A. H., Williams K. H., Stegen J. C., Hobson C. and Wilkins M. J. (2016) Seasonal hyporheic dynamics control coupled microbiology and geochemistry in Colorado River sediments. *J. Geophys. Res. Biogeosciences* **121**, 2976–2987.

Delaney J. and Lundeen S. (1990) The LLNL thermodynamical database: Lawrence Livermore National Laboratory Report. *Ucrl-21658* **Report UCR**, 150.

Dokken K. M., Parsons J. G., McClure J. and Gardea-Torresdey J. L. (2009) Synthesis and structural analysis of copper(II) cysteine complexes. Inorganica Chim. Acta 362, 395–401.

Donovan P. M., Blum J. D., Demers J. D., Gu B., Brooks S. C. and Peryam J. (2014) Identification of multiple mercury sources to stream sediments near Oak Ridge, TN, USA. *Environ. Sci. Technol.* **48**, 3666–3674.

Dublet G., Juillot F., Morin G., Fritsch E., Fandeur D., Ona-Nguema G. and Brown G. E. (2012) Ni speciation in a New Caledonian lateritic regolith: A quantitative X-ray absorption spectroscopy investigation. *Geochim. Cosmochim. Acta* **95**, 119–133.

Ekstrom E. B. and Morel F. M. M. (2008) Cobalt limitation of growth and mercury methylation in sulfate-reducing bacteria. *Environ. Sci. Technol.* **42**, 93–99.

Van Der Ent A., Callahan D. L., Noller B. N., Mesjasz-Przybylowicz J., Przybylowicz W. J., Barnabas A. and Harris H. H. (2017) Nickel biopathways in tropical nickel hyperaccumulating trees from Sabah (Malaysia). Sci. Rep. 7.

Van Der Ent A., Mak R., De Jonge M. D. and Harris H. H. (2018) Simultaneous hyperaccumulation of nickel and cobalt in the tree *Glochidion* cf. *sericeum* (Phyllanthaceae): Elemental distribution and chemical speciation. *Sci. Rep.* **8**.

Ermler U., Grabarse W., Shima S., Goubeaud M. and Thauer R. K. (1997) Crystal structure of methyl-coenzyme M reductase: The key enzyme of biological methane formation. *Science* **278**, 1457–1462.

Falkowski P. G., Barber R. T. and Smetacek V. (1998) Biogeochemical controls and feedbacks on ocean primary production. *Science* **281**, 200–206.

Flynn T. M., Koval J. C., Greenwald S. M., Owens S. M., Kemner K. M. and Antonopoulos D. A. (2017) Parallelized, Aerobic, single carbon-source enrichments from different natural environments contain divergent microbial communities. *Front. Microbiol.* **8**, 2321.

Flynn T. M., O'Loughlin E. J., Mishra B., DiChristina T. J. and Kemner K. M. (2014) Sulfur-mediated electron shuttling during bacterial iron reduction. *Science* **344**, 1039–1042.

Ford R. G. and Sparks D. L. (2000) The nature of Zn precipitates formed in the presence of pyrophyllite. *Environ. Sci. Technol.* **34**, 2479–2483.

Frierdich A. J. and Catalano J. G. (2012a) Controls on Fe(II)-activated trace element release from goethite and hematite. Environ. Sci. Technol. 46, 1519–1526.

Frierdich A. J. and Catalano J. G. (2012b) Fe(II)-mediated reduction and repartitioning of structurally incorporated Cu, Co, and Mn in iron oxides. Environ. Sci. Technol. 46, 11070–11077.

Frierdich A. J., Luo Y. and Catalano J. G. (2011) Trace element cycling through iron oxide minerals during redox-driven dynamic recrystallization. Geology 39, 1083–1086.

Fulda B., Voegelin A., Ehlert K. and Kretzschmar R. (2013a) Redox transformation, solid phase speciation and solution dynamics of copper during soil reduction and reoxidation as affected by sulfate availability. *Geochim. Cosmochim. Acta* **123**, 385–402.

Fulda B., Voegelin A., Maurer F., Christl I. and Kretzschmar R. (2013b) Copper redox transformation and complexation by reduced and oxidized soil humic acid. 1. X-ray absorption spectroscopy study. *Environ. Sci. Technol.* **47**, 10903–10911.

Gärtner P., Ecker A., Fischer R., Linder D., Fuchs G. and Thauer R. K. (1993) Purification and properties of N^5-methyltetrahydromethanopterin: coenzyme M methyltransferase from Methanobacterium thermoautotrophicum. *Eur. J. Biochem.* **213**, 537–545.

George G. N., Gnida M., Bazylinski D. A., Prince R. C. and Pickering I. J. (2008) X-ray absorption spectroscopy as a probe of microbial sulfur biochemistry: The nature of bacterial sulfur globules revisited. *J. Bacteriol.* **190**, 6376–6383.

Glass J. B. and Orphan V. J. (2012) Trace metal requirements for microbial enzymes involved in the production and consumption of methane and nitrous oxide. *Front. Microbiol.* **3**, 1–20.

Glatzel S., Forbrich I., Krüger C., Lemke S. and Gerold G. (2008) Small scale controls of greenhouse gas release under elevated N deposition rates in a restoring peat bog in NW Germany. *Biogeosciences* **5**, 925–935.

Glodowska M., Stopelli E., Schneider M., Rathi B., Straub D., Lightfoot A., Kipfer R., Berg M., Jetten M. and Kleindienst S. (2020) Arsenic mobilization by anaerobic iron-dependent methane oxidation. *Commun. Earth Environ.* **1**, 1–7.

Granger J. and Ward B. B. (2003) Accumulation of nitrogen oxides in copper-limited cultures of denitrifying bacteria. *Limnol. Oceanogr.* **48**, 313–318.

Graulis S., Chateigner D., Downs R. T., Yokochi A. F. T., Quirós M., Lutterotti L., Manakova E., Butkus J., Moeck P. and Le Bail A. (2009) Crystallography Open Database - An open-access collection of crystal structures. *J. Appl. Crystallogr.* **42**, 726–729.

Groffman P. M., Gold A. J. and Jacinthe P. A. (1998) Nitrous oxide production in riparian zones and groundwater. *Nutr. Cycl. Agroecosystems* **52**, 179–186.

Hansel C. M., Lentini C. J., Tang Y., Johnston D. T., Wankel S. D. and Jardine P. M. (2015)

Dominance of sulfur-fueled iron oxide reduction in low-sulfate freshwater sediments. *ISME J.* **9**, 2400–2412.

Harmsen J. (2007) Measuring Bioavailability: From a Scientific Approach to Standard Methods. *J. Environ. Qual.* **36**, 1420–1428.

Hassan N. M., Rasmussen P. E., Dabek-Zlotorzynska E., Celo V. and Chen H. (2007) Analysis of environmental samples using microwave-assisted acid digestion and inductively coupled plasma mass spectrometry: Maximizing total element recoveries. *Water. Air. Soil Pollut.* **178**, 323–334.

Hlaváčová E., Rulík M. and Čáp L. (2005) Anaerobic microbial metabolism in hyporheic sediment of a gravel bar in a small lowland stream. *River Res. Appl.* **21**, 1003–1011.

Hofacker A. F., Behrens S., Voegelin A., Kaegi R., Lösekann-Behrens T., Kappler A. and Kretzschmar R. (2015) *Clostridium* species as metallic copper-forming bacteria in soil under reducing conditions. *Geomicrobiol. J.* **32**, 130–139.

Hofacker A. F., Voegelin A., Kaegi R. and Kretzschmar R. (2013a) Mercury mobilization in a flooded soil by incorporation into metallic copper and metal sulfide nanoparticles. *Environ. Sci. Technol.* **47**, 7739–7746.

Hofacker A. F., Voegelin A., Kaegi R., Weber F. A. and Kretzschmar R. (2013b) Temperature-dependent formation of metallic copper and metal sulfide nanoparticles during flooding of a contaminated soil. *Geochim. Cosmochim. Acta* **103**, 316–332.

Huerta-Diaz M. A., Tessier A. and Carignan R. (1998) Geochemistry of trace metals associated with reduced sulfur in freshwater sediments. *Appl. Geochemistry* **13**, 213–233.

Jacquat O., Voegelin A. and Kretzschmar R. (2009) Soil properties controlling Zn speciation and fractionation in contaminated soils. *Geochim. Cosmochim. Acta* **73**, 5256–5272.

Jacquot J. E., Horak R. E. A., Amin S. A., Devol A. H., Ingalls A. E., Armbrust E. V., Stahl D. A. and Moffett J. W. (2014) Assessment of the potential for copper limitation of ammonia oxidation by Archaea in a dynamic estuary. *Mar. Chem.* **162**, 37–49.

Janot N., Lezama Pacheco J. S., Pham D. Q., O'Brien T. M., Hausladen D., Noël V., Lallier F., Maher K., Fendorf S., Williams K. H., Long P. E. and Bargar J. R. (2016) Physico-chemical heterogeneity of organic-rich sediments in the Rifle Aquifer, CO: Impact on uranium biogeochemistry. *Environ. Sci. Technol.* **50**, 46–53.

Kaplan D. I., Smith R., Parker C. J., Baker M., Cabrera T., Ferguson B. O., Kemner K. M., Laird M., Logan C., Lott J., Manglass L., Martinez N. E., Montgomery D., Seaman J. C., Shapiro M. and Powell B. A. (2020) Uranium attenuated by a wetland 50 years after release into a stream. *ACS Earth Sp. Chem.* **4**, 1360–1366.

Kelly R. A., Andrews J. C. and DeWitt J. G. (2002) An X-ray absorption spectroscopic investigation of the nature of the zinc complex accumulated in Datura innoxia plant tissue culture. Microchem. J. 71, 231–245.

Kelly S. D., Hesterberg D. and Ravel B. (2015) Analysis of soils and minerals using x-ray absorption spectroscopy. In *Methods of Soil Analysis, Part 5: Mineralogical Methods* Soil Science Society of America, Madison. pp. 387–463.

Kirschke S., Bousquet P., Ciais P., Saunois M., Canadell J. G., Dlugokencky E. J., Bergamaschi P., Bergmann D., Blake D. R., Bruhwiler L., Cameron-Smith P., Castaldi S., Chevallier F., Feng L., Fraser A., Heimann M., Hodson E. L., Houweling S., Josse B., Fraser P. J., Krummel P. B., Lamarque J. F., Langenfelds R. L., Le Quéré C., Naik V., O'doherty S., Palmer P. I., Pison I., Plummer D., Poulter B., Prinn R. G., Rigby M., Ringeval B., Santini M., Schmidt M., Shindell D. T., Simpson I. J., Spahni R., Steele L. P., Strode S. A., Sudo K., Szopa S., Van Der Werf G. R., Voulgarakis A., Van Weele M., Weiss R. F., Williams J. E. and Zeng G. (2013) Three decades of global methane sources and sinks. *Nat. Geosci.* **6**, 813–823.

Knorr K. H. and Blodau C. (2009) Impact of experimental drought and rewetting on redox transformations and methanogenesis in mesocosms of a northern fen soil. *Soil Biol. Biochem.* **41**, 1187–1198.

Kocar B. D. and Fendorf S. (2009) Thermodynamic constraints on reductive reactions influencing the biogeochemistry of arsenic in soils and sediments. *Environ. Sci. Technol.* **43**, 4871–4877.

Kopittke P. M., Menzies N. W., de Jonge M. D., Mckenna B. A., Donner E., Webb R. I., Paterson D. J., Howard D. L., Ryan C. G., Glover C. J., Scheckel K. G. and Lombi E. (2011) In situ distribution and speciation of toxic copper, nickel, and zinc in hydrated roots of cowpea. *Plant Physiol.* **156**, 663–673.

Koretsky C. M., Haveman M., Beuving L., Cuellar A., Shattuck T. and Wagner M. (2007) Spatial variation of redox and trace metal geochemistry in a minerotrophic fen. *Biogeochemistry* **86**, 33–62.

Koretsky C. M., Moore C. M., Lowe K. L., Meile C., Dichristina T. J. and Van Cappellen P. (2003) Seasonal oscillation of microbial iron and sulfate reduction in saltmarsh sediments (Sapelo Island, GA, USA). *Biogeochemistry* **64**, 179–203.

LaRowe D. E. and Van Cappellen P. (2011) Degradation of natural organic matter: A thermodynamic analysis. *Geochim. Cosmochim. Acta* **75**, 2030–2042.

Lau G. E., Cosmidis J., Grasby S. E., Trivedi C. B., Spear J. R. and Templeton A. S. (2017) Low-temperature formation and stabilization of rare allotropes of cyclooctasulfur (β-S_8 and

γ-S_8) in the presence of organic carbon at a sulfur-rich glacial site in the Canadian High Arctic. *Geochim. Cosmochim. Acta* **200**, 218–231.

Lett R. E. W. and Fletcher W. K. (1980) Syngenetic sulphide minerals in a copper-rich bog. *Miner. Depos.* **15**, 61–67.

Van Lonkhuyzen R. A. and LaGory K. E. (1994) *Wetlands of Argonne National Laboratory-East DuPage County, Illinois*., Argonne National Lab., IL (United States).

Van Lonkhuyzen R. A., Lagory K. E. and Kuiper J. A. (2004) Modeling the suitability of potential wetland mitigation sites with a geographic information system. *Environ. Manage.* **33**, 368–375.

Lu X., Johs A., Zhao L., Wang L., Pierce E. M. and Gu B. (2018) Nanomolar copper enhances mercury methylation by *Desulfovibrio desulfuricans* ND132. *Environ. Sci. Technol. Lett.* **5**, 372–376.

Luo Y., Giammar D. E., Huhmann B. L. and Catalano J. G. (2011) Speciation of selenium, arsenic, and zinc in Class C fly ash. Energy Fuels 25, 2980–2987.

Manceau A., Marcus M. A. and Tamura N. (2002) Quantitative speciation of heavy metals in soils and sediments by synchrotron X-ray techniques. *Rev. Mineral. Geochemistry* **49**, 341–428.

Manceau A., Marcus M. A., Tamura N., Proux O., Geoffroy N. and Lanson B. (2004) Natural speciation of Zn at the micrometer scale in a clayey soil using X-ray fluorescence, absorption, and diffraction. *Geochim. Cosmochim. Acta* **68**, 2467–2483.

Manceau A. and Nagy K. L. (2012) Quantitative analysis of sulfur functional groups in natural organic matter by XANES spectroscopy. *Geochim. Cosmochim. Acta* **99**, 206–223.

Manceau A., Schlegel M., Nagy K. L. and Charlet L. (1999) Evidence for the formation of trioctahedral clay upon sorption of CCo^{2+} on quartz. *J. Colloid Interface Sci.* **220**, 181–197.

Manceau A., Simionovici A., Lanson M., Perrin J., Tucoulou R., Bohic S., Fakra S. C., Marcus M. A., Bedell J. P. and Nagy K. L. (2013) Thlaspi arvense binds Cu(II) as a bis-(L-histidinato) complex on root cell walls in an urban ecosystem. Metallomics 5, 1674–1684.

Manceau A., Tommaseo C., Rihs S., Geoffroy N., Chateigner D., Schlegel M., Tisserand D., Marcus M. A., Tamura N. and Chen Z. S. (2005) Natural speciation of Mn, Ni, and Zn at the micrometer scale in a clayey paddy soil using X-ray fluorescence, absorption, and diffraction. *Geochim. Cosmochim. Acta* **69**, 4007–4034.

Mantha H., Schindler M. and Hochella M. F. (2019) Occurrence and formation of incidental metallic Cu and CuS nanoparticles in organic-rich contaminated surface soils in Timmins,

Ontario. *Environ. Sci. Nano* **6**, 163–179.

McClain M. E., Boyer E. W., Dent C. L., Gergel S. E., Grimm N. B., Groffman P. M., Hart S. C., Harvey J. W., Johnston C. A., Mayorga E., McDowell W. H. and Pinay G. (2003) Biogeochemical hot spots and hot moments at the interface of terrestrial and aquatic ecosystems. *Ecosystems* **6**, 301–312.

McNear D. H., Chaney R. L. and Sparks D. L. (2007) The effects of soil type and chemical treatment on nickel speciation in refinery enriched soils: A multi-technique investigation. *Geochim. Cosmochim. Acta* **71**, 2190–2208.

Mehlhorn J., Besold J., Lezama Pacheco J. S., Gustafsson J. P., Kretzschmar R. and Planer-Friedrich B. (2018) Copper mobilization and immobilization along an organic matter and redox gradient - Insights from a Mofette Site. *Environ. Sci. Technol.* **52**, 13698–13707.

Merrot P., Juillot F., Noël V., Lefebvre P., Brest J., Menguy N., Guigner J. M., Blondeau M., Viollier E., Fernandez J. M., Moreton B., Bargar J. R. and Morin G. (2019) Nickel and iron partitioning between clay minerals, Fe-oxides and Fe-sulfides in lagoon sediments from New Caledonia. *Sci. Total Environ.* **689**, 1212–1227.

Montargès-Pelletier E., Chardot V., Echevarria G., Michot L. J., Bauer A. and Morel J. L. (2008) Identification of nickel chelators in three hyperaccumulating plants: An X-ray spectroscopic study. Phytochemistry 69, 1695–1709.

Nachtegaal M., Scheidegger A. M., Dähn R., Chateigner D. and Furrer G. (2005) Immobilization of Ni by Al-modified montmorillonite: A novel uptake mechanism. *Geochim. Cosmochim. Acta* **69**, 4211–4225.

Nachtegaal M. and Sparks D. L. (2003) Nickel sequestration in a kaolinite-humic acid complex. *Environ. Sci. Technol.* **37**, 529–534.

Neumann R. B., Blazewicz S. J., Conaway C. H., Turetsky M. R. and Waldrop M. P. (2016) Modeling CH_4 and CO_2 cycling using porewater stable isotopes in a thermokarst bog in Interior Alaska: results from three conceptual reaction networks. *Biogeochemistry* **127**, 57–87.

Newville M. (2001) IFEFFIT: Interactive XAFS analysis and FEFF fitting. *J. Synchrotron Radiat.* **8**, 322–324.

Noël V., Juillot F., Morin G., Marchand C., Ona-Nguema G., Viollier E., Prévot F., Dublet G., Maillot F., Delbes L., Marakovic G., Bargar J. R. and Brown G. E. (2017) Oxidation of Ni-rich mangrove sediments after isolation from the sea (Dumbea Bay, New Caledonia): Fe and Ni behavior and environmental implications. *ACS Earth Sp. Chem.* **1**, 455–464.

Noël V., Morin G., Juillot F., Marchand C., Brest J., Bargar J. R., Muñoz M., Marakovic G.,

Ardo S. and Brown G. E. (2015) Ni cycling in mangrove sediments from New Caledonia. *Geochim. Cosmochim. Acta* **169**, 82–98.

Pansu M. and Gautheyrou J. (2006) *Handbook of soil analysis: Mineralogical, organic and inorganic methods*., Springer Science & Business Media.

Parks J. M., Johs A., Podar M., Bridou R., Hurt R. A., Smith S. D., Tomanicek S. J., Qian Y., Brown S. D., Brandt C. C., Palumbo A. V., Smith J. C., Wall J. D., Elias D. A. and Liang L. (2013) The genetic basis for bacterial mercury methylation. *Science* **339**, 1332–1335.

Prietzel J., Thieme J., Tyufekchieva N., Paterson D., McNulty I. and Kögel-Knabner I. (2009) Sulfur speciation in well-aerated and wetland soils in a forested catchment assessed by sulfur K-edge X-ray absorption near-edge spectroscopy (XANES). *J. Plant Nutr. Soil Sci.* **172**, 393–403.

Ratié G., Garnier J., Calmels D., Vantelon D., Guimarães E., Monvoisin G., Nouet J., Ponzevera E. and Quantin C. (2018) Nickel distribution and isotopic fractionation in a Brazilian lateritic regolith: Coupling Ni isotopes and Ni K-edge XANES. *Geochim. Cosmochim. Acta* **230**, 137–154.

Raj C. J., Joshi R. K. and Varma K. B. R. (2011) Synthesis from zinc oxalate, growth mechanism and optical properties of ZnO nano/micro structures. Cryst. Res. Technol. 46, 1181–1188.

Ravel B. and Newville M. (2005) ATHENA, ARTEMIS, HEPHAESTUS: Data analysis for X-ray absorption spectroscopy using IFEFFIT. *J. Synchrotron Radiat.* **12**, 537–541.

Riscassi A., Miller C. and Brooks S. (2016) Seasonal and flow-driven dynamics of particulate and dissolved mercury and methylmercury in a stream impacted by an industrial mercury source. *Environ. Toxicol. Chem.* **35**, 1386–1400.

Rozan T. F., Taillefert M., Trouwborst R. E., Glazer B. T., Ma S., Herszage J., Valdes L. M., Price K. S. and Luther G. W. (2002) Iron-sulfur-phosphorus cycling in the sediments of a shallow coastal bay: Implications for sediment nutrient release and benthic macroalgal blooms. *Limnol. Oceanogr.* **47**, 1346–1354.

Rudnick R. L. and Gao S. (2003) Composition of the continental crust In *Treatise on Geochemistry* (eds. K.K. Turekian and H.D. Holland). In *Treatise on Geochemistry. Pergamon, Oxford* Elsevier. pp. 1–64.

Schaefer J. K., Kronberg R. M., Morel F. M. M. and Skyllberg U. (2014) Detection of a key Hg methylation gene, *hgcA*, in wetland soils. *Environ. Microbiol. Rep.* **6**, 441–447.

Schlegel M. L., Manceau A., Charlet L., Chateigner D. and Hazemann J. L. (2001) Sorption of metal ions on clay minerals. III. Nucleation and epitaxial growth of Zn phyllosilicate on the edges of hectorite. *Geochim. Cosmochim. Acta* **65**, 4155–4170.

Schönheit P., Moll J. and Thauer R. K. (1979) Nickel, cobalt, and molybdenum requirement for growth of *Methanobacterium thermoautotrophicum*. *Arch. Microbiol.* **123**, 105–107.

Schwartz G. E., Olsen T. A., Muller K. A. and Brooks S. C. (2019) Ecosystem controls on methylmercury production by periphyton biofilms in a contaminated stream: Implications for predictive modeling. *Environ. Toxicol. Chem.* **38**, 2426–2435.

Schwertmann U. and Cornell R. M. (2000) Iron Oxides in the Laboratory: Preparation and Synthesis. VCH Publishers, New York.

Segarra K. E. A., Schubotz F., Samarkin V., Yoshinaga M. Y., Hinrichs K. U. and Joye S. B. (2015) High rates of anaerobic methane oxidation in freshwater wetlands reduce potential atmospheric methane emissions. *Nat. Commun.* **6**, 7477.

Siebecker M. G., Chaney R. L. and Sparks D. L. (2018) Natural speciation of nickel at the micrometer scale in serpentine (ultramafic) topsoils using microfocused X-ray fluorescence, diffraction, and absorption. *Geochem. Trans.* **19**, 14.

Siebecker M. G., Chaney R. L. and Sparks D. L. (2017) Nickel speciation in several serpentine (ultramafic) topsoils via bulk synchrotron-based techniques. *Geoderma* **298**, 35–45.

Singer M. B., Harrison L. R., Donovan P. M., Blum J. D. and Marvin-DiPasquale M. (2016) Hydrologic indicators of hot spots and hot moments of mercury methylation potential along river corridors. *Sci. Total Environ.* **568**, 697–711.

Skyllberg U. (2008) Competition among thiols and inorganic sulfides and polysulfides for Hg and MeHg in wetland soils and sediments under suboxic conditions: Illumination of controversies and implications for MeHg net production. *J. Geophys. Res. Biogeosciences* **113**, G00C03.

Southworth G., Mathews T., Greeley M., Peterson M., Brooks S. and Ketelle D. (2013) Sources of mercury in a contaminated stream-implications for the timescale of recovery. *Environ. Toxicol. Chem.* **32**, 764–772.

Sparks D. L., Page A. L., Helmke P. A., Loeppert R. H., N. S. P., Tabatabai M. A., T. J. C. and Sumner M. E. (1996) *Methods of soil analysis. Part 3: Chemical Methods*., Soil Science Society of America, Madison.

Spratt H. G. and Morgan M. D. (1990) Sulfur cycling in a cedar-dominated, freshwater wetland. *Limnol. Oceanogr.* **35**, 1586–1593.

St Louis V. L., Rudd J. W. M., Kelly C. A., Beaty K. G., Bloom N. S. and Flett R. J. (1994) Importance of wetlands as sources of methyl mercury to boreal forest ecosystems. *Can. J. Fish. Aquat. Sci.* **51**, 1065–1076.

Sun L., Zheng C., Yang J., Peng C., Xu C., Wang Y., Feng J. and Shi J. (2016) Impact of sulfur (S) fertilization in paddy soils on copper (Cu) accumulation in rice (*Oryza sativa* L.) plants under flooding conditions. *Biol. Fertil. Soils* **52**, 31–39.

Swanner E. D., Webb S. M. and Kappler A. (2019) Fate of cobalt and nickel in mackinawite during diagenetic pyrite formation. *Am. Mineral.* **104**, 917–928.

Thauer R. K. (1998) Biochemistry of methanogenesis: a tribute to Marjory Stephenson:1998 Marjory Stephenson Prize Lecture. *Microbiology* **144**, 2377–2406.

Thirumalai K., Singh A. and Ramesh R. (2011) A MATLAB^{TM} code to perform weighted linear regression with (correlated or uncorrelated) errors in bivariate data. *J. Geol. Soc. India* **77**, 377–380.

Tian H., Chen G., Lu C., Xu X., Ren W., Zhang B., Banger K., Tao B., Pan S., Liu M., Zhang C., Bruhwiler L. and Wofsy S. (2015) Global methane and nitrous oxide emissions from terrestrial ecosystems due to multiple environmental changes. *Ecosyst. Heal. Sustain.* **1**, 1–20.

Vile M. A., Bridgham S. D., Wieder R. K. and Novák M. (2003) Atmospheric sulfur deposition alters pathways of gaseous carbon production in peatlands. *Global Biogeochem. Cycles* **17**, 1058.

Voegelin A., Jacquat O., Pfister S., Barmettler K., Scheinost A. C. and Kretzschmar R. (2011) Time-dependent changes of zinc speciation in four soils contaminated with zincite or sphalerite. *Environ. Sci. Technol.* **45**, 255–261.

Voegelin A., Pfister S., Scheinost A. C., Marcus M. A. and Kretzschmar R. (2005) Changes in zinc speciation in field soil after contamination with zinc oxide. *Environ. Sci. Technol.* **39**, 6616–6623.

Webb S. M. (2005) SIXpack: A graphical user interface for XAS analysis using IFEFFIT. *Phys. Scr. T* **T115**, 1011–1014.

Webb S. M. and Gaillard J. F. (2015) Zinc speciation in contaminated sediments: quantitative determination of zinc coordination by X-ray absorption spectroscopy. *Aquat. Geochemistry* **21**, 295–312.

Weber F. A., Voegelin A., Kaegi R. and Kretzschmar R. (2009a) Contaminant mobilization by metallic copper and metal sulphide colloids in flooded soil. *Nat. Geosci.* **2**, 267–271.

Weber F. A., Voegelin A. and Kretzschmar R. (2009b) Multi-metal contaminant dynamics in temporarily flooded soil under sulfate limitation. *Geochim. Cosmochim. Acta* **73**, 5513–5527.

Weber K. A., Urrutia M. M., Churchill P. F., Kukkadapu R. K. and Roden E. E. (2006) Anaerobic redox cycling of iron by freshwater sediment microorganisms. *Environ. Microbiol.* **8**, 100–113.

Wieder R. K. and Lang G. E. (1988) Cycling of inorganic and organic sulfur in peat from Big Run Bog, West Virginia. *Biogeochemistry* **5**, 221–242.

Wieder R. K., Lang G. E. and Granus V. A. (1985) An evaluation of wet chemical methods for quantifying sulfur fractions in freshwater wetland peat. *Limnol. Oceanogr.* **30**, 1109–1115.

Williams A. G. B., Scheckel K. G., McDermott G., Gratson D., Neptune D. and Ryan J. A. (2011) Speciation and bioavailability of zinc in amended sediments. *Chem. Speciat. Bioavailab.* **23**, 143–154.

Woodward G. L., Peacock C. L., Otero-Fariña A., Thompson O. R., Brown A. P. and Burke I. T. (2018) A universal uptake mechanism for cobalt(II) on soil constituents: Ferrihydrite, kaolinite, humic acid, and organo-mineral composites. *Geochim. Cosmochim. Acta* **238**, 270–291.

Worms I., Simon D. F., Hassler C. S. and Wilkinson K. J. (2006) Bioavailability of trace metals to aquatic microorganisms: importance of chemical, biological and physical processes on biouptake. *Biochimie* **88**, 1721–1731.

Xia B., Qiu H., Knorr K. H., Blodau C. and Qiu R. (2018) Occurrence and fate of colloids and colloid-associated metals in a mining-impacted agricultural soil upon prolonged flooding. *J. Hazard. Mater.* **348**, 56–66.

Yang J., Zhu S., Zheng C., Sun L., Liu J. and Shi J. (2015) Impact of S fertilizers on pore-water Cu dynamics and transformation in a contaminated paddy soil with various flooding periods. *J. Hazard. Mater.* **286**, 432–439.

Yang Z., Fang W., Lu X., Sheng G. P., Graham D. E., Liang L., Wullschleger S. D. and Gu B. (2016) Warming increases methylmercury production in an Arctic soil. *Environ. Pollut.* **214**, 504–509.

Yoon S. joung, Yáñez C., Bruns M. A., Martínez-Villegas N. and Martínez C. E. (2012) Natural zinc enrichment in peatlands: Biogeochemistry of ZnS formation. *Geochim. Cosmochim. Acta* **84**, 165–176.

Zarnetske J. P., Haggerty R., Wondzell S. M. and Baker M. A. (2011) Dynamics of nitrate production and removal as a function of residence time in the hyporheic zone. *J. Geophys. Res. Biogeosciences* **116**, G01025.

Zhang Z., Zimmermann N. E., Stenke A., Li X., Hodson E. L., Zhu G., Huang C. and Poulter B. (2017) Emerging role of wetland methane emissions in driving 21st century climate change.

Proc. Natl. Acad. Sci. U. S. A. **114**, 9647–9652.

Zhao C. M., Campbell P. G. C. and Wilkinson K. J. (2016) When are metal complexes bioavailable? *Environ. Chem.* **13**, 425–433.

Zheng K., Ngo P. D., Owens V. L., Yang X. P. and Mansoorabadi S. O. (2016) The biosynthetic pathway of coenzyme F430 in methanogenic and methanotrophic archaea. *Science* **354**, 339–342.

CHAPTER 4

EVALUATION OF POTENTIAL NICKEL LIMITATIONS ON METHANE PRODUCTION FROM MARSH AND RIPARIAN WETLAND SOILS

4.1 ABSTRACT

Freshwater wetland soils are foci of biogeochemical cycling as they serve as key sources of methane to the atmosphere. An array of metalloenzymes is essential to anaerobic microbial carbon transformations. Nickel is notably recognized as playing key roles in the enzymatic pathways of methanogenesis. Low availability of trace metals limits microbial element cycling in laboratory studies, but the occurrence of such limitations in natural subsurface aquatic systems is poorly understood. Microcosm incubation studies were carried out using two distinct wetland soils, one from a marsh wetland and the second from a riparian wetland, to explore the effect of dissolved Ni concentrations on methane production. Dissolved Ni concentrations were substantially lower than the optimal range for methanogenesis identified in pure culture studies but both wetland soils continuously produced methane over a 7 to 10 weeks incubation period. Methane production by the marsh wetland soil did not change when dissolved Ni concentrations were increased to 0.5 to 4 µM through amendment to parallel incubations, indicating a lack of Ni limitation. In contrast, amending the riparian wetland soil to increase dissolved Ni concentrations to 0.4 to 1.3 µM stimulated up to a ~75% increase in methane production from 3 to 10 weeks of incubation time. The water at the marsh wetland contained substantially greater dissolved sulfate concentration than for the riparian wetland (576 µM versus 8 µM), which may have impacted apparent methane production through substrate competition or promotion of anaerobic methane oxidation. Incubations of marsh wetland soils in sulfate-free water also displayed no evidence for Ni limitations. This study indicates that methane production by freshwater wetland soils displays variable responses to changing Ni availability.

4.2 INTRODUCTION

Aquatic systems, especially freshwater wetlands, are the single largest natural source of the greenhouse gas methane (CH_4) to the atmosphere (Chen and Prinn, 2006; Bousquet et al., 2011; Kirschke et al., 2013). In addition, these terrestrial ecosystems are the primary control on the interannual variability of CH_4 emissions (Bousquet et al., 2006; Dlugokencky et al., 2009). Global climate models predict that CH_4 emissions will increase as global mean temperature rises because of greater inundation from increased rainfall as well as the thawing of large regions of the Arctic underlain by permafrost (Ringeval et al., 2011). However, regional and global models of methane biogeochemistry have large uncertainties in their prediction of future CH_4 emissions (Bohn and Lettenmaier, 2010; Wania et al., 2010; Avis et al., 2011; Hodson et al., 2011; Hopcroft et al., 2011; Riley et al., 2011; Ringeval et al., 2011; Spahni et al., 2011; Ringeval et al., 2012; Tian et al., 2012; Melton et al., 2013; Ringeval et al., 2013; Zürcher et al., 2013), and require improved descriptions of the environmental controls on CH_4 production (Riley et al., 2011; Tang et al., 2013; Xu et al., 2014). The large radiative forcing induced by increasing CH_4 concentrations in the atmosphere makes it critical to understand the chemical and physical parameters that affect CH_4 production in wetlands.

CH_4 is produced in the anaerobic subsurface of wetlands through microbial carbon cycling (Serrano-Silva et al., 2014). Temperature is a major control on CH_4 production and recent work has shown that methanogenesis in terrestrial ecosystems displays a high activation energy (Yvon-Durocher et al., 2014), indicating that increasing temperature will result in a substantial increase in the CH_4 emissions from wetlands. However, it has also been shown that this relationship overpredicts the temperature response of CH_4 production in many systems (Hoehler and Alperin, 2014), suggesting that other substantial limitations on methanogenesis are present. A potentially

important limitation on CH_4 production in wetlands that has been largely overlooked to date is trace metal availability. Methanogens have exceptionally high enzymatic requirements for trace metals (Fe, Ni, Co, Zn, and Mo or W) (Patel et al., 1978; Thauer, 1998; Glass and Orphan, 2012; Glass et al., 2014). Laboratory studies, primarily involving pure cultures of methanogens or anaerobic bioreactors, have shown that limited availability of trace metals inhibits methanogenesis (Williams et al., 1986; Kida et al., 2001; Demirel and Scherer, 2011; Glass et al., 2014) but such limitations have not been investigated extensively for wetland soils. Amendment of peat from five wetlands with a mixture of Fe^{3+}, Ni^{2+}, and Co^{2+} showed no systematic effects on CH_4 production (Basiliko and Yavitt, 2001), but this work may have been compromised by the addition of ferric iron, which serves as a competing terminal electron acceptor. A separate study of peatland soils found no evidence for trace metal (Ni, Co, Cu, or Fe) limitations on CH_4 production, but that study first attempted to remove available metals from the soil using toxic levels of dissolved Pb^{2+} (2 mM) (Keller and Wade, 2018). Notably, both of these studies primarily examined acidic peat soils (pH ~4), which may have distinct metal availability from circumneutral aquatic systems. A recent study of sediments from a tidal-fluvial bar deposit observed a 20 to 50% increase in CH_4 production following addition of Cu, Mo, or Fe, both individually and in various mixtures (Giannopoulos et al., 2020). However, the incubations were only 96 h in duration, far shorter than typically explored (Chowdhury et al., 2015), the study did not report dissolved metal concentrations, and neither Co nor Ni were investigated despite their essential role in methanogenesis (Glass and Orphan, 2012). The accumulation of sulfate has also been shown to suppress methane production (Watson and Nedwell, 1998; Gauci et al., 2002; Vile et al., 2003; Gauci et al., 2004), because sulfate reducing bacteria compete with methanogens for substrates (Sela-Adler et al., 2017) while sulfate also serves as an electron acceptor for anaerobic oxidation

of methane (AOM) (Segarra et al., 2015). Although the effect of sulfate suppression on methane production has not been considered here, the presence of sulfate concentrations elevated above those observed in typical freshwater systems could potentially affect the influence of Ni limitation. Therefore, it is also key to study the effect of sulfate on trace metal limitation in wetlands.

Despite fundamental biochemical evidence that trace metal availability is an important control on methanogenesis, it is still unclear whether such limitations exist in natural and human-impacted wetlands. Trace metal contents in wetland soils are generally low but atmospheric and hydrologic inputs may affect their abundances (Koretsky et al., 2006). Terrestrial wetlands are diverse in their parent materials, show complex variations in trace metal distributions, and may be susceptible to metal leaching because of the higher solubility of trace metals under anoxic conditions (Roden and Wetzel, 1996; Loeb et al., 2007; Antcibor et al., 2014). The current understanding of metal availability in wetlands and the resulting impact on CH_4 fluxes is inadequate to predict how anthropogenic perturbations (e.g., land use changes, industrial emissions, climate change) affect greenhouse gas production. In addition, both inherited metal availability and global trace element cycling could lead to regional differences in CH_4 fluxes from these systems. Parameterization of models (e.g., Tang et al., 2010; Wania et al., 2010; Riley et al., 2011; Ringeval et al., 2011; Spahni et al., 2011; Ringeval et al., 2012; Tian et al., 2012) to account for trace metal limitations cannot be made until the role of metal availability in controlling methanogenesis in wetlands is determined.

In order to assess how trace metals alter methane production in aquatic systems, a series of microcosm incubations were conducted. These incubations explored the impact of Ni addition on CH_4 production in both marsh wetland and riparian wetland soils. Soils were suspended in an aqueous solution having the same major elements concentrations as surface waters overlying the

wetland soils at both field sites. Gas samples were collected and measured chromatographically over the course to compare methane production under different Ni amendments. The supernatant fluid was analyzed to determine the dissolved Ni concentration in each experiment.

4.3 MATERIALS AND METHODS

4.3.1 Sites Description

Two wetlands were investigated to contrast marsh and riparian systems; these sites are described in detail in a previous study (Yan et al., 2022). Marsh wetlands at Argonne National Laboratory (ANL) in Lemont, Illinois, U.S.A. were sampled in September 2020. Two different locations were sampled, and the sample used in this study is from the surface layer (0-5 cm) layer of the Marsh 1 site (41°42’19.69”N 87°59’55.04”W WGS 84). It contained shallow surface water back in the year of 2019 but became unsaturated during prolonged dry periods. The second site is a riparian wetland in the Tims Branch (TB) watershed at Savannah River Site in Aiken County, South Carolina, U.S.A. Samples were collected in October 2020. The soil samples used in this study were collected at the “Riparian 2” location (33°20'9.24"N 81°43'8.04"W WGS 84) (Yan et al., 2022). This forest site varies in its water inundation throughout the year and in summer may lack surface water for short periods of time.

4.3.2 Solid Phase Characterization

Soils were mixed and homogenized in an anaerobic chamber containing 3% of hydrogen and 97% of nitrogen. Total nitrogen, carbon, and sulfur contents were determined using these dried soil samples by combustion elemental analysis using an Elementar vario MACRO cube CHNS analyzer. The total metal concentrations in the soils and sediments were estimated using a

microwave digestion analysis method (Hassan et al., 2007). Details of soil sample processing and analysis method have been descried in Yan et al., 2022.

4.3.3 Microcosm Incubation Preparation

Artificial site water was made to replicate the major element compositions of surface waters overlying the sampled soils from the wetland sites (Yan et al., 2022). The compositions of the artificial site waters are shown in Table 4.1.

Table 4.1. Artificial site water compositions.

Soil	Mg^{2+} (µM)	Ca^{2+} (µM)	K^{+} (µM)	Na^{+} (µM)	Cl^{-} (µM)	SO_4^{2-} (µM)
Marsh wetland	288	366	165	170	413	576
Riparian wetland	27	25	5	60	155	8
Marsh wetland sulfate-free	288	366	165	170	989	0

All materials used in the microcosm study were autoclaved at 121 °C for 30 min before use. Artificial site water for the marsh wetland study was made at Ni concentrations of 0, 670, 780, 890, and 1090 µM by addition of $NiCl_2 \cdot 6H_2O$. These additions correspond to 0, 6.7, 7.8, 8.9, and 10.9 µmol Ni/g soil, respectively (see experimental proportions of soil and water below). For the riparian wetland study, water was made at Ni concentrations of 0, 25, 50, 75, and 100 µM, corresponding to 0, 0.25, 0.5, 0.75, and 1.0 µmol Ni/g soil, respectively. The added Ni concentrations were determined by preliminary metal uptake measurement to identify the amount needed to produce optimal dissolved Ni concentrations (0.1 -2 µM) for methanogenesis (Glass and Orphan, 2012) after accounting for the effect of adsorption to the soil materials. An

additional study of the marsh wetland soil explored the impact of removing sulfate from the site water to determine if this was potentially masking the effects of potential metal limitations. For this study, a different batch of marsh wetland artificial water was made by replacing SO_4^{2-} with Cl^-, with the concentration used accounting for charge differences. This experiment utilized a different homogenized subsample of the soil core from the march wetland site, and this displayed slightly lower nickel adsorption. Dissolved Ni concentrations in the artificial site water from this sulfate study were 0 µM, 50 µM, 100 µM, 150 µM, and 200 µM, corresponding to 0, 0.5, 1.0, 1.5, and 2.0 µmol Ni/g soil, respectively. These concentration values were also chosen by the preliminary metal uptake experiment, though the amount of Ni needed was very different from the first marsh wetland incubation study. Samples with original artificial site water (containing 576 µM SO_4^{2-}) was also prepared with Ni concentrations 0 µM, 50 µM, and 100 µM for comparison purposes because methane production may differ for this second soil sample.

For each microcosm sample, a certain amount of wet soil (~ 1.2 g, equivalent to 1 g of dry soil) was mixed with 10 mL of artificial site water in a serum bottle. After mixing, serum bottles were sealed with blue butyl rubber stopper and fastened with aluminum crimp cap. pH was determined before and after incubation. The headspace was evacuated and flushed with ultrahigh purity N_2 to ensure anoxic conditions and also for the purpose to eliminate H_2. After nitrogen flushing, samples were shaken by hand and by the Vortex Mixer to ensure homogeneous mix. Serum bottles were then wrapped by aluminum foils and stored upside down in the drawer at room temperature (22 °C) to avoid exposure of sunlight. For gas sampling, a 5 mL Halmiton SUPELCO #1005 gastight syringe was used with an Male Luer Lock to Removable Needle RN Hub (L) Adapter attached to it for a stronger needle connection. BD PrecisonGlide needles (23 gauge, 1 inch length) were used for gas sampling. On each sampling

day, 3 mL of gas were taken from the serum bottle into the gas-tight syringe, which was then injected into a 3 mL pre-evacuated vial (Labco Exetainer). Then 3 mL of ultrahigh purity N_2 was injected back to the serum bottles to maintain the original gas pressure and prevent formation of a vacuum. Gas samples were stored in the dark until analysis. Previous work has shown that Exetainer vials maintain constant gas compositions for at least 6 weeks during storage and contain residual CH_4 concentrations <0.3 ppm (Sturm et al., 2015).

Gas samples were taken in the initial study of the marsh wetland soil on the 2nd, 4th, 6th, 8th, 10th, 13th, 17th, 20th, 23th, 25th, 28th, 30th, 35th, 38th, 40th, and 50th day. The sampling schedule for riparian wetland soil was set as 2nd, 4th, 6th, 8th, 10th, 12th, 15th, 17th, 20th, 22th, 25th, 28th, 30th, 34th, 41th, 44th, 48th, 57th, and 71th day. In second march soil study exploring removal of sulfate from the system, gas samples were taken on the 2nd, 4th, 6th, 8th, 11th, 14th, 17th, 22th, 27th, 33th, 38th, 45th, and 51th day.

4.3.4 Fluid Analysis

After the full experimental duration, the microcosm serum bottles were brought back into the anaerobic chamber for water sampling. The fluids from each bottle were transferred into centrifuged tubes and centrifuged at 4500 rpm for 10 minutes to remove suspended fine particles. The supernatant was then filtered by the 0.22 μm polypropylene syringe filters. 5 mL of the supernatant was acidified with 2% trace metal grade nitric acid for inductively-coupled plasma mass spectrometry (ICP-MS) analysis of dissolve metal concentrations. Dissolved Ni, Co, Cu, Zn, and Fe concentrations were measured by ICP-MS using a Thermo ICAP Q instrument. Dissolved Co concentrations from marsh and riparian incubations were not reported in this version of manuscript due to analysis problem. Uncertainties in the measured concentrations

were calculated from the standard deviation of triplicate samples. The other portion of the supernatant was retained unacidified for anion analysis.

4.3.5 Analysis of Gas Composition

Headspace gas concentrations were determined using gas chromatography. Measurements were made using a Thermo Trace 1310 gas chromatograph (GC) equipped with a pulsed discharge detector (PDD) and a TriPlus RSH headspace autosampler. The GC used He carrier gas (99.9999% purity, Airgas) at a flow rate of 30 mL per min and ultrahigh purity N_2 as the flush gas for the autosampler. Gas sample components were separated using a Supelco Carboxen 1010 Plot Fused Silica capillary column (30m x 0.32 mm). Gas samples of 1 mL volume were introduced into the GC using a split injection (split rate of 10:1) with the inlet heated to 130 °C. The column was maintained at 50 °C for 7.5 min after injection and was then ramped to 130 °C at a rate of 20 °C per min; this temperature was then maintained for 2 min. The PDD was maintained at 150 °C during the measurements. The GC was calibrated using standards at target CH_4 concentrations of 25 ppm, 50 ppm, 75 ppm, 100 ppm, 500 ppm, 1000 ppm, 2000 ppm, 3000 ppm, 4000 ppm, and 5000 ppm. These were prepared from volumetric mixtures of certified standards containing 100 ppm or 1% CH_4 and ultrahigh purity N_2. The reported methane compositions are averages and standard deviations from triplicate samples. Corrections were made for the amount of CH_4 dissolved in water using Henry's Law equation and for dilution cause by removal of 3 mL of headspace during sampling followed by replacement with an equal volume of N_2.

4.4 RESULTS AND DISCUSSION

4.4.1 Solid Phase Soil Composition

In this study, the total carbon contents varied among the sites (Figure 4.1). Soils from marsh wetlands displayed higher concentrations while the riparian ones showed less. Marsh 1 has 9.8±0.2 wt.% carbon while Riparian 2 only has 3.6±0.5 wt.%. Nitrogen showed a similar pattern of variation as carbon despite that nitrogen concentrations were a magnitude lower than carbon. The sulfur contents in the marsh wetlands were higher than the riparian wetlands, with Marsh 1 the highest. Riparian wetland soils have similar amount of sulfur (~0.05 wt. %), while sulfur contents in the marsh wetlands varied more. Iron contents were similar among all samples except for location Riparian 2, which contained less than half of the iron of the other locations.

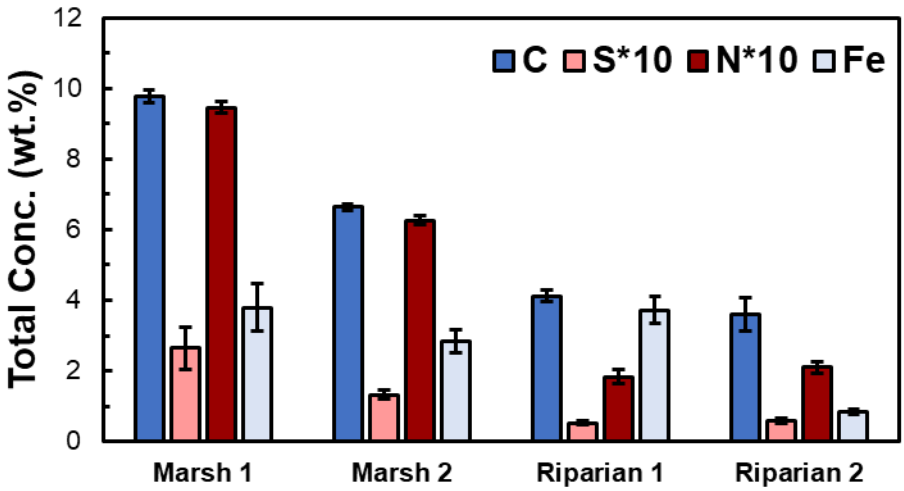

Figure 4.1. Total carbon, sulfur, and iron contents in the surface layer of the soils at the study sites. The error bars reflect the standard deviations of the triplicate analyses of the individual cores.

Solid-phase trace metal concentrations (Figure 4.2) were determined by microwave-assisted acid digestion. Trace metal concentrations follow the trend of: Zn > Cu ≈ Ni > Co. Variations in the abundance of each trace metal among the field sites generally tracked one another. The marsh wetlands contained the higher solid-phase Cu, Ni, and Zn contents. The riparian wetlands' lower solid phase trace metal contents are consistent with the low abundance of low major element (C, S, and Fe) concentrations. The concentrations of the trace metals (0.9 to 12 μg g^{-1} Co, 7 to 45 μg g^{-1} Ni, 21 to 56 μg g^{-1} Cu, and 23 to 223 μg g^{-1} Zn) were in a similar range of the geological background (Rudnick and Gao, 2003).

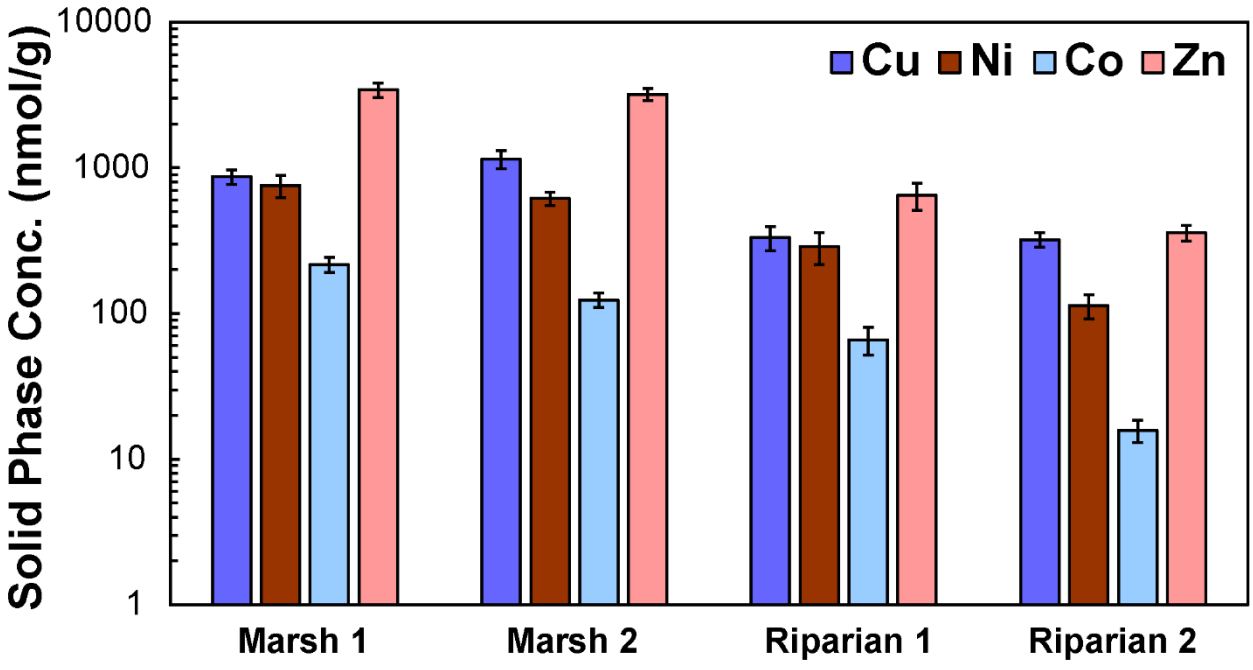

Figure 4.2. Total solid phase trace metal concentrations of the study sites. The error bars reflect the calibration-derived uncertainties for samples from individual cores.

4.4.2 Riparian Wetland Soils Incubation

The microcosm study using the riparian wetland soils continuously produced CH_4 over the 71 days of incubation, although CH_4 production was slowed down after ~15 days (Figure 4.3). There was substantial variability between triplicate samples, but the soil clearly displayed a substantial response to Ni addition. Samples with 0.25 µmol/g Ni addition produces most methane (2.5 µmol/g), while samples with no Ni addition yield the least amount of methane (1.5±0.4 µmol/g). Greater Ni addition did not enhance CH_4 production to the same extent, but these still generated more CH_4 than the sample with no Ni addition.

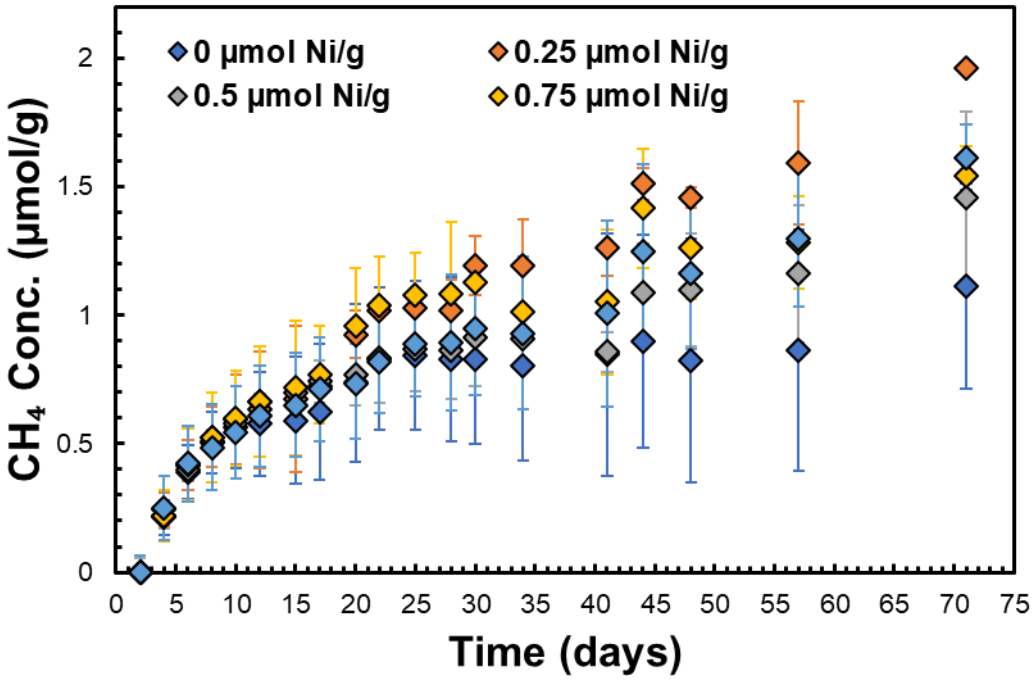

Figure 4.3. Cumulative methane produced from the riparian wetland soils at 5 different Ni concentrations in 71 days incubation. Compositions are averages and standard deviations from triplicate samples; correction of dissolved gas and gas remover during sampling was included.

Dissolved Ni concentration with no metal addition in the riparian soils was ~0.1 µM, Ni addition brought this to as high as 1.3±0.2 µM (Figure 4.4). Dissolved Zn concentrations were not affected by the addition of Ni and were within the range of ~0.3 to ~0.4 µM for all samples. Dissolved Cu concentrations increased from 0.4±0.1 µM to 0.9±0.8 µM with increasing Ni addition. This may reflect competitive binding between these two metals, although the Cu concentration varied substantially between samples and this may not be a statistically significant trend. Dissolved Fe concentrations varied but showed no meaningful trend with increasing Ni addition. The pH decreased slightly during incubation for the samples with no to low Ni addition levels (Figure 4.5A).

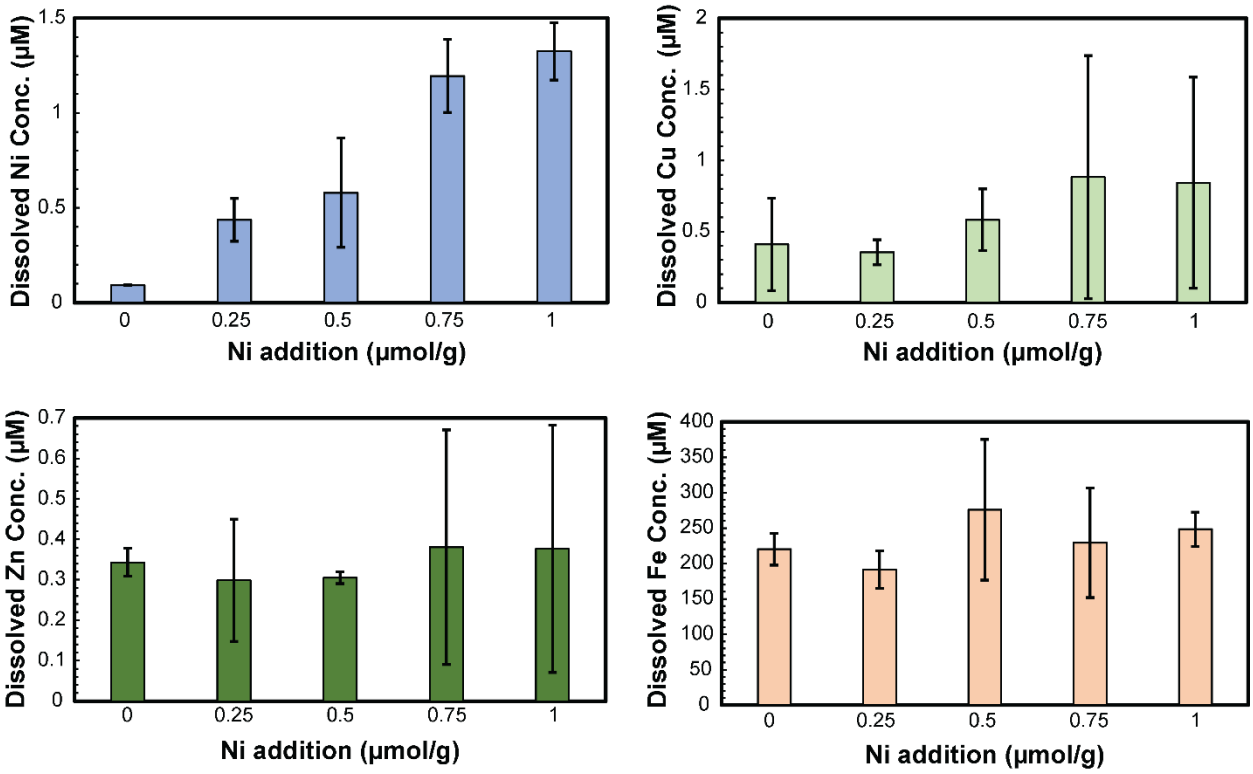

Figure 4.4. Dissolved Cu, Ni, Zn, and Fe concentrations in the final filtrate solutions from the riparian wetland soil after 71 d incubation.

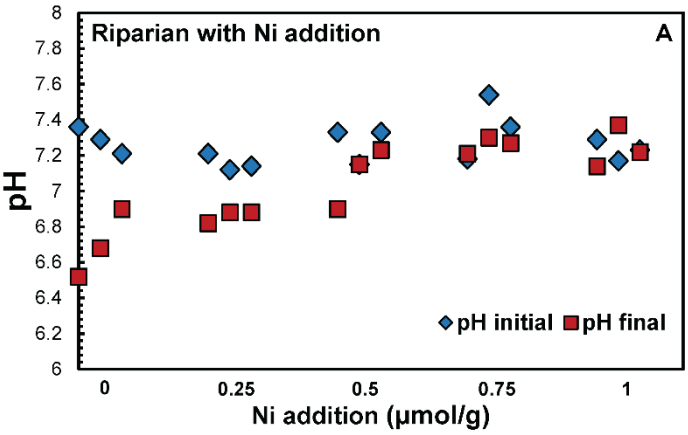
Riparian with Ni addition
A
pH
8
7.8
7.6
7.4
7.2
7
6.8
6.6
6.4
6.2
6
pH initial
pH final
0
0.25
0.5
0.75
1
Ni addition (µmol/g)

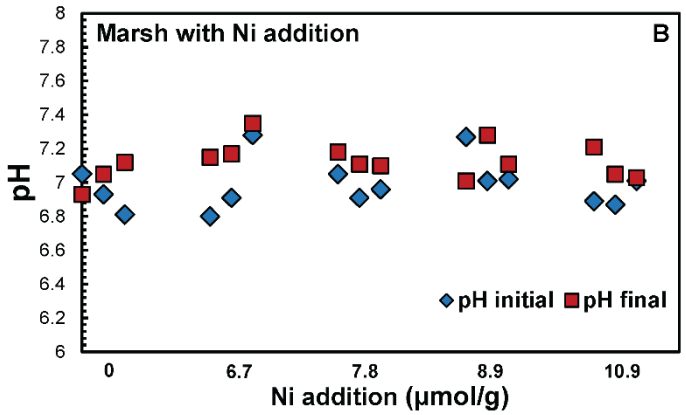
Marsh with Ni addition
B
pH
8
7.8
7.6
7.4
7.2
7
6.8
6.6
6.4
6.2
6
pH initial
pH final
0
6.7
7.8
8.9
10.9
Ni addition (µmol/g)

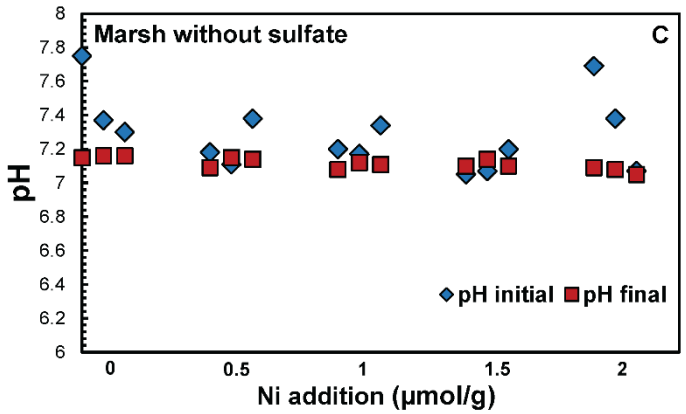
Marsh without sulfate
C
pH
8
7.8
7.6
7.4
7.2
7
6.8
6.6
6.4
6.2
6
pH initial
pH final
0
0.5
1
1.5
2
Ni addition (µmol/g)

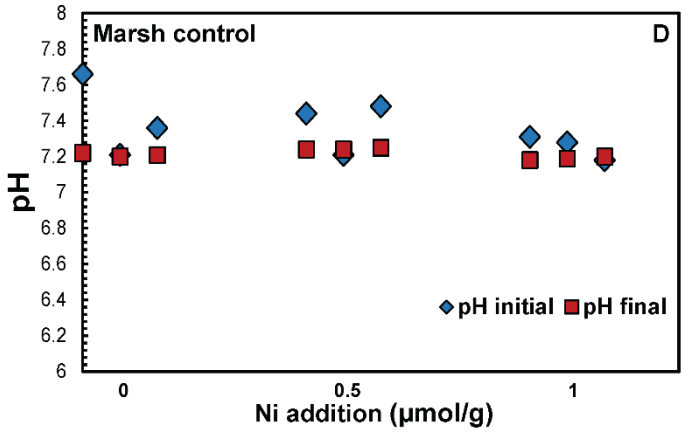
Marsh control
D
pH
8
7.8
7.6
7.4
7.2
7
6.8
6.6
6.4
6.2
6
pH initial
pH final
0
0.5
1
Ni addition (µmol/g)

Figure 4.5. pH change in (A) Riparian wetland microcosm incubation study (B) Marsh wetland microcosm incubation (C) and (D) Secondary incubations of the marsh wetland soil with and without sulfate. Triplicate results were shown for each Ni addition concentration. The plotting pH range was scaled to 6-8 for comparison.

4.4.3 Marsh Wetland Soils Incubation

Incubation of soils from the marsh wetland yield approximately 11.6±0.4 to 12.4±0.4 μmol/g methane after 50 d (Figure 4.6). Total CH_4 production produced from this site was six times of what was observed for the riparian wetlands (Figure 4.3). The primary cause for the different methane production is likely the greater carbon content of the soil at the Marsh 1 site, as Riparian 2 has only one-third of the carbon content as Marsh 1 (Figure 4.1). Although dissolved organic carbon was not measured in the soil waters of this study, it is known from our previous study that DOC content at the Marsh 1 site is approximately 3 times greater than at the Riparian 2 site (Yan et al., 2022). This suggests that available carbon for methanogenesis is more abundant in the marsh wetland.

Other factors may also contribute to greater methane production in incubations of the marsh wetland soil. While this soil has greater total Fe content, it is unclear if this may enhance or inhibit methanogenesis. Iron bioavailability is essential for methanogenesis (Glass and Orphan, 2012) and greater Fe content may thus enhance methane production. However, some prior studies have not observed iron availability to limit methane production (Giannopoulos et al., 2020). Iron oxide reduction may also suppress sulfate reduction and methanogenesis, and can also be coupled to anaerobic oxidation of methane in soils and sediments (Lovley and Phillips, 1987; Roden and Wetzel, 1996; Egger et al., 2017). Quantitative Fe XANES and EXAFS speciation study has revealed more than 20% Fe was present in iron oxide form in Riparian 2

samples, while Marsh 1 soils contain no iron oxide species (Yan et al., 2022), though Fe(III) in clay minerals may still be accessible for microbial reduction. These presence of iron oxides in the riparian wetland soils may thus have suppressed methanogenesis. Moreover, methanogenesis may also be limited by fermentation rates, which are affected by nitrogen availability (Valentine et al., 1994). The marsh wetlands contains greater solid-phase nitrogen content as well as greater dissolved and extractable nitrate and ammonium (Yan et al., 2022), which should favor increased fermentation rates.

In contrast with what was observed in the riparian wetland, little variation in CH_4 production is observed for different Ni addition levels to the marsh soil. No systematic trends were observed and CH_4 concentrations at nearly all sampling points were within error of the samples with different Ni additions. The accumulation of methane over 50 days of incubation is nearly linear and no plateau in production was observed.

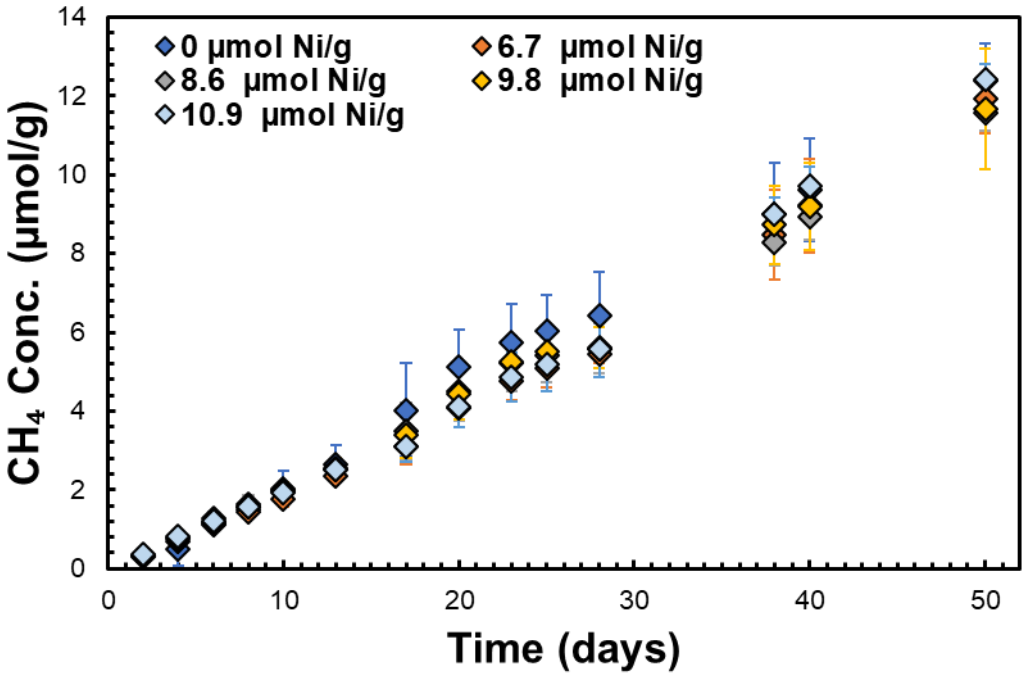

Figure 4.6. Cumulative methane produced from the marsh wetland soils at 5 different Ni concentrations in 50 days incubation. Compositions are averages and standard deviations from triplicate samples; correction of dissolved gas and gas remover during sampling was included.

Dissolved Ni concentrations in marsh wetland soils at 50 d of incubation with no addition of the metal was ~0.14 µM (Figure 4.7). Addition of Ni to the incubations increased this value to 0.5±0.1 to 4.1±0.5 µM. The different addition levels required to produce similar dissolved concentrations reflect marsh wetland soil having a much greater adsorption capacity than the riparian wetland soil. For both soils, >98% of the added Ni adsorbed to the soil. The final dissolved Ni concentrations are all within or exceed the optimal range identified in pure culture studies for acetolactic (2 µM) or hydrogenotrophic (0.2 to 1 µM) methanogenesis (Glass and Orphan, 2012).

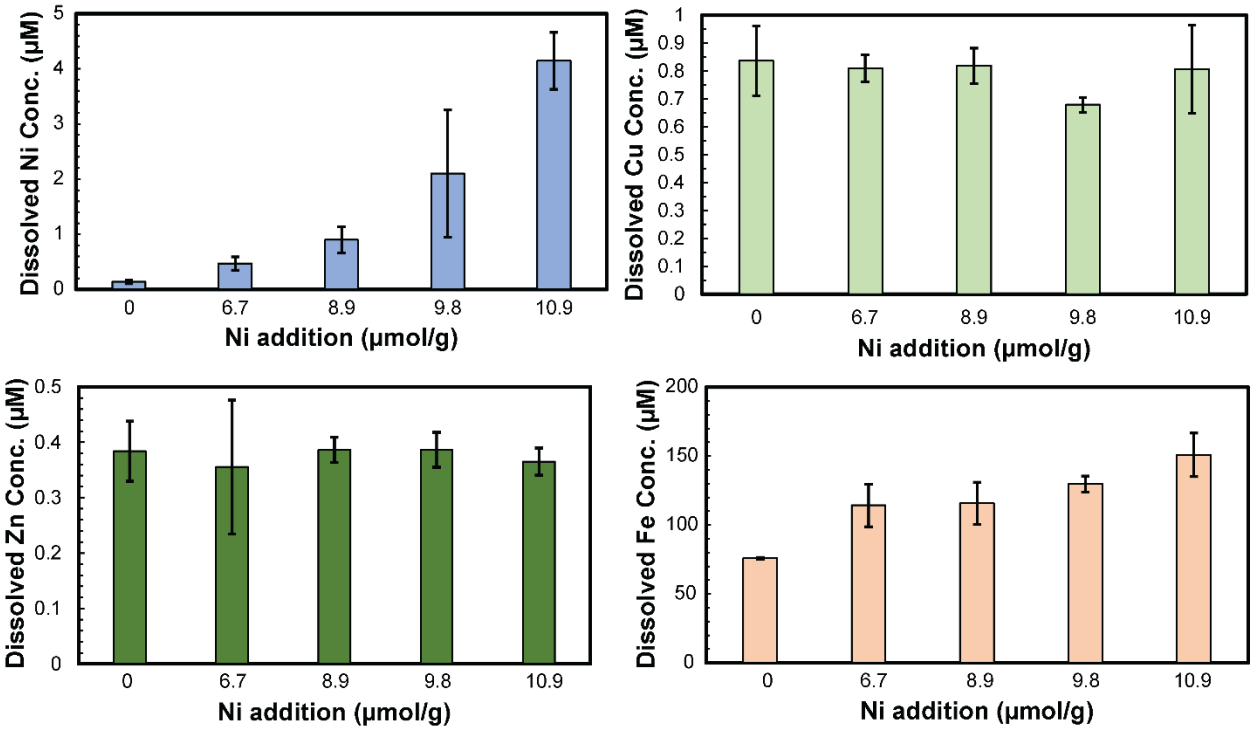

Figure 4.7. Dissolved Cu, Ni, Zn, and Fe concentrations in the final filtrate solutions from the marsh wetland soil after 50 d incubation.

Dissolved Zn and Cu concentrations (Figure 4.7) showed no variation with increasing Ni addition, with Zn concentrations from ~0.36 to ~0.39 µM, and Cu concentrations from ~0.7 to ~0.8 µM. Dissolved Fe concentrations showed a systematic increase with increasing Ni concentration. In marsh wetland experiment, pH did not change substantially during the incubations (Figure 4.5B). The starting pH was from 6.8 to 7.3, while the range of ending pH changed to 6.9 to 7.4.

4.4.4 Impacts of Sulfate on Ni Limitations in the Marsh Wetland Soil

The divergent responses of the two wetland soils to Ni addition occurred despite similar dissolved Ni concentrations for the unamended soils. One substantial difference between the two

wetland sites is the dissolved sulfate concentrations, with the marsh wetland surface water having ~70× sulfate of the riparian system. The marsh wetland contains 576 µM dissolved sulfate, which corresponds to 5.76 µmol SO_4^{2-}/g soil in the soil incubations, approximately 50% of the total CH_4 produced. The process of sulfate reduction converts sulfate to sulfide and oxidizes organic matter and H_2, consuming possible electron donors for methane production. Sulfate reducing bacteria are also more efficient competitors for labile carbon and hydrogen. Though the suppression of methane emission was mostly observed in marine systems, which commonly contain high sulfate concentrations, such effects are also observed in freshwater peatland and wetland systems (Dise and Verry, 2001; Gauci et al., 2002; Gauci et al., 2004; Gauci et al., 2008). This study was not planned to investigate the suppression effect of sulfate on methane production, but relatively high concentration of sulfate in marsh wetland may potentially impact Ni limitation effects. The competition between sulfate reduction and methanogenesis pathways could cause a partial substrate limitation, which results in the prevention of the appearance of Ni limitation. Previous studies have demonstrated a decrease in methane production caused by substrate constraints (Lokshina and Vavilin, 1999; Kelley et al., 2012; Chan-Yam et al., 2021). Alternatively, the reduction of sulfate may have led to greater Ni-S aqueous complexes, which may not be available to methanogens (Gauci et al., 2004; Shakeri Yekta et al., 2014; Yekta et al., 2017).

A second set of incubations were conducted using the marsh soil to evaluate whether the sulfate present in the artificial site was affecting CH_4 production and possibly masking potential Ni limitations. This experiment used a different subsample of the surface layer soils collected from the marsh wetland and displayed somewhat lower metal binding capacity compared to the soil used in the original marsh incubations. This necessitated the addition of different amount of

Ni compared to the prior experiment to achieve similar final dissolved concentrations. For these reasons, experiments were performed with and without sulfate present to better enable direct comparison. CH_4 production showed no differences within error for different Ni addition levels or sulfate loadings over a ~7 week incubation period (Figure 4.8). This experiment indicates that sulfate did not affect CH_4 production in this soil and that Ni limitations were not present.

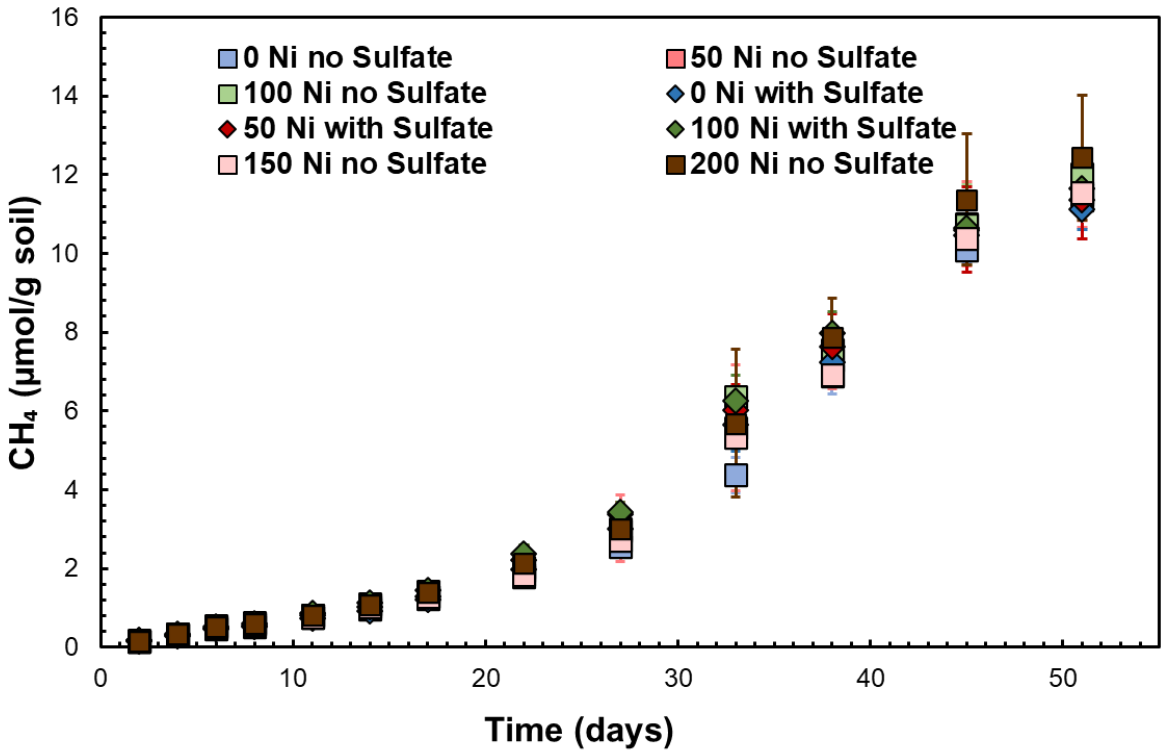

Figure 4.8. Cumulative methane produced from the marsh wetland soils at 5 different Ni concentrations with and without sulfate in 51 days incubation. The unit of Ni addition is µmol/Ni per gram of soil. Compositions are averages and standard deviations from triplicate samples; correction of dissolved gas and gas remover during sampling was included.

Secondary incubations of the marsh wetland soil with and without sulfate in the artificial site water produced similar dissolved SO_4^{2-} concentrations (Figure 4.9), which suggests sulfate in the marsh wetland site water was nearly completely reduced. Ni concentrations with and without sulfate addition were within error for each Ni addition level. This indicates that the presence of sulfate in the marsh wetland soil does not enhance Ni binding, and this does not likely affect Ni availability. The overall Zn and Cu concentrations were slightly higher in the sulfate-free samples. However, dissolved Co concentrations were identical within errors under all conditions studied. In addition, the pH values for both the sulfate-free samples and the samples incubated with sulfate were in the range of 7.15-7.20 (Figure 4.5C and 4.5D), indicating that the presence of sulfate did not affect the pH of the incubation experiments.

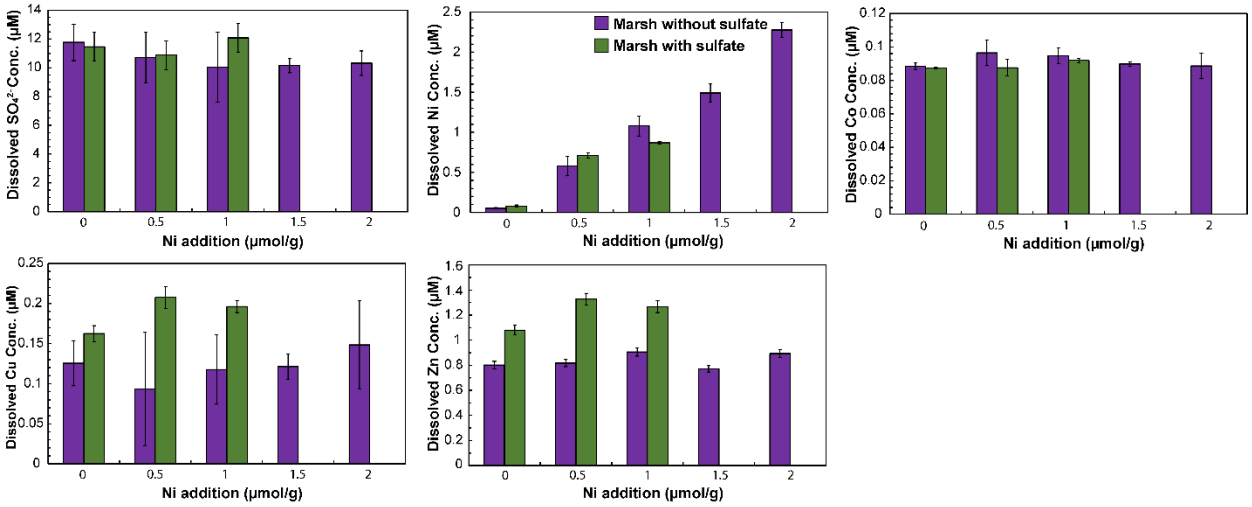

Figure 4.9. Dissolved SO_4^{2-}, Cu, Ni, Co, and Zn concentrations in the final filtrate solutions from the marsh wetland soil with and without sulfate after 51 d incubation.

4.4.5 Comparison to CH_4 Production in Prior Studies

Though marsh wetland yields more than 12 μmol/g of methane, which was 6 times than the riparian site does, this amount seems to be high in this study but was relatively low compared

to other microcosm studies (Basiliko and Yavitt, 2001; Chowdhury et al., 2015). In a study that investigates the temperature response of CO_2 and CH_4 production, up to 75 µmol/g CH_4 was formed at +8 °C at the Low-Centered Polygon center location in a 60-day incubation (Chowdhury et al., 2015). The same sample collected from the Low-Centered Polygon ridge position only yield around 11 µmol/g in a 55-day incubation, which is similar to what we observed at the marsh wetlands (Chowdhury et al., 2015). Another study that carried out at the same room temperature (22 °C) as our study also observes a larger amount of methane production (Basiliko and Yavitt, 2001). More than 50 µmol/g of methane was produced within 20 days of incubation in Basiliko and Yavitt, 2001. A recent study has shown the addition of the trace metals Mo, Cu, and Fe could increase methane production from wetland sediments (Giannopoulos et al., 2020). Up to ~0.9 mmoles of CH_4 was formed within 96 hours of incubation, in which methane emission rate far exceeds what we observed in the current study. Separately, Giannopoulos et al., 2020 has around 17 times of total organic carbon than marsh samples in this study, and yields 50 times more methane; Chowdhury et al., 2015 possesses 4 times carbon than the current study, and produces around 17 times higher methane concentration. A similar study conducted incubation on three peatland soils and found that trace metal limitation did not occur at the study sites (Keller and Wade, 2018). $PbCl_2$ washed samples produced either similar or less amount of CH_4 than unamended sediments (Keller and Wade, 2018).

4.4.6 Environmental Implications

Freshwater wetlands play critical roles in global warming as they serve as important reservoirs for carbon. They act as the most effective carbon sinks and can also serve as a primary

control on the variability of methane emissions (Bousquet et al., 2006; Dlugokencky et al., 2009; Spahni et al., 2011). Previous studies have investigated methane production in a diverse set of wetlands, which produce distinct amounts of methane emission (Chowdhury et al., 2015; Keller and Wade, 2018; Giannopoulos et al., 2020; Chan-Yam et al., 2021). Soil samples from marsh wetland and riparian wetland in this study also yield very different concentration of CH_4, with the former six times greater than the latter. These two aquatic systems displayed different responses to Ni addition, with riparian wetland soil showing a clear increase in methane production variation with increased Ni concentrations while the marsh wetland soil displayed no response. This indicates that the function of wetland sites as carbon sinks and sources may vary geographically. The riparian and marsh wetland investigated in this study have shown surprising uniformity in the speciation of trace metals while geographically distant (Yan et al., 2022), which suggests aquatic systems with similar chemical properties can still display large variations in greenhouse gas production.

In contrasts with previous studies (Basiliko and Yavitt, 2001; Giannopoulos et al., 2020), the marsh wetland soil in the present study does not show stimulation of methane production by trace metal addition. However, the riparian wetland soil did show increased methane production upon Ni addition. Both soils had similar apparent Ni availability during the incubations. These observations indicate that methane production by freshwater wetland soils displays inconsistent responses to changing dissolved Ni concentrations. This may result a substantial fraction of the dissolved Ni pool in one site was not available to methanogens, such as from differences in complexation by inorganic ligands or DOC. Results from this study along with previous research may serve as indication of the complex relationship between trace metal availability and methane emissions by aquatic systems.

4.5 CONCLUSIONS

Microcosm incubation of soils from two wetland sites were carried out and both yield observable amount of methane despite low trace metal availability. The marsh wetland yields much more methane than the riparian wetland, primarily because the former has a greater organic carbon content than the latter. Limitation of methane production from low Ni availability does not occur in the marsh wetland but do affect the emission from the riparian wetlands. pH display very minor change during the incubation process for the two sites regardless of the amount of Ni added or whether sulfate was present in the site water. The elevated sulfate concentration in marsh wetland did not mask possible limitation effects of Ni on methane production. This study demonstrates that Ni limitations occur to variable extents in freshwater wetlands despite the naturally low dissolved concentration of this trace metal in such systems.

4.6 ACKNOWLEDGEMENTS

This project was supported by U.S. Department of Energy, Office of Science, Office of Biological and Environmental Research, Subsurface Biogeochemical Research program through award no. DE-SC0019422 to Washington University. We thank Dr. Kun Wang and Dr. Piers Koefoed for their assistance with ICP-MS measurement.

4.7 REFERENCES

Antcibor I., Eschenbach A., Zubrzycki S., Kutzbach L., Bolshiyanov D. and Pfeiffer E. M. (2014) Trace metal distribution in pristine permafrost-affected soils of the lena river delta and its hinterland, northern Siberia, Russia. *Biogeosciences* **11**, 1–15.

Avis C. A., Weaver A. J. and Meissner K. J. (2011) Reduction in areal extent of high-latitude wetlands in response to permafrost thaw. *Nat. Geosci.* **4**, 444–448.

Basiliko N. and Yavitt J. B. (2001) Influence of Ni, Co, Fe, and Na additions on methane production in Sphagnum-dominated Northern American peatlands. *Biogeochemistry* **52**, 133–153.

Bohn T. J. and Lettenmaier D. P. (2010) Systematic biases in large-scale estimates of wetland methane emissions arising from water table formulations. *Geophys. Res. Lett.* **37**, L22401.

Bousquet P., Ciais P., Miller J. B., Dlugokencky E. J., Hauglustaine D. A., Prigent C., Van Der Werf G. R., Peylin P., Brunke E. G., Carouge C., Langenfelds R. L., Lathière J., Papa F., Ramonet M., Schmidt M., Steele L. P., Tyler S. C. and White J. (2006) Contribution of anthropogenic and natural sources to atmospheric methane variability. *Nature* **443**, 439–443.

Bousquet P., Ringeval B., Pison I., Dlugokencky E. J., Brunke E. G., Carouge C., Chevallier F., Fortems-Cheiney A., Frankenberg C., Hauglustaine D. A., Krummel P. B., Langenfelds R. L., Ramonet M., Schmidt M., Steele L. P., Szopa S., Yver C., Viovy N. and Ciais P. (2011) Source attribution of the changes in atmospheric methane for 2006-2008. *Atmos. Chem. Phys.* **11**, 3689–3700.

Chan-Yam K., Meyer T., Ashley Scott J. and Basiliko N. (2021) Methane production potential of pulp mill sludges: Microbial community and substrate constraints. *FEMS Microbiol. Lett.* **368**, 1–10.

Chen Y. H. and Prinn R. G. (2006) Estimation of atmospheric methane emissions between 1996 and 2001 using a three-dimensional global chemical transport model. *J. Geophys. Res. Atmos.* **111**, D10307.

Chowdhury T. R., Herndon E. M., Phelps T. J., Elias D. A., Gu B., Liang L., Wullschleger S. D. and Graham D. E. (2015) Stoichiometry and temperature sensitivity of methanogenesis and CO_2 production from saturated polygonal tundra in Barrow, Alaska. *Glob. Chang. Biol.* **21**, 722–737.

Demirel B. and Scherer P. (2011) Trace element requirements of agricultural biogas digesters during biological conversion of renewable biomass to methane. *Biomass and Bioenergy* **35**, 992–998.

Dise N. B. and Verry E. S. (2001) Suppression of peatland methane emission by cumulative sulfate deposition in simulated acid rain. *Biogeochemistry* **53**, 143–160.

Dlugokencky E. J., Bruhwiler L., White J. W. C., Emmons L. K., Novelli P. C., Montzka S. A.,

Masarie K. A., Lang P. M., Crotwell A. M., Miller J. B. and Gatti L. V. (2009) Observational constraints on recent increases in the atmospheric CH_4 burden. *Geophys. Res. Lett.* **36**, L18803.

Egger M., Hagens M., Sapart C. J., Dijkstra N., van Helmond N. A. G. M., Mogollón J. M., Risgaard-Petersen N., van der Veen C., Kasten S., Riedinger N., Böttcher M. E., Röckmann T., Jørgensen B. B. and Slomp C. P. (2017) Iron oxide reduction in methane-rich deep Baltic Sea sediments. *Geochim. Cosmochim. Acta* **207**, 256–276.

Gauci V., Dise N. B., Howell G. and Jenkins M. E. (2008) Suppression of rice methane emission by sulfate deposition in simulated acid rain. *J. Geophys. Res. Biogeosciences* **113**, 143–160.

Gauci V., Dise N. and Fowler D. (2002) Controls on suppression of methane flux from a peat bog subjected to simulated acid rain sulfate deposition. *Global Biogeochem. Cycles* **16**, 4-1-4–12.

Gauci V., Matthews E., Dise N., Walter B., Koch D., Granberg G. and Vile M. (2004) Sulfur pollution suppression of the wetland methane source in the 20th and 21st centuries. *Proc. Natl. Acad. Sci. U. S. A.* **101**, 12583–12587.

Giannopoulos G., Hartop K. R., Brown B. L., Song B., Elsgaard L. and Franklin R. B. (2020) Trace metal availability affects greenhouse gas emissions and microbial functional group abundance in freshwater wetland sediments. *Front. Microbiol.* **11**, 560861.

Glass J. B. and Orphan V. J. (2012) Trace metal requirements for microbial enzymes involved in the production and consumption of methane and nitrous oxide. *Front. Microbiol.* **3**, 1–20.

Glass J. B., Yu H., Steele J. A., Dawson K. S., Sun S., Chourey K., Pan C., Hettich R. L. and Orphan V. J. (2014) Geochemical, metagenomic and metaproteomic insights into trace metal utilization by methane-oxidizing microbial consortia in sulphidic marine sediments. *Environ. Microbiol.* **16**, 1592–1611.

Hassan N. M., Rasmussen P. E., Dabek-Zlotorzynska E., Celo V. and Chen H. (2007) Analysis of environmental samples using microwave-assisted acid digestion and inductively coupled plasma mass spectrometry: Maximizing total element recoveries. *Water. Air. Soil Pollut.* **178**, 323–334.

Hodson E. L., Poulter B., Zimmermann N. E., Prigent C. and Kaplan J. O. (2011) The El Niño-Southern Oscillation and wetland methane interannual variability. *Geophys. Res. Lett.* **38**, L08810.

Hoehler T. M. and Alperin M. J. (2014) Biogeochemistry: Methane minimalism. *Nature* **507**, 436–437.

Hopcroft P. O., Valdes P. J. and Beerling D. J. (2011) Simulating idealized Dansgaard-Oeschger events and their potential impacts on the global methane cycle. *Quat. Sci. Rev.* **30**, 3258–3268.

Keller J. K. and Wade J. (2018) No evidence for trace metal limitation on anaerobic carbon mineralization in three peatland soils. *Geoderma* **314**, 95–101.

Kelley C. A., Poole J. A., Tazaz A. M., Chanton J. P. and Bebout B. M. (2012) Substrate limitation for methanogenesis in hypersaline environments. *Astrobiology* **12**, 89–97.

Kida K., Shigematsu T., Kijima J., Numaguchi M., Mochinaga Y., Abe N. and Morimura S. (2001) Influence of Ni^{2+} and Co^{2+} on methanogenic activity and the amounts of coenzymes involved in methanogenesis. *J. Biosci. Bioeng.* **91**, 590–595.

Kirschke S., Bousquet P., Ciais P., Saunois M., Canadell J. G., Dlugokencky E. J., Bergamaschi P., Bergmann D., Blake D. R., Bruhwiler L., Cameron-Smith P., Castaldi S., Chevallier F., Feng L., Fraser A., Heimann M., Hodson E. L., Houweling S., Josse B., Fraser P. J., Krummel P. B., Lamarque J. F., Langenfelds R. L., Le Quéré C., Naik V., O'doherty S., Palmer P. I., Pison I., Plummer D., Poulter B., Prinn R. G., Rigby M., Ringeval B., Santini M., Schmidt M., Shindell D. T., Simpson I. J., Spahni R., Steele L. P., Strode S. A., Sudo K., Szopa S., Van Der Werf G. R., Voulgarakis A., Van Weele M., Weiss R. F., Williams J. E. and Zeng G. (2013) Three decades of global methane sources and sinks. *Nat. Geosci.* **6**, 813–823.

Koretsky C. M., Haas J. R., Ndenga N. T. and Miller D. (2006) Seasonal variations in vertical redox stratification and potential influence on trace metal speciation in minerotrophic peat sediments. *Water. Air. Soil Pollut.* **173**, 373–403.

Loeb R., Van Daalen E., Lamers L. P. M. and Roelofs J. G. M. (2007) How soil characteristics and water quality influence the biogeochemical response to flooding in riverine wetlands. *Biogeochemistry* **85**, 289–302.

Lokshina L. Y. and Vavilin V. A. (1999) Kinetic analysis of the key stages of low temperature methanogenesis. *Ecol. Modell.* **117**, 285–303.

Lovley D. R. and Phillips E. J. P. (1987) Competitive Mechanisms for Inhibition of Sulfate Reduction and Methane Production in the Zone of Ferric Iron Reduction in Sediments. *Appl. Environ. Microbiol.* **53**, 2636–2641.

Melton J. R., Wania R., Hodson E. L., Poulter B., Ringeval B., Spahni R., Bohn T., Avis C. A., Beerling D. J., Chen G., Eliseev A. V., Denisov S. N., Hopcroft P. O., Lettenmaier D. P., Riley W. J., Singarayer J. S., Subin Z. M., Tian H., Zürcher S., Brovkin V., Van Bodegom P. M., Kleinen T., Yu Z. C. and Kaplan J. O. (2013) Present state of global wetland extent and wetland methane modelling: Conclusions from a model inter-comparison project (WETCHIMP). *Biogeosciences* **10**, 753–788.

Patel G. B., Khan A. W. and Roth L. A. (1978) Optimum levels of sulphate and iron for the cultivation of pure cultures of methanogens in synthetic media. *J. Appl. Bacteriol.* **45**, 347–356.

Riley W. J., Subin Z. M., Lawrence D. M., Swenson S. C., Torn M. S., Meng L., Mahowald N. M. and Hess P. (2011) Barriers to predicting changes in global terrestrial methane fluxes: Analyses using CLM4Me, a methane biogeochemistry model integrated in CESM. *Biogeosciences* **8**, 1925–1953.

Ringeval B., Decharme B., Piao S. L., Ciais P., Papa F., De Noblet-Ducoudré N., Prigent C.,

Friedlingstein P., Gouttevin I., Koven C. and Ducharne A. (2012) Modelling sub-grid wetland in the ORCHIDEE global land surface model: Evaluation against river discharges and remotely sensed data. *Geosci. Model Dev.* **5**, 941–962.

Ringeval B., Friedlingstem P., Koven C., Ciais P., de Noblet-Ducoudre N., Decharm B. and Cadule P. (2011) Climate-CH_4 feedback from wetlands and its interaction with the climate-CO_2 feedback. *Biogeosciences Discuss.* **8**, 3203.

Ringeval B., Hopcroft P. O., Valdes P. J., Ciais P., Ramstein G., Dolman A. J. and Kageyama M. (2013) Response of methane emissions from wetlands to the Last Glacial Maximum and an idealized Dansgaard–Oeschger climate event: Insights from two models of different complexity. *Clim. Past* **9**, 149–171.

Roden E. E. and Wetzel R. G. (1996) Organic carbon oxidation and suppression of methane production by microbial Fe(III) oxide reduction in vegetated and unvegetated freshwater wetland sediments. *Limnol. Oceanogr.* **41**, 1733–1748.

Rudnick R. L. and Gao S. (2003) Composition of the continental crust In *Treatise on Geochemistry* (eds. K.K. Turekian and H.D. Holland). In *Treatise on Geochemistry. Pergamon, Oxford* Elsevier. pp. 1–64.

Segarra K. E. A., Schubotz F., Samarkin V., Yoshinaga M. Y., Hinrichs K. U. and Joye S. B. (2015) High rates of anaerobic methane oxidation in freshwater wetlands reduce potential atmospheric methane emissions. *Nat. Commun.* **6**, 7477.

Sela-Adler M., Ronen Z., Herut B., Antler G., Vigderovich H., Eckert W. and Sivan O. (2017) Co-existence of methanogenesis and sulfate reduction with common substrates in sulfate-rich estuarine sediments. *Front. Microbiol.* **8**, 766.

Serrano-Silva N., Sarria-Guzmán Y., Dendooven L. and Luna-Guido M. (2014) Methanogenesis and methanotrophy in soil: A review. *Pedosphere* **24**, 291–307.

Shakeri Yekta S., Svensson B. H., Björn A. and Skyllberg U. (2014) Thermodynamic modeling of iron and trace metal solubility and speciation under sulfidic and ferruginous conditions in full scale continuous stirred tank biogas reactors. *Appl. Geochemistry* **47**, 61–73.

Spahni R., Wania R., Neef L., Van Weele M., Pison I., Bousquet P., Frankenberg C., Foster P. N., Joos F., Prentice I. C. and Van Velthoven P. (2011) Constraining global methane emissions and uptake by ecosystems. *Biogeosciences* **8**, 1643–1665.

Sturm K., Keller-Lehmann B., Werner U., Raj Sharma K., Grinham A. R. and Yuan Z. (2015) Sampling considerations and assessment of Exetainer usage for measuring dissolved and gaseous methane and nitrous oxide in aquatic systems. *Limnol. Oceanogr. Methods* **13**, 375–390.

Tang J. Y., Riley W. J., Koven C. D. and Subin Z. M. (2013) CLM4-BeTR, a generic biogeochemical transport and reaction module for CLM4: model development, evaluation, and application. *Geosci. Model Dev.* **6**, 127–140.

Tang J., Zhuang Q., Shannon R. D. and White J. R. (2010) Quantifying wetland methane

emissions with process-based models of different complexities. *Biogeosciences* **7**, 3817–3837.

Thauer R. K. (1998) Biochemistry of methanogenesis: a tribute to Marjory Stephenson:1998 Marjory Stephenson Prize Lecture. *Microbiology* **144**, 2377–2406.

Tian H., Lu C., Chen G., Tao B., Pan S., Del Grosso S. J., Xu X., Bruhwiler L., Wofsy S. C., Kort E. A. and Prior S. A. (2012) Contemporary and projected biogenic fluxes of methane and nitrous oxide in North American terrestrial ecosystems. *Front. Ecol. Environ.* **10**, 528–536.

Valentine D. W., Holland E. A. and Schimel D. S. (1994) Ecosystem and physiological controls over methane production in northern wetlands. *J. Geophys. Res.* **99**, 1563.

Vile M. A., Bridgham S. D., Wieder R. K. and Novák M. (2003) Atmospheric sulfur deposition alters pathways of gaseous carbon production in peatlands. *Global Biogeochem. Cycles* **17**, 1058.

Wania R., Ross I. and Prentice I. C. (2010) Implementation and evaluation of a new methane model within a dynamic global vegetation model: LPJ-WHyMe v1.3.1. *Geosci. Model Dev.* **3**, 565–584.

Watson A. and Nedwell D. B. (1998) Methane production and emission from peat. *Atmos. Environ.* **32**, 3239–3245.

Williams C. M., Shih J. C. H. and Spears J. W. (1986) Effect of nickel on biological methane generation from a laboratory poultry waste digester. *Biotechnol. Bioeng.* **28**, 1608–1610.

Xu X., Schimel J. P., Thornton P. E., Song X., Yuan F. and Goswami S. (2014) Substrate and environmental controls on microbial assimilation of soil organic carbon: A framework for Earth system models. *Ecol. Lett.* **17**, 547–555.

Yan J., Sharma N., Flynn E. D., Giammar D. E., Schwartz G. E., Brooks S. C., Weisenhorn P., Kemner K. M., O'Loughlin E. J., Kaplan D. I. and Catalano J. G. (2022) Consistent controls on trace metal micronutrient speciation in wetland soils and stream sediments. *Geochim. Cosmochim. Acta* **317**, 234–254.

Yekta S. S., Skyllberg U., Danielsson Å., Björn A. and Svensson B. H. (2017) Chemical speciation of sulfur and metals in biogas reactors – Implications for cobalt and nickel bio-uptake processes. *J. Hazard. Mater.* **324**, 110–116.

Yvon-Durocher G., Allen A. P., Bastviken D., Conrad R., Gudasz C., St-Pierre A., Thanh-Duc N. and Del Giorgio P. A. (2014) Methane fluxes show consistent temperature dependence across microbial to ecosystem scales. *Nature* **507**, 488–491.

Zürcher S., Spahni R., Joos F., Steinacher M. and Fischer H. (2013) Impact of an abrupt cooling event on interglacial methane emissions in northern peatlands. *Biogeosciences* **10**, 1963–1981.